

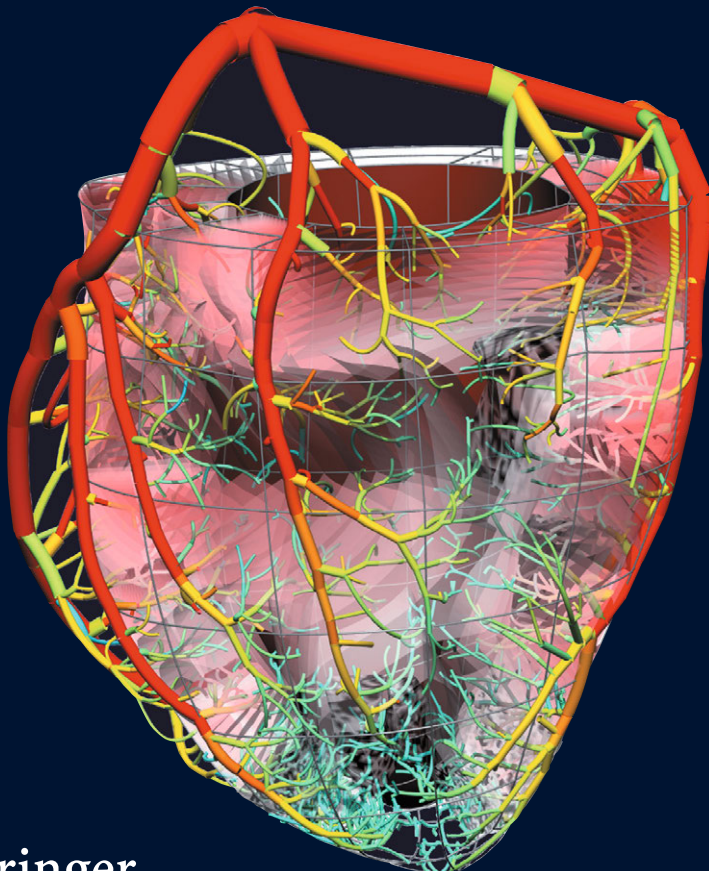
**Volume 14**

# Modeling the Heart and the Circulatory System

Alfio Quarteroni *Editor*

**MS&A**

Modeling, Simulation & Applications



Springer

# **MS&A**

---

## **Volume 14**

---

*Editor-in-Chief*

A. Quarteroni

*Series Editors*

T. Hou

C. Le Bris

A.T. Patera

E. Zuazua

More information about this series at  
<http://www.springer.com/series/8377>

Alfio Quarteroni *Editor*

# **Modeling the Heart and the Circulatory System**



*Editor*

Alfio Quarteroni  
École Polytechnique Fédérale de Lausanne (EPFL)  
Lausanne, Switzerland

ISSN 2037-5255

ISSN 2037-5263 (electronic)

MS&A – Modeling, Simulation & Applications

ISBN 978-3-319-05229-8

ISBN 978-3-319-05230-4 (eBook)

DOI 10.1007/978-3-319-05230-4

Springer Cham Heidelberg New York Dordrecht London

Library of Congress Control Number: 2014954657

© Springer International Publishing Switzerland 2015

This work is subject to copyright. All rights are reserved by the Publisher, whether the whole or part of the material is concerned, specifically the rights of translation, reprinting, reuse of illustrations, recitation, broadcasting, reproduction on microfilms or in any other physical way, and transmission or information storage and retrieval, electronic adaptation, computer software, or by similar or dissimilar methodology now known or hereafter developed.

The use of general descriptive names, registered names, trademarks, service marks, etc. in this publication does not imply, even in the absence of a specific statement, that such names are exempt from the relevant protective laws and regulations and therefore free for general use.

The publisher, the authors and the editors are safe to assume that the advice and information in this book are believed to be true and accurate at the date of publication. Neither the publisher nor the authors or the editors give a warranty, express or implied, with respect to the material contained herein or for any errors or omissions that may have been made.

Cover illustration: Vascular flow velocity and pore pressure distribution in diastole. Courtesy of Jack Lee, Andrew Cookson, Radomir Chabiniok, Simone Rivolo, Eoin Hyde, Matthew Sinclair, Christian Michler, Taha Sochi and Nicolas Smith. From Chapter 3 – Multiscale Modelling of Cardiac Perfusion,

Cover design: Beatrice &, Milano, Italy

Typesetting with L<sup>A</sup>T<sub>E</sub>X: PTP-Berlin, Protago T<sub>E</sub>X-Production GmbH, Germany ([www.ptp-berlin.de](http://www.ptp-berlin.de))

Springer is a part of Springer Science+Business Media ([www.springer.com](http://www.springer.com))

# Preface

This book contains a selection of the contributions presented at MPF2013 in June 2013 in Chia Laguna (Sardinia), the fifth edition of a series devoted to the mathematical and numerical modeling of physiological flows.

The focus of this fifth symposium was on data analysis, digital imaging, mathematical models, and numerical simulation of the human circulatory system as a whole, and more specifically on cardiac mechanics and electrophysiology, heart perfusion, ventricular fluid dynamics, fluid-vessel wall interactions, multiscale analysis of blood rheology in small vessels, and system integration. The contributions presented in this book provide a very interesting overview on the state of the art of some of these topics and contain several original contributions to the field. What follows is a short account of the most relevant contents of each chapter.

In the first chapter, written by N. Trayanova and coauthors, it is explained how biophysically detailed simulations can clarify experimental observations and help reveal how organ-scale arrhythmogenic phenomena emerge from pathological effects at the tissue, cell, and protein levels. This “virtual heart” approach seeks to use experiments and simulation to quantitatively characterize the action potential response of cardiac cells to electrical stimuli.

The construction of multiscale models of the electrical functioning of the heart aims at representing the integrative behavior from the molecule to the entire organ and is an essential methodological step towards clinical applications of cardiac organ modeling. This chapter focuses on both achievements in mechanistic understanding of heart function and dysfunction and on the trends in the computational medicine aspect of biophysically detailed cardiac modeling applications.

Key in attaining predictive capabilities of multiscale biophysically detailed cardiac models at the level of the organ has been the use of geometrically realistic (typically MRI- or CT-based) models of the ventricles and the application of diffusion tensor imaging to measure the anatomy, fiber, and sheet structure of the heart in ex vivo studies. Models of cardiac function have benefitted significantly from this revolution in medical imaging. Cardiac models have been used to gain insights into mechanisms of arrhythmia in many disease settings and to understand how external currents can terminate ventricular arrhythmias.

The most frequently applied approach to model the mechanics of cardiac tissue is based on continuum mechanics. There is, however, another possibility based on the use of discrete mechanical approaches. In Chapter 2, written by A.V. Panfilov and coauthors, discrete mechanical models are proposed for the simulation of the mechanoelectrical feedback (MEF) on the process of spiral wave formation in cardiac tissue. The two principal ways of formulating discrete mechanical models of cardiac tissue are presented. The so-called off-lattice models, which describe cells as not being restricted to a regular grid, allow the description of biological phenomena such as cell division and growth without causing immediate mechanical long-range effects. Lattice-based models are instead more appropriate for describing mechanical long-range interactions such as the finite elastic deformations of the heart tissue.

MEF is the effect of the deformation of cardiac tissue on its excitation processes. This chapter shows that MEF substantially affects the process of spiral wave initiation and discusses several new mechanisms that are found using the proposed discrete mechanical approach.

Another study concerns the effect of structural changes in cardiac tissue on the heart's mechanical properties and, further, how these effects may cause cardiac arrhythmia. The authors also propose and investigate how to couple a discrete mechanical model to a reaction-diffusion model for continuous electrical pulse propagation.

In Chapter 3, N. Smith and co-authors investigate the mechanisms governing coronary blood flow in healthy and diseased coronaries, with the aim of understanding the relationship between the structure of the coronary vasculature and its function, which exhibits distinct characteristics over multiple scales. More specifically, the coupled fluid-structure model of coronary flow outlined in this chapter aims to bring together the principal components of the system to establish an integrated framework for investigating and, later, predicting myocardial perfusion on an individual-specific basis in a physiologically relevant manner. To this end a model of flow in macroscopic arteries [the left anterior descending (LAD), left circumflex (LCx), and right coronary (RCA) arteries], a multicompartiment Darcy model representing myocardial perfusion over a range of vessel sizes, and a poroelastic model capturing the flow phenomena in the beating heart are proposed. Wave intensity analysis and tissue signal in perfusion MRI, both of which representing the current state of the art in invasive and noninvasive cardiological exams, create a basis for clinical translation of the present work.

In Chapter 4, written by F. Nicoud and coauthors, the geometry of the heart cavities and associated wall motion are extracted from 4D medical images while the valves of the heart are simulated by using low-order geometrical models. Equations are solved using a fourth-order low-dissipative finite-volume scheme and a mixed arbitrary Lagrangian-Eulerian/immersed boundary framework.

Recent technological innovations in imaging techniques have provided valuable opportunities for direct noninvasive *in vivo* assessment of hemodynamics. Blood flow velocities can be measured *in vivo* using phase-contrast magnetic resonance. Medical images are then used to generate a moving patient-specific domain, in which the blood flow equations are solved. Heart geometry movements are generated from a 4D sequence. The authors devote specific attention to the generation of high-quality

mesh that deforms consistently with the heart motion. On such a high-quality grid the unsteady turbulent flow is simulated by a large eddy simulation technique in the left heart described by ECG-gated 3D CT scan. The results show that fluid inertia makes the flow differ from one cycle to another in the upper part of the left atrium, where the collision of the jets issuing from the pulmonary veins makes the flow chaotic. In the left ventricle, velocity fluctuations are reported mainly during late diastole.

In Chapter 5, G. Karniadakis and H. Lei present a comprehensive computational framework based on the mesoscale dissipative particle dynamics (DPD) method to investigate the three key hallmarks (heterogeneous morphology, rheology, and vaso-occlusion) of the hematological disorder sickle cell anemia (SCA). The multiscale nature of the DPD model allows the authors to address the different dynamic processes over a wide range of length and time scales involved in this disease. A coarse-grained stochastic model is built up to represent the development of the intracellular aligned sickle hemoglobin polymer domain for sickle red blood cells (SS-RBC). Using only the experimentally measured bulk growth rate of the sickle hemoglobin polymer as the input, the model successfully predicted the typical sickle cell morphologies without introducing further ad hoc assumptions. The inferred cell morphologies enabled the authors to further explore the rheology of heterogeneous SS-RBCs suspensions with accurate prediction of the shear viscosity for the different cell rigidity and morphologies. In particular, their simulations of the hemodynamics of SS-RBC suspensions suggested that the sickle/elongated SS-RBC suspension, once in microcirculation, does not induce vaso-occlusion by itself. Moreover the flow resistance induced by this cell group could be even lower than that induced by other cell groups. Despite being counterintuitive, this result is consistent with recent experimental studies on vaso-occlusion crisis.

In Chapter 6, written by A. Gizzi and coauthors, the mathematical model formulation of the mechanochemical coupling in single cardiomyocytes based on an active strain approach has been analyzed and extended to realistic three-dimensional geometries. The proposed activation mechanism is consistent with a thermodynamic framework entailing a nonlinear coupling among calcium dynamics and local stretches. The continuum approach adopted is along the line of recent bio-chemomechanical models of single cells formulated in terms of active-strain hyperelasticity. The model is capable of reproducing the propagation of calcium waves and the corresponding spontaneous contraction within the cell, as well as the bending behavior, peculiar features of a three-dimensional structure. A finite element method is used to discretize the model equations; a set of numerical experiments comparing two- and three-dimensional reconstructed cardiomyocyte geometries provide evidence of the main features of the model and its ability to predict calcium propagation patterns and contractility, in good agreement with experimental observations. Different boundary conditions are considered to reproduce physiological constraints. The corresponding resulting stress patterns are then analyzed.

Chapter 7, written by K.A. Mardal and O. Evju, develops a critical review on the assumption of laminar flow in physiological flow applications. Most fluid flows in our human body are believed to be laminar in healthy individuals, an exception being the blood flow in the heart and aorta. On the other hand, various pathologies, such

as atherosclerosis and aneurysms, involve anatomical alterations causing distributed flow and possibly even turbulent flow. This may lead to an unhealthy mechanotransduction (the process whereby cells convert mechanical stimuli to chemical activity, which is vital in the remodeling that occurs in vessels), causing remodeling of the vasculature that again increases flow disturbances. Recent research has therefore challenged the assumption of laminar flow in such pathologies and placed the focus on the possible role of transitional or turbulent flow.

While the laminar regime and in many applications the fully developed turbulent regime are reasonably well understood from both a modeling and a numerical point of view, the transitional regime with occasional turbulence poses additional challenges. Modeling is difficult in particular because it is challenging to precisely predict the onset of the turbulent spots. Instead of modeling the turbulence, one might increase the resolution in space and time and resolve all scales of the turbulent flow numerically, a technique called direct numerical simulation (DNS).

The authors address blood flow in cerebral aneurysms, discussing the consequences of the assumption of laminar flow, and validate the use of stabilization techniques and time discretizations on numerical dissipation. They also review clinical and biomechanical findings suggesting that transitional flow is common or at least not unusual in several pathologies. Finally they discuss cerebral aneurysms in depth and show that for some aneurysms transition may occur at a Reynolds number as low as 300.

In Chapter 8, P. Zunino and coauthors investigate the effects of poroelasticity on fluid-structure interaction in arteries. Blood flow is modeled as an incompressible Newtonian fluid confined by a poroelastic wall. A two-layer model is used for the artery, where the inner layers (the endothelium and the intima) behave as a thin membrane modeled as a linearly elastic Koiter shell, while the outer part of the artery (the media and adventitia) is described by the Biot model. The assumptions are made that the membrane can transduce displacements and stresses to the artery and that it is permeable to flow. Because of poroelasticity, the interaction of the fluid and the structure at the interface is more complicated than in the case of a standard fluid-structure interaction problem. The weak enforcement of interface conditions based on Nitsche's type mortaring techniques guarantees stability. In particular, the authors are interested in qualitatively characterizing how the presence of intramural flow coupled to the arterial wall deformation affects the displacement field as well as the propagation of pressure waves. Their results suggest that accounting for the intramural plasma filtration significantly affects the arterial wall displacement as well as the propagation of pressure waves. However, it is observed that resorting to a poroelastic material model is not essential to capture these effects. A simpler model based on Darcy equations combined with approximate kinematic conditions may be adequate to capture similar effects.

Chapter 9, written by Y. Vassilevski and coauthors, addresses the process of generating anatomical meshes of the entire human body. According to the authors, the ideal approach for construction of an anatomically correct 3D geometric model is to produce 3D geometry from individual medical images (CT, MRI, or other slice-like data). This requires strong involvement of human expertise. Moreover, such data

can be unavailable or may feature low quality due to several factors. The authors propose an alternative approach that consists in fitting a reference anatomically correct model based on either individual data or detailed post-mortem examination or a conventional database.

For patient-specific body meshing the authors adopt a four-stage algorithm which relies on the assumption that the patient has the same structural body composition as the reference VHP (the Visible Human Project) model, i.e., the same set of tissues and organs. First, they apply the semiautomatic segmentation of the reference VHP images. Second, they perform the anthropometric mapping of the reference model to the patient dimensions. Third, for selected cross-section planes they generate a piecewise affine transformation to map the reference segmentation to the patient segmentation on the basis of user-defined control points on both references and patient images.

For patient-specific vascular network reconstruction the open source library VMTK is adopted to produce vascular centerlines on the basis of CT/MRI data followed by the automated “skeletonization” algorithm. The produced vascular graph possesses all the necessary geometric data for hemodynamic simulation. The authors demonstrate the applicability of their approach to predictive personalized postsurgical blood flow simulations.

Lausanne, October 2014

Alfio Quarteroni

## Acknowledgements

I would like to express my warmest thanks to my co-organizers, Simone Deparis and Luca Dedè from EPFL, Davide Ambrosi from Politecnico di Milano, Gianluigi Rozza from EPFL (now at SISSA, Trieste); to Corinne Craman from EPFL; and to Francesca Bonadei and Francesca Ferrari from Springer for their help and dedication during the review process and the editorial preparation of this book. I would also like to acknowledge my ERC Advanced Grant MATHCARD (ERC-2008-AdG-2270058) for the generous support of my research on this subject during the past five years and for having made this Conference possible.

# Contents

- 1 **Cardiac Arrhythmias: Mechanistic Knowledge and Innovation from Computer Models** ..... 1  
Natalia A. Trayanova and Patrick M. Boyle
- 2 **Discrete Mechanical Modeling of Mechanoelectrical Feedback in Cardiac Tissue: Novel Mechanisms of Spiral Wave Initiation** ..... 29  
Louis D. Weise and Alexander V. Panfilov
- 3 **Multiscale Modelling of Cardiac Perfusion** ..... 51  
Jack Lee, Andrew Cookson, Radomir Chabinick, Simone Rivolo, Eoin Hyde, Matthew Sinclair, Christian Michler, Taha Sochi and Nicolas Smith
- 4 **Using Image-based CFD to Investigate the Intracardiac Turbulence** . 97  
Christophe Chnafa, Simon Mendez, Ramiro Moreno and Franck Nicoud
- 5 **Multiscale Modeling of Sickle Cell Anemia** ..... 119  
Huan Lei and George Em Karniadakis
- 6 **A Three-dimensional Continuum Model of Active Contraction in Single Cardiomyocytes** ..... 157  
Alessio Gizzi, Ricardo Ruiz-Baier, Simone Rossi, Aymen Laadhari, Christian Cherubini, and Simonetta Filippi
- 7 **On the Assumption of Laminar Flow in Physiological Flows: Cerebral Aneurysms as an Illustrative Example** ..... 177  
Øyvind Evju and Kent-Andre Mardal
- 8 **Effects of Poroelasticity on Fluid-Structure Interaction in Arteries: a Computational Sensitivity Study** ..... 197  
Martina Bukac, Ivan Yotov, Rana Zakerzadeh and Paolo Zunino

<b>9 Personalized Anatomical Meshing of the Human Body with Applications .....</b>	221
Yuri Vassilevski, Alexander Danilov, Yuri Ivanov, Sergey Simakov and Timur Gamilov	

---

# Cardiac Arrhythmias: Mechanistic Knowledge and Innovation from Computer Models

Natalia A. Trayanova and Patrick M. Boyle

**Abstract** Computational simulation is increasingly recognized as an integral aspect of modern cardiovascular research. Realistic and biophysically detailed models of the cardio-circulatory system can help interpret complex experimental observations, dissect underlying mechanisms, and explain emerging organ-scale phenomena resulting from subtle changes at the tissue, cellular, and/or sub-cellular scales. This chapter provides an overview of recent advances in the simulation of cardiac electrical behavior, focusing specifically on detailed models of the initiation, perpetuation, and termination of ventricular arrhythmias, including fibrillation. The development and validation of such models has opened several noteworthy avenues of research, including close scrutiny of arrhythmia dynamics in healthy and diseased hearts, dissection of arrhythmogenic and cardioprotective properties of specialized cardiac tissue regions such as the Purkinje system, and exploration of emerging paradigms for anti-arrhythmia treatment, such as optogenetics. Excitingly, the clinical community is currently taking the first steps towards using patient-specific ventricular models to stratify arrhythmia risk, personalize treatment planning, and optimize device placement for difficult or unusual procedures.

## 1.1 Introduction

Computer modeling has emerged as a powerful platform for the investigation of lethal heart rhythm disorders. Biophysically detailed simulations can clarify experimental observations and help reveal how organ-scale arrhythmogenic phenomena (ectopic heartbeats, conduction failure, electrical turbulence, etc.) emerge from pathological effects at the tissue, cell, and protein levels. The development of this ex-

---

N.A. Trayanova (✉) · P.M. Boyle

Institute for Computational Medicine, Johns Hopkins University, 3400 N Charles St, 316 Hackerman Hall, Baltimore MD 21218, USA

e-mail: ntrayanova@jhu.edu; pmboyle@jhu.edu

tensive “virtual heart” methodology [88, 119, 126, 132] builds upon a strong foundation of research that seeks to use experiments and simulation to quantitatively characterize the action potential response of cardiac cells to electrical stimuli. Simulated action potentials arise from the solution of coupled ordinary differential equation (ODE) systems that model transmembrane current flow through ion channels, pumps, and exchangers as well as the movement of calcium ions between sub-cellular domains. The governing equation for transmembrane current ( $I_m$ ) is:

$$I_m = C_m \frac{\partial V_m}{\partial t} + I_{ion}, \quad (1.1)$$

where  $C_m$  is the membrane capacitance,  $V_m$  is the potential difference between the intracellular and extracellular spaces, and  $I_{ion}$  is the sum of all ionic currents through membrane channels, pumps, and exchangers. Individual terms added to  $I_{ion}$  are also governed by differential equations; for example, the classical description of the fast sodium current ( $I_{Na}$ ) is:

$$I_{Na} = \bar{g}_{Na} m^3 h (V_m - E_{Na}), \quad (1.2)$$

where  $\bar{g}_{Na}$  is the maximal conductance (based on single channel conductance and overall expression levels),  $m$  and  $h$  are gating variables defining channel kinetics, and  $E_{Na}$  is the reversal potential for sodium ions. The ODE for  $m$  is:

$$\frac{\partial m}{\partial t} = \alpha_m (1 - m) - \beta_m m = \left[ \frac{0.1 (25 - V_m)}{e^{0.1(25 - V_m)} - 1} \right] (1 - m) - \left[ 4e^{-\frac{V_m}{18}} \right] m, \quad (1.3)$$

where  $\alpha_m$  and  $\beta_m$  are forward and reverse rate constants, respectively. Other gating variables, for  $I_{Na}$  and other  $I_{ion}$  components, are governed by equations of similar form with parameters tuned to match experimentally observed behavior.

More recently, cardiac modeling has also progressed to the level of the tissue and the whole heart, where the propagation of a wave of action potentials is simulated by a reaction–diffusion partial differential equation (PDE):

$$\nabla \cdot \overline{\sigma}_m \nabla V_m = \beta I_m, \quad (1.4)$$

where  $\overline{\sigma}_m$  is the tissue conductivity tensor and  $\beta$  is the myocyte surface area-to-volume ratio. This PDE, known as the monodomain formulation, describes current flow through tissue composed of myocytes that are electrically connected via low-resistance gap junctions. Cardiac tissue has orthotropic electrical conductivities that arise from the cellular organization of the myocardium (cardiac muscle) into fibers and laminar sheets. Global conductivity values are obtained by combining fiber and sheet organization with myocyte-specific local conductivity values. Current flow in the tissue is driven by ionic exchanges across cell membranes during the myocyte action potential. Simultaneous solution of the PDE with the set of action potential ODEs over the tissue volume represents simulation of electrical wave propagation in the myocardium. In certain cases, such as when external current delivery to the

myocardium is simulated, a system of coupled PDEs is used:

$$\nabla \cdot (\bar{\sigma}_i + \bar{\sigma}_e) \nabla \phi_e = -\nabla \cdot \bar{\sigma}_i \nabla V_m - I_e \quad (1.5)$$

$$\nabla \cdot \bar{\sigma}_i \nabla V_m = -\nabla \cdot \bar{\sigma}_i \nabla \phi_e + \beta I_m, \quad (1.6)$$

where  $\bar{\sigma}_i$  and  $\bar{\sigma}_e$  are the intracellular and extracellular conductivity tensors,  $\phi_e$  is the extracellular potential, and  $I_e$  is the current density of extracellular stimulus. This pair of PDEs, known as the bidomain formulation, allows for the explicit representation of current flow in the interstitial (extracellular) space outside cells. Readers interested in a more detailed discussion of the underlying mathematics of cardiac simulations are advised to consult the excellent introductory textbook on bioelectricity by Plonsey and Barr as a starting point [93].

As documented in reviews by Fink et al. [52] and Roberts et al. [101], recent advancements in single-cell action potential modeling have produced building blocks for constructing models of the atria [43, 56, 89], the ventricles [53, 57, 91, 121] and the cardiac conduction system [13, 71, 108, 112, 124] with unprecedented levels of biophysical detail and accuracy. Such developments have helped to fuel the exciting progress made in simulating cardiac electrical behavior at the organ level, which this review is devoted to chronicling. In general, many of the emergent, integrative behaviors in the heart result not only from complex interactions within a specific level but also from feed-forward and feedback interactions that connect a broad range of hierarchical levels of biological organization. The ability to construct multi-scale models of the electrical functioning of the heart, representing integrative behavior from the molecule to the entire organ, is of particular significance since it paves the way for clinical applications of cardiac organ modeling. The review below, while not exhaustive, focuses on both achievements in mechanistic understanding of heart function and dysfunction, and on the trends in the computational medicine aspect of biophysically detailed cardiac modeling applications.

## 1.2 Basic Cardiac Electrophysiology under Normal and Arrhythmic Conditions

The conduction pathways that underlie normal ventricular activation are shown schematically in Fig. 1.1. During a typical heartbeat (a sequence of events often referred to as normal sinus rhythm), excitation originates spontaneously from a specialized tissue region in the right atrium called the sinoatrial node (SAN). Activation then propagates through the atria to the atrioventricular node (AVN), which is normally the only electrical link between the heart's upper and lower chambers. Excitation then enters the His Bundle (HB), which penetrates into the ventricular septum and divides into the Tawara branches, also called the left and right bundle branches; activation then spreads through the Purkinje system (PS), a topologically complex branching network of fast-conducting fibers that are electrically isolated from underlying myocytes except at endpoints, known as Purkinje-myocardial junctions (PMJs). Finally, coordinated activation of the working ventricular myocardium

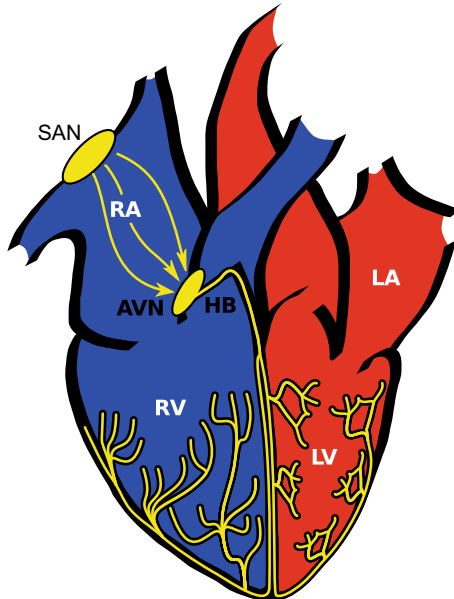


**Fig. 1.1.** Schematic illustration of cardiac structures involved in normal electrical activation during a heartbeat. The right atrium and ventricle (RA and RV; blue), left atrium and ventricle (LA and LV; red), and specialized conduction system (yellow) are highlighted. In a typical heartbeat, electrical activity initiates spontaneously in the sinoatrial node (SAN) then propagates through the RA to the atrioventricular node (AVN); excitation then spreads into the His bundle (HB) and then the Purkinje system (branching network in LV and RV), which is electrically isolated from ventricular myocardium except at its endpoints. Modified with permission from [30]

is initiated by the emergence of excitatory wavefronts from the spatially distributed PMJ network, which covers a large part of the endocardial surface.

Under certain conditions, normal sinus rhythm can be interfered with or completely subverted by aberrant sources of activation. This state, known as arrhythmia, can be driven by spontaneous ectopic excitations originating from deranged tissue outside the SAN or by reentrant activations, which are periodic self-sustaining waves that rotate around organizing centers. Readers interested in a comprehensive review of concepts and terminology related to reentrant sources and an extensive discussion of implications for cardiac arrhythmia dynamics should consult the excellent review recently published by Pandit and Jalife [92].

### 1.3 Simulation of Cardiac Arrhythmia

#### 1.3.1 Pro-Arrhythmic Effects of the Cardiac Conduction System

The PS plays a critical role in the coordination of ventricular excitation but it has also been implicated as a key player in arrhythmia initiation and maintenance [36, 44, 45, 102]. Unfortunately, detailed analysis of PS contributions is difficult because its spatiotemporal excitation sequence in the intact heart must be inferred from low-amplitude electrograms [102]. Moreover, chemical ablation of the PS to isolate arrhythmogenic mechanisms is non-selective, since it also destroys several layers of endocardial cells [37]. Circumventing these limitations, computational modeling has provided important insights on arrhythmias involving the PS that would be impossible to achieve otherwise [14, 32, 33]. For example, ectopic activations from the PS are known to drive catecholaminergic polymorphic ventricular tachycardia (CPVT) [36] but exact organ-scale mechanisms are unknown; Baher et al. [14] proposed an explanation using a 2D ventricular slice model including a representation of the PS. Their study showed that simulation of reciprocating delayed afterpolarization-induced ectopic activations from the left and right sides of the PS gave rise to a bidirectional ECG pattern consistent with CPVT. Another recent study [32] used models of the ventricles with and without the PS to clarify whether elevated endocardial activation rates observed during ventricular fibrillation (VF) were due to activity from nearby PS terminals. Simulations revealed that although PS effects increased the local complexity of VF, transmural rate heterogeneity was most likely caused instead by locally increased expression of ATP-sensitive potassium channels. Finally, in arrhythmias where the PS is a critical part of the reentrant pathway, simulations can be used to guide improvements in clinical diagnosis and treatment. In some patients, the existence of an accessory pathway (AcP) – an abnormal conductive pathway between the atria and ventricles – creates a substrate for macroreentrant supraventricular arrhythmia. Boyle et al. [33] used models with and without AcPs to identify optimal sites for overdrive pacing, a technique used to distinguish AcP-mediated arrhythmia from other tachyarrhythmias [125]. As shown in Fig. 1.2, the diagnostic value of this maneuver was greatly improved by pacing near the suspected AcP and far from PS endpoints. For the case where the ventricles were paced from a site near the PS (Fig. 1.2b), the QRS complexes with AcP (left) and without (right) were indistinguishable; in contrast, for second case (Fig. 1.2c), where the pacing site was located far from PS terminals, the “fused” QRS complex from the simulation with the AcP (left) was visibly different from the purely paced case (right). These studies demonstrate how computer modeling can bypass limitations of in vitro experiments to provide mechanistic insights on arrhythmias involving the PS.

Thus far, arrhythmia contributions have only been studied with simple branching network models of the PS, such as those described above [14, 32, 33]; these models adequately simulate the macroscopic functional role of the specialized tissue but lack geometric complexity. In dissected hearts, PS fibers on the endocardium form a distinct network but 3D imaging of these structures remains difficult [109]; as such, another recent research trajectory has focused on the generation of anatomically re-

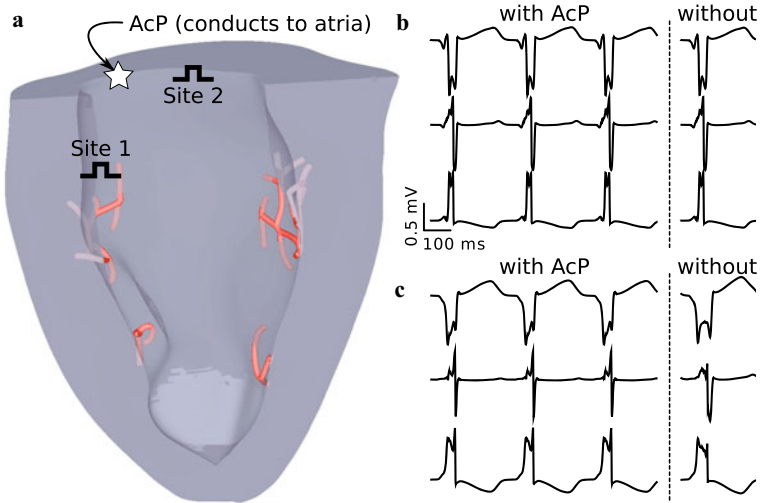


**Fig. 1.2.** (a) Model of the rabbit ventricles (blue) and Purkinje system (PS; red) with two possible ventricular overdrive pacing sites for diagnosis of supraventricular tachycardia, possibly involving an accessory pathway (AcP) between the atria and the ventricles; (b) and (c) Pseudo-ECG recordings (leads I, II, and III) during overdrive pacing from sites 1 and 2, respectively; sites closer to the PS (e.g., site 1) are a poor choice in terms of diagnostic quality because they fail to produce distinct (“fused”) QRS complexes in simulations with (left) versus without (right) the accessory pathway. Modified with permission from [33]

alistic PS models that mimic the physiological network, which could provide insight on how interactions of myocardial tissue with the conduction system affect ventricular arrhythmia dynamics. Ijiri et al. used fractal growth patterns to generate networks that qualitatively resembled the physiological PS [61]. Other groups have adapted this technique [28, 109] to construct patient-specific PS models and explore how PS network complexity affects sinus activation sequence. It will be interesting to see what new insights on PS-mediated arrhythmia dynamics can be gained from simulations that incorporate PS models with increased geometric complexity, which are now a possibility.

### 1.3.2 Mechanisms Underlying Turbulent Dynamics of Cardiac Arrhythmia

Simulation studies of ventricular electrophysiology have made major contributions to understanding the onset of alternans and the dynamics of VF, the most lethal of all arrhythmias. Particularly interesting are the studies on human hearts [114], which revealed that human VF is driven by a small number of reentrant sources, and is thus much more organized than VF in animal hearts of comparable size; the human action potential duration (APD) was found to be responsible for the specific VF dynamics in the human heart. Electrical alternans, which is beat-to-beat varia-

tion in APD, has long been recognized as a precursor to the development of VF. Alternans can be concordant, with the entire tissue experiencing the same phase of oscillation, or discordant, with opposite-phase regions distributed throughout the tissue. The APD restitution curve slope has been viewed as a major factor both in the onset of arrhythmias following the development of discordant alternans and in the dynamic destabilization of reentrant waves leading to the transition of VT into VF. In what has become known as the restitution hypothesis, flattening the APD restitution curve is postulated to inhibit alternans development and subsequent conduction block, and prevent the onset of VF [54]. Simulation studies employing ventricular models [41, 68, 69] have made important contributions to ascertaining the intricate set of mechanisms by and the conditions under which steep APD restitution could lead to VF onset. These include, but are not limited to, the role of electrotonic and memory effects in suppressing alternans and stabilizing reentrant waves, and the effect of heterogeneous restitution properties on human VF.

Wavefront breakup due to steep APD restitution is not the only possible cause of electrical turbulence seen in VF; Alonso et al. recently showed that in a ventricular model with modestly reduced excitability and APD, the organizing centers (filaments) around which scroll waves rotate tend to increase in length, a phenomenon called “negative tension” [4]. As first characterized in geometrically simple 3D models [5, 51], negative tension destabilizes scroll waves, causing increased vorticity and leading to degradation from orderly, VT-like arrhythmias into chaotic VF. Better understanding of negative filament tension could explain situations where VF can be induced despite flat APD restitution.

### ***1.3.3 Mediation of Arrhythmia Dynamics by Mechanically-sensitive Ionic Currents***

One of the most important mechanisms of mechanoelectric coupling in the heart is the existence of sarcolemmal channels that are activated by mechanical stimuli. Of these, stretch-activated channels (SACs) have long been implicated as important contributors to the pro-arrhythmic substrate in the heart. However, uncovering the mechanisms by which SACs contribute to ventricular arrhythmogenesis is hampered by the lack of experimental methodologies that can record the 3D electrical and mechanical activity simultaneously and with high spatiotemporal resolution. Thus, computer simulations have emerged as a valuable tool to dissect the mechanisms by which SACs contribute to the ventricular arrhythmogenic substrate.

Early whole-heart modeling attempts to address the role of SACs in the initiation and termination of arrhythmia by a mechanical impact to the chest used pseudo-electromechanical models, in which mechanical activity was not represented but its effect on ventricular electrophysiology was, through SAC recruitment [74, 75]. True electromechanical models of the ventricles have been recently developed [60, 67], aimed at investigating the effect of mechanoelectric coupling via SACs on ventricular reentrant wave stability. The study by Hu [60] used an MRI-based electromechanical model of the human ventricles to test the hypothesis that SAC recruitment

affects scroll wave stability differently depending on SAC reversal potential and conductance. The study thus provided a mechanistic insight into the change of organization of VF under abnormal stretch.

### ***1.3.4 Virtual Pharmacological Screening for Arrhythmogenic Drugs***

Relating effects of drugs on ion channels beyond the action potential requires virtual tissue or whole heart organ simulation, so that arrhythmia onset, termination and prevention can be explored. Moreno et al. incorporated both state-dependent Markov modeling of drug effects and full integration to the human action potential (AP), human tissue, and finally realistic MRI image-based human heart [84]. This is the first instance of such massive integration across the space and time scales at play. Their study showed that the effects of flecainide and lidocaine on  $I_{Na}$  block are globally similar in response to dynamic protocols. However, clinical trials have shown previously that flecainide tended to be pro-arrhythmic at therapeutic doses, while lidocaine was not. Simulation results made clear that neither simple reduction in  $I_{Na}$ , nor single cell behavior could explain this paradox. However, at the macroscopic scale, the vulnerable window was greater for flecainide than for lidocaine (especially in heart failure simulations due to shortened diastole) and reentrant arrhythmia in the ventricle persisted; as discovered by examining Markov states, this was due to the relatively slow accumulation of and recovery from use-dependent block with flecainide.

A common approach to testing potential drugs for cardiotoxicity is to measure hERG channel binding affinity, which indicates whether a compound will prolong the QT interval of the ECG by blocking the rapid delayed rectifier potassium current ( $I_{Kr}$ ). Many recent studies have sought to use computer modeling to overcome limitations of this screening methodology, such as its high rate of false positives and false negatives. Wilhelms et al. [130] used detailed multiscale models of healthy and ischemic hearts to examine the effects of two drugs that both fail the hERG screening test: cisapride, which is pro-arrhythmic, and amiodarone, which is anti-arrhythmic. Simulations revealed the amiodarone is comparatively safe because in addition to QT prolongation (which was seen for both drugs on simulated ECGs) it also flattened APD restitution. This study and others [35, 48, 136] demonstrate the feasibility of predicting specific drug dose effects on the thoracic ECG. It is hoped that this approach will lead to the development of screening systems that will accelerate cardiotoxicity testing by providing improved reliability compared to the present standard.

### ***1.3.5 Modeling Pathological States to Identify Arrhythmogenic Factors***

Simulations have also been conducted to understand ventricular arrhythmia mechanisms for a variety of diseases. Models representing acute myocardial ischemia have characterized the substrate for arrhythmogenesis during the delayed phase (also

called phase 1B), 15 to 45 minutes following coronary artery occlusion; phase 1B is characterized by the presence of an inexcitable midmyocardial layer between still-viable endocardial and epicardial layers; the latter are referred to as border zones. One study [64] showed that heterogeneous coupling between the inexcitable layer and the border zones was pro-arrhythmic; in the case of complete decoupling, reentry could not be induced. In subsequent work [65], the same authors showed that critical levels of sub-epicardial potassium elevation, decoupling between layers, and border zone width were necessary to induce reentry during ischemia phase 1B. Jie et al. [63] used a model of the beating rabbit ventricles to gain insight into the role of electromechanical dysfunction in arrhythmogenesis during acute regional ischemia, both in the induction of ventricular premature beats and in their subsequent degeneration into ventricular arrhythmia.

Computer simulations of ventricular ischemia and infarction and the corresponding body surface potentials have also been used to determine how the extent of the ischemic zone is reflected in the 12-lead ECG. Specifically, modeling research has provided insight on how ECG signals are influenced by the size and shape of acute [127] and healed [135] myocardial infarction. Simulations have also been employed to distinguish between diseases that have similar ECG properties but different underlying cause, which can confound diagnosis and treatment. Potse et al. [95] used ventricular models to show that left bundle branch block and diffuse electrical uncoupling, both of which prolong the QRS complex, can be differentiated by examining ECG amplitude.

Uncovering arrhythmia mechanisms in genetically inherited diseases has also benefited significantly from models of ventricular function [2, 46, 59, 134]. Adeniran et al. [2] developed a Markov model of a mutant  $I_{Kr}$  channel known to cause short QT syndrome. Whole heart simulations revealed that increased arrhythmia susceptibility was due to a both APD abbreviation caused by the mutation and intrinsic transmural heterogeneity of  $I_{Kr}$  channel expression; when combined, these two factors gave rise to arrhythmogenic APD dispersion. Deo et al. [46] characterized an inward rectifier potassium channel ( $I_K1$ ) mutation from an individual with a different type of short QT syndrome. In addition to reproducing the electrocardiographic phenotype, ventricular simulations with the mutant channel showed that slight (20%)  $I_{Na}$  reduction dramatically increased arrhythmia inducibility, suggesting that the use of class I anti-arrhythmic drugs must be closely monitored in the patient. Finally, Hoogendijk et al. [59] showed that  $I_{Na}$  reduction, which is associated with Brugada syndrome, leads to conduction block due to source-sink mismatch at microscopic tissue heterogeneities; simulations revealed that the severity of this effect is modulated by other Brugada-linked mutations, such as increased transient outward potassium current and decreased L-type calcium current.

### ***1.3.6 Modeling to Identify Individuals with a High Risk of Developing Arrhythmia***

Robust methods for stratifying the risk of lethal cardiac arrhythmias decrease morbidity and mortality in patients with cardiovascular disease and reduce health care costs [55]. The most widely used approaches currently used for stratifying cardiac arrhythmia risk involve testing for ECG abnormalities, then using the results to identify patients who would benefit from implantable cardioverter defibrillator (ICD) therapy. However, the mechanisms underlying these ECG indices, and their relationship to lethal arrhythmias, are not fully understood. Computational models of the heart have made inroads in this clinical cardiology arena [17, 18, 38, 47, 66, 85, 90, 137]. Specifically, research has reported a strong correlation between increased arrhythmia risk and the presence of microvolt T-wave alternans (MTWA) [26,58]. However, the mechanistic basis of MTWA preceding lethal ventricular arrhythmias has been under debate since MTWA is most successful in stratifying risk in patients at heart rates < 110 bpm, where APD restitution is flat [86]. Computational models of the left ventricular (LV) wall in combination with clinical data revealed that abnormal intracellular calcium handling underlies alternans in action potential voltage, which result in MTWA at heart rates < 110 bpm [17, 85]; abnormalities in intracellular calcium have long been linked to ventricular fibrillation [80, 129]. Computational modeling studies have also shown that under conditions of abnormal calcium dynamics, the T-wave alternans magnitude is enhanced by structural heterogeneities in the myocardium [47].

Recently, a computational model of the human ventricles was used to demonstrate that detecting instabilities in the QT interval in the clinical ECGs could predict the onset of VT, particularly in patients with acute myocardial infarction [38]. The study explored the effect of frequency of premature activation, which was controlled in the model by shortening the beat-to-beat coupling interval for different numbers of randomly-selected beats in minute-long sinus activation sequences; increased frequency of premature activation was found to precede VT onset by leading to instability in the QT interval. Therefore, screening the QT interval of the ECG for instabilities using the novel algorithm developed by Chen and Trayanova [38, 40] could potentially be a robust risk stratification method for patients with acute myocardial infarction. Recently, the approach was successfully applied to stratify the risk of arrhythmias in 114 patients with ICDs [39]. These studies pave the way for executing computer simulations to determine patient-specific thresholds for arrhythmia stratification ECG indices, rather than relaying on clinical guidelines based on large and diverse patient cohorts. Another approach to arrhythmia risk stratification that has recently gained traction is the use of computer models to predict the arrhythmia outcome in patients that exhibit potentially lethal mutations in genes encoding cardiac proteins associated with long QT syndrome [18, 66, 90, 137]. These studies chart new directions for future genotype-based risk stratification and personalized gene therapy.

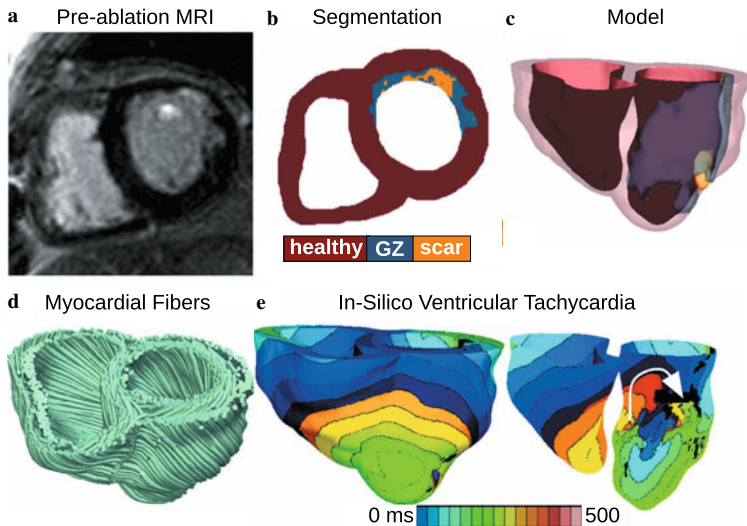


**Fig. 1.3.** (a) and (b) Clinical MRI scan of an infarcted patient heart and the corresponding segmentation; (c) 3D geometric model of the patient heart with the epicardium and the infarct border zone rendered semi-transparent; (d) Estimated fiber orientations; (e) Simulated activation map of ventricular tachycardia (VT) revealing reentry on the left ventricular endocardium. VT frequency is 3.05 Hz. Color bar indicates activation times. White arrow indicates path of reentrant wave. Modified with permission from [132]

### 1.3.7 Clinical Applications of Simulation-based Arrhythmia Research

Recent years have witnessed revolutionary advances in imaging, including ex vivo structural and diffusion tensor (DT) magnetic resonance imaging (MRI) that facilitate acquisition of the intact structure of explanted hearts with high resolution. Leveraging these advances, a new generation of whole-heart image-based models with unprecedented detail has emerged [22, 123]. Such models are currently being used, in combination with experimental electrophysiological data, to provide better understanding of the role of the individual infarct region morphology in the generation and maintenance of infarct-related VT, the most frequent clinical ventricular arrhythmia, present in 64% of patients with ventricular rhythm disorder and in 89% of patients with sudden cardiac death [111]. Using a model of the infarcted pig ventricles reconstructed from ex-vivo MRI and DT-MRI data, Pop et al. [94] demonstrated good correspondence between in-silico and experimental electroanatomical voltage maps, and successfully predicted infarct-related VT inducibility after programmed electrical stimulation. Arevalo et al. [8] examined the role infarct border zone extent in arrhythmogenesis, establishing that a minimum volume of remodeled tissue is needed for VT maintenance and demonstrating that the organizing center of infarct-related VT is located within the border zone, regardless of the pacing site from which VT

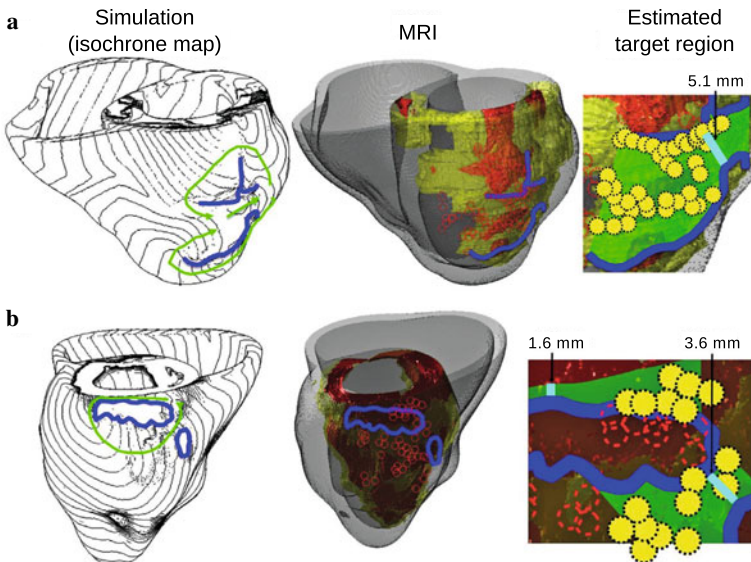


**Fig. 1.4.** (a) and (b) Comparison between simulation-guided and standard electrophysiological approaches for identifying ablation targets in two patients with infarct-related VTs. Left column: propagation pathways (green) and lines of conduction block (blue) are overlaid over VT activation maps simulated in image-based patient heart models. Middle column: pre-ablation infarct geometry (infarct scar: orange, border zone: yellow, non-infarcted: gray) along with ablation lesions delivered by the standard approach (red circles) and conduction block lines as calculated from ventricular simulations. Right column: optimal ablation zones (green shading) predicted by simulations, with narrowest isthmuses indicated (cyan); in both cases, only a fraction of the ablation sites from the standard approach were within the predicted optimal ablation zone (yellow circles). Modified with permission from [12]

is induced. Such simulation methodology could have a major clinical impact in predicting the optimal targets for catheter ablation of infarct-related VT in individual hearts, should the methodology be able to reconstruct patient hearts from clinical imaging data and evaluate the 3D patterns of infarct-related VT in the patient. The first attempts in this direction have already been made. Figure 1.3 presents a simulation of arrhythmia in a patient-specific model of the infarcted ventricles; it shows model generation from clinical MR scans of the patient heart as well as simulated infarct-related ventricular tachycardia [132]. Figure 1.4, from the recent study by Ashikaga et al., [12] demonstrates that non-invasive simulation prediction of optimal targets for ablation of infarct-related VT could result in lesions that are much smaller than those executed in the clinic.

Several additional studies are noteworthy. Zhu et al. [138] showed that models of the heart can be used to carry out non-invasive localization of accessory pathways in patients with Wolff-Parkinson-White syndrome. Ng et al. [87] demonstrated the feasibility of using simulations to predict VT circuits. Relan et al. [99] used a hy-

brid X-ray and MR environment to image a patient heart, which was further personalized with voltage measurements. The results demonstrated that the heart model could successfully be used to assess infarct-related VT inducibility from sites not accessible in the clinic. Further translation of ventricular simulations in the clinic will be facilitated by the development of methodologies to estimate patient-specific fiber orientations from clinical MRI scans [16, 122].

## 1.4 Simulation of Cardiac Arrhythmia Termination

Controlling the complex spatio-temporal dynamics underlying life-threatening cardiac arrhythmias such as fibrillation is extremely difficult because of the nonlinear interaction of excitation waves within the heterogeneous anatomical substrate. In the absence of a better strategy, strong electrical shocks have remained the only reliable treatment for cardiac fibrillation. Over the years, biophysically-detailed multi-scale models of defibrillation [3, 6, 105, 107] have made major contributions to understanding how defibrillation shocks used in clinical practice interact with cardiac tissue [7, 9, 11, 29, 50, 78, 103, 104, 115, 118]; these models have been validated by comparing to the results of optimal mapping experiments [20, 24, 25]. Computer modeling of whole-heart defibrillation has been instrumental in the development of the virtual electrode polarization (VEP) theory for defibrillation. Research has found that mechanisms for shock success or failure are multifactorial, depending mainly on the postshock distribution of transmembrane potential as well as the timing and propagation speed of shock-induced wavefronts. Recent simulation studies have been instrumental in understanding mechanisms of the isoelectric window that follows defibrillation shocks with strength near the defibrillation threshold (DFT): one of the proposed explanations for the isoelectric window duration is propagation of postshock activations in intramural excitable areas (“tunnel propagation”), bounded by long-lasting postshock depolarization of the cardiac surfaces [10, 42].

Ventricular simulations have also ascertained the role of cardiac microstructure in the mechanisms of defibrillation. For example, Bishop et al. applied shocks to a very high-resolution ( $\sim 25 \mu\text{m}$  voxel size) image-based rabbit ventricular model; VEPs formed at the boundaries between blood vessels and myocardium [19], which gave rise to secondary sources that eliminated excitable gaps and led to successful defibrillation [23]. Simulations have also contributed to understanding of the process of defibrillation in hearts with myocardial ischemia and infarction [96, 105, 106], uncovering the role of electrophysiological and structural remodeling in the failure or success of the shock. Finally, simulations were conducted in a rabbit ventricular electromechanics model to examine vulnerability to strong shocks and defibrillation under the conditions of LV dilation and determine the mechanisms by which mechanical deformation may lead to increased vulnerability and elevated DFT [72, 117, 120]. The results suggested that ventricular geometry and the rearrangement of fiber architecture in the deformed ventricles is responsible for the reduced defibrillation efficacy in the dilated ventricles.

### **1.4.1 Model-Based Innovation to Improve Arrhythmia Termination by Electric Shocks**

Recently, defibrillation modeling has focused on the development of new methodologies for low-voltage termination of lethal arrhythmias or for applying defibrillation in novel, less damaging ways. The study by Tandri et al. [113] used sustained kilohertz-range alternating current (AC) fields for arrhythmia termination. Termination of arrhythmia with AC fields has been attempted previously in simulations [81–83] with limited success; the frequencies used in these studies were, however, substantially lower. The premise of the Tandri et al. study was that such fields have been known to instantaneously and reversibly block electrical conduction in nerve tissue. Aided by ventricular modeling, the article provided proof of the concept that electric fields, such as those used for neural block, when applied to cardiac tissue, similarly produce reversible block of cardiac impulse propagation and lead to successful defibrillation; it also showed that this methodology could potentially be a safer means for terminating life-threatening reentrant arrhythmias. Since the same AC fields block equally well both neural and cardiac activity, the proposed defibrillation methodology could possibly be utilized to achieve high-voltage yet painless defibrillation. The follow-up study by Weinberg et al. [128] provided, again using ventricular simulations, a deeper analysis of the mechanisms that underlie the success and failure of this novel mode of defibrillation.

Recent experimental studies have shown that applied electric fields delivering multiple far-field stimuli at a given cycle length can terminate VT, atrial flutter, and atrial fibrillation with less total energy than a single strong shock [73, 76, 79]. However, the mechanisms and full range of applications of this new mode of defibrillation have remained poorly explored. The recent simulation study by Rantner et al. [97] aimed to elucidate these mechanisms and to develop an optimal low-voltage defibrillation protocol. Based on the simulation results using a complex high-resolution MRI-based ventricular wall model, a novel two-stage low-voltage defibrillation protocol was proposed that did not involve the delivery of the stimuli at a constant cycle length. Instead, the first stage converted VF into VT by applying low-voltage stimuli at instants of maximal excitable gap, capturing large tissue volume and synchronizing depolarization. The second stage was designed to terminate VT, in cases where it persisted, by multiple low-voltage stimuli given at constant cycle lengths. The energy required for successful defibrillation using this protocol was 57.42% of the energy for low-voltage defibrillation when stimulating at the optimal fixed-duration cycle length.

### 1.4.2 Exploration of an Emerging Paradigm for Anti-arrhythmia Treatment: Cardiac Optogenetics

Cardiac optogenetics is an emerging field that involves inserting light-sensitive ion channels (opsins) in heart tissue to enable control of bioelectric behavior with illumination instead of electric current [49, 131]. This technology is poised to open a new avenue for the development of safe and effective anti-arrhythmia therapies by enabling the evocation of spatiotemporally precise responses in targeted cells or tissues. Abilez et al. [1] conducted ventricular simulations with a Markov model of light-sensitive current incorporated at the cell scale in selected regions; a later study from the same group [133] showed that differences between optically and electrically stimulated cells were limited to mild changes in intracellular sodium and potassium concentrations. Boyle et al. [34] developed a comprehensive whole-heart optogenetics simulation platform that incorporates realistic representations of opsin delivery as well as the response to illumination at the molecular, cell, tissue, and organ scales. This framework was then used to explore how opsin delivery characteristics determine energy requirements for optical stimulation and to identify cardiac structures that are potential pacemaking targets with low optical excitation threshold. As shown in Fig. 1.5, optical stimulation was more efficient when cell-specific optogenetic targeting was used to express opsins in the PS compared to ventricular cells. This finding is particularly noteworthy because direct pacing of the His bundle has therapeutic advantages compared to conventional pacing for cardiac resynchronization [15], but the practical usefulness of this maneuver is limited by high energy requirements and low selectivity (i.e., electrical stimuli capture the ventricular septum as well as the His bundle). Results from optogenetics simulations indicate that both

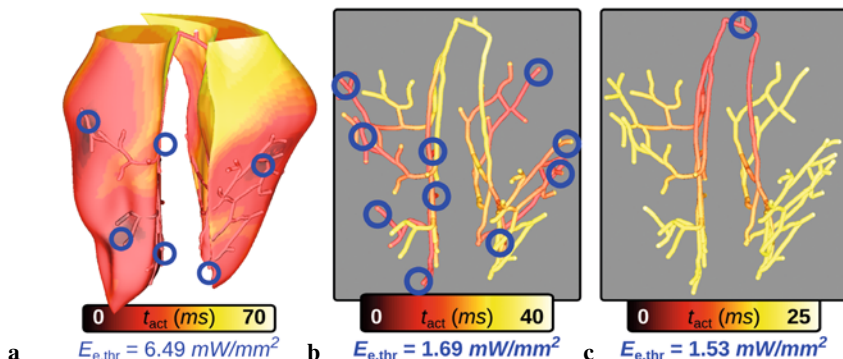


**Fig. 1.5.** Activation sequences in response to intracardiac optical stimulation (blue circles) in a model of the rabbit ventricles and PS with simulated optogenetic delivery of light-sensitive ion channels targeted to ventricular cells only (a) or Purkinje system (PS) cells only (b, c). The threshold irradiance ( $E_{e,thr}$ ) to elicit a propagating AP response by illumination was significantly lower in cases where the PS was targeted. All activation times ( $t_{act}$ ) are measured with respect to the delivery of a 2 ms light pulse at  $1.1 \times E_{e,thr}$  to the endocardial surface under each site shown. Modified with permission from [34]

of these shortcomings could be overcome by using a light-based approach for the same type of stimulation. Modeling will provide valuable insights to help guide the development of this type of low-energy solution for managing cardiac arrhythmias.

As summarized in a recent editorial [31], innovative developments in light-sensitive protein engineering [77], intracardiac optics [70], and cardiac gene therapy [27, 62] suggest that such optogenetics-based arrhythmia termination therapies could be a reality in the not-so-distant future. However, the clinical feasibility of these strategies remains largely untested. Simulations conducted in virtual light-sensitized hearts will provide valuable insights to help guide the development of experiments that will lay the groundwork for therapeutic applications of cardiac optogenetics. For example, Boyle et al. reported [31] that simulated gene delivery of the light-sensitive protein channelrhodopsin-2 (ChR2) to a model of the diseased human atria enables cardioversion of arrhythmias by illumination of the endocardial surface.

#### ***1.4.3 Leveraging Patient-Specific Models to Optimize Difficult Clinical Procedures***

Finally, a recent study [98] has made the first attempt towards clinical translation of computer models of arrhythmia termination. It addressed a clinical need: ICDs with transvenous leads often cannot be implanted in a standard manner in pediatric and congenital heart defect (CHD) patients; currently, there is no reliable approach to predict the optimal ICD placement in these patients. The study provided proof-of-concept that patient-specific, biophysically detailed computer simulations of the dynamic process of defibrillation could be used to predict optimal ICD lead location in these patients. A pipeline for constructing personalized, electrophysiological heart-and-torso models from clinical MRI scans was developed and applied to a pediatric CHD patient, and the optimal ICD placement was determined using patient-specific simulations of defibrillation. In a patient with tricuspid valve atresia, two configurations with epicardial leads were found to have the lowest defibrillation threshold. As shown in Fig. 1.6, the optimal configurations were associated with significantly lower defibrillation thresholds compared to alternative lead/can combinations. The study demonstrated that by using such methodology the optimal ICD placement in pediatric/CHD patients could be predicted computationally, which could reduce defibrillation energy if the pipeline is used as part of ICD implantation planning.

### **1.5 Computational Complexity of Cardiac Electrophysiology Simulations**

Although it would be impractical to provide model details and runtime information for all of the 100+ models cited in this review, we provide here a brief discussion of computational complexity in cardiac simulations, which is an important practical consideration for the field. Many factors contribute to the overall complexity of each individual model, including the type of activity being simulated; the scale

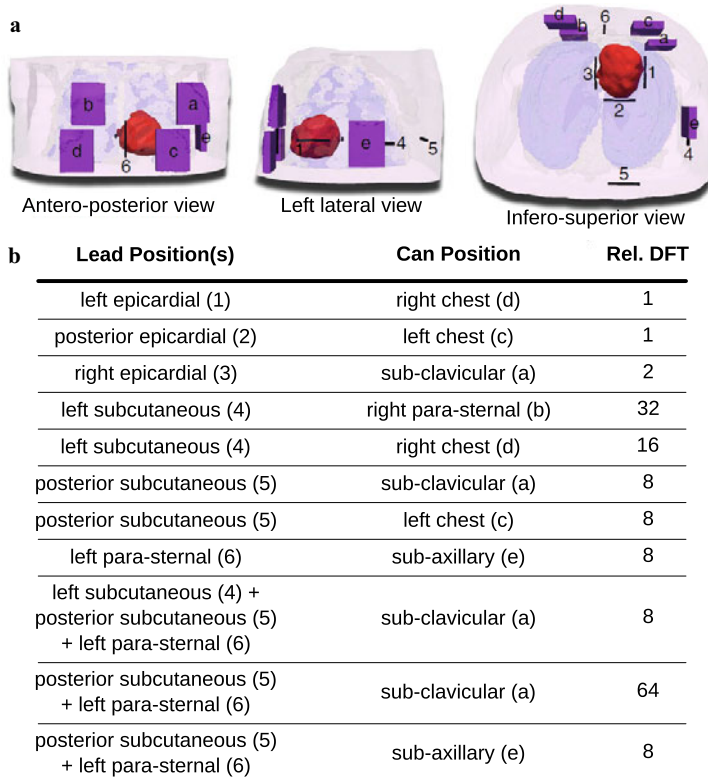


**Fig. 1.6.** (a) Patient-specific model of heart (red) and torso with skin (pink), lungs (blue), and bones (white); possible locations for the implantable cardioverter defibrillator (ICD) can (purple; a–e) and lead (black; 1–6) are also superimposed; (b) Lead and can positions and relative defibrillation thresholds (DFT) for each of the 11 ICD configurations tested in the study are tabulated. Relative DFT values are calculated with respect to those determined for the first two cases (top lines in table). Modified with permission from [98]

and resolution of the cardiac geometry; and, the size and characteristics of the ODE system representing myocyte membrane kinetics. These factors and their impact on the computational resources required vary dramatically from study to study. Simulations that require application of the bidomain formulation (e.g., defibrillation studies [23, 44, 96, 97, 116]) are more time-consuming than those in which the monodomain formulation is adequate. Mesh size varies dramatically depending on the size of the model and the resolution necessary to capture details relevant to phenomena of interest; this review discusses studies involving models with degrees of freedom (i.e., mesh nodes) ranging from hundreds of thousands [32, 33, 44, 45, 104–107] to millions [19, 21–23, 96–98] and even tens of millions [95]. At the cell level, ionic models that aim to represent different levels of detail vary considerably in terms of the size of the associated ODE system; for example, the Courtemanche human atrial

model has 19 equations [43], the O’Hara human ventricular model has 43 [91], and the Sampson human Purkinje fiber model has 83 [108]. Furthermore, in cases where these ODE systems are stiff (i.e., rate constants associated with individual state variables in the model differ dramatically), computational complexity increases because it becomes necessary to use extremely short time steps or implement higher-order ODE solvers (e.g., Runge-Kutta or Rosenbrock schemes) [110]. Due to these many layers of complexity, biophysically detailed whole heart simulations tend to be extremely time consuming, even when state-of-the-art computing resources are used – one recent review estimated that compute time generally lags real time by 3 to 4 orders of magnitude (i.e., a one-second heart beat takes 1000 to 10000 seconds to simulate) [119]. As of this writing, simulations conducted on the most powerful supercomputer ever used to conduct high-resolution, organ-scale cardiac modeling research still lagged real-time by 12% [100].

## 1.6 The Future of Computational Cardiac Electrophysiology

As this review demonstrates, the key in attaining predictive capabilities of multi-scale biophysically-detailed cardiac models at the level of the organ has been the use of geometrically realistic (typically MRI- or CT- based) models of the ventricles, and the application of diffusion tensor DT-MRI to measure the anatomy, fiber, and sheet structure of the heart, in cases of ex-vivo studies. This has led to a new generation of image-based ventricular models with unprecedented structural and bio-physical detail. Clearly, models of cardiac function have benefited significantly from this revolution in medical imaging.

As outlined above, cardiac models have been used to gain insights into mechanisms of arrhythmia in many disease settings and to understand how external currents can terminate ventricular arrhythmias. In addition, a major thrust in computational cardiac electrophysiology is to use models as a test bed for evaluation of new antiarrhythmic drugs. It is now possible to test hypotheses regarding mechanisms of drug action on the scale of the whole heart. Multi-scale heart models of antiarrhythmic drug interactions with ion channels have provided insights into why certain pharmaceutical interventions result in pro-arrhythmia, whereas others do not. This work has the potential to more effectively guide the drug development pipeline – a process that currently has high failure rates and high costs.

The use of heart models in personalized diagnosis, treatment planning, and prevention of sudden cardiac death is also slowly becoming a reality, as reviewed here. The feasibility of subject-specific modeling has been demonstrated through the use of heart models reconstructed from clinical MRI scans. Computer simulations of the function of the diseased heart represent a profound example of a research avenue in the new discipline of computational medicine. Biophysically detailed models of the heart assembled with data from clinical imaging modalities that incorporate electrophysiological and structural remodeling in cardiac disease are poised to become a first line of screening for new therapies and approaches, new diagnostic develop-

ments, and new methods for disease prevention. Implementing patient-specific cardiac simulations at the patient bedside could become one of the most thrilling examples of computational science and engineering approaches in translational medicine.

**Acknowledgements** This research was supported by the following grants: NIH-DP1-HL123271, NIH-R01-HL103428, NIH-R01-HL105216, NIH-R01-HL094610, and NSF-CDI-1124804.

## References

1. Abilez, O.J., Wong, J., Prakash, R., Deisseroth, K., Zarins, C.K., Kuhl, E.: Multiscale computational models for optogenetic control of cardiac function. *Biophys. J.* **101**(6), 1326–34 (2011)
2. Adeniran, I., McPate, M.J., Witchel, H.J., Hancox, J.C., Zhang, H.: Increased vulnerability of human ventricle to re-entrant excitation in herg-linked variant 1 short QT syndrome. *PLoS. Comput. Biol.* **7**(12), e1002313 (2011)
3. Aguel, F., Debruin, K.A., Krassowska, W., Trayanova, N.A.: Effects of electroporation on the transmembrane potential distribution in a two-dimensional bidomain model of cardiac tissue. *J. Cardiovasc. Electrophysiol.* **10**(5), 701–14 (1999)
4. Alonso, S., Bar, M., Panfilov, A.V.: Negative tension of scroll wave filaments and turbulence in three-dimensional excitable media and application in cardiac dynamics. *Bull. Math. Biol.* **75**(8), 1351–76 (2013)
5. Alonso, S., Panfilov, A.V.: Negative filament tension at high excitability in a model of cardiac tissue. *Phys. Rev. Lett.* **100**(21), 218,101 (2008)
6. Anderson, C., Trayanova, N., Skouibine, K.: Termination of spiral waves with biphasic shocks: role of virtual electrode polarization. *J. Cardiovasc. Electrophysiol.* **11**(12), 1386–96 (2000)
7. Anderson, C., Trayanova, N.A.: Success and failure of biphasic shocks: results of bidomain simulations. *Math. Biosci.* **174**(2), 91–109 (2001)
8. Arevalo, H., Plank, G., Helm, P., Halperin, H., Trayanova, N.: Tachycardia in post-infarction hearts: Insights from 3D image-based ventricular models. *PLoS. One.* **8**(7), e68,872 (2013)
9. Arevalo, H., Rodriguez, B., Trayanova, N.: Arrhythmogenesis in the heart: Multiscale modeling of the effects of defibrillation shocks and the role of electrophysiological heterogeneity. *Chaos* **17**(1), 015,103 (2007)
10. Ashihara, T., Constantino, J., Trayanova, N.A.: Tunnel propagation of postshock activations as a hypothesis for fibrillation induction and isoelectric window. *Circ. Res.* **102**(6), 737–45 (2008)
11. Ashihara, T., Trayanova, N.A.: Asymmetry in membrane responses to electric shocks: insights from bidomain simulations. *Biophys. J.* **87**(4), 2271–82 (2004)
12. Ashikaga, H., Arevalo, H., Vadakkumpadan, F., Blake R. C., Bayer, J.D., Nazarian, S., Muz Zviman, M., Tandri, H., Berger, R.D., Calkins, H., Herzka, D.A., Trayanova, N.A., Halperin, H.R.: Feasibility of image-based simulation to estimate ablation target in human ventricular arrhythmia. *Heart Rhythm* **10**(8), 1109–16 (2013)
13. Aslanidi, O.V., Sleiman, R.N., Boyett, M.R., Hancox, J.C., Zhang, H.: Ionic mechanisms for electrical heterogeneity between rabbit Purkinje fiber and ventricular cells. *Biophys. J.* **98**(11), 2420–31 (2010)

14. Baher, A.A., Uy, M., Xie, F., Garfinkel, A., Qu, Z., Weiss, J.N.: Bidirectional ventricular tachycardia: ping pong in the His-Purkinje system. *Heart Rhythm* **8**(4), 599–605 (2011)
15. Barba-Pichardo, R., Manovel Sanchez, A., Fernandez-Gomez, J.M., Morina-Vazquez, P., Venegas-Gamero, J., Herrera-Carranza, M.: Ventricular resynchronization therapy by direct His-bundle pacing using an internal cardioverter defibrillator. *Europace* **15**(1), 83–8 (2013)
16. Bayer, J.D., Blake, R.C., Plank, G., Trayanova, N.A.: A novel rule-based algorithm for assigning myocardial fiber orientation to computational heart models. *Ann. Biomed. Eng.* **40**(10), 2243–54 (2012)
17. Bayer, J.D., Narayan, S.M., Lalani, G.G., Trayanova, N.A.: Rate-dependent action potential alternans in human heart failure implicates abnormal intracellular calcium handling. *Heart Rhythm* **7**(8), 1093–101 (2010)
18. Benson, A.P., Al-Owais, M., Holden, A.V.: Quantitative prediction of the arrhythmogenic effects of de novo hERG mutations in computational models of human ventricular tissues. *Eur. Biophys. J* **40**(5), 627–39 (2011)
19. Bishop, M.J., Boyle, P.M., Plank, G., Welsh, D.G., Vigmond, E.J.: Modeling the role of the coronary vasculature during external field stimulation. *IEEE Trans. Biomed. Eng.* **57**(10), 2335–45 (2010)
20. Bishop, M.J., Gavaghan, D.J., Trayanova, N.A., Rodriguez, B.: Photon scattering effects in optical mapping of propagation and arrhythmogenesis in the heart. *J. Electrocardiol.* **40**(6 Suppl.), S75–80 (2007)
21. Bishop, M.J., Plank, G.: The role of fine-scale anatomical structure in the dynamics of reentry in computational models of the rabbit ventricles. *J. Physiol.* **590**(Pt 18), 4515–35 (2012)
22. Bishop, M.J., Plank, G., Burton, R.A., Schneider, J.E., Gavaghan, D.J., Grau, V., Kohl, P.: Development of an anatomically detailed MRI-derived rabbit ventricular model and assessment of its impact on simulations of electrophysiological function. *Am. J. Physiol. Heart Circ. Physiol.* **298**(2), H699–718 (2010)
23. Bishop, M.J., Plank, G., Vigmond, E.: Investigating the role of the coronary vasculature in the mechanisms of defibrillation. *Circ Arrhythm Electrophysiol* **5**(1), 210–9 (2012)
24. Bishop, M.J., Rodriguez, B., Eason, J., Whiteley, J.P., Trayanova, N., Gavaghan, D.J.: Synthesis of voltage-sensitive optical signals: application to panoramic optical mapping. *Biophys. J.* **90**(8), 2938–45 (2006)
25. Bishop, M.J., Rodriguez, B., Qu, F., Efimov, I.R., Gavaghan, D.J., Trayanova, N.A.: The role of photon scattering in optical signal distortion during arrhythmia and defibrillation. *Biophys. J* **93**(10), 3714–26 (2007)
26. Bloomfield, D.M., Bigger, J.T., Steinman, R.C., Namerow, P.B., Parides, M.K., Curtis, A.B., Kaufman, E.S., Davidenko, J.M., Shinn, T.S., Fontaine, J.M.: Microvolt t-wave alternans and the risk of death or sustained ventricular arrhythmias in patients with left ventricular dysfunction. *J. Am. Coll. Cardiol.* **47**(2), 456–63 (2006)
27. Bolli, R., Chugh, A.R., D'Amario, D., Loughran, J.H., Stoddard, M.F., Ikram, S., Beache, G.M., Wagner, S.G., Leri, A., Hosoda, T., Sanada, F., Elmore, J.B., Goichberg, P., Cappetta, D., Solankhi, N.K., Fahsah, I., Rokosh, D.G., Slaughter, M.S., Kajstura, J., Anversa, P.: Cardiac stem cells in patients with ischaemic cardiomyopathy (SCIPIO): initial results of a randomised phase 1 trial. *Lancet* **378**(9806), 1847–57 (2011)
28. Bordas, R., Gillow, K., Lou, Q., Efimov, I.R., Gavaghan, D., Kohl, P., Grau, V., Rodriguez, B.: Rabbit-specific ventricular model of cardiac electrophysiological function including specialized conduction system. *Prog. Biophys. Mol. Biol.* **107**(1), 90–100 (2011)

29. Bourn, D.W., Gray, R.A., Trayanova, N.A.: Characterization of the relationship between preshock state and virtual electrode polarization-induced propagated graded responses resulting in arrhythmia induction. *Heart Rhythm* **3**(5), 583–95 (2006)
30. Boyle, P.M.: Roles of the Purkinje system during electric shocks and arrhythmia. Doctoral dissertation, University of Calgary (2011)
31. Boyle, P.M., Entcheva, E., Trayanova, N.A.: See the light: can optogenetics restore healthy heartbeats? and, if it can, is it really worth the effort? *Expert Review of Cardiovascular Therapy* **12**(1), 1–4 (2014)
32. Boyle, P.M., Masse, S., Nanthakumar, K., Vigmond, E.J.: Transmural IK(ATP) heterogeneity as a determinant of activation rate gradient during early ventricular fibrillation: Mechanistic insights from rabbit ventricular models. *Heart Rhythm* **10**, 1710–7 (2013)
33. Boyle, P.M., Veenhuyzen, G.D., Vigmond, E.J.: Fusion during entrainment of orthodromic reciprocating tachycardia is enhanced for basal pacing sites but diminished when pacing near Purkinje system end points. *Heart Rhythm* **10**(3), 444–51 (2013)
34. Boyle, P.M., Williams, J.C., Ambrosi, C.M., Entcheva, E., Trayanova, N.A.: A comprehensive multiscale framework for simulating optogenetics in the heart. *Nat. Commun.* **4**, 2370 (2013)
35. Carusi, A., Burrage, K., Rodriguez, B.: Bridging experiments, models and simulations: an integrative approach to validation in computational cardiac electrophysiology. *Am. J. Physiol. Heart Circ. Physiol.* **303**(2), H144–55 (2012)
36. Cerrone, M., Noujaim, S.F., Tolkacheva, E.G., Talkachou, A., O'Connell, R., Berenfeld, O., Anumonwo, J., Pandit, S.V., Vikstrom, K., Napolitano, C., Priori, S.G., Jalife, J.: Arrhythmogenic mechanisms in a mouse model of catecholaminergic polymorphic ventricular tachycardia. *Circ. Res.* **101**(10), 1039–48 (2007)
37. Cha, Y.M., Uchida, T., Wolf, P.L., Peters, B.B., Fishbein, M.C., Karagueuzian, H.S., Chen, P.S.: Effects of chemical subendocardial ablation on activation rate gradient during ventricular fibrillation. *Am. J. Physiol.* **269**(6 Pt 2), H1998–2009 (1995)
38. Chen, X., Hu, Y., Fetis, B.J., Berger, R.D., Trayanova, N.A.: Unstable QT interval dynamics precedes ventricular tachycardia onset in patients with acute myocardial infarction: a novel approach to detect instability in qt interval dynamics from clinical ECG. *Circ. Arrhythm. Electrophysiol.* **4**(6), 858–66 (2011)
39. Chen, X., Tereshchenko, L.G., Berger, R.D., Trayanova, N.A.: Arrhythmia risk stratification based on QT interval instability: an intracardiac electrocardiogram study. *Heart Rhythm* **10**(6), 875–80 (2013)
40. Chen, X., Trayanova, N.A.: A novel methodology for assessing the bounded-input bounded-output instability in qt interval dynamics: Application to clinical ECG with ventricular tachycardia. *IEEE Trans. Biomed. Eng.* **59**(8), 2111–7 (2012)
41. Cherry, E., Fenton, F.: Suppression of alternans and conduction blocks despite steep apd restitution: electrotonic, memory, and conduction velocity restitution effects. *Am J Physiol. Heart Circ. Physiol.* **286**(6), H2332–2341 (2004)
42. Constantino, J., Long, Y., Ashihara, T., Trayanova, N.A.: Tunnel propagation following defibrillation with icd shocks: hidden postshock activations in the left ventricular wall underlie isoelectric window. *Heart Rhythm* **7**(7), 953–61 (2010)
43. Courtemanche, M., Ramirez, R.J., Nattel, S.: Ionic mechanisms underlying human atrial action potential properties: insights from a mathematical model. *Am. J. Physiol.* **275**(1 Pt 2), H301–21 (1998)
44. Deo, M., Boyle, P., Plank, G., Vigmond, E.: Arrhythmogenic mechanisms of the Purkinje system during electric shocks: a modeling study. *Heart Rhythm* **6**(12), 1782–9 (2009)

45. Deo, M., Boyle, P.M., Kim, A.M., Vigmond, E.J.: Arrhythmogenesis by single ectopic beats originating in the Purkinje system. *Am. J. Physiol. Heart Circ. Physiol.* **299**(4), H1002–11 (2010)
46. Deo, M., Ruan, Y., Pandit, S.V., Shah, K., Berenfeld, O., Blaufox, A., Cerrone, M., Noujaim, S.F., Denegri, M., Jalife, J., Priori, S.G.: KCNJ2 mutation in short QT syndrome 3 results in atrial fibrillation and ventricular proarrhythmia. *Proc. Natl. Acad. Sci. USA* **110**(11), 4291–6 (2013)
47. Doshi, A.N., Idriss, S.F.: Effect of resistive barrier location on the relationship between t-wave alternans and cellular repolarization alternans: a 1-D modeling study. *J. Electrocardiol.* **43**(6), 566–71 (2010)
48. Dux-Santoy, L., Sebastian, R., Felix-Rodriguez, J., Ferrero, J.M., Saiz, J.: Interaction of specialized cardiac conduction system with antiarrhythmic drugs: a simulation study. *IEEE Trans. Biomed. Eng.* **58**(12), 3475–8 (2011)
49. Entcheva, E.: Cardiac optogenetics. *Am. J. Physiol. Heart Circ. Physiol.* **304**(9), H1179–91 (2013)
50. Entcheva, E., Trayanova, N.A., Claydon, F.J.: Patterns of and mechanisms for shock-induced polarization in the heart: a bidomain analysis. *IEEE Trans. Biomed. Eng.* **46**(3), 260–70 (1999)
51. Fenton, F.H., Cherry, E.M., Hastings, H.M., Evans, S.J.: Multiple mechanisms of spiral wave breakup in a model of cardiac electrical activity. *Chaos* **12**(3), 852–892 (2002)
52. Fink, M., Niederer, S.A., Cherry, E.M., Fenton, F.H., Koivumaki, J.T., Seemann, G., Thul, R., Zhang, H., Sachse, F.B., Beard, D., Crampin, E.J., Smith, N.P.: Cardiac cell modelling: Observations from the heart of the cardiac physiome project. *Progress in Biophysics & Molecular Biology* **104**(1–3), 2–21 (2011)
53. Fink, M., Noble, D., Virag, L., Varro, A., Giles, W.R.: Contributions of hERG K<sup>+</sup> current to repolarization of the human ventricular action potential. *Prog. Biophys. Mol. Biol.* **96**(1–3), 357–76 (2008)
54. Garfinkel, A., Kim, Y.H., Voroshilovsky, O., Qu, Z., Kil, J.R., Lee, M.H., Karagueuzian, H.S., Weiss, J.N., Chen, P.S.: Preventing ventricular fibrillation by flattening cardiac restitution. *Proc. Natl. Acad. Sci. USA* **97**(11), 6061–6 (2000)
55. Goldberger, J.J., Buxton, A.E., Cain, M., Costantini, O., Exner, D.V., Knight, B.P., Lloyd-Jones, D., Kadish, A.H., Lee, B., Moss, A., Myerburg, R., Olglin, J., Passman, R., Rosenbaum, D., Stevenson, W., Zareba, W., Zipes, D.P.: Risk stratification for arrhythmic sudden cardiac death: identifying the roadblocks. *Circulation* **123**(21), 2423–30 (2011)
56. Grandi, E., Pandit, S.V., Voigt, N., Workman, A.J., Dobrev, D., Jalife, J., Bers, D.M.: Human atrial action potential and Ca<sup>2+</sup> model: sinus rhythm and chronic atrial fibrillation. *Circ. Res.* **109**(9), 1055–66 (2011)
57. Grandi, E., Pasqualini, F.S., Bers, D.M.: A novel computational model of the human ventricular action potential and Ca transient. *J Mol Cell Cardiol* **48**(1), 112–21 (2010)
58. Hohnloser, S.H., Ikeda, T., Cohen, R.J.: Evidence regarding clinical use of microvolt t-wave alternans. *Heart Rhythm* **6**(3 Suppl), S36–44 (2009)
59. Hoogendoijk, M.G., Potse, M., Vinet, A., de Bakker, J.M., Coronel, R.: ST segment elevation by current-to-load mismatch: an experimental and computational study. *Heart Rhythm* **8**(1), 111–8 (2011)
60. Hu, Y., Gurev, V., Constantino, J., Bayer, J.D., Trayanova, N.A.: Effects of mechano-electric feedback on scroll wave stability in human ventricular fibrillation. *PLoS. One.* **8**(4), e60,287 (2013)

61. Ijiri, T., Ashihara, T., Yamaguchi, T., Takayama, K., Igarashi, T., Shimada, T., Namba, T., Haraguchi, R., Nakazawa, K.: A procedural method for modeling the Purkinje fibers of the heart. *J. Physiol. Sci.* **58**(7), 481–6 (2008)
62. Jessup, M., Greenberg, B., Mancini, D., Cappola, T., Pauly, D.F., Jaski, B., Yaroshinsky, A., Zsebo, K.M., Dittrich, H., Hajjar, R.J.: Calcium Upregulation by Percutaneous Administration of Gene Therapy in Cardiac Disease, I.: Calcium upregulation by percutaneous administration of gene therapy in cardiac disease (CUPID): a phase 2 trial of intracoronary gene therapy of sarcoplasmic reticulum Ca<sup>2+</sup>-ATPase in patients with advanced heart failure. *Circulation* **124**(3), 304–13 (2011)
63. Jie, X., Gurev, V., Trayanova, N.: Mechanisms of mechanically induced spontaneous arrhythmias in acute regional ischemia. *Circ. Res.* **106**(1), 185–92 (2010)
64. Jie, X., Rodriguez, B., de Groot, J.R., Coronel, R., Trayanova, N.: Reentry in survived subepicardium coupled to depolarized and inexcitable midmyocardium: insights into arrhythmogenesis in ischemia phase 1b. *Heart Rhythm* **5**(7), 1036–44 (2008)
65. Jie, X., Trayanova, N.A.: Mechanisms for initiation of reentry in acute regional ischemia phase 1b. *Heart Rhythm* **7**(3), 379–86 (2010)
66. Jons, C., O-Uchi, J., Moss, A.J., Reumann, M., Rice, J.J., Goldenberg, I., Zareba, W., Wilde, A.A., Shimizu, W., Kanters, J.K., McNitt, S., Hofman, N., Robinson, J.L., Lopes, C.M.: Use of mutant-specific ion channel characteristics for risk stratification of long QT syndrome patients. *Sci. Transl. Med.* **3**(76), 76ra28 (2011)
67. Keldermann, R.H., Nash, M.P., Gelderblom, H., Wang, V.Y., Panfilov, A.V.: Electromechanical wavebreak in a model of the human left ventricle. *Am. J. Physiol. Heart Circ. Physiol.* **299**(1), H134–43 (2010)
68. Keldermann, R.H., ten Tusscher, K.H., Nash, M.P., Bradley, C.P., Hren, R., Taggart, P., Panfilov, A.V.: A computational study of mother rotor VF in the human ventricles. *Am. J. Physiol. Heart Circ. Physiol.* **296**(2), H370–9 (2009)
69. Keldermann, R.H., ten Tusscher, K.H., Nash, M.P., Hren, R., Taggart, P., Panfilov, A.V.: Effect of heterogeneous apd restitution on VF organization in a model of the human ventricles. *Am. J. Physiol. Heart Circ. Physiol.* **294**(2), H764–74 (2008)
70. Kim, R.H., Kim, D.H., Xiao, J., Kim, B.H., Park, S.I., Panilaitis, B., Ghaffari, R., Yao, J., Li, M., Liu, Z., Malyarchuk, V., Kim, D.G., Le, A.P., Nuzzo, R.G., Kaplan, D.L., Omenetto, F.G., Huang, Y., Kang, Z., Rogers, J.A.: Waterproof AlInGaP optoelectronics on stretchable substrates with applications in biomedicine and robotics. *Nat. Mater.* **9**(11), 929–37 (2010)
71. Li, P., Rudy, Y.: A model of canine purkinje cell electrophysiology and Ca(2+) cycling: rate dependence, triggered activity, and comparison to ventricular myocytes. *Circ. Res.* **109**(1), 71–9 (2011)
72. Li, W., Gurev, V., McCulloch, A.D., Trayanova, N.A.: The role of mechanolectric feedback in vulnerability to electric shock. *Prog. Biophys. Mol. Biol.* **97**(2-3), 461–78 (2008)
73. Li, W., Janardhan, A.H., Fedorov, V.V., Sha, Q., Schuessler, R.B., Efimov, I.R.: Low-energy multistage atrial defibrillation therapy terminates atrial fibrillation with less energy than a single shock. *Circ. Arrhythm. Electrophysiol.* **4**(6), 917–25 (2011)
74. Li, W., Kohl, P., Trayanova, N.: Induction of ventricular arrhythmias following mechanical impact: a simulation study in 3D. *J. Mol. Histol.* **35**(7), 679–86 (2004)
75. Li, W., Kohl, P., Trayanova, N.: Myocardial ischemia lowers precordial thump efficacy: an inquiry into mechanisms using three-dimensional simulations. *Heart Rhythm* **3**(2), 179–86 (2006)

76. Li, W., Ripplinger, C.M., Lou, Q., Efimov, I.R.: Multiple monophasic shocks improve electrotherapy of ventricular tachycardia in a rabbit model of chronic infarction. *Heart Rhythm* **6**(7), 1020–7 (2009)
77. Lin, J.Y., Knutson, P.M., Muller, A., Kleinfeld, D., Tsien, R.Y.: ReaChR: a red-shifted variant of channelrhodopsin enables deep transcranial optogenetic excitation. *Nat. Neurosci.* **16**(10), 1499–508 (2013)
78. Lindblom, A.E., Roth, B.J., Trayanova, N.A.: Role of virtual electrodes in arrhythmogenesis: pinwheel experiment revisited. *J. Cardiovasc. Electrophysiol.* **11**(3), 274–85 (2000)
79. Luther, S., Fenton, F.H., Kornreich, B.G., Squires, A., Bittihn, P., Hornung, D., Zabel, M., Flanders, J., Gladuli, A., Campoy, L., Cherry, E.M., Luther, G., Hasenfuss, G., Krinsky, V.I., Pumir, A., Gilmour R. F., J., Bodenschatz, E.: Low-energy control of electrical turbulence in the heart. *Nature* **475**(7355), 235–9 (2011)
80. Merchant, F.M., Armandas, A.A.: Role of substrate and triggers in the genesis of cardiac alternans, from the myocyte to the whole heart: implications for therapy. *Circulation* **125**(3), 539–49 (2012)
81. Meunier, J.M., Eason, J.C., Trayanova, N.A.: Termination of reentry by a long-lasting ac shock in a slice of canine heart: a computational study. *J. Cardiovasc. Electrophysiol.* **13**(12), 1253–61 (2002)
82. Meunier, J.M., Trayanova, N.A., Gray, R.A.: Sinusoidal stimulation of myocardial tissue: effects on single cells. *J. Cardiovasc. Electrophysiol.* **10**(12), 1619–30 (1999)
83. Meunier, J.M., Trayanova, N.A., Gray, R.A.: Entrainment by an extracellular AC stimulus in a computational model of cardiac tissue. *J. Cardiovasc. Electrophysiol.* **12**(10), 1176–84 (2001)
84. Moreno, J.D., Zhu, Z.I., Yang, P.C., Bankston, J.R., Jeng, M.T., Kang, C., Wang, L., Bayer, J.D., Christini, D.J., Trayanova, N.A., Ripplinger, C.M., Kass, R.S., Clancy, C.E.: A computational model to predict the effects of class I anti-arrhythmic drugs on ventricular rhythms. *Sci. Transl. Med.* **3**(98), 98ra83 (2011)
85. Narayan, S.M., Bayer, J.D., Lalani, G., Trayanova, N.A.: Action potential dynamics explain arrhythmic vulnerability in human heart failure: a clinical and modeling study implicating abnormal calcium handling. *J. Am. Coll. Cardiol.* **52**(22), 1782–92 (2008)
86. Narayan, S.M., Franz, M.R., Lalani, G., Kim, J., Sastry, A.: T-wave alternans, restitution of human action potential duration, and outcome. *J. Am. Coll. Cardiol.* **50**(25), 2385–92 (2007)
87. Ng, J., Jacobson, J.T., Ng, J.K., Gordon, D., Lee, D.C., Carr, J.C., Goldberger, J.J.: Virtual electrophysiological study in a 3-dimensional cardiac magnetic resonance imaging model of porcine myocardial infarction. *J. Am. Coll. Cardiol.* **60**(5), 423–30 (2012)
88. Noble, D.: Modeling the heart—from genes to cells to the whole organ. *Science* **295**(5560), 1678–1682 (2002)
89. Nygren, A., Fiset, C., Firek, L., Clark, J.W., Lindblad, D.S., Clark, R.B., Giles, W.R.: Mathematical model of an adult human atrial cell: the role of K<sup>+</sup> currents in repolarization. *Circ. Res.* **82**(1), 63–81 (1998)
90. O'Hara, T., Rudy, Y.: Arrhythmia formation in subclinical ("silent") long QT syndrome requires multiple insults: Quantitative mechanistic study using the KCNQ1 mutation q357r as example. *Heart Rhythm* **9**(2), 275–82 (2012)
91. O'Hara, T., Virag, L., Varro, A., Rudy, Y.: Simulation of the undiseased human cardiac ventricular action potential: model formulation and experimental validation. *PLoS. Comput. Biol.* **7**(5), e1002,061 (2011)
92. Pandit, S.V., Jalife, J.: Rotors and the dynamics of cardiac fibrillation. *Circ. Res.* **112**(5), 849–62 (2013)

93. Plonsey, R., Barr, R.C.: Bioelectricity : a quantitative approach, 3rd edn. Springer, New York, NY (2007)
94. Pop, M., Sermesant, M., Mansi, T., Crystal, E., Ghate, S., Peyrat, J., Lashevsky, I., Beiping, Q., McVeigh, E., Ayache, N., Wright, G.A.: Correspondence between simple 3-D MRI-based computer models and in-vivo ep measurements in swine with chronic infarctions. *IEEE Trans. Biomed. Eng.* **58**(12), 3483–6 (2011)
95. Potsе, M., Krause, D., Bacharova, L., Krause, R., Prinzen, F.W., Auricchio, A.: Similarities and differences between electrocardiogram signs of left bundle-branch block and left-ventricular uncoupling. *Europace* **14**(Suppl 5), v33–v39 (2012)
96. Rantner, L.J., Arevalo, H.J., Constantino, J.L., Efimov, I.R., Plank, G., Trayanova, N.A.: Three-dimensional mechanisms of increased vulnerability to electric shocks in myocardial infarction: Altered virtual electrode polarizations and conduction delay in the peri-infarct zone. *J. Physiol.* **590**(Pt 18), 4537–4551 (2012)
97. Rantner, L.J., Tice, B.M., Trayanova, N.A.: Terminating ventricular tachyarrhythmias using far-field low-voltage stimuli: Mechanisms and delivery protocols. *Heart Rhythm* **10**(8), 1209–17 (2013)
98. Rantner, L.J., Vadakkumpadan, F., Spevak, P.J., Crosson, J.E., Trayanova, N.A.: Placement of implantable cardioverter-defibrillators in paediatric and congenital heart defect patients: A pipeline for model generation and simulation prediction of optimal configurations. *J. Physiol.* **591**, 4321–34 (2013)
99. Relan, J., Chinchapatnam, P., Sermesant, M., Rhode, K., Ginks, M., Delingette, H., Rinaldi, C.A., Razavi, R., Ayache, N.: Coupled personalization of cardiac electrophysiology models for prediction of ischaemic ventricular tachycardia. *Interface Focus* **1**(3), 396–407 (2011)
100. Richards, D.F., Glosli, J.N., Draeger, E.W., Mirin, A.A., Chan, B., Fattebert, J.L., Krauss, W.D., Oppelstrup, T., Butler, C.J., Gunnels, J.A., Gurev, V., Kim, C., Magerlein, J., Reumann, M., Wen, H.F., Rice, J.J.: Towards real-time simulation of cardiac electrophysiology in a human heart at high resolution. *Comput. Methods Biomed. Engin.* **16**(7), 802–5 (2013)
101. Roberts, B.N., Yang, P.C., Behrens, S.B., Moreno, J.D., Clancy, C.E.: Computational approaches to understand cardiac electrophysiology and arrhythmias. *Am. J. Physiol. Heart Circ. Physiol.* **303**(7), H766–H783 (2012)
102. Robichaux, R.P., Dosdall, D.J., Osorio, J., Garner, N.W., Li, L., Huang, J., Ideker, R.E.: Periods of highly synchronous, non-reentrant endocardial activation cycles occur during long-duration ventricular fibrillation. *J. Cardiovasc. Electrophysiol* **21**(11), 1266–73 (2010)
103. Rodriguez, B., Eason, J.C., Trayanova, N.: Differences between left and right ventricular anatomy determine the types of reentrant circuits induced by an external electric shock. a rabbit heart simulation study. *Prog Biophys Mol Biol* **90**(1-3), 399–413 (2006)
104. Rodriguez, B., Li, L., Eason, J.C., Efimov, I.R., Trayanova, N.A.: Differences between left and right ventricular chamber geometry affect cardiac vulnerability to electric shocks. *Circ. Res.* **97**(2), 168–75 (2005)
105. Rodriguez, B., Tice, B.M., Eason, J.C., Aguel, F., Ferrero J. M., J., Trayanova, N.: Effect of acute global ischemia on the upper limit of vulnerability: a simulation study. *Am. J. Physiol. Heart Circ. Physiol.* **286**(6), H2078–88 (2004)
106. Rodriguez, B., Tice, B.M., Eason, J.C., Aguel, F., Trayanova, N.: Cardiac vulnerability to electric shocks during phase 1a of acute global ischemia. *Heart Rhythm* **1**(6), 695–703 (2004)

107. Rodriguez, B., Trayanova, N.: Upper limit of vulnerability in a defibrillation model of the rabbit ventricles. *J. Electrocardiol.* **36**(Suppl.), 51–6 (2003)
108. Sampson, K.J., Iyer, V., Marks, A.R., Kass, R.S.: A computational model of Purkinje fibre single cell electrophysiology: implications for the long QT syndrome. *J. Physiol.* **588**(Pt 14), 2643–55 (2010)
109. Sebastian, R., Zimmerman, V., Romero, D., Sanchez-Quintana, D., Frangi, A.F.: Characterization and modeling of the peripheral cardiac conduction system. *IEEE Trans. Med. Imaging* **32**(1), 45–55 (2013)
110. Spiteri, R.J., Dean, R.C.: Stiffness analysis of cardiac electrophysiological models. *Ann. Biomed. Eng.* **38**(12), 3592–604 (2010)
111. Stevenson, W.G., Brugada, P., Waldecker, B., Zehender, M., Wellens, H.J.: Clinical, angiographic, and electrophysiologic findings in patients with aborted sudden death as compared with patients with sustained ventricular tachycardia after myocardial infarction. *Circulation* **71**(6), 1146–52 (1985)
112. Stewart, P., Aslanidi, O.V., Noble, D., Noble, P.J., Boyett, M.R., Zhang, H.: Mathematical models of the electrical action potential of Purkinje fibre cells. *Philos. Trans. A Math. Phys. Eng. Sci.* **367**(1896), 2225–55 (2009)
113. Tandri, H., Weinberg, S.H., Chang, K.C., Zhu, R., Trayanova, N.A., Tung, L., Berger, R.D.: Reversible cardiac conduction block and defibrillation with high-frequency electric field. *Sci. Transl. Med.* **3**(102), 102ra96 (2011)
114. Ten Tusscher, K.H., Hren, R., Panfilov, A.V.: Organization of ventricular fibrillation in the human heart. *Circ. Res.* **100**(12), e87–101 (2007)
115. Trayanova, N., Constantino, J., Ashihara, T., Plank, G.: Modeling defibrillation of the heart: approaches and insights. *IEEE Rev Biomed Eng* **4**, 89–102 (2011)
116. Trayanova, N., Eason, J., Aguel, F.: Cardiac defibrillation: A look inside the heart. *Computing and Visualization in Science* **3**, 259–270 (2002)
117. Trayanova, N., Li, W., Eason, J., Kohl, P.: Effect of stretch-activated channels on defibrillation efficacy. *Heart Rhythm* **1**(1), 67–77 (2004)
118. Trayanova, N., Skouibine, K., Moore, P.: Virtual electrode effects in defibrillation. *Prog. Biophys. Mol. Biol.* **69**(2-3), 387–403 (1998)
119. Trayanova, N.A.: Whole-heart modeling: applications to cardiac electrophysiology and electromechanics. *Circ. Res.* **108**(1), 113–28 (2011)
120. Trayanova, N.A., Gurev, V., Constantino, J., Hu, Y.: Mathematical models of ventricular mechano-electric coupling and arrhythmia, 2nd edn., pp. 258–268. Oxford University Press, Oxford, New York (2011)
121. ten Tusscher, K.H., Panfilov, A.V.: Alternans and spiral breakup in a human ventricular tissue model. *Am. J. Physiol. Heart Circ. Physiol.* **291**(3), H1088–100 (2006)
122. Vadakkumpadan, F., Arevalo, H., Ceritoglu, C., Miller, M., Trayanova, N.: Image-based estimation of ventricular fiber orientations for personalized modeling of cardiac electrophysiology. *IEEE Trans. Med. Imaging* **31**(5), 1051–60 (2012)
123. Vadakkumpadan, F., Arevalo, H., Prassl, A.J., Chen, J., Kickinger, F., Kohl, P., Plank, G., Trayanova, N.: Image-based models of cardiac structure in health and disease. *Wiley Interdiscip. Rev. Syst. Biol. Med.* **2**(4), 489–506 (2010)
124. Vaidyanathan, R., O'Connell, R.P., Deo, M., Milstein, M.L., Furspan, P., Herron, T.J., Pandit, S.V., Musa, H., Berenfeld, O., Jalife, J., Anumonwo, J.M.: The ionic bases of the action potential in isolated mouse cardiac Purkinje cell. *Heart Rhythm* **10**(1), 80–7 (2013)

125. Veenhuyzen, G.D., Coverett, K., Quinn, F.R., Sapp, J.L., Gillis, A.M., Sheldon, R., Exner, D.V., Mitchell, L.B.: Single diagnostic pacing maneuver for supraventricular tachycardia. *Heart Rhythm* **5**(8), 1152–8 (2008)
126. Vigmond, E., Vadakkumpadan, F., Gurev, V., Arevalo, H., Deo, M., Plank, G., Trayanova, N.: Towards predictive modelling of the electrophysiology of the heart. *Exp. Physiol.* **94**(5), 563–77 (2009)
127. Wang, L., Wong, K.C., Zhang, H., Liu, H., Shi, P.: Noninvasive computational imaging of cardiac electrophysiology for 3-D infarct. *IEEE Trans. Biomed. Eng.* **58**(4), 1033–43 (2011)
128. Weinberg, S.H., Chang, K.C., Zhu, R., Tandri, H., Berger, R.D., Trayanova, N.A., Tung, L.: Defibrillation success with high frequency electric fields is related to degree and location of conduction block. *Heart Rhythm* **10**(5), 740–8 (2013)
129. Weiss, J.N., Nivala, M., Garfinkel, A., Qu, Z.: Alternans and arrhythmias: from cell to heart. *Circ. Res.* **108**(1), 98–112 (2011)
130. Wilhelms, M., Rombach, C., Scholz, E.P., Dossel, O., Seemann, G.: Impact of amiodarone and cisapride on simulated human ventricular electrophysiology and electrocardiograms. *Europace* **14**(Suppl 5), v90–v96 (2012)
131. Williams, J.C., Xu, J., Lu, Z., Klimas, A., Chen, X., Ambrosi, C.M., Cohen, I.S., Entcheva, E.: Computational optogenetics: empirically-derived voltage- and light-sensitive channelrhodopsin-2 model. *PLoS. Comput. Biol.* **9**(9), e1003220 (2013)
132. Winslow, R.L., Trayanova, N., Geman, D., Miller, M.I.: Computational medicine: translating models to clinical care. *Sci. Transl. Med.* **4**(158), 158rv11 (2012)
133. Wong, J., Abilez, O.J., Kuhl, E.: Computational optogenetics: A novel continuum framework for the photoelectrochemistry of living systems. *J. Mech. Phys. Solids* **60**(6), 1158–1178 (2012)
134. Xia, L., Zhang, Y., Zhang, H., Wei, Q., Liu, F., Crozier, S.: Simulation of Brugada syndrome using cellular and three-dimensional whole-heart modeling approaches. *Physiol. Meas.* **27**(11), 1125–42 (2006)
135. Yang, F.: Simulation of electrocardiographic manifestation of healed infarctions using a 3D realistic rabbit ventricular model. *Int. J. Cardiol.* **152**(1), 121–3 (2011)
136. Zemzemi, N., Bernabeu, M.O., Saiz, J., Cooper, J., Pathmanathan, P., Mirams, G.R., Pitt-Francis, J., Rodriguez, B.: Computational assessment of drug-induced effects on the electrocardiogram: from ion channel to body surface potentials. *Br. J. Pharmacol.* **168**(3), 718–33 (2013)
137. Zhao, J.T., Hill, A.P., Varghese, A., Cooper, A.A., Swan, H., Laitinen-Forsblom, P.J., Rees, M.I., Skinner, J.R., Campbell, T.J., Vandenberg, J.I.: Not all hERG pore domain mutations have a severe phenotype: g584s has an inactivation gating defect with mild phenotype compared to g572s, which has a dominant negative trafficking defect and a severe phenotype. *J. Cardiovasc. Electrophysiol.* **20**(8), 923–30 (2009)
138. Zhu, X., Wei, D., Okazaki, O.: Computer simulation of clinical electrophysiological study. *Pacing Clin. Electrophysiol.* **35**(6), 718–29 (2012)

---

# Discrete Mechanical Modeling of Mechanoelectrical Feedback in Cardiac Tissue: Novel Mechanisms of Spiral Wave Initiation

Louis D. Weise and Alexander V. Panfilov

**Abstract** Discrete mechanical modeling offers an attractive alternative to continuum mechanics approaches in studies of finite elastic deformations of cardiac tissue. However, discrete mechanical approaches are not widely used in cardiac modeling. We discuss applications of discrete mechanical modeling, and review our work on the study of the effect of mechano-electrical feedback (MEF) on the process of spiral wave formation in cardiac tissue. MEF is the effect of the deformation of cardiac tissue on its excitation processes. It has been shown that MEF can cause cardiac arrhythmias, which are often underpinned by spiral waves of excitation. We show that MEF substantially affects the process of spiral wave initiation and discuss several new mechanisms which we found using our discrete mechanical approach. Overall, we illustrate the value of discrete mechanical modeling to study MEF in cardiac tissue.

## 2.1 Introduction

The heart is an organ which pumps blood through the body. The rhythmical pumping of the heart is governed by nonlinear waves of electrical excitation. These electrical waves form at a special pacemaking region in the heart, from where they propagate through the cardiac muscle and initiate its contraction. The propagation of electrical activity in the heart is possible, because cardiomyocytes are electrically coupled and excitable. At resting state, the cardiomyocyte maintains a transmembrane potential of around  $-0.1\text{V}$ . When the cell is depolarized above a certain threshold e.g. from an excited neighboring cell, it generates an action potential. During the action potential the conductivity of several ion channels changes with specific dynamics, first causing

---

L.D. Weise · A.V. Panfilov (✉)

Department of Physics and Astronomy, Ghent University, Ghent, Belgium  
e-mail: Louis.Weise@UGent.be; Alexander.Panfilov@UGent.be

a rapid depolarization, followed by a plateau phase of approximately one third of a second, before the cell returns to its resting state and becomes excitable again.

In the normal physiological situation, electrical waves of excitation originate only from the natural pacemaker in the heart. However, abnormal sources of excitation can emerge which cause cardiac arrhythmias. One type of abnormal source of excitation is a rotating spiral wave. When a single spiral wave is present in cardiac tissue it rotates with a high frequency compared to the pacing of the heart's natural pacemaker, which causes a very rapid heartbeat, an arrhythmia called tachycardia [74]. If a single spiral wave breaks up into a complex state where many wave sources are present it results in an arrhythmia called fibrillation [47]. During ventricular fibrillation the electrical activity of the heart is disorganized and the synchronized mechanical contraction stops. This causes immediate loss of consciousness and soon after death. Understanding the mechanisms of onset of arrhythmias, and thus the initiation of spiral waves, is one of the most important tasks in cardiology.

The contraction of a cardiac muscle cell is caused by its excitation via the process of excitation-contraction coupling [2]. However, deformation of a cardiomyocyte is not only caused by electrical excitation, but also feeds back on it. The most immediate, and perhaps most important effect of this "mechano-electrical-feedback" (MEF), is the activation of stretch-activated depolarizing currents (Isac) [21], which has been shown to be able to cause excitation in the heart after mechanical stimulation. Isac occur as there are special stretch-activated ion channels present in the cardiomyocyte, and thus deformation directly affects its excitation. Two examples of immediate MEF with clinical relevance are connected to the heart's response to a mechanical impact. An impact of a ball or a hockey puck on the chest of a healthy person can cause severe arrhythmia and sudden cardiac death. This phenomenon has been reported by clinicians at the end of the 19th century, and is known today as commotio cordis. Another example is that a strong punch on the chest of a patient who is in a state of severe cardiac arrhythmia may immediately restore normal cardiac rhythm. This clinical procedure is called precordial thump. Thus, MEF is not only able to cause arrhythmia, but also to abolish it. For a further review on MEF see [30].

Mathematical modeling of the heart is a valuable tool in cardiology, it experienced a rapid growth in 1962 when Denis Noble extended the Hodgkin-Huxley theory of neuronal cell excitability [20] to cardiac cells [45]. Many models for cardiac electrophysiology were developed at cell, tissue, and whole organ level. These cardiac models have been shown to be able to reproduce experimental findings, and more importantly, also to be able to make robust predictions, which often get experimental confirmation. For example, computer simulations of cardiac tissue provided predictions on the structure and dynamics of rotating spiral waves of electrical excitation, that were validated afterwards in experiments [18, 50, 78].

Yet, despite the success of mathematical models of the heart's excitation processes, they do not include mechanical effects and thus are not directly applicable to study MEF. Early studies on MEF did not describe the excitation-contraction coupling, but assumed a constantly stretched tissue [63, 66]. Later, mathematical models started to describe electromechanical coupling, but they did not account for MEF

effects [17, 39]. The first electromechanical models that described some MEF effects were [23, 40], but they did not account for the most immediate MEF effect of Isac. The first electromechanical model that included MEF via Isac was from Nash et al. [48] who coupled a low-dimensional model for cardiac excitation to a continuous mechanical model. They applied this model to study basic effects of MEF on the heart's functioning. They showed that MEF via Isac causes new phenomena, mechanically caused pacemaking activity in a tissue that without deformation is non-oscillatory [48], spiral drift and breakup [49]. From that point on many electromechanical models were created on various levels of complexity, where the most sophisticated account for the heart's anatomy and its complex excitation-contraction coupling [26, 28]. For a review on electromechanical models of the heart from single cell to whole organ level see [64].

There are two principal ways to formulate mechanical models of cardiac tissue. The most frequently applied approach is to model the mechanics of cardiac tissue in terms of continuum mechanics [24]. It is a challenging problem to implement a continuum mechanics approach in a computationally efficient manner, especially with high spatio-temporal resolution. There is also a possibility to describe cardiac tissue using discrete mechanical approaches. Compared to continuous methods these discrete approaches are not often used in cardiac modeling; however, they have some advantages. In this text we will discuss the application of discrete mechanical approaches in cardiac modeling. In the main part of this text we will focus on our discrete mechanical modeling approach that we developed to study basic effects of MEF. This approach couples a lattice-based discrete mechanical model to models of cardiac excitation and contraction [68, 71].

We applied our discrete mechanical model to systematically study mechanisms of spiral wave initiation. Using the discrete mechanical approach we found that MEF substantially affects the process of spiral wave formation causing novel mechanisms for its initiation [69, 70]. Overall, in this text we demonstrate the value of discrete mechanical modeling of cardiac tissue to study MEF.

## 2.2 Discrete Mechanical Modeling of Cardiac Tissue

Cardiac tissue is a complex material, it is non-homogeneous and anisotropic, as it consists of interconnected sheets of muscle fibers organized by extracellular matrix [33, 39, 67]. Furthermore, the cardiac muscle consists not only of cardiomyocytes which take up approximately 75% of the heart's volume, but also of other cell types with their own characteristic mechanical properties.

The most common approach for modeling the elastic deformations of the heart is to apply the theory of continuum mechanics, and to use finite element techniques to solve the equations [24, 25]. In that approach the passive elastic properties of the cardiac tissue is given by phenomenological macroscopic constitutive relations between stress and strain. Often, cardiac tissue is assumed to be an hyperelastic material when constitutive relations are energy density functions of strain components. In simpli-

fied models the energy density function can e.g. be expressed by the Mooney-Rivlin material relation [40, 48, 49], which was formulated for rubber-like materials. More accurate hyperelastic material relations for cardiac tissue were proposed, for example by the Pole-zero energy density function of Hunter et al. [23] and the material relation of Guccione et al. [16].

Continuum mechanics is widely used in mechanical engineering; however, its application to cardiac tissue is not straightforward. Cardiac tissue is not a continuous material, but an inherently discrete medium. Continuous models for cardiac mechanics do not account for individual structural components, and thus are difficult to use to include structural changes that are known to happen in cardiac disease [13]. In general, the main volume fraction of cardiac tissue is built up by cardiomyocytes which are approximately 100 microns long and interconnected to a network by various mechanical junctions organised by extracellular matrix. It is therefore a natural approach to model cardiac tissue as a structure of discrete elements. In modeling the electrical activity of the heart, this approach is normally used, properties of individual cells and their locations directly come into the equations for electrical excitation. There are experimental techniques to measure the mechanical properties of isolated cardiomyocytes [5, 77] which can be used to built up a mechanical model for the cardiac tissue. However, also the extracellular matrix has a substantial effect on the heart's mechanical properties [13]. There are attempts to measure contributions and the structure of components of the extracellular matrix on mechanical properties, and they can also be modeled as discrete elements [13]. There are still many problems to be solved until a mechanical model for the heart based on properties of discrete elements and tissue structures will be available.

Discrete mechanical modeling in general is used in various fields, for example to describe solids that discontinuously deform such as in fracture and plastic deformation processes [46, 55]. It is also used to model mechanical properties of tissues. There are different classes of discrete mechanical tissue models. A class named off-lattice models describes cells as not being restricted to a regular grid, and to directly interact with neighboring cells only. This model type allows to describe biological phenomena such as growth, cell division and growth without causing immediate mechanical long-range effects [53]. Another class of discrete tissue model form the lattice-based models in which cells are constrained to a regular grid. Lattice-based models are considered not to be applicable to describe the above mentioned relatively slow biological processes (e.g. growth, cell motion) [53]. However, these models are good to describe mechanical long-range interactions such as the finite elastic deformations of the heart tissue. The class of lattice-based discrete models is computationally efficient, and therefore often applied in various fields such as computer graphics [41], tissue visualization [12], and also for developing mechanical models of anisotropic materials [4].

To our knowledge, the first applications of lattice-based discrete mechanical models of cardiac tissue were done by the group of Olaf Dössel. This group developed three-dimensional lattice-based discrete models for the heart [35–37]. These models describe the incompressibility and anisotropy of cardiac tissue by using a method introduced by Bourguignon et al. [4]. They also extended their discrete modeling

approach to perfectly describe advanced hyperelastic material relations such as the Pole-zero or the Guccione law [14].

The papers mentioned above show that lattice-based discrete mechanical models can reproduce known constitutive laws and follow incompressibility constraints, thus they can be used for simulations similar to those using continuous models. However, these models do not provide a direct relation from individual cell mechanical properties and tissue structure to macroscopic deformation laws. This problem on how one can obtain macroscopic constitutive laws from microscopic properties was investigated in a series of papers by Raoult, Caillerie and coauthors [7, 8]. In this work they considered a regular network of cardiac myocytes as a model for cardiac tissue. The individual cells were represented as elastic bars with prescribed local constitutive laws. The group applied homogenization techniques on the tissue structure and properties of individual elements to derive macroscopic constitutive relations for the tissue. Unfortunately, this approach has not been further extended yet to include measured properties of the individual cardiac cells.

We believe that we will see a lot of developments in the discrete modeling approach for cardiac applications in the future, both on the relation of tissue structure to constitutive relations, and on the direct modeling of cardiac tissue as a discrete mechanical system.

In the next section we will explain the setting up of a discrete lattice-based model for cardiac tissue to study basic effects of MEF. Then we will present the results we achieved with this model to study which influence MEF has on basic mechanisms of spiral wave formation.

## 2.3 A Discrete Mechanical Model for Cardiac Tissue

Our electromechanical model for cardiac tissue combines models for cardiac excitation and excitation-contraction coupling with a discrete mechanical model. Here we explain the model setup using generic models for cardiac excitation and contraction-coupling, that were also applied in [48]. The same approach can easily be extended to other models for cardiac excitation and contraction. For example, in [71] we coupled the discrete mechanical model to an detailed ionic model for cardiac excitability of Tusscher et al. [61, 62], and a biophysical model for cardiac contraction of Niederer et al. [42, 44].

The Aliev-Panfilov model [1] provides a low-dimensional description of excitation for cardiac cells. The equations of this model are

$$\frac{\partial u}{\partial t} = \Delta u - ku(u-a)(u-1) - uv - I_s \quad (2.1)$$

$$\frac{\partial v}{\partial t} = \varepsilon(u)(ku-v), \quad (2.2)$$

where  $u$  is represents the transmembrane potential, and  $v$  is the conductance of a slow repolarizing current. The term  $-ku(u-a)(u-1)$  describes the fast excitation pro-

cess of the action potential. The parameter  $a = 0.08$  describes the activation threshold, and  $k = 8$  is the magnitude of the transmembrane current.  $\varepsilon(u)$  is a step function which sets the time scale of the recovery and the contraction process ( $\varepsilon(u) = 1$  for  $u < 0.05$ , and  $\varepsilon(u) = 0.1$  for  $u \geq 0.05$ ). A repolarizing current is given by  $-uv$ . The term  $I_s$  is a generic description of Isac which we describe later in Eq. (2.9). The term  $\Delta u$  models the propagation of electrical excitation through the tissue [27]. In a non-deforming medium Eqs. (2.1), (2.2) describe non-oscillatory cardiac tissue.

During the action potential of a cell its contraction is initiated by an increase in calcium concentration. We describe the excitation-contraction coupling using a generic model

$$\frac{\partial T_a}{\partial t} = \varepsilon(u)(k_T u - T_a), \quad (2.3)$$

where  $T_a$  modulates active contraction force given by Eq. (2.5) to mass points of the medium. The parameter  $k_T = 1.5$  controls the rate of active force development. The Eq. (2.3) was also used in the continuous mechanical model [48] to account for the active stress.

To model the mechanical part of the model we use a two-dimensional mass-spring lattice that is illustrated in Fig. 2.1a. This forms an ideal crystal lattice whose unit cell is shown in Fig. 2.1b. Each mass point is connected to its neighbouring mass points by springs that follow Hooke's law. Horizontal and vertical springs produce active contraction forces. The resting length of a horizontal and vertical spring is  $r_0$ , and it is  $\sqrt{2}r_0$  for a diagonal spring. As in a previous continuous mechanical model [48] we assume elastostatics. Therefore, the stationary deformations corresponding to each given configuration of active forces and boundary conditions are computed. At steady state, the total force at each node is zero. If the configuration of the active forces is changed the mass points will be deformed to the new corresponding stationary configuration. For efficient computations of this system, viscous forces are added to dampen possible oscillations. Figure 2.1c demonstrates main forces and the displacements of active and passive lattice springs connecting the mass point ① to

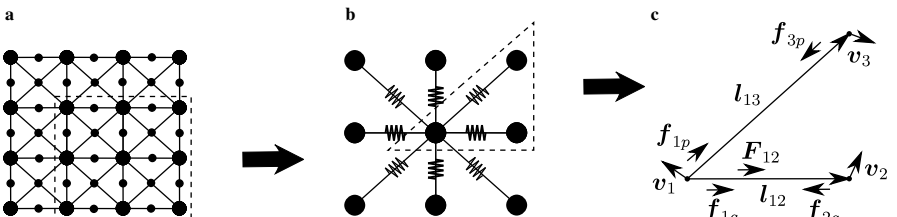


**Fig. 2.1.** (a) Coupled mechanical and electrical mesh of the model. The mass points are indicated as large black dots. The finite difference points to solve Eqs. (2.1)–(2.3), (2.9) are indicated as small white dots. The lattice springs are indicated as black lines; (b) Unit cell of the lattice. Mass point ① and its horizontal and vertical neighbors are connected with active springs. Diagonal neighbors are connected with passive springs. Springs are indicated by zigzagging lines, where fat lines represent active springs, and thin lines passive springs. Dotted contours indicate insets; (c) Vectors used in Eqs. (2.4)–(2.6). From [68]

the mass points ❷ and ❸. The positions of the mass points are given by  $\mathbf{x}_1$ ,  $\mathbf{x}_2$ ,  $\mathbf{x}_3$ , with the corresponding velocities  $\mathbf{v}_1$ ,  $\mathbf{v}_2$  and  $\mathbf{v}_3$ . Mass points ❶ and ❷ are connected by an active spring. The force generated by this spring on the mass points is given by

$$\mathbf{f}_{1a} = -\mathbf{f}_{2a} = \left[ c \left( \frac{\|\mathbf{l}_{12}\| - r_0}{r_0} \right) - d \frac{(\mathbf{i}_{12} \cdot \mathbf{l}_{12})}{\|\mathbf{l}_{12}\|} \right] \frac{\mathbf{l}_{12}}{\|\mathbf{l}_{12}\|} + \mathbf{F}_{12}, \quad (2.4)$$

where  $\mathbf{l}_{12} = \mathbf{x}_2 - \mathbf{x}_1$  is a vector along an active spring,  $\mathbf{i}_{12} = \mathbf{v}_2 - \mathbf{v}_1$  is the time derivative of the spring vector  $\mathbf{l}_{12}$ , parameters  $c = 1$  and  $d = 30$  (in mechanical inhomogeneity:  $d = 10 \times c$ ) are the stiffness and damping constants. The active force between mass points ❶ and ❷ is

$$\mathbf{F}_{12} = p \left( \frac{T_a(1) + T_a(2)}{2} \right) \frac{\mathbf{l}_{12}}{\|\mathbf{l}_{12}\|}, \quad (2.5)$$

where  $T_a(i)$  is the value of variable  $T_a$  from Eq. (2.3) at the  $i$ th mass point. Parameter  $p$  is a scaling factor which we apply to model mechanical heterogeneity in active tension development ( $p = 1$  in normal tissue). Mass points ❶ and ❸ are connected by a passive spring. The force generated by this spring is given by

$$\mathbf{f}_{1p} = -\mathbf{f}_{3p} = 1/2 \left[ c \left( \frac{\|\mathbf{l}_{13}\| - \sqrt{2}r_0}{\sqrt{2}r_0} \right) - d \frac{(\mathbf{i}_{13} \cdot \mathbf{l}_{13})}{\|\mathbf{l}_{13}\|} \right] \frac{\mathbf{l}_{13}}{\|\mathbf{l}_{13}\|}. \quad (2.6)$$

Each mass point follows Newton's law of motion:

$$\sum_{\alpha=1}^N \mathbf{f}_{i\alpha} = m \ddot{\mathbf{x}}_i, \quad (2.7)$$

where  $N$  is the number of springs connected to mass point  $i$  with mass  $m$ , and  $\alpha$  indicates connected springs. By solving Eq. (2.7) to mechanical equilibrium ( $\sum_{\alpha=1}^N \mathbf{f}_{i\alpha} = 0$ ), the steady state configuration of the lattice for each given distribution of active forces generated by the excitation processes is found. Note that the "mechanical" time variable  $\tau$ , damping parameter  $d$  and the mass of a node  $m = 1$  have no physical relevance in this model, but can be chosen for optimal efficiency of computations. Here we did not aim at developing a model where mass points, springs and mesh structure represent a direct biophysical property, but focussed on creating a computationally efficient, generic model for cardiac tissue with given material properties. However, our approach can be extended in that aspect, to include the parameters with a direct physical meaning.

It is possible to formulate the elastic properties of the discrete mechanical model model in terms of an equivalent continuous material. The mass-lattice structure (Fig. 2.1b) in this paper was extensively studied for various aspects of elasticity. In most cases the mass-lattice model was studied under conditions of small deformations (linear elasticity). Schargott et al. showed that if the stiffness ratio of diagonal to active springs was 1/2, the lattice would be macroscopically isotropic for small deformations [57]. We apply this stiffness ratio in our model. In this case the constitutive

tutive relations simplify to the generalized Hooke's law [57]. We demonstrated in a numerical study that the model can be considered in good approximation as isotropic for deformations occurring during our simulations. Krivtsov et al. explained in [32], that even for non-linear deformations, the elastic properties of our model can be approximated by a generalization of Hooke's law for finite deformations (Seth material) [58].

$$\sigma_{ij} = 2\mu E_{ij} + \lambda(\text{tr}\mathbf{E})\delta_{ij}, \quad (2.8)$$

where  $\sigma_{ij}$  are elements of Cauchy's stress tensor,  $E_{ij}$  elements Almansi's finite strain tensor  $\mathbf{E}$ ,  $\delta_{ij}$  is the Kronecker delta and  $\lambda$  and  $\mu$  are the Lamé coefficients, which in this case are equal to each other [57]. The two-dimensional Young's modulus in terms of the spring stiffness is  $E_{2D} = 4/3c$ , and Poisson's ratio  $\nu_{2D} = 1/3$  [57].

Experimental studies showed that the direct physiological influence of contraction on cardiac tissue is given by depolarising stretch-activated current Isac through stretch activated channels [30]. Experimental studies have shown, that these channels are activated instantaneously with mechanical stretch and follow a linear current-voltage relationship [22, 76]. Linear models have been proposed for Isac [63, 66], and are often used in electromechanical models for cardiac tissue [48, 49]. Therefore we use a very similar term of a generic stretch-activated current

$$I_s = G_s(\sqrt{A} - 1)(u - E_s), \quad (2.9)$$

where  $G_s$  and  $E_s$  are the maximal conductance and reversal potential of the stretch activated channels. We also follow [48, 49], and set  $E_s = 1$ . Variable  $A$  is the surface area of a quadrilateral formed by 4 neighboring mass points (see Fig. 2.1a) normalized using the reference surface area of this quadrilateral in undeformed state ( $r_0^2 \text{ s.u.}^2$ ). The stretch activated current is active only if  $A > 1$  (stretch). We vary  $G_s$  in different simulations.

### 2.3.1 Numerical Methods

The model was solved with a hybrid integration approach which combines an explicit Euler method for the electrical system (Eqs. (2.1)–(2.3)) with a Verlet integration scheme [65] to solve the mechanical problem (Eqs. (2.4)–(2.7)). Using the Verlet method the position of a mass point  $i$  for the integration time  $\tau + m\tau$  is computed by

$$\mathbf{x}_i(\tau + m\tau) = 2\mathbf{x}_i(\tau) - \mathbf{x}_i(\tau - m\tau) + \ddot{\mathbf{x}}_i(\tau) \times (m\tau)^2,$$

where  $m\tau = 0.01$  is the Verlet integration time step and  $\tau$  is the integration time. The acceleration of a mass point  $\ddot{\mathbf{x}}_i(\tau)$  is given by Eq. (2.7). At each time step the velocities of the mass points are calculated by

$$\mathbf{v}_i(\tau) = \frac{\mathbf{x}_i(\tau) - \mathbf{x}_i(\tau - m\tau)}{m\tau}.$$

The solution procedure of the model is as follows: following a time integration step for the electrical system, the equations of the mechanical system are solved for all springs until the sum of forces for each mass point is under the convergence thresh-

old  $2e - 5$  (dimensionless force units [f.u.]). Euler computations were performed on a quadratic deforming grid of finite difference points using no-flux boundary conditions. We used for all simulations an Euler integration time step of  $ht = 0.001$  (dimensionless time units [t.u.]) and a space integration step of  $hx = hy = 0.3$  (dimensionless space units [s.u.]). During the simulations the boundaries of the medium were fixed in space. This approach was applied in similar models [48, 49]. This assumption corresponds to the isometric contraction in tissue experiments, and is similar to the isovolumic phases of the cardiac cycle at the whole organ level.

## 2.4 Mechanisms of Spiral Wave Initiation Due to MEF

In this section we present results on our study on how MEF affects the formation of spiral waves in cardiac tissue. However, before we do it we will give some background information on classical mechanisms of spiral wave initiation. Here we mention only two classical mechanisms of spiral wave initiation, for more mechanisms see [52].

Two classical mechanisms for the initiation of spiral waves are due to heterogeneities in the refractory period in the tissue and the so-called vulnerability phenomenon. The mechanism of spiral formation caused by an inhomogeneity in refractory period was found by Krinsky [31]. We illustrate it in Fig. 2.2. To explain this mechanism let us consider a thin slice of cardiac tissue with an inhomogeneity in which the refractory period  $R_{inh}$  is longer than in the rest of the tissue ( $R < R_{inh}$ ). Let us consider two plain waves (Fig. 2.2a). In this situation wave break occurs, when the coupling interval  $T$  lies within the refractory periods of the inhomogeneity and the bulk medium ( $R < T < R_{inh}$ ). In this situation the second wave can not propagate into the inhomogeneous region as it is still refractory from the excitation

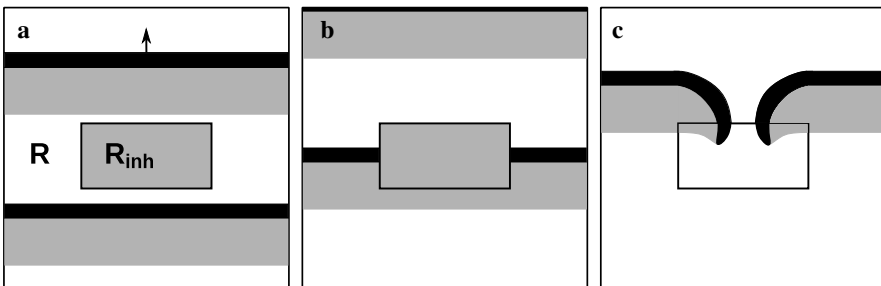


**Fig. 2.2.** Spiral wave formation due to inhomogeneity in refractory period (schematic). The inhomogeneity with longer refractory period ( $R_{inh}$ ) than the surrounding medium ( $R$ ) is shown as a rectangle. The wave front is indicated as black, refractory wave back is indicated grey. Propagation direction of waves is upwards. (a) Two connected waves propagate through the medium, the medium in the inhomogeneity is still refractory from the excitation from the first wave, (b) and causes a wave break of a second wave (c), which results in two counter-rotating spiral waves

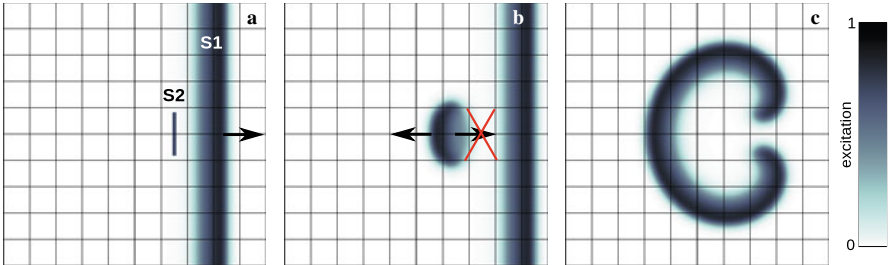


**Fig. 2.3.** Spiral wave formation due to classical vulnerability. (a) A stimulus “S2” is applied in the vulnerable zone of a traveling wave “S1”; (b) The resulting wave from the S2 stimulus is able to propagate away from the S1 wave, but is blocked towards it because of the refractory tail of the S1 wave; (c) The unidirectionally blocked S2 wave forms a pair of counter-rotating spiral waves System size was 60 s.u.

of the previous wave (Fig. 2.2b). After some while, the two wave fronts, which resulted from the wave break can enter the previously inexcitable region, and form two counter-rotating spiral waves (Fig. 2.2c).

Another mechanism for spiral wave formation is connected to the vulnerability phenomenon [59], which has been described in 1946 by Wiener and Rosenblueth in a modeling study [73], and validated experimentally 1988 by Chen et al. [9]. In this protocol a “secondary stimulus” (S2) is applied in the back of a previously initiated “S1 wave” (Fig. 2.3a). If S2 is applied at the boundary of the refractory tail of the S1 wave, then its wave response can be blocked towards the S1 wave (Fig. 2.3b). As a result a pair of counter-rotating spiral waves occurs (Fig. 2.3c).

It is important to realize that the vulnerability phenomenon can contribute to the onset of spiral activity during normal heart activity, because S1 waves are naturally present. Thus, a critically timed external S2 stimulus may cause cardiac arrhythmias. Note that due to MEF via Isac such a scenario is also possible when the S2 stimulus is due to a mechanical impact, which may be the mechanism for commotio cordis [34].

### 2.4.1 Mechanically Caused Vulnerability

Above we explained the classical vulnerability phenomenon using our model without considering deformations. To study how MEF due to Isac affects the vulnerable zone we performed S1S2 experiment in our full, deforming model. For most S2 stimulation positions and strengths we found similar results as for the undeformed case, the classical vulnerable zone is present, and only the parametric regime is slightly altered. However, we found a new type of vulnerability for longer S1S2 coupling intervals which is illustrated in Fig. 2.4. As in the previous example, where we illustrated classical vulnerability, we applied an S2 stimulus in the back of a previously initiated wave, which results in a wave response. However, in this case unidirectional block takes place not in forward but in backward direction which results in

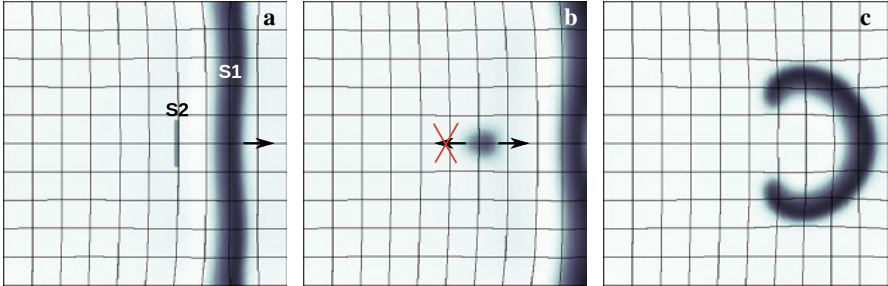


**Fig. 2.4.** Spiral wave formation due to mechanically caused vulnerability. (a) A S2 stimulus is applied in the mechanically caused vulnerable zone; (b) Unidirectional block due to mechanically caused vulnerability occurs opposite compared to classical vulnerability; (c) A pair of counter-rotating spiral waves emerges which rotates oppositely compared to the classical mechanism shown in Fig. 2.3. System size was 60 s.u. and  $G_s = 2.6$ . From [69]

the onset of a counter-rotating pair of spiral waves rotating oppositely compared to the classical vulnerability (compare Figs. 2.3 and 2.4).

To understand this new mechanism one must note that a depolarizing current has two effects on the excitability of a cardiomyocyte. First, it has an immediate effect of increasing the excitability by bringing it closer to a threshold of critical transmembrane potential which triggers an action potential. However, in addition it has a slow effect of decreasing its excitability by the so-called accommodation effect, which happens due to a closing of sodium ion channels. In our generic model accommodation is respected by the slow variable  $v$  (see Eq. (2.2)).

We illustrate the influence of deformation on the wave back in Fig. 2.5. We can see from this figure, that in absence of deformation transmembrane potential  $u$  monotonically decreases to zero (red line). However, in the presence of deformation, we see a transient increase of the transmembrane potential  $u$  (black line for  $33 \text{ s.u.} < \text{position} < 40 \text{ s.u.}$ ) which is a result of  $I_s$ . This makes the tissue more excitable. Around the local maximum of transmembrane potential  $u$  the medium is most excitable and less excitable around it. We illustrate the mechanically caused vulnerable zone in Figure 2.5 as the region within dotted lines. Right from the dotted region the excitability decreases due to the recovery tail of the S1 wave (classical vulnerability), whereas left from the dotted region it decreases because of an accumulation of variable  $v$  (mechanically caused vulnerability). Thus, a S2 wave response within the mechanically caused vulnerable zone may travel along with the S1 wave, and be blocked from propagation away from it forming a pair of rotating spiral waves (see Fig. 2.4).

It is interesting to note here that the accommodation effect has been studied in electrophysiology since 1936 [19, 20]. However, the connection of accommodation to deformation became clear only recently in a study of Panfilov et al. [49]. In this study it was shown that deformation can cause accommodation via Isac, and that it can result in a block of waves during spiral wave rotation.

We gave a short explanation of the emergence of the mechanically caused vulnerability. For a more detailed explanation see [69].

#### 2.4.1.1 Self-generation of Spiral Waves

Above we reported that deformation can cause a new vulnerable zone in which a counter-rotating pair of spiral waves can be initiated via the S1S2 protocol for longer S1S2 coupling intervals compared to the classical vulnerability. We found that this new mechanism of spiral wave formation occurs in this numerical experiment in a small region of S2 stimulation strengths. However, it may still be an important mechanisms as the new vulnerable zone is located at the position of highest excitability, and a wave may itself cause an S2 stimulus due to its mechanical activity [48]. Thus, a wave itself can induce spiral wave activity. Indeed, we found that this phenomenon of “self-generation” of spiral waves occurs in many situations. We illustrate this phenomenon in the following examples.

The first example is connected to a phenomenon that can occur in real tissue, is the diffraction of a travelling wave at an isthmus. This phenomenon has been studied extensively in cardiac electrophysiology [6]. We found that the induction of curvature by such a diffraction event can cause spiral wave self-generation in our model via the new mechanism. We illustrate this phenomenon in Fig. 2.6. A plain wave ① is initiated at a border of a thin slice of tissue (Fig. 2.6a). The wave ① is then diffracted at an isthmus (Fig. 2.6b). The curvature of wave ① causes high stretch in the location of the highest excitability which initiates an additional wave ② (Fig. 2.6c). The new wave ② is blocked due to the mechanically caused vulnerability

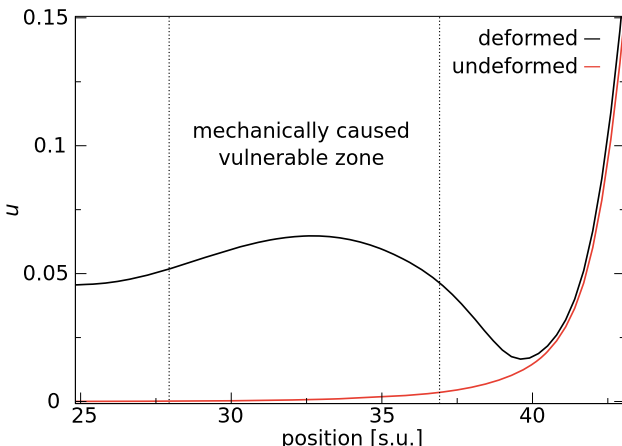


**Fig. 2.5.** Effect of deformation on the vulnerable zone. Transmembrane potential  $u$  is shown in the back of the S1 waves from systems shown in Figs. 2.4 and 2.3 immediately prior the S2 stimulus (along horizontal center). The mechanically caused vulnerable zone lies within dotted lines. Data is from systems shown in Figs. 2.3 and 2.4.

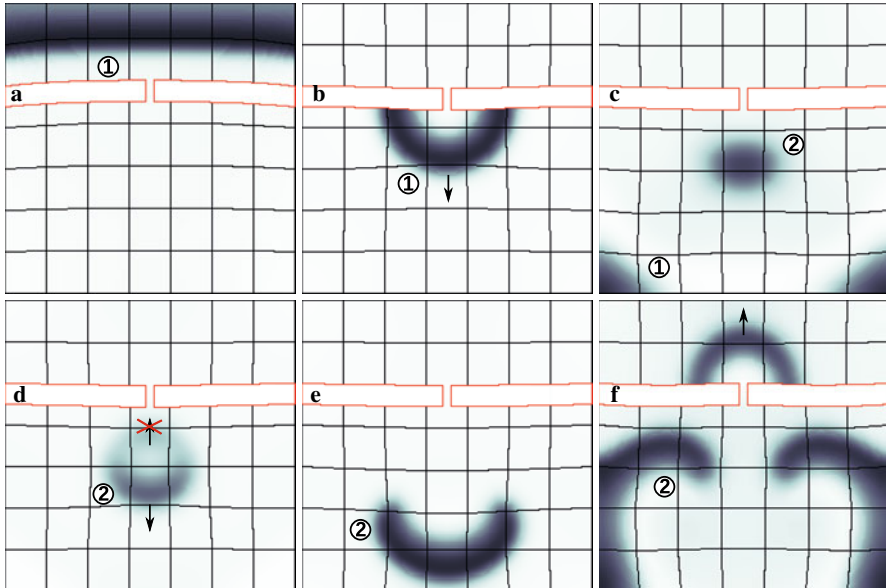


**Fig. 2.6.** Spiral wave formation following a wave diffraction at an isthmus. (a) A plain wave propagates towards an isthmus ( $t = 5.5 \text{ t.u.}$ ); (b) Plain wave is diffracted at the isthmus ( $t = 20.5 \text{ t.u.}$ ); (c) Diffracted wave produces stretch activated current that initiates a new wave ( $t = 37.5 \text{ t.u.}$ ); (d) Initiated wave is unidirectionally blocked in the mechanically induced vulnerable zone of wave ( $t = 41.5 \text{ t.u.}$ ); (e) New wave forms a counter-rotating spiral wave pair ( $50.5 \text{ t.u.}$ ); (f) Spiral wave pair after 1.5 rotations ( $75.5 \text{ t.u.}$ ). System size  $42.0 \text{ s.u.}$  and  $G_s = 2.0$ . Stiffness of the isthmus (contoured red) is twofold the stiffness in medium ( $2 \times c$ ). From [69]

opposite to the propagation of wave ① (Fig. 2.6d). A pair of counter-rotating spiral waves forms via the new mechanism (Fig. 2.6e,f).

Another more complex scenario for mechanical spiral wave initiation is presented in Fig. 2.7. In this example a wave ① propagates around a non-conducting obstacle (Fig. 2.7a). The obstacle curves the wave ① which causes high stretch in the tissue initiating a new wave ② (Fig. 2.7b) due to  $I_s$ . Note that for this first mechanically caused wave the mechanical stimulus is strong, so that no spiral is initiated but a connected wave (Fig. 2.7b). This new wave ② itself is curved and initiates another wave ③ (Fig. 2.7c,d). However, this new wave is caused by a weaker mechanical stimulus close above threshold, so that ③ is unidirectionally blocked by the mechanically caused vulnerability of wave ② (Fig. 2.7e). In result a rotating spiral wave is initiated (Fig. 2.7f).

In all the examples shown above the formation of new spiral waves is caused by mechanically induced “close-above-threshold” in the location of maximal excitability, thus in the areas prone to the new mechanism of spiral wave formation.

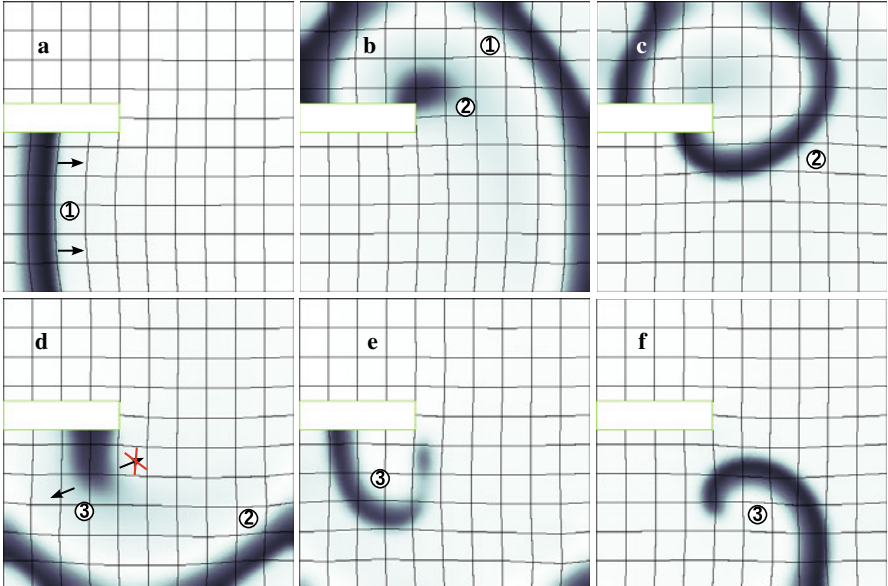


**Fig. 2.7.** Spiral wave formation following a wave deflection. (a) A plain wave propagates around a non-conducting static block ( $t = 8.0$  t.u.); (b) A new wave is initiated due to  $I_s$  ( $t = 41.8$  t.u.); (c) New Wave propagates around non-conducting static block ( $t = 53.8$  t.u.); (d) A third sequent wave is caused which is unidirectionally blocked by the mechanically caused vulnerable zone of previous wave ( $t = 71.8$  t.u.); (e) A rotating spiral wave forms ( $t = 78.0$  t.u.); (f) Rotating spiral wave after one rotation ( $t = 100.0$  t.u.). System size is 60 s.u. and  $G_s = 2.0$ . The static block is contoured green. From [69]

#### 2.4.2 Mechanical Heterogeneity

In the beginning of this section we stated that electrical heterogeneity is known to be an important determinant for the initiation of spiral waves. However, many forms of cardiac disease cause also mechanical heterogeneity. Despite this fact, basic mechanisms of how mechanical inhomogeneity can cause spiral wave activity have not systematically been studied yet. Therefore, we used our model to study basic mechanisms of spiral wave formation due to mechanical heterogeneity. For this study we considered a thin piece of cardiac tissue where a local mechanical inhomogeneity is present. This local inhomogeneity possesses different active and passive mechanical properties compared to the rest of the tissue. In this system we initiated a wave at one border. We found that self-sustaining spiral wave patterning emerges for a wide space of mechanical parameters of the inhomogeneity, and found five basic mechanisms involved. Here, we will briefly explain the mechanisms. For a detailed presentation of this research see [70].

In Fig. 2.8 we illustrate mechanisms of spiral formation due to mechanical heterogeneity in our model. In Fig. 2.8 I we see that the initial wave ① causes a wave ②

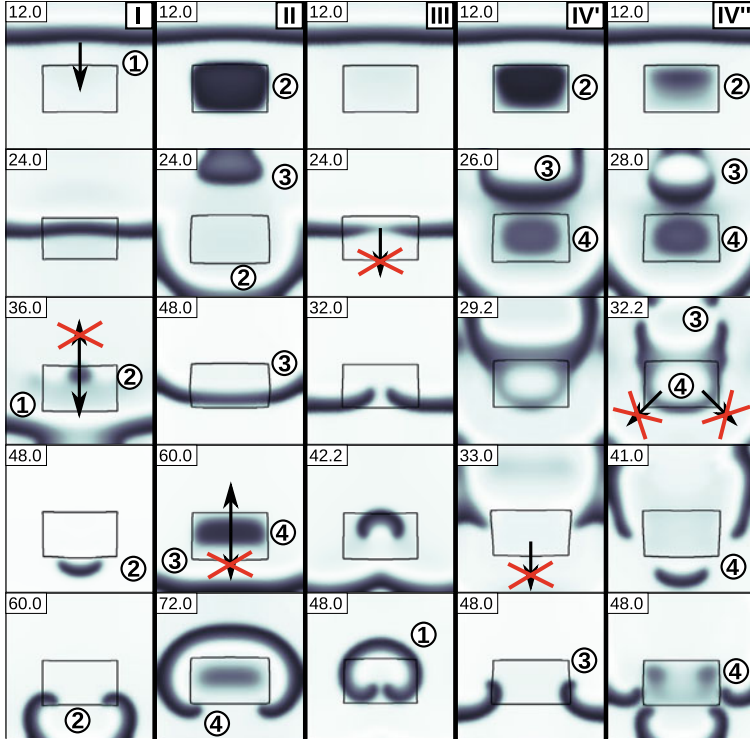


**Fig. 2.8.** Spiral wave formation caused by a mechanical inhomogeneity. The mechanical parameters ( $p, c$ ) in the inhomogeneity are I: (1.00, 0.51), II: (0.00, 0.75), III: (0.50, 1.20), IV': (0.25, 0.68), and IV'': (0.25, 0.92). System size was 60 s.u., and  $G_s = 2.5$ . Waves are labeled by order of appearance. From [70]

in the inhomogeneity at time 36 t.u.. This occurs because the stiffness of the tissue is reduced in the inhomogeneity which causes high stretch and  $I_s$ , and the tissue is most excitable there due to the effect of mechanically caused vulnerability. The new wave ② is then unidirectionally blocked by the mechanically caused vulnerable zone. This results in a pair of counter-rotating spiral waves (Fig. 2.8 I, 48 t.u., 60 t.u.). Note the similarity of this mechanism to the mechanism shown in the previous section, where spiral waves also form due to an S2 stimulus in the mechanically caused vulnerable zone. However, here this S2 stimulus occurs because of the mechanical inhomogeneity.

In Fig. 2.8 II we illustrate a mechanism where the mechanical inhomogeneity can cause an S2 stimulus in the classical vulnerable zone of a wave ③. However, we found this mechanism to appear in a very small parametric regime compared to the other mechanisms. Note that here the S2 stimulus which causes spiral activity did not occur to the initial wave, but to a sequent wave, after the initial wave ① waves ② and ③ are formed, but they do not cause spirals.

In Fig. 2.8 III we illustrate another mechanism of spiral wave formation due to mechanical heterogeneity. The increased stretch in the inhomogeneity causes accommodation of the tissue, it becomes temporarily inexcitable, and thus causes a break of the traveling wave front at time 24 t.u.. After some while, the tissue in the inhomogeneity becomes excitable again, and the two waves that resulted from the wave break can propagate into the tissue causing a counter-rotating pair of spiral waves (Fig. 2.8 III, 32 t.u., 42 t.u., 48 t.u.). Note that this mechanism was first shown in [49] where break occurs to a spiral wave, and also in whole heart whole heart models in [26, 28].

In Fig. 2.8 IV' we illustrate a similar mechanism, where wave break also occurs in the inhomogeneity. However, here it emerges because of an incomplete excitation in the inhomogeneity. At time 26 t.u. we see a pulse forming in the inhomogeneity; yet, it can not propagate further. A wave ③ breaks at this region which is temporarily inexcitable (29.2 t.u., 33.0 t.u.). It results in a pair of counter-rotating spiral waves (48.0 t.u.).

Note the similarity of the mechanisms III and IV' compared to the mechanism we illustrated in Fig. 2.2. In both mechanisms spiral waves form after a traveling wave breaks. However, in Fig. 2.8 wave break occurred because of an inhomogeneity in refractory period, whereas here it is because of a mechanical inhomogeneity.

In Fig. 2.8 IV'' we illustrate another mechanism that is caused by an incomplete excitation in the inhomogeneity. Here, a wave ④ forms in the inhomogeneity (28 t.u.), and it can exit the inhomogeneity partially (41 t.u.), which causes pairs of spiral waves (48 t.u.).

## 2.5 Discussion

The aim of this text was to demonstrate the value of discrete mechanical modeling to study MEF in cardiac tissue. After a small section where we discussed the discrete mechanical modeling approach for cardiac tissue, we explained the setup of our lattice-based discrete mechanical model to study MEF in cardiac tissue, and showed novel mechanisms of spiral wave formation that emerge in the model as a consequence of MEF.

The discrete mechanical modeling of cardiac tissue is an attractive approach. It may be possible to study the effect of structural changes in cardiac tissue on the heart's mechanical properties, and further how these effects may cause cardiac arrhythmia. We believe such relationships are likely to be found as our studies showed that mechanical inhomogeneities may well underly basic mechanisms for spiral wave formation.

It may also be possible to use discrete mechanical modeling of cardiac tissue as a modeling setup to include patient specific data. Biopsies in different regions of the heart of a patient may provide properties of discrete elements and the tissue structures. First steps on incorporating measured cell mechanical properties into a discrete mechanical model have been done in [38]. Moreover, the computational efficiency of discrete mechanical models may allow such patient-specific modeling

studies on “clinical timescales”, which means that a model is providing modeling results within “time critical needs of clinical scenarios” [43].

In this review we explained a discrete mechanical model for cardiac tissue in which we coupled a discrete mechanical model to a reaction-diffusion model for continuous electrical pulse propagation. Most frequently used models for cardiac tissue make the assumption of continuity in wave propagation, when the tissue is described as a regular arrangement of excitable units connected by resistances [10]. This assumption of continuous propagation is often legitimated by a close match between experimental and theoretical results on important macroscopic properties [29]. However, cardiac tissue has a granular structure built up of myocytes, extracellular tissue and other cell types, and therefore electrical pulse propagation in cardiac tissue interacts with structural boundaries. In fact, discontinuous electrical pulse propagation has been shown to be able to substantially affect mechanisms of arrhythmias [29]. It would be interesting to add discrete description of electrical activity to our electromechanical model. Such a full discrete model of cardiac tissue can be a valuable tool for studying discrete effects on arrhythmia initiation, for example in fibrotic cardiac tissue.

One of the important feedback mechanisms in the heart is the Frank-Starling relationship, which is the ability of cardiac tissue to produce greater contraction force in response to stretch [15]. The underlying mechanisms of the Frank Starling effect are not completely understood yet; however, it has been shown to be caused by proteins of the sarcomere affecting the process of cross-bridge cycling [15]. A discrete mechanical model for cardiac tissue offers the possibility to directly describe the sarcomere. It would be interesting to develop a discrete mechanical model of cardiac tissue to study the mechanisms of the Frank-Starling relationship, and how they affect mechanisms of onset of cardiac arrhythmias. In our current model [71], the Frank-Starling relationship is qualitatively embedded into the equations for active cardiac contraction (the Niederer-Hunter-Smith model [42, 44]).

In our model we assume deformations to occur at mechanical equilibrium, ignoring dissipative energy loss. Although this approach can be used as an approximation, and is commonly applied in modeling studies on MEF from generic two-dimensional models to sophisticated whole heart models [28, 40, 71] it is not formally thermodynamically correct. In a more realistic model, contraction development should be set as an irreversible thermodynamic process. Examples for thermodynamically consistent models of muscular tissues have been proposed in [56, 60]. In these papers the authors formulate the first and second law of thermodynamics in terms of continuum mechanics, and deduce an evolution equation for the mechanical activity of cardiac and smooth muscle tissue. It would be interesting to formulate a thermodynamically consistent discrete mechanical model for cardiac tissue, and to compare its predictions with currently used methodology.

The computation time of the model scales linearly against the number of mechanical nodes in the medium [68]. This allows to increase the model’s spatial resolution with minimal computational cost. High spatial resolution of the model may be important to study the effect of MEF on cardiac arrhythmias, where the excitation patterns

are more complex compared to the normal excitation of the heart which can cause steeper deformation gradients.

The modeling results reviewed in this text were achieved in a generic formulation for cardiac tissue [68]. The most important insight is that MEF may cause new mechanisms of spiral wave formation. Moreover, the results highlight the importance of mechanical heterogeneity in cardiac tissue. It can cause wave breaks via accommodation or incomplete excitation, and induce spirals via classical and mechanically caused vulnerability. Thus, even though our model is generic, our results still may lead to a better understanding of the underlying causes for the onset of cardiac arrhythmia.

The novel mechanisms for spiral wave formation that we identified emerge as a consequence of MEF via Isac, they are either connected to a new type of mechanically caused vulnerability, or to wave break caused by a mechanical inhomogeneity. However, other classical concepts important for spiral wave formation have not been studied yet. A well known phenomenon that can cause wavebreak and thus spirals is the alternans phenomenon, a heterogeneity in cardiac tissue can occur because of dynamical instabilities [72]. It must be studied how the occurrence of alternans is affected by MEF. Moreover, also the curvature of a wave is known to be an important determinant for spiral wave formation [51, 54]. We are currently using our discrete mechanical approach [68, 71] to address these open questions.

The results of our studies were performed in low-dimensional models for cardiac excitation and contraction coupling. As a next step, these mechanisms need to be studied in more biophysical model formulations. We extended our model by coupling our discrete mechanical approach to biophysical models of cardiac excitation and contraction coupling [71]. It must be tested if the previously found mechanisms hold also in this more accurate model.

Most importantly, our results need to be studied in experiments. It might be possible to test some of our predictions in experimental systems similar to our two-dimensional setup, for example in slices of cardiac tissue [3] or cell cultures [11, 75].

**Acknowledgements** We acknowledge and appreciate funding made available by the German Research Foundation (DFG; research fellowship to LD Weise, Grant No. WE 5519/1-1). We thank Prof. Annie Raoult for a helpful discussion.

## References

1. Aliev, R., Panfilov, A.: A simple two-variable model of cardiac excitation. *Chaos, Solitons and Fractals* **7**, 293–301 (1996)
2. Bers, D.: *Excitation-Contraction Coupling and Cardiac Excitation Force*. 3rd Edition. Kluwer Academic Publishers, Dordrecht, The Netherlands (2001)
3. de Boer, T.P., Camelliti, P., Ravens, U., Kohl, P.: Myocardial tissue slices: organotypic pseudo-2D models for cardiac research & development. *Future Cardiology* **5**(5), 425–430 (2009)

4. Bourguignon, D., Cani, M.P.: Controlling anisotropy in mass-spring systems. In: Eurographics Workshop on Computer Animation and Simulation (EGCAS), Springer Computer Science, pp. 113–123. Springer-Verlag (2000). Proceedings of the 11th Eurographics Workshop, Interlaken, Switzerland, August 21–22, 2000
5. Brady, A.J.: Mechanical properties of isolated cardiac myocytes. *Physiological reviews* **71**(2), 413–428 (1991)
6. Cabo, C., Pertsov, A.M., Baxter, W.T., Davidenko, J.M., Gray, R.A., Jalife, J.: Wave-front curvature as a cause of slow conduction and block in isolated cardiac muscle. *Circ. Res.* **75**, 1014–1028 (1994)
7. Caillerie, D., Milišić, V., Mourad, A., Raoult, A.: Modelling and simulation of fibrous biological tissues via discrete homogenization methods. *PAMM* **7**(1), 1121,601–1121,602 (2007)
8. Caillerie, D., Mourad, A., Raoult, A.: Cell-to-muscle homogenization. application to a constitutive law for the myocardium. *Math. Model. Numer. Anal.* **37**, 681–698 (2003)
9. Chen, P., Wolf, P., Dixon, E., Daniele, N., Frazier, D., Smith, W., Ideker, R.: Mechanism of ventricular vulnerability to single premature stimuli in open-chest dogs. *Circ. Res.* **62**, 1191–1209 (1988)
10. Clayton, R.H., Panfilov, A.V.: A guide to modelling cardiac electrical activity in anatomically detailed ventricles. *Progress in Biophysics and Molecular Biology* **96**(1£3), 19–43 (2008)
11. De Diego, C., Pai, R.K., Chen, F., Xie, L., De Leeuw, J., Weiss, J.N., Valderrábano, M.: Electrophysiological consequences of acute regional Ischemia/Reperfusion in neonatal rat ventricular myocyte monolayers. *Circulation* **118**(23), 2330–2337 (2008)
12. Delingette, H.: Towards realistic soft-tissue modelling in medical simulation. *Proceedings of the IEEE* **86**(3), 512–523 (1998)
13. Fomovsky, G.M., Thomopoulos, S., Holmes, J.W.: Contribution of extracellular matrix to the mechanical properties of the heart. *Journal of Molecular and Cellular Cardiology* **48**(3), 490–496 (2010)
14. Fritz, T., Jarrousse, O., Dössel, O.: Adapting a mass-spring system to energy density function describing myocardial mechanics. In: J. Vander Sloten, P. Verdonck, M. Nyssen, H. J. (eds.) 4th European Conference of the International Federation for Medical and Biological Engineering, pp. 2003–2006. Springer, Berlin, Heidelberg (2009)
15. Fukuda, N., Terui, T., Ohtsuki, I., Ishiwata, S., Kurihara, S.: Titin and troponin: Central players in the frank-starling mechanism of the heart. *Current Cardiology Reviews* **5**(2), 119–124 (2009)
16. Guccione, J., McCulloch, A., Waldman, L.: Passive material properties of intact ventricular myocardium determined from a cylindrical model. *J. Biomech. Eng.* **113**(1), 42–55 (1991)
17. Guccione, J.M., Costa, K.D., McCulloch, A.D.: Finite element stress analysis of left ventricular mechanics in the beating dog heart. *Journal of Biomechanics* **28**(10), 1167–1177 (1995)
18. Gul'ko, F., Petrov, A.: Mechanism of the formation of closed pathways of conduction in excitable media. *Biofizika* **17**, 261–270 (1972)
19. Hill, A.: Excitation and accommodation in nerve. *Proc. R. Soc. Lond.* **119**, 305–355 (1936)
20. Hodgkin, A., Huxley, A.: A quantitative description of membrane current and its application to conduction and excitation in nerve. *J. Physiol.* **117**, 500–544 (1952)
21. Hu, H., Sachs, F.: Stretch-activated ion channels in the heart. *Journal of Molecular and Cellular Cardiology* **29**(6), 1511–1523 (1997)

22. Hu, H., Sachs, F.: Stretch-activated ion channels in the heart. *J Mol Cell Cardiol.* **29**, 1511–1523 (1997)
23. Hunter, P., Nash, M., Sands, G.: Computational Electromechanics of the Heart. In: A. Panfilov, A. Holden (eds.) *Computational Biology of the Heart*, pp. 345–407. Wiley, Chichester, United Kingdom (1997)
24. Hunter, P., Smaill, B.: The analysis of cardiac function: A continuum approach. *Progress in Biophysics and Molecular Biology* **52**(2), 101–164 (1988)
25. Hunter, P.J., Nielsen, P.M., Smaill, B.H., LeGrice, I.J., Hunter, I.W.: An anatomical heart model with applications to myocardial activation and ventricular mechanics. *Critical reviews in biomedical engineering* **20**(5-6), 403–426 (1992)
26. Jie, X., Gurev, V., Trayanova, N.: Mechanisms of mechanically induced spontaneous arrhythmias in acute regional ischemia. *Circ Res* **106**(1), 185–192 (2010)
27. Keener, J., Sneyd, J.: *Mathematical physiology*. Springer-Verlag, New York, Heidelberg, Berlin (1998)
28. Keldermann, R.H., Nash, M.P., Gelderblom, H., Wang, V.Y., Panfilov, A.V.: Electromechanical wavebreak in a model of the human left ventricle. *Am J Physiol Heart Circ Physiol* **299**(1), H134–143 (2010)
29. Kleber, A.G., Rudy, Y.: Basic mechanisms of cardiac impulse propagation and associated arrhythmias. *Physiol Rev.* **84**, 431–488 (2004)
30. Kohl, P., Hunter, P., Noble, D.: Stretch-induced changes in heart rate and rhythm: Clinical observations, experiments and mathematical models. *Prog. Biophys. Molec. Biol.* **71**, 91–138 (1999)
31. Krinsky, V.: Spread of excitation in an inhomogeneous medium (state similar to cardiac fibrillation). *Biofizika* **11**, 776–784 (1966)
32. Krivtsov, A.: Constitutive equations of the nonlinear crystal lattice. *Z. angew. Math. Mech.* **79**(S2), 419–420 (1999)
33. LeGrice, I., Hunter, P., Smaill, B.: Laminar structure of the heart. II. Mathematical model. *Am. J. Physiol.* **269**, H571–H582 (1995)
34. Li, W., Kohl, P., Trayanova, N.: Induction of ventricular arrhythmias following mechanical impact: a simulation study in 3D. *J. Mol. Histol.* **35**, 679–686 (2004)
35. Mohr, M., Blümcke, L., Sachse, F., Seemann, G., Dössel, O.: Hybrid deformation model of myocardium. In: A. Murray (ed.) *Computers in Cardiology*, 2003, pp. 319–322. IEEE, NY, USA (2003)
36. Mohr, M., Blümcke, L., Seemann, G., Sachse, F., Dössel, O.: Volume modeling of myocard defomation with a spring mass system. In: N. Ayache, H. Delingette (eds.) *Surgery Simulation and Soft Tissue Modeling*, pp. 332–339. Springer, Berlin, Heidelberg (2003)
37. Mohr, M., Seemann, G., Sachse, F., Dössel, O.: Modeling of myocardial deformation with an extended spring mass system. *Biomedical Engineering* **48**(1), 6–7 (2003)
38. Mourad, A.: Description topologique de l'architecture fibreuse et modélisation mécanique du myocarde. PhD thesis, Institut national polytechnique de Grenoble (2003)
39. Nash, M., Hunter, P.: Computational mechanics of the heart: from tissue structure to ventricular function. *J. Elasticity* **61**, 113–141 (2000)
40. Nash, M., Panfilov, A.: Electromechanical model of excitable tissue to study reentrant cardiac arrhythmias. *Prog. Biophys. Mol. Biol.* **85**, 501–522 (2004)
41. Nealen, A., Müller, M., Keiser, R., Boxermann, E.M.C.: Physically based deformable models in computer graphics. *Computer Graphics Forum* **25**, 809–836 (2006)
42. Niederer, S., Hunter, P., Smith, N.: A quantitative analysis of cardiac myocyte relaxation: a simulation study. *Biophys. J.* **90**(5), 1697–1722 (2006)

43. Niederer, S., Mitchell, L., Smith, N., Plank, G.: Simulating human cardiac electrophysiology on clinical time-scales. *Frontiers in Physiology* **2** (2011)
44. Niederer, S., Smith, N.: An improved numerical method for strong coupling of excitation and contraction models in the heart. *Prog. Biophys. Mol. Biol.* **96**(1-3), 90–111 (2008)
45. Noble, D.: A modification of the Hodgkin–Huxley equation applicable to Purkinje fiber action and pacemaker potential. *J. Physiol.* **160**, 317–352 (1962)
46. Ostermeyer, G., Popov, V.: Many-particle non equilibrium interaction potentials in the mesoparticle method. *Phys Mesomechanics* **2**(6), 31–36 (1999)
47. Panfilov, A.: Spiral breakup as a model of ventricular fibrillation. *Chaos* **8**, 57–64 (1998)
48. Panfilov, A., Keldermann, R., Nash, M.: Self-organized pacemakers in a coupled reaction-diffusion-mechanics system. *Phys. Rev. Lett.* **95**(25), 258,104 (2005)
49. Panfilov, A., Keldermann, R., Nash, M.: Drift and breakup of spiral waves in reaction-diffusion-mechanics systems. *Proc. Natl. Acad. Sci. U.S.A.* **104**(19), 7922–7926 (2007)
50. Panfilov, A., Pertsov, A.: Spiral waves in active media. reverberator in the fitzhugh-nagumo model. In: *Autowave Processes in systems with diffusion*, pp. 77–84. Acad. Sci. USSR, Gorky (1981)
51. Panfilov, A., Pertsov, A.: Mechanism of spiral waves initiation in active media connected with critical curvature phenomenon. *Biofizika* **27**, 886–888 (1982)
52. Panfilov, A.V.: Theory of reentry. In: D.P. Zipes, J. Jalife (eds.) *Cardiac electrophysiology. From cell to bedside*, 5th edition, pp. 329–337. Elsevier, New York (2009)
53. Pathmanathan, P., Cooper, J., Fletcher, A., Mirams, G., Murray, P., Osborne, J., Pitt-Francis, J., Walter, A., Chapman, S.J.: A computational study of discrete mechanical tissue models. *Physical biology* **6**(3), 036,001 (2009)
54. Pertsov, A.M., Panfilov, A.V., Medvedeva, F.U.: Instabilities of autowaves in excitable media associated with critical curvature phenomena. *Biofizika* **28**(1), 100–102 (1983)
55. Popov, V., S.G., P.: Theoretical principles of modelling elastoplastic media by moveable cellular automata method. i: Homogenous media. *Phys Mesomechanics* **4**, 15–25 (2001)
56. Rossi, S., Lassila, T., Ruiz-Baier, R., Sequeira, A., Quarteroni, A.: Thermodynamically consistent orthotropic activation model capturing ventricular systolic wall thickening in cardiac electromechanics. *European Journal of Mechanics - A/Solids* (2013)
57. Schargott, M., Popov, V., Heß, M.: Macroscopic isotropy of two- and three-dimensional elastic lattice models. *Tribology International* **40**(6), 937–941 (2007)
58. Seth, B.: Finite strain in elastic problems. *Phil. Trans. R. Soc. Lond. A* **234**, 231–264 (1935)
59. Starmer, C.F., Biktashev, V.N., Romashko, D.N., Stepanov, M.R., Makarova, O.N., Krinsky, V.I.: Vulnerability in an excitable medium: Analytical and numerical studies. *Bioophys. J.* **65**, 1775–1787 (1993)
60. Stålhandske, J., Klarbring, A., Holzapfel, G.A.: A mechanochemical 3D continuum model for smooth muscle contraction under finite strains. *Journal of theoretical biology* **268**(1), 120–130 (2011)
61. Ten Tusscher, K., Noble, D., Noble, P., Panfilov, A.: A model for human ventricular tissue. *Am. J. Physiol. Heart Circ. Physiol.* **286**, H1573–H1589 (2004)
62. Ten Tusscher, K., Panfilov, A.: Alternans and spiral breakup in a human ventricular tissue model. *Am. J. Physiol. Heart Circ. Physiol.* **291**, H1088–100 (2006)
63. Trayanova, N., Li, W., Eason, J., Kohl, P.: Effect of stretch activated channels on defibrillation efficacy. *Heart Rhythm* **1**, 67–77 (2004)
64. Trayanova, N.A., Rice, J.J.: Cardiac electromechanical models: from cell to organ. *Frontiers in physiology* **2**, 43 (2011). PMID: 21886622

65. Verlet, L.: Computer “experiments” on classical fluids. i. thermodynamical properties of lennard-jones molecules. *Phys. Rev.* **159**(1), 98 (1967)
66. Vetter, F., McCulloch, A.: Mechanoelectric feedback in a model of the passively inflated left ventricle. *Ann Biomed Eng.* **29**, 414–426 (2001)
67. Weber, K.T.: Cardiac interstitium in health and disease: The fibrillar collagen network. *Journal of the American College of Cardiology* **13**(7), 1637–1652 (1989)
68. Weise, L.D., Nash, M.P., Panfilov, A.V.: A discrete model to study reaction-diffusion-mechanics systems. *PLoS ONE* **6**(7), e21,934 (2011)
69. Weise, L.D., Panfilov, A.V.: New mechanism of spiral wave initiation in a reaction-diffusion-mechanics system. *PLoS ONE* **6**(11), e27,264 (2011)
70. Weise, L.D., Panfilov, A.V.: Emergence of spiral wave activity in a mechanically heterogeneous reaction-diffusion-mechanics system. *Phys. Rev. Lett.* **108**, 228,104 (2012)
71. Weise, L.D., Panfilov, A.V.: A discrete electromechanical model for human cardiac tissue: Effects of stretch-activated currents and stretch conditions on restitution properties and spiral wave dynamics. *PLoS ONE* **8**(3), e59,317 (2013)
72. Weiss, J., Karma, A., Shiferaw, Y., Chen, P., Garfinkel, A., Qu, Z.: From pulsus to pulseless: the saga of cardiac alternans. *Circ. Res.* **98**, 1244–1253 (2006)
73. Wiener, N., Rosenblueth, A.: The mathematical formulation of the problem of conduction of impulses in a network of connected excitable elements, specifically in cardiac muscle. *Arch. Inst. Cardiol. Mex.* **16**, 205–265 (1946)
74. Winfree, A.T.: Electrical instability in cardiac muscle: Phase singularities and rotors. *J.Theor. Biol.* **138**, 353–405 (1989)
75. Zhang, Y., Sekar, R.B., McCulloch, A.D., Tung, L.: Cell cultures as models of cardiac mechanoelectric feedback. *Progress in Biophysics and Molecular Biology* **97**, 367–382 (2008)
76. Zhang, Y., Youm, J., Sung, H., Lee, S., Ryu, S., Ho, W., Earm, Y.: Stretch-activated and background non-selective cation channels in rat atrial myocytes. *J. Physiol.* **523**, 607–619 (2000)
77. Zile, M.R., Richardson, K., Cowles, M.K., Buckley, J.M., Koide, M., Cowles, B.A., Gharpuray, V., Cooper, G.: Constitutive properties of adult mammalian cardiac muscle cells. *Circulation* **98**(6), 567–579 (1998)
78. Zykow, V.: Simulation of Wave Processes in Excitable Media. Manchester University Press, Manchester, United Kingdom (1987)

---

## Multiscale Modelling of Cardiac Perfusion

**Jack Lee, Andrew Cookson, Radomir Chabiniok, Simone Rivolo, Eoin Hyde, Matthew Sinclair, Christian Michler, Taha Sochi and Nicolas Smith**

**Abstract** To elucidate the mechanisms governing coronary blood flow in health and disease requires an understanding of the structure–function relationship of the coronary system, which exhibits distinct characteristics over multiple scales. Given the complexities arising from the multiscale and distributed nature of the coronary system and myocardial mechanical coupling, computational modelling provides an indispensable tool for advancing our understanding. In this work, we describe our strategy for an integrative whole-organ perfusion model, and illustrate a series of examples which apply the framework within both basic science and clinical translation settings. In particular, the one-dimensional reduced approach common in vascular modelling is combined with a new poromechanical formulation of the myocardium that is capable of reproducing the full contractile cycle, to enable simulation of the dynamic coronary and myocardial blood flow. In addition, a methodology for estimating continuum porous medium parameters from discrete network geometry is presented. The benefit of this framework is first demonstrated via an application to coronary wave intensity analysis, a technique developed to study time-dependent aspects of pulse waves invasively measured in the vessels. It is shown that, given experimentally-acquired boundary conditions the 1D model is capable of reproducing a wave behaviour broadly consistent with that observed *in vivo*, however, its utility is limited to a phenomenological level. The integrated 1D-poromechanical model on the other hand enables a mechanistic investigation of wave generation thus allowing the influence of contractile function and distal hemodynamic states on coronary flow to be described. In addition, when coupled with the advection-

---

J. Lee · A. Cookson · R. Chabiniok · S. Rivolo · E. Hyde · M. Sinclair · C. Michler · T. Sochi  
Department of Biomedical Engineering, Division of Imaging Sciences and Biomedical Engineering, King's College London, King's Health Partners, St. Thomas' Hospital, London, SE1 7EH, United Kingdom  
e-mail: jack.lee@kcl.ac.uk

N. Smith (✉)  
Faculty of Engineering, The University of Auckland, Auckland, New Zealand  
e-mail: np.smith@auckland.ac.nz

diffusion-reaction equation, the integrated model can be used to study the transport of tracers through the vascular network, thus allowing the dependence of noninvasive imaging signal intensities on the diffusive properties of the contrast agent to be quantified. A systematic investigation of the commonly used clinical indices and whole-organ modelling results are illustrated. Taken together, the proposed model provides a comprehensive framework with which to apply quantitative analysis in whole organ coronary artery disease diagnosis using noninvasive perfusion imaging modalities. The added value of the model in clinical practice lies in its ability to combine comprehensive patient-specific information into therapy. In this regard, we close the chapter with a discussion on potential model-aided strategies of disease management.

### 3.1 Introduction

To elucidate the mechanisms governing coronary blood flow in health and disease requires an understanding of the relationship between the structure of the coronary vasculature and its function, which exhibits distinct characteristics over multiple scales. The coronary vessels feature diameters which span over three orders of magnitude from  $\mu\text{m}$  to mm scales, and are organised in a morphometrically asymmetric branching network of vessels. A common classification of vessels derives from both structural and functional considerations, attributing major conducting, resistance, exchange and capacitance functions to the epicardial arteries, arterioles, capillaries and veins respectively. The unique mechanical environment of continual contractile cycles within which the coronary system operates, leads to a substantial fluid-structure interaction within each vessel and results in the phasic and asynchronous flow patterns observed over the vascular hierarchy. Integrated over the whole network, these interactions indirectly couple coronary blood flow to many important factors governing cardiac function, including contractility, venous return and systemic afterload.

Given the complexities arising from the multiscale and distributed nature of the coronary system and myocardial mechanical coupling, computational modelling provides an indispensable tool for advancing our understanding of cardiac function. Specifically, this approach provides the potential for quantitative and integrative insights that are currently inaccessible to experimental modes of investigation. Such a framework can be used to gain mechanistic insights into the physiological determinants of flow, aid in the design and optimisation of medical technology, and be directly applied in the clinics for diagnosis and treatment planning. The coupled fluid-structure model of coronary flow outlined in this chapter aims to bring together the principal components of the system to establish an integrated framework for investigating, and later, predicting cardiac perfusion on an individual-specific basis. Whilst the characterisation of the autoregulatory mechanisms and remodelling remains a challenge outside the current scope, in the following sections we will provide a series of examples of how our model is being applied in the realm of basic science as well as clinical translation.

## 3.2 Background

### 3.2.1 Basic Anatomy and Perfusion Territories

The large epicardial conducting arteries of the coronary network – with three main stems being left anterior descending (LAD), left circumflex (LCx) and right coronary artery (RCA) – originate from the coronary ostia situated at the aortic sinus and give rise to many intramural vessels that are predominantly oriented in the transmural direction towards the subendocardium [91]. These vessels further branch into arterioles that provide significant resistance to flow. From the terminal arterioles stem capillaries, which are closely integrated with bundles of myocytes and serve as the principal site of gas and nutrient exchange. These vessels are then collected into venules and larger veins, which finally collect blood from the coronary circulation into the right atrium via the coronary sinus. The optimal design underlying the branching patterns of vascular segments have been the subject of morphometric measurement [55], theoretical [110] and data driven [54, 62] analyses.

Aside from this intrinsic compartmentalisation of the vascular hierarchies, the sub-networks of the coronary vasculature are spatially arranged into distinct territories occupying different regions of the myocardium [91]. Typically the LAD supplies the anterolateral myocardium and a part of the septum, the LCx, the lateral wall of the left ventricle, whereas the RCA supplies the right ventricle, a part of the septum and a part of the inferior wall. The exact extension of these perfusion regions is subject to inter-individual variations, for example the inferior and inferolateral wall of the left ventricle can be supplied by RCA (the so-called right dominant coronary circulation), or by LCx (left-dominant circulation) or by both RCA and LCx (co-dominant circulation). All these possibilities are considered as variants of anatomical norm [32] and need to be reflected in the patient-specific modelling. The flow supplies to different territories are separate at the distal level [29], unless collateral vessels exist between the regions at a lower hierarchy. In healthy humans no angiographically identifiable collaterals are found, but their development in the presence of disease has been reported [36]. The functional relevance of the human coronary collaterals is gauged via indirect methods [98] and has been under debate [40, 104]. However, the beneficial effects of the recruitable collaterals to long-term survival have been documented [65].

### 3.2.2 Distribution of Resistance and Volume

Under resting conditions and intact vasomotor tone, it is estimated that approximately two thirds of the vascular resistance resides in the microvessels [18]. In this situation the large epicardial vessels contribute very little to the overall resistance unless significant stenoses are present. However, substantial redistribution of resistance may occur during vasodilation induced by exercise, a compensation due to disease or after administering a pharmacological agent e.g. during clinical examination. These changes are predominantly caused by the vasodilation taking place in the microcirculation, made possible because at resting conditions microvessels are in a

state of spontaneous constriction. The degree of such constriction (or tone) in relation to the maximal dilation of the vessel walls determines the flow reserve which can be recruited in times of increased demand.

Although estimates vary, it is reported that the coronary volume is divided among the arterial (around 20% of coronary blood volume), capillaries (approximately 30% of coronary blood volume) and venous compartments (around 50% of blood volume), altogether occupying roughly 12–15% of the total myocardial volume [90]. An important observation is that within the timescale of a single cardiac cycle, this percentage can decrease by a factor of two [52] indicating a significant storage effect in the governance of coronary flow. This capacitance is, of course, a consequence of the compliance of individual vascular segments. Experimental estimates place most of this capacitance effect as residing within veins and venules, which exhibit the largest compartmental volume and compliance.

### ***3.2.3 Mechanical Coupling of Coronary Flow and Myocardium***

Around 80% of the anterograde arterial flow occurs in the coronary system during diastole. In contrast, the venous flow is greatest during systole and is reduced in diastole. Such phasic flow patterns are the consequence of the extravascular forces interacting with the hemodynamics of the coronary system [3, 38]. During systole, the large compressive stress developed within the myocardium is transmitted to the embedded vasculature, whereupon it acts in a manner akin to a pump, driving the movement of the fluid accumulated by the enhanced proximal flow during diastole. The direction of the flow depends on the pressure gradient within the local vascular hierarchy. That is, proximal vessels are largely under the influence of the rising perfusion pressure and thus experience a reduced, but still anterograde net flow. With lower pressures in the venous vessels on the other hand, the compressive forces act to augment the net flow during systole.

The historical development of coronary-myocardial coupling has been previously reviewed [105]. Earlier modelling concepts have regarded intramyocardial pressure (IMP) to directly reflect the left ventricular cavity pressure transmitted through the extracellular space. However, subsequent experiments have demonstrated that the flow-impeding influence of myocardial contraction is of similar magnitude even when the ventricle is empty and the heart is beating against zero afterload, thereby suggesting a much stronger role of the specific microstructural coupling between the coronary vasculature and myocyte architecture. The direct action of myofibre thickening on the adjacent vessels is thus revealed as a significant driving mechanism. Conclusive evidence has been difficult to obtain due to the experimental inaccessibility of the system, however, there is a general consensus that IMP exhibits a transmural gradient and that its magnitude can exceed that of left ventricular pressure. Accordingly, the fluid-structure coupling of the coronary flow depends strongly on the hierarchical position of the vessel under consideration and its location within the myocardium, as well as the specific manner and scale of its structural coupling with the surrounding constituents of the myocardial tissue.

### 3.2.4 Invasive Clinical Indices of Coronary Disease

Coronary disease may manifest over a spectrum of disorders spanning focal/diffuse stenoses in the large vessels to microvascular dysfunction. Although they are non-mutually exclusive conditions, historically clinical investigations were mainly focussed on the large vessel disease first, perhaps due to their accessibility.

In the 1980s when coronary angiography became widely adopted, diagnosis of coronary disease focused on the anatomical measures of stenosis. Nowadays, it is known that solely-angiographic indices are poor at characterising the consequential severity of a stenosis [31, 96]. For this reason, modern clinical assessments of coronary function chiefly aim to quantify the flow reserve i.e. the capacity of the coronary system to match the supply in times of increased demand. Invasive examinations involve catheter measurements of pressure and/or velocity waveforms in selected vessels under resting and induced hyperaemic conditions. The Coronary Flow Velocity Reserve (CFVR) is a derived index, defined as the ratio of maximal hyperaemic blood flow velocity to the resting flow velocity. Whereas in healthy individuals CFVR may reach a maximum value of around 4, in disease it can be reduced below a value of 2 [37]. Note however that it is difficult to define an unambiguous clinical threshold for CFVR, since the resting flow rate is maintained at a near-constant level across a wide range of coronary pressure (thus reflecting a wide range of vasodilatory states of the distal bed) by coronary autoregulation [12].

In order to isolate a clinical assessment to focus exclusively on the stenotic severity free from confounding distal physiologic parameters, the Relative CFVR metric has been proposed. For this index, the ratio of hyperaemic velocity during maximum vasodilation in a stenotic vessel to a normal vessel velocity is calculated. In practice, however, this measure would require *a priori* knowledge of the location of normal vessels, which may be difficult to obtain (an additional catheter inside a healthy artery poses additional risk and multi-vessel disease may exist). The Fractional Flow Reserve (FFR) [78] circumvents this problem by directly measuring the ratio of pressures distal and proximal to a stenosis in the same vessel during maximal hyperaemia. This provides a surrogate measure of the hyperaemic flow that is actually obtained in the presence of the stenosis versus maximum attainable flow, if the vessel were non-stenotic. FFR has the advantage of being intrinsically normalised between 0 and 1, but requires the realisation of minimal distal resistance using pharmacological means for an accurate and reproducible assessment.

In a subset of cases, CFVR and FFR will give contradictory diagnoses. These differences likely reflect the divergent extremes of the balance between large and small vessel diseases, and reinforce the point that a full understanding of coronary disease requires characterisation of both epicardial and myocardial resistance to flow [51].

### 3.2.5 Non-invasive Imaging Modalities

Clinically, non-invasive imaging modalities provide a low-risk and cost-effective means to stratify patient cohorts and rule out negative cases before proceeding to the more invasive and costly catheter laboratory. Broadly speaking, non-invasive

imaging may be applied in two different ways, angiographic imaging which visualises vessel lumen anatomy (using computed tomography (CT) or magnetic resonance (MR)), and perfusion imaging which focuses on characterising the delivery of blood to the myocardium. In addition, some modalities offer the means to assess localised plaque composition which is related to the risk of rupture leading to thrombosis [63, 67, 82].

While there is no clinical non-invasive angiographic imaging modality that outperforms the traditional X-ray angiography in terms of resolution, CT offers a number of advantages including the imaging of three dimensional morphology and coronary artery calcification. Modern CT scanners can offer up to  $330\text{ }\mu\text{m}$  spatial and 75 ms temporal resolution. Furthermore, large clinical studies have demonstrated that low ionisation (1–2 mSv) and contrast-free CT-derived calcium scores have a negative predictive value of 99% making it an ideal screening tool for intermediate-risk patients experiencing chest pain [74].

Patients with microvascular or multi-vessel disease, previous infarcts and other associated cardiac conditions may benefit from the diagnostic information provided by the assessment of perfusion, which is a measure of blood supplied to the cells of the organ. With these increased complexities, shifting the focus away from the large epicardial vessels to the whole myocardium can reveal a more complete picture. Perfusion imaging is often conducted with a stress-protocol, during which higher flow demand of myocardium is induced to reveal regions of unmatched supply (thus again revealing the flow reserve). Major modalities for perfusion imaging include Single Photon Emission Computed Tomography (SPECT), Positron Emission Tomography (PET) and perfusion MR Imaging. While nuclear medicine techniques have an advantage in robust absolute quantifications and have the potential to target specific metabolic consequences of tissue perfusion [8], one of the strong points of perfusion MRI lies in its significantly higher spatio-temporal resolution (1.2 mm in-plane/1 s imaging time for MRI vs 5 mm/1 min imaging time for PET). This resolution in turn provides the observation of localised perfusion defects which may otherwise be obscured. A further advantage of MRI is its ability to combine imaging of cardiac function, scar and other diagnostic targets into a single session, providing the potential to serve as a “one-stop shop” for cardiac diagnosis. And yet more, the zero ionising property makes MRI suitable for regular follow-up of patients.

### **3.2.6 Research Modalities**

Often in research applications, far greater image resolutions can be obtained when compared to clinical modalities since *ex vivo* techniques can be applied with extended imaging time. In terms of coronary anatomical imaging, vascular casting combined with high-resolution modalities has brought routine automation to what was once a labour-intensive task two decades ago. The imaging cryomicrotome, microCT and confocal microscopy all fall into this category, offering resolutions ranging from 1–25  $\mu\text{m}$  [92]. In terms of functional characterisation, it would appear that similar breakthroughs have yet to take place, and the microsphere injection technique [80] remains the gold standard for flow measurements in the myocardium.

### 3.3 Model Description

#### 3.3.1 Coronary Flow Modelling

As outlined in the previous sections, mathematical modelling of cardiac perfusion necessitates a multiscale framework. The anatomical and functional nature of cardiac perfusion means that no single modelling approach can accommodate all aspects of the integrated system. The series of models presented in this chapter aims to capture the dominant physical phenomena at each representative scale, guided by the need to simulate and predict clinically-relevant quantities. We emphasise, however, that our contribution is primarily directed at characterising the whole organ tissue perfusion and its surrogate measures observable in the clinics. This means that certain major aspects of coronary disease including fluid patterns in the presence of stenoses, and *in silico* FFR quantification, which require the determination of detailed localised flow dynamics will not be covered. Correspondingly, a framework to represent the 3D flow regime based on the Navier-Stokes equations is excluded. Nevertheless, there is a wealth of literature available on these topics, and the interested reader will find an entry point to the key contributions in [95] and references therein.

Wave propagation phenomena in the upper arterial vessels of the coronary network is an emerging clinical target which can be effectively addressed by a one-dimensional Navier Stokes flow model, at a fraction of the computational complexity of its 3D alternative. The key characteristics of the Stokes regime flow in the microvascular network can be captured by a porous media approach which bypasses the requirement for modelling individual vascular segments and allows for extended applications that informs protocols associated with non-invasive perfusion imaging. Such an approach also enables the natural extension of incorporating the effects of cardiac contraction via the poromechanical framework. A brief description of each of these models is provided in the following sections.

#### 3.3.2 1D Blood Flow Model

The physiological lengths of the coronary pulse waves are large compared to the vessels' diameters so that the wave propagation occurs mainly in the axial direction. The one-dimensional approximation is the preferred approach in network flow modelling since it can accurately reproduce the wave-propagation phenomena resulting from cardiac events, which cannot be accommodated by lumped parameter models. Furthermore, it affords numerical tractability in large multi-scale simulations where 3D Navier-Stokes becomes intractable [61]. The mathematical background behind the 1D blood flow formulation has been extensively described in literature both from a theoretical [43, 77] and computational [2, 33, 35, 85, 87] perspective. This framework has been widely applied for investigating wave propagation in the systemic arteries, as reviewed in [99], and has been validated both *in vitro* [64] and *in vivo* [83]. The application of the 1D blood flow framework to the coronary arteries is a relatively recent field [61, 89]. However, the suitability of this modelling approach has been

recently strengthened by *in vivo* validation in the left coronary circulation of animal subjects [69]. The following section provides an overview of the selected 1D blood flow modelling approach with brief comparisons to other options available in literature. We refer to more extensive reviews for further details [2, 35, 61, 99].

### 3.3.2.1 Modelling Framework

Each vessel of the coronary network is modelled as a one dimensional impermeable tube of length  $l$  with cross-sectional area  $A(x, t)$ , where  $A(x, t) = \int_S d\sigma$  is defined as the area of a generic cross section  $S$  along the axial coordinate  $x$ . The cross-sectional area is allowed to vary non-uniformly thus making  $A(x, t)$  both space- and time-dependent. The underlying assumption is that the local curvature is small enough so that the problem can be described in one spatial dimension [43, 77, 87, 89, 99]. Blood flow in the vessel is described as  $Q(x, t) = A(x, t)u(x, t)$ , where  $u(x, t) = \frac{1}{A(x, t)} \int_S \hat{u} d\sigma$  is the axial velocity averaged over the cross-sectional area. Radial velocity is assumed to be negligible compared to the axial component.

As reviewed previously [83, 99], circular cross-sectional areas and axisymmetry are assumed meaning that the axial velocity can be represented as a function of radius, space and time. Furthermore, the axial velocity is assumed to be the product of a radially-dependent profile function and a mean velocity component that is space- and time-dependent  $u(x, t)$ . Several different ways to model the velocity profile can be found in literature [99]. Our choice here is to model the velocity profile with a blunt shape based on experimental observations [89].

Blood is modelled as an incompressible Newtonian fluid such that density  $\rho$  and dynamic viscosity  $\mu$  can be considered constant at the scale considered here. In addition, flow is considered to be laminar due to the low Reynolds number throughout the coronary network in physiological conditions.

### 3.3.2.2 Governing Equations

The 1D blood flow equations can be derived from first principles [43, 77, 85, 99] or, alternatively, they can be obtained by averaging the 3D Navier-Stokes equations [89] over the cross-section of an axisymmetric circular cylinder. The equations have been widely described in literature [2, 35, 43, 77, 85, 89, 99]. They comprise statements of the conservation of mass and momentum which can be written as

$$\frac{\partial A}{\partial t} + \frac{\partial Q}{\partial x} = 0, \quad (3.1)$$

$$\frac{\partial Q}{\partial t} + \frac{\partial}{\partial x} \left( \alpha \frac{Q^2}{A} \right) + \frac{A}{\rho} \frac{\partial p}{\partial x} + \kappa \frac{Q}{A} = 0. \quad (3.2)$$

The unstressed area  $A_0$  can vary spatially to model a tapering geometry of a coronary vessel. The term

$$\alpha(x, t) = \frac{\int_S \hat{u}^2 d\sigma}{A u^2} \quad (3.3)$$

is a non-dimensional correction factor for momentum flux which accounts for the shape of velocity profile over the cross-sectional area. The variable  $\alpha$  is usually assumed to be constant since it leads to considerable mathematical simplifications [33, 89, 99]. In the results below we assume  $\alpha = 1.1$ , following [89], for all the results presented unless otherwise stated. The variable  $\kappa$  is obtained from the integration of the 3D incompressible Navier-Stokes equations and represents the viscous resistance of the flow per unit length of vessel [89].

To close the system of equations and solve for the three unknowns  $(A, Q, p)$ , a constitutive law, relating pressure to area, has to be introduced. Several different forms have been proposed in literature, mainly derived from a linear elastic shell model [61, 99]. A commonly-employed example of these types of constitutive relations, used in our modelling framework, is of the following form

$$p = p_{ext} + \frac{\beta(x)}{A_0} \left( \sqrt{A(x)} - \sqrt{A_0(x)} \right), \quad (3.4)$$

where  $p_{ext}$  is an extravascular pressure and  $\beta(x) = \frac{4\sqrt{\pi}E(x)h(x)}{3}$  is a parameter both dependent on the Young modulus  $E(x)$  and the vessel wall thickness  $h(x)$  [5]. This relation assumes a static equilibrium in the radial direction of a cylindrical tube.

In the general case,  $p$  is spatially dependent through its dependence on the underlying variables i.e.  $p = p(\beta(x), A(x), A_0(x))$  such that

$$\frac{\partial p}{\partial x} = \frac{\partial p}{\partial \beta} \frac{\partial \beta}{\partial x} + \frac{\partial p}{\partial A} \frac{\partial A}{\partial x} + \frac{\partial p}{\partial A_0} \frac{\partial A_0}{\partial x} \quad (3.5)$$

should be taken into account for the vessel tapering and the spatial variation in material properties. Note that, as demonstrated in [33], additional terms can be included in the constitutive law to model the impact of wall inertia, viscoelasticity and longitudinal vessel pre-stress. However, these additional terms are generally assumed to have secondary effects and are difficult to parameterise thus they are not considered in the current modelling approach.

The solution system can be written in quasi-linear form as

$$\frac{\partial \mathbf{U}}{\partial t} + \mathbf{H}(\mathbf{U}) \frac{\partial \mathbf{U}}{\partial x} = \mathbf{B}(\mathbf{U}), \quad (3.6)$$

where  $\mathbf{U} = \begin{bmatrix} A \\ Q \end{bmatrix}$ , and the Jacobian  $\mathbf{H}(\mathbf{U})$ ,

$$\mathbf{H}(\mathbf{U}) = \frac{\partial \mathbf{F}}{\partial \mathbf{U}} = \begin{pmatrix} 0 & 1 \\ -\alpha \frac{Q^2}{A^2} + c^2 & 2\alpha \frac{Q}{A} \end{pmatrix}, \quad (3.7)$$

and the right-hand term  $\mathbf{B}(\mathbf{U})$ ,

$$\mathbf{B}(\mathbf{U}) = \begin{bmatrix} 0 \\ -\kappa \frac{Q}{A} - \frac{A}{\rho} \left( \frac{\partial p}{\partial \beta} \frac{\partial \beta}{\partial x} + \frac{\partial p}{\partial A_0} \frac{\partial A_0}{\partial x} \right) \end{bmatrix}. \quad (3.8)$$

In (3.7),  $c(x) = \sqrt{\frac{\beta}{2\rho A_0}} A^{\frac{1}{4}}$  denotes the wave propagation velocity.

The analysis of this characteristic system has been performed in literature, to which we refer for further details [33, 85, 87]. However, it is important to highlight that, under the necessary condition that  $A > 0$ , the equation system (3.6) has two real and distinct eigenvalues

$$\lambda_{1,2}(\mathbf{U}) = \alpha u \pm \sqrt{c^2 + \alpha(\alpha - 1)u^2}. \quad (3.9)$$

With the physiological condition  $c \gg u$ , (3.6) results in a hyperbolic system. This means that from each point of the computational domain, two characteristic curves originate, one directed towards the inlet and one towards the outlet of the vessel. As a consequence, an inflow and an outflow boundary conditions have to be specified.

From a numerical implementation point of view several different approaches have been pursued in literature, including second order Taylor-Galerkin schemes [33] and discontinuous Galerkin formulations [85, 87]. Our current model [60] is based on the spectral/hp elements scheme reported in [87]. The temporal discretisation has been performed with a Crank-Nicolson scheme, which is implicit and second-order accurate.

The numerical problem requires the specification of a full set of boundary conditions for (3.1)–(3.2) at the inlet and outlet, even if the differential problem requires only one physical boundary condition per boundary [33, 87]. To address this, the current implementation projects the differential equations along the outgoing characteristic curves [34], fully retaining the differential equations' non-linearities. Other approaches in literature rely on characteristic extrapolation [33, 85].

### 3.3.2.3 Network Formulation

The single-vessel formulation outlined above can be extended to a network of vessels by imposing suitable coupling conditions at the junctions. The junctions can either include [33] or ignore the impact of the branching angles, and be represented as a single point or a separate tract containing the branch [94]. Our modelling choice here is to represent junctions as a single point and to exclude the impact of the branching angles and momentum loss through junctions, since they play a minor role in the physiological range of pressure and velocity [33].

The coupling conditions imposed are based on physical conservation laws [33, 35, 60, 85, 87]. Under the assumption that no fluid can be stored in the junctions, the mass conservation equation in an  $n$ -vessel junction states that

$$\sum_j Q_j = 0, \quad j = 1 \dots n, \quad (3.10)$$

where  $Q_j$  denotes the flow into the junction from the  $j^{th}$  vessel. Imposing the conservation of total pressure across the junction according to Bernoulli's law

$$p_j + \frac{1}{2}\rho u_j^2 = p_{j+1} + \frac{1}{2}\rho u_{j+1}^2, \quad j = 1..n-1 \quad (3.11)$$

combined with the mass equation provides  $n$  equations in  $2n$  variables ( $A_j, Q_j$ ),  $j = 1 \dots n$ . The remaining  $n$  equations are obtained by imposing the *compatibility equations* [34] which prescribe appropriate conditions on the characteristics.

### 3.3.2.4 Boundary Conditions

A key challenge in formulating the boundary conditions for the 1D system arises from the requirement that the complex physiological responses originating from outside the simulation domain must be adequately reproduced. A brief overview of the most commonly used types is provided here.

Due to the hyperbolic nature of the problem as highlighted in Sect. 3.3.2.2, both an inlet and an outlet boundary condition must be prescribed. For the inlet boundary condition two possible approaches include the straightforward prescription of a measured waveform (pressure or flow) or a lumped model of the heart [14, 57].

Outflow boundary conditions on the other hand have to reproduce the effects of the truncated vasculature distal to the terminal vessels of a model. The simplest distal boundary condition is to impose a given pressure or a pressure-dependent flow (resistive boundary condition) at vessel terminals, however this brings with it the undesirable effect of unphysiological numerical wave reflections in the computational domain [86, 107]. Reflections can be avoided altogether using a non-reflecting boundary condition where the backward-traveling wave is prescribed as zero [33], although this is also unphysiological as it assumes an outlet vessel of infinite length.

An improved physiological outflow boundary condition is provided by lumped parameter Windkessel models, which appropriately reproduces the input impedance measured in the epicardial arteries [57, 106, 107]. Windkessel models with different levels of complexity have been successfully used both in modelling the systemic arteries [2, 35, 99] as well as the coronary vasculature [57]. A Windkessel model composed of several resistance–compliance (R–C) components combined with a time-varying distal pressure has been coupled to a coronary epicardial network for validation purposes [69], showing good agreement with *in vivo* measurements.

On the other hand, the Windkessel model parameters for  $R$  and  $C$  of the truncated network are difficult to estimate from *in vivo* measurements due in part to the cardiac contraction. Furthermore the Windkessel model does not faithfully reproduce high-frequency flow features [106]. The poor performance of Windkessel models in the high frequency range has been addressed with impedance boundary conditions, calculated as the root impedance of structured networks distal to the modelled vascular segment [75, 103], yielding an improvement over the Windkessel approach. However, these types of boundary conditions give rise to additional derivation and implementation issue that are not always straightforward to apply, as highlighted in [61]. Significant work remains to be done to parameterise the Windkessel and impedance boundary conditions in the coronary circulation.

A further alternative approach to modelling outflow boundary condition is to use a tapering vessel, which reproduces a series of reflected waves similar to a distal

network [68]. Finally, in order to capture the spatial heterogeneity of flow in the distal circulation, the 1D blood flow model can be coupled to a 3D porous medium representing the distal circulation (see Sect. 3.3.3.3).

### 3.3.3 Regional Perfusion Modelling by Porous Media Flow

While appropriate for modelling flow within the systemic and major coronary arteries, the 1D flow model is unsuitable for whole-organ perfusion modelling for a number of reasons: (i) the level of discrete vascular detail acquired via clinical imaging modalities cannot resolve beyond the largest epicardial vessels; (ii) the large number of branching vessels represent a significant computational challenge even with a 1D formulation; and (iii) if the discrete network was not fully-formed (i.e. the entire network was described from arteries to veins, inclusive of the capillaries), then a large number of intramural terminal vessels would require the prescription of boundary conditions which are difficult, if not impossible, to determine.

In contrast, mathematical models of flow through porous media provide a promising alternative framework whereby the flow at the microvascular scale is approximated by a spatially-averaged flow on the macroscopic scale. In the context of perfusion modelling, it is generally assumed that the medium consists of two overlapping phases – the solid matrix and the fluid (pore space), each occupying a fraction of the volume at every point. In this work, we assume that the pore space is fully interconnected and saturated.

The most commonly applied porous media flow model is *Darcy's Law*, whereby the Darcy velocity,  $\vec{w}$ , is linearly proportional to the gradient of the fluid pressure,  $p$

$$\mathbf{w} + \mathbf{K} \cdot \nabla p = \mathbf{0} \quad \text{in } \Omega, \quad (3.12a)$$

$$\nabla \cdot \mathbf{w} = S_v \quad \text{in } \Omega, \quad (3.12b)$$

where  $\mathbf{K}$  is the permeability of the porous medium  $\Omega$ ,  $\rho$  denotes fluid density and  $S_v$  is a fluid volumetric source field. Darcy's Law has been used by previous perfusion models for biological tissues [17, 101]. Furthermore, the continuum approach has the additional advantage of matching the level of detail observable in clinical perfusion imaging which is inherently spatially-averaged, readily allowing comparison without ambiguity in postprocessing.

#### 3.3.3.1 Multi-compartment Static Darcy

In practice, when a vascular tree spanning a broad scale range is considered, the lumping of all pore spaces into a common compartment as represented by (3.12) becomes an inadequate assumption. These situations lead us to consider a multi-compartment extension of the model as outlined here.

From high resolution imaging studies of coronary anatomy, the close spatial proximity of vessels with widely-varying length and diameter scales is well-known [92] and would be expected to lead to a corresponding heterogeneity in pressure and flow.

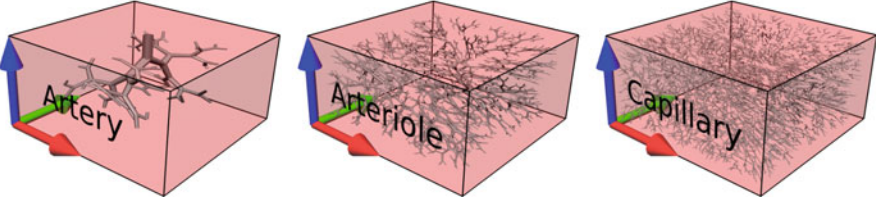


**Fig. 3.1.** Illustration of multiple spatially coexisting Darcy compartments. Each point of the physical domain  $\Omega$  will have a set of parameters and state variables for each compartment, with the particular parameters dependent on the vessels assigned to the compartment after vascular model partition. Note the decreasing scale of vessel in each compartment from *left* to *right*

Thus, to characterise the flow occurring within widely-disparate vessel scales, the approach taken below in our work is to employ *multiple* porous compartments, with each compartment representing a different range of vascular scale. Each compartment spatially coexists with all other compartments and occupies its own fractional volume (Fig. 3.1). Note that in perfusion modelling, the contribution of the interstitial volume is generally disregarded, due to the comparatively limited flux of fluid across the capillary membranes, and the slower diffusion-driven mode of transport in the interstitial space. The multi-compartment static Darcy system, and the methods used to parameterise the material properties of the porous domains, are presented below.

The multi-compartment Darcy system extends the single compartment Darcy model to  $N$  porous domains, and has been applied to previous perfusion modelling problems [21, 102]. The Darcy system for a compartment  $i \in [1, N]$  is (Einstein summation is not in use):

$$\mathbf{w}_i + \mathbf{K}_i \cdot \nabla p_i = 0 \quad \text{in } \Omega, \quad (3.13a)$$

$$\nabla \cdot \mathbf{w}_i = S_{v_i} - \sum_{k=1}^N \beta_{i,k} (p_i - p_k) \quad \text{in } \Omega, \quad (3.13b)$$

where subscripts  $i$  and  $k$  are compartment indices and  $\boldsymbol{\beta}$  is a matrix of inter-compartment pressure-coupling coefficients. Note that  $\beta_{i,k} \in \mathbb{R}_0^+$  and  $\beta_{i,k} = \beta_{k,i}$  for  $i, k = 1, \dots, N$  in order to conserve fluid mass across the system. Eqs. (3.13) were set on an open bounded domain  $\Omega \subset \mathbb{R}^n$  with spatial dimension  $n$  and a piece-wise smooth boundary  $\partial\Omega$ , upon which zero flux boundary conditions were enforced.

As previously mentioned, the permeability tensor field  $\mathbf{K}$  contains the coefficients of proportionality relating the Darcy velocity  $\mathbf{w}$  to the pressure gradient. The permeability  $\mathbf{K}$  is a material property of the porous medium and it has the following key properties related to the physical constraints of the system [6]:

- $\mathbf{K}$  is symmetric, by the Onsager's reciprocal relation. This ensures that there is no bias in the material and a reversal in the pressure gradient should lead to a matching reversal in flow.

- $\mathbf{K}$  is positive definite. This property ensures that the direction of flow is always in the same direction as the pressure drop, i.e. fluid flows from region of high pressure to lower pressure.

### 3.3.3.2 Poroelasticity

The static Darcy perfusion model developed thus far lacks the ability to capture fluid-solid interactions as it assumes a rigid solid skeleton. In certain physiological applications, it is crucial to account for such interactions in order to capture the dynamics of the cardiac phase dependence of flow. For this reason, we now extend the porous flow framework to a general poromechanical one in which deformation of the medium and the resulting interactions with the pore fluid are defined. The application of poromechanical models in the context of perfusion in a contracting myocardium has been limited to a small number of studies to date [17, 44]. The comprehensive theoretical background can be found in [23, 24], which establishes a finite strain theory of poromechanics. Where applicable, we defer the description of specific constitutive relations and geometrical modelling choices employed to the results in Sect. 3.4.1.3.

#### *Kinematics*

In the poromechanical framework adopted here, a porous medium is treated as a superposition of solid and fluid continua, each occupying a fraction of the total volume at every point in the material. The smallest relevant unit of the material is termed a Representative Elementary Volume (REV), denoted as  $d\Omega$ , and contains a sufficient number of pores to allow a macroscopically averaged description. Thus an REV is not infinitesimal but must satisfy the requirement of being “small” relative to the total body, which is dependent on the particular problem under consideration. Note the standard terminologies *matrix* and *skeleton* indicate a distinction between the microscopic and macroscopic (averaged) solid phases, respectively.

The volume fraction occupied by the fluid is referred to as *porosity*, defined by  $\phi = \frac{d\Omega^f}{d\Omega}$  where superscript *f* refers to fluid. Fully saturated and connected pores are assumed in this work, which leads to the solid fraction being  $\phi^s = 1 - \phi = \frac{d\Omega^s}{d\Omega}$ , where *s* refers to solid. In the following, a Lagrangian reference frame (i.e. tied to the skeleton) is employed since skeletal deformation is most readily observable, and it leads to similar results familiar from existing work in cardiac mechanical modelling.

Briefly, a skeleton particle at position  $\mathbf{X}$  in the reference configuration is identified with the particle at deformed position  $\mathbf{x}$ , such that  $\mathbf{x} = \mathbf{x}(\mathbf{X}, t)$ . This leads to the standard definitions of deformation gradient  $\mathbf{F} = \nabla_{\mathbf{X}}\mathbf{x}$ , Jacobian  $J = \det(\mathbf{F})$ , and the right Cauchy-Green deformation tensor  $\mathbf{C} = \mathbf{F}^T\mathbf{F}$ . The Green-Lagrange strain tensor is then defined to be  $\mathbf{E} = \frac{1}{2}(\mathbf{C} - \mathbf{I})$ .

An alternative definition of  $J$  is expressed as  $J = \frac{d\Omega}{d\Omega_o}$ , where the subscript *o* refers to the reference configuration, and  $d\Omega$  now refers to the REV in the current configuration. In addition, because  $d\Omega$  in general changes with altered fluid content, the

change in pore volume is better captured by the *Lagrangian porosity*  $J\phi = \frac{d\Omega^f}{d\Omega_o}$ , which expresses the ratio of the current fluid content to the reference volume.

A common assumption made in cardiac mechanics is the incompressibility of the myocardial tissue. In the context of poromechanical models, however, such an assumption requires a further clarification. Considering the macroscopic skeleton to be an incompressible medium would be inappropriate as the net flow in and out of the tissue can always cause a bulk volume change. Rather, it is the solid matrix which we regard as incompressible. Assuming there is no solid mass creation occurring within the time scale under consideration, the conservation of solid phase can be written as

$$\rho^s(1 - \phi)d\Omega = \rho_o^s(1 - \phi_o)d\Omega_o \quad (3.14)$$

which, upon inserting the incompressibility condition of density  $\rho^s = \rho_o^s$ , can be expressed as

$$J - J\phi = 1 - \phi_o = \phi^s. \quad (3.15)$$

This can be contrasted with the hyperelastic incompressibility condition  $J - 1 = 0$ .

### *Conservation Laws*

The fluid continuity equation is expressed as

$$\frac{dm}{dt} + \nabla_{\mathbf{X}} \cdot (\rho^f \mathbf{W}) = S, \quad (3.16)$$

where  $m$  represents the current additional fluid mass content per unit reference volume, and  $S$ , a mass source term.  $\mathbf{W}$  is a Lagrangian counterpart to the Eulerian Darcy velocity  $\mathbf{w}$  which is now generalised to be

$$\mathbf{w} = \phi (\mathbf{v}^f - \mathbf{v}^s) = \phi \left( \frac{dx^f}{dt} - \frac{dx^s}{dt} \right). \quad (3.17)$$

The conservation of momentum is often described for the combined medium, such that

$$\nabla_{\mathbf{X}} \cdot (\mathbf{F} \mathbf{S}) + m^s(\mathbf{f} - \mathbf{a}^s) + m^f(\mathbf{f} - \mathbf{a}^f) = 0, \quad (3.18)$$

where  $\mathbf{S}$  represents the second Piola-Kirchoff stress, and  $\mathbf{f}$  and  $\mathbf{a}$  represent body force density and acceleration, respectively. Variables  $m^s$  and  $m^f$  can be regarded as density-like quantities which denote respectively the skeletal and fluid mass content per unit reference volume. Note that  $m^f$  and  $m$  are related via

$$m^f = \rho_o^f \phi_o + m. \quad (3.19)$$

### *Constitutive Relation*

Formulation of a constitutive relation for an open porous medium involves many challenges. Thermodynamic considerations can help to identify appropriate state variables and equations which are consistent with the assumptions made for a specific medium. In a continuum mechanics framework the entropy condition is expressed by the Clausius-Duhem inequality, the general expression for a porous

medium of which is [27]

$$D = \mathbf{S} : \frac{d\mathbf{E}}{dt} + p \frac{d(J\phi)}{dt} - S \frac{dT}{dt} - \frac{d\Psi^s}{dt}, \quad (3.20)$$

which states that the intrinsic dissipation  $D$  is dependent on both skeletal and pore strain work rates and entropy variation. Here,  $S$  and  $T$  denote entropy and temperature respectively and  $\Psi^s$  denotes the Lagrangian free energy density of the skeleton. In cardiac modelling, further simplification can be made if we assume the myocardial tissue to be an isothermal, *poroelastic* medium, for which dissipation is zero, yielding

$$\frac{d\Psi^s}{dt} = \mathbf{S} : \frac{d\mathbf{E}}{dt} + p \frac{d(J\phi)}{dt} \quad (3.21)$$

giving the state equations

$$\mathbf{S} = \frac{\partial\Psi^s}{\partial\mathbf{E}}, \quad p = \frac{\partial\Psi^s}{\partial(J\phi)} \quad (3.22)$$

stating that  $\mathbf{S}$  and  $p$  respectively are the thermodynamic forces driving the changes in  $\mathbf{E}$  and  $J\phi$ .

Additional requirements can be posed on the general form of the free energy function  $\Psi^s(J\phi, \mathbf{E})$  to address the cases when the porosity reaches the physical limits of 0 or 1. However, in the incompressible regime, (3.15) implies that  $\phi < 1$  for  $0 < J < \infty$ , thus we focus our attention on the compaction limit ( $\phi \rightarrow 0$ ). Following [30], an effective barrier potential would remain inactive (contributes zero pressure and stiffness) until compaction is approached, but once activated, provides pressure and stiffness which tend toward infinity thus preventing further extraction of the pore fluid. Thus we seek to construct a barrier potential  $\Theta(J\phi)$  which satisfies

$$\frac{\partial\Theta}{\partial(J\phi)} = \frac{\partial^2\Theta}{\partial(J\phi)^2} = 0, \quad \text{for } J \geq 1, \quad (3.23)$$

$$-\frac{\partial\Theta}{\partial(J\phi)} \rightarrow +\infty, \quad \text{for } J\phi \rightarrow 0, \quad (3.24)$$

$$\frac{\partial^2\Theta}{\partial(J\phi)^2} \rightarrow +\infty, \quad \text{for } J\phi \rightarrow 0. \quad (3.25)$$

This leads to the general form of free energy

$$\Psi^s = \Phi(\mathbf{E}, J\phi) + \Theta(J\phi). \quad (3.26)$$

As there is substantial work still to be undertaken in designing and validating a specific cardiac poroelastic constitutive law, at this stage we propose a further decomposition of  $\Psi^s$  such that

$$\Psi^s = \bar{\Phi}(\mathbf{E}) + \hat{\Phi}(J\phi) + \Theta(J\phi) \quad (3.27)$$

which enables the previously characterised hyperelastic constitutive laws and coronary pressure-volume relationships to be substituted.

In addition, in a contracting myocardium the stress tensor is augmented by an active component such that

$$\mathbf{S} = \mathbf{S}_p + \mathbf{S}_a \quad (3.28)$$

where  $\mathbf{S}_p$  and  $\mathbf{S}_a$  represent the passive and active components, respectively. The active stress is assumed to act along the fibre direction  $\mathbf{f}$  in the deformed configuration, thus yielding the active component of the Cauchy stress tensor

$$\boldsymbol{\sigma}_a = T_a \mathbf{f} \otimes \mathbf{f} \quad (3.29)$$

which is related to the second Piola–Kirchoff stress tensor via

$$\mathbf{S}_a = J \mathbf{F}^{-1} \boldsymbol{\sigma}_a \mathbf{F}^{-T}. \quad (3.30)$$

The fibre active stress  $T_a$  is calculated by an auxiliary model of time-dependent fibre stress development and  $\mathbf{f}$  denotes the deformed fibre axis direction. The specific relations we have used to represent the components of the constitutive law are outlined in Sect. 3.4.1.3.

### 3.3.3.3 Vascular-porous Medium Coupling

For applications that warrant subject-specific anatomy, coronary–contraction coupling or involve integrative physiological mechanistic investigations, combining the 1D framework with the porous approach may be instrumental. The 1D–3D coupling can also address the problem of potentially reversing inflow boundary conditions in the porous domain, and more accurately represent the distal mechanical interactions responsible for wave generation, thereby helping to overcome the shortcomings in each respective model.

Anatomically, the interface domain between the explicit proximal vascular segments and porous medium consists of meso-scale arterioles which transition into the microcirculation over several bifurcating generations. Therefore, instead of treating the interface as a point-to-point coupling – which would result in concentrated tissue inflow and thus unphysiological pressure peaks – we assume that the exchange of fluid between a vessel terminal and the porous tissue occurs in a distributed manner over the volume  $\Omega_{int}$  in the neighbourhood of the terminal, such that

$$\rho^f Q_{1D}(t) = \int_{\Omega_{int}} S(\mathbf{x}, t) d\Omega. \quad (3.31)$$

For clarity, variables in the 1D flow model are denoted with a subscript  $1D$  here. We choose to express  $S$  via a distribution function  $f$  such that

$$S(\mathbf{x}, t) = \rho^f Q_{1D}(t) f(\mathbf{x}) \quad (3.32)$$

which, together with (3.31) implies that

$$\int_{\Omega_{int}} f(\mathbf{x}) d\Omega = 1 \quad (3.33)$$

must be held. The pressure–flow relationship of the coupling interface is described by observing that the meso-scale vessels are predominantly resistive elements comprising thick-walled arterioles, leading to

$$Q_{1D}(t) = \frac{p_{1D}(t) - \bar{p}(t)}{R_{meso}} \quad (3.34)$$

where  $R_{meso}$  is the resistance of the coupling interface. As a first approximation, we define the average pore pressure  $\bar{p}$  as

$$\bar{p} = \int_{\Omega_{int}} p(\mathbf{x}, t) f(\mathbf{x}) d\Omega. \quad (3.35)$$

The coupling problem therefore seeks to find values of  $Q_{1D}$  and  $p$  which satisfy (3.34) and (3.35). Several strategies can be envisioned to specify the function  $f(\mathbf{x})$ , including an analytic derivation from an assumed branching structure, or directly characterised from detailed network morphology. In the absence of such data however, we employ a simpler approach in this work and approximate  $f$  with a Gaussian function. To ensure (3.33) holds,  $f$  is formulated as

$$f(\mathbf{x}) = \frac{1}{\int_{\Omega_{int}} G(\mathbf{x} - \mathbf{x}_{term}) d\Omega} G(\mathbf{x} - \mathbf{x}_{term}) \quad (3.36)$$

where  $\mathbf{x}_{term}$  denotes the position of the vessel terminal, and  $G$  is a standard Gaussian kernel.

### 3.3.3.4 Parameterisation of Porous Medium

We now depart from the largely theoretical focus examined up to this point and briefly consider the issue of characterising the porous medium parameters from real-world data. This will assist in addressing questions such as whether the continuum approach is a suitable one for modelling coronary network flow, and how a detailed anatomical network morphology can be condensed into equivalent porous medium parameters. The methods outlined below necessitates the use of high-resolution animal data, but in exchange offers the means by which to determine the appropriate parameter ranges in health and disease, as a basis for extrapolation to humans as is common in medical research. Further discussions on clinical translational strategies are provided in Sect. 3.5.

Models of the discrete vascular network reconstructed from high-resolution imaging data [100] are well-suited for the distillation of important microvascular characteristics into continuum parameters. To enable the parameterisation of the individual compartments, one must first compartmentalise (or longitudinally partition) the vascular model. The so-called *hierachic parameter* vascular model field is used for this purpose. This is a monotonically decreasing field with respect to a proximal-distal direction of flow, with the value 1 at the proximal node of the network, 0 at all distal terminal nodes, and the value of the summed length of all distal vessels at intermedi-

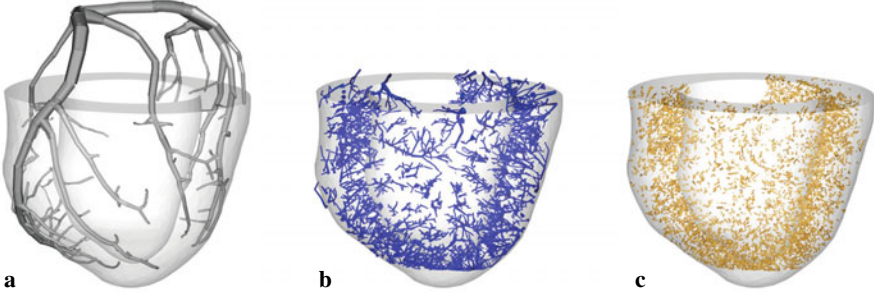


**Fig. 3.2.** Compartmentalisation of a porcine arterial network derived from cryomicrotome data. This example, which assumes two Darcy compartments, consists of (a) the 1D portion which drives the fluid flow in the continuum model, and the compartment 1 and 2 discrete vessels that will be spatially-averaged into macroscale continuum permeability parameters ((b) and (c), respectively)

ate nodes divided by the summed length of all vessels. Note that pressure solutions from a discrete flow model have also been previously applied to define the hierachic parameter field [102]. This robust partitioning metric preserves the “natural order” of flow, i.e. proximal vessels are allocated to proximal Darcy compartments. Ultimately the particular hierachic parameter values that dictate the vascular partition must be selected on an application-dependent basis. For instance, Fig. 3.2 shows an example compartmentalisation of a porcine arterial model for use in parameterising a two-compartment porous perfusion model. For simplicity of this illustration, an approximate equal split in the number of vessels to be spatially-averaged between Darcy compartments 1 and 2 was applied.

Once compartmentalised, spatial-averaging techniques (using an averaging window of constant size, denoted  $d\Omega$ ) are employed to extract the effective parameter fields, such as the porosity of compartment  $i$ , defined to be

$$\phi_i(x) = \frac{\sum_{v \in V_i(x)} vol_v}{vol_{d\Omega}}, \quad (3.37)$$

where  $V_i(x)$  is the set of vessels assigned to Darcy compartment  $i$  within the averaging volume centered at a point  $x \in \Omega$ , and  $vol_\epsilon$  is defined as the volume of a domain  $\epsilon$  that intersects  $\Omega$ . Thus the total porosity of the material is

$$\phi(x) = \sum_{i=1}^N \phi_i(x). \quad (3.38)$$

Importantly, we use a discrete Poiseuille flow model solution to produce local variables that are dependent on the entire network topology. Specifically, the Poiseuille pressure at a node in the discrete vascular model is calculated using the Poiseuille network matrix [79]. Note that the pressure derived from the linear Poiseuille model is also dependent on the boundary conditions applied. However we have pre-

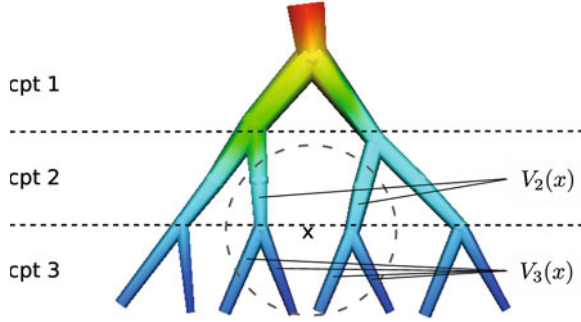


**Fig. 3.3.** Schematic of a simple network to illustrate the vessels involved in parameterising the continuum permeabilities at a point  $x$ . The averaging window is delineated by the dashed circle, with centrepoint  $x$  ( $x$  is typically a finite element mesh node). Note that for this example point,  $V_1(x)$  and the compartment-connecting vessel sets  $c_{1,2}(x)$  and  $c_{1,3}(x)$  are equal to the null set, whereas  $c_{2,3}(x) = V_2(x)$  as both vessels in  $V_2(x)$  are connected to vessels in  $V_3(x)$

viously shown the robustness of using the Poiseuille model to characterise flow parameters with respect to varying boundary conditions [47]. Thus, we define the spatially-averaged discrete pressure for vessels in the  $i^{th}$  compartment to be

$$\bar{p}_i(x) = \frac{\sum_{v \in V_i(x)} P_v \text{vol}_v}{\sum_{v \in V_i(x)} \text{vol}_v}, \quad (3.39)$$

where  $P_v$  is the averaged discrete pressure (mean of the two nodal values) for the  $v^{th}$  vessel within  $V_i(x)$ , and  $\Delta p_v$  is the difference in pressure across the vessel.

The discrete mass flux between compartments is a key variable in the evolution of multi-compartment porous flow. The set of all vessels within  $d\Omega$  that belong to compartment  $k$  but share a node with a compartment  $i$  vessel is denoted by  $c_{i,k}$  (see Fig. 3.3 for a schematic illustrating these sets of compartment-connecting vessels). The flux from compartments  $i$  to  $k$  is then

$$Q_{i,k}(x) = \sum_{v \in c_{i,k}(x)} \frac{\pi r_v^4}{8\mu l_v} (\Delta p_v). \quad (3.40)$$

From the perspective of the Darcy model,  $\beta_{i,k}$  can be viewed as the local constant of proportionality between the fluid flux transfer and the difference in the Darcy pressures. Thus, we use the data derived from the discrete model to define these continuum fields via

$$\beta_{i,k}(x) = \begin{cases} 0 & \text{if } \bar{p}_i(x) - \bar{p}_k(x) = 0. \\ \frac{Q_{i,k}(x)}{|\bar{p}_i(x) - \bar{p}_k(x)|}, & \text{otherwise.} \end{cases} \quad (3.41)$$

Unsurprisingly, these inter-compartment coupling fields play a major role in determining the overall fluid flow within the model, due to their widespread heterogeneity

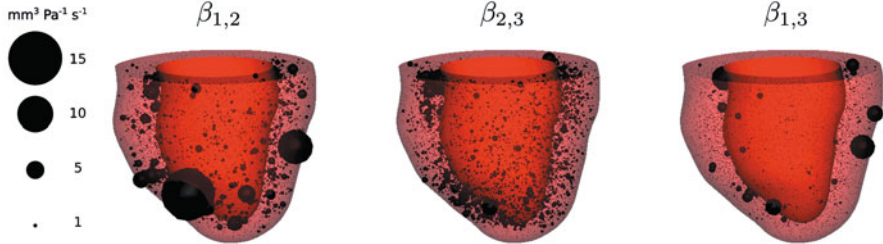


**Fig. 3.4.** The spatial distribution of the continuum  $\beta$  fields allows for heterogeneous mass transfer amongst compartments. Here we consider a three-compartment Darcy model, where the left ventricular endocardial surface is opaque while the epicardial surface is transparent. Each finite element mesh node is represented by a spherical glyph whose diameter is equal to the  $\beta$  value at that node. Note in particular the heterogeneous  $\beta_{1,3}$  field, which illustrates the level of non-adjacent compartment coupling in this  $N = 3$  model scenario

and the presence of “long-range” coupling, i.e. coupling between non-neighbouring compartments (Fig. 3.4).

Finally, we present two methods which may be applied to parameterise the permeability tensor fields, depending on the level of discrete data available. The simpler method is to assume a porosity-scaled isotropic permeability, i.e.

$$K_i(x) = c_{Ki} \phi_i(x) I, \quad (3.42)$$

where  $I \in \mathbb{M}_{3 \times 3}$  is the identity tensor with assumed units of  $\text{mm}^2 \text{ Pa}^{-1} \text{ s}^{-1}$ , and  $c_{Ki}$  is a constant scalar of the permeability which is solved for in a post-processing minimisation problem to best match the continuum pressures with the spatially-averaged discrete pressures [46]. Alternatively, one can use a previously proposed method [45] whereby the permeability tensor is defined as

$$K_{ij} = \frac{\pi}{128 vol_d \Omega \delta x_0 \mu} \sum_{ns} \frac{d_{ns}^4 \Delta x_{ns,i} \Delta x_{ns,j}}{l_{ns}}, \quad i, j = 1, 2, 3, \quad (3.43)$$

with  $\delta x_0$  being an infinitesimal element of their hierarchic parameter,  $ns$  is the set of vessels within the hierarchic parameter range  $\delta x_0$ ,  $d$  is the vessel diameter, and  $\Delta x_{ns,i}$  is the absolute difference in spatial coordinate  $i$  between the vessel end points.

### 3.4 Model Applications

In this section we present clinically-oriented applications of the modelling framework described in the previous sections. Selected examples include a model for *in silico* wave intensity analysis featuring varying degrees of complexity, and a myocardial transport model for calculating contrast agent dynamics. The reduced complexity WIA model is aimed particularly at time-bound interventional clinical settings, whereas the full poroelastic model enables the interpretation of limited data

collectable in these situations through mechanistic investigation unachievable with the simpler model. These examples illustrate our efforts to address real-world problems in which the quantity of observable data and time constraints play a significant role in directing the appropriate modelling approach. The transport model, on the other hand, allows the perfusion simulations to be compared directly with clinically-acquired data, thus closing the loop between modelling and imaging. Taken together, these applications focus on assessing the combined states of myocardial perfusion and function.

### 3.4.1 Coronary Wave Intensity Analysis

Due to the technological advancements over the past decade in coronary catheter wires which enabled simultaneous measurements of pressure and velocity, wave intensity analysis (WIA) has emerged as a useful tool with which to study the underlying cardiac and hemodynamic function. Its application to the human coronary system has identified six major waves, each attributed to different events of the cardiac cycle [25], the characteristics of which are now being applied for clinical diagnosis. Simultaneous measurements of pressure and velocity acquired *in vivo* in a human LAD are shown along with the calculated WIA in Fig. 3.5 for illustrative purposes.

#### 3.4.1.1 Theoretical Background

This section outlines the mathematical background for calculating wave intensity from coronary waveforms. For an in-depth theoretical and practical discussion, we refer the readers to a recent review [76]. The catheter-acquired pressure and velocity raw data in the clinic are ensemble averaged and then smoothed using the Savitzky-Golay filter. The time derivatives of the pressure and velocity signal can be obtained directly from the filter or estimated as the time increments of the smoothed pressure  $p(t)$  and velocity  $u(t)$  signals, as

$$dp = p(t + dt) - p(t), \quad du = u(t + dt) - u(t), \quad (3.44)$$

where  $dt$  indicates the sampling time. Using the water hammer equations, relating changes in velocity and change in pressure in a wavefront

$$dp_+ = \rho cdu_+ \quad \text{for forward travelling waves} \quad (3.45)$$

$$dp_- = -\rho cdu_- \quad \text{for backward travelling waves} \quad (3.46)$$

where  $\rho$  denotes fluid density. It is then possible to compute the wave intensity as

$$dI(t) \equiv \frac{dp(t)}{dt} \frac{du(t)}{dt}. \quad (3.47)$$

Dividing the time increments by  $dt$  avoids the dependence of WIA on the sampling time step size. The fundamental property of wave intensity is that at each sampling point of the measured waveform,  $dI(t)$  highlights if the forward or backward trav-

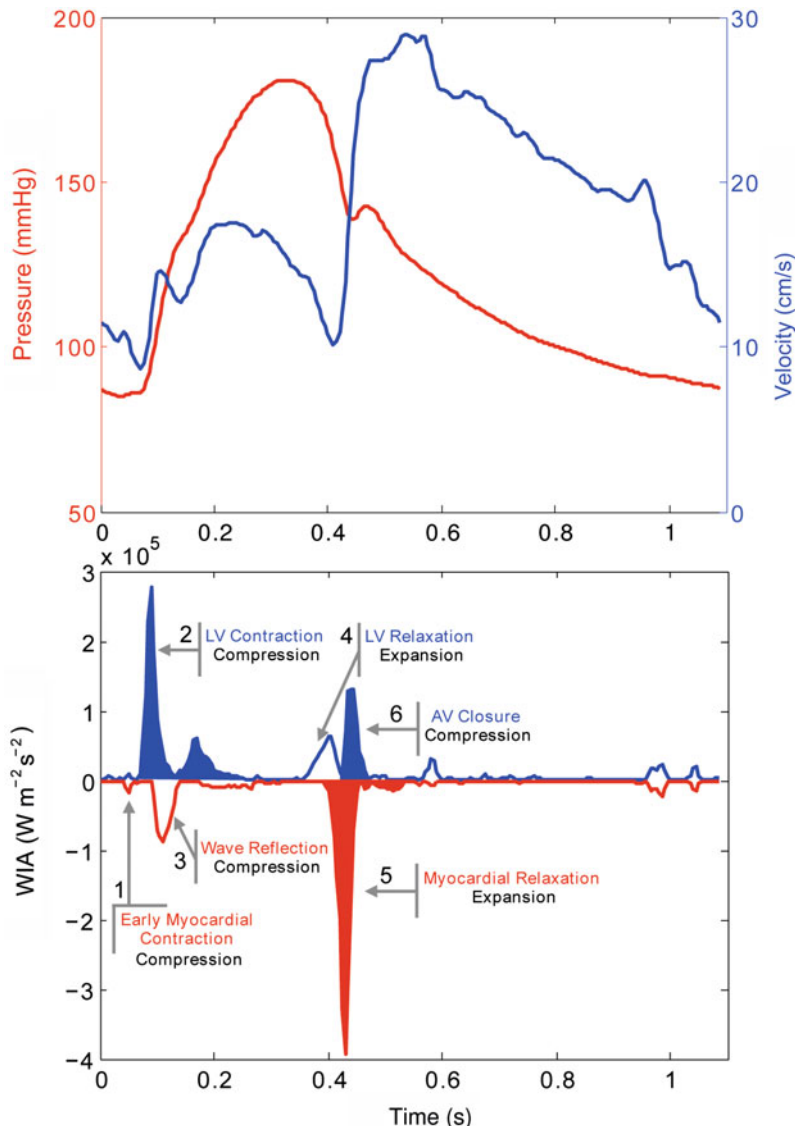


**Fig. 3.5.** The pressure and velocity signals, acquired *in vivo* in a human subject, have been ensemble-averaged over 9 beats (*top*). The resulting forward and backward separated waves are shown (*bottom*). For each of the major waves the related cardiac event and the associated change in coronary pressure are highlighted (compression=increase, expansion=decrease). The coloured waves are associated with flow acceleration whereas the uncoloured ones indicate flow deceleration. The waves have been numbered following [25]. It is important to highlight that the wave 1 is not always detectable due to the relatively low amplitude. AV = aortic valve, LV = left ventricle

elling wave is dominant at that instance. With the further assumption that forward and backward travelling waves sum linearly when interacting

$$dp = dp_+ + dp_- , \quad du = du_+ + du_- , \quad (3.48)$$

combined with (3.45), it is possible to separate the simultaneous forward and backward travelling waves

$$dI_{\pm} \equiv \frac{dp_{\pm}}{dt} \frac{du_{\pm}}{dt} = \pm \frac{1}{4\rho c} \left( \frac{dp}{dt} \pm \rho c \frac{du}{dt} \right)^2 , \quad (3.49)$$

where

$$dp_{\pm} = \frac{1}{2}(dp \pm \rho c du) , \quad du_{\pm} = \frac{1}{2} \left( du \pm \frac{dp}{\rho c} \right) . \quad (3.50)$$

The pulse wave speed (PWS) of the coronary vessel ( $c$ ) is then usually estimated by using the sum-of-squares method [1, 25]

$$c = \frac{1}{\rho} \sqrt{\frac{\sum dp^2}{\sum du^2}} , \quad (3.51)$$

which is to date the only single point method published. It is important to stress that the summations have to be taken over an integer number of cardiac cycles. Finally, the separated component of pressure and velocity can be computed as follows

$$p_{\pm}(t) = \sum_0^t dp_{\pm}(t) + p_0 , \quad u_{\pm}(t) = \sum_0^t du_{\pm}(t) + u_0 , \quad (3.52)$$

where  $p_0 = p(t = 0)$  and  $u_0 = u(t = 0)$ .

### 3.4.1.2 Physiological Applications

Applying the theoretical framework outlined in Sect. 3.4.1.1, the key question we seek to answer first is whether or not the one-dimensional coronary model, presented in Sect. 3.3.2, can appropriately capture the epicardial flow and reproduce the main waves of the WIA profile. To address this question the model setup combines a patient-specific geometry and a RCR Windkessel boundary condition with a time-varying distal pressure (representing the LV pressure impact), as previously applied in [57, 69].

The motivations behind this modelling setup are practical. Firstly, if interventional clinical translations are of interest then the computation of the model must be fast. Secondly, the model inputs are constrained by the data available in the clinic, commonly limited to simultaneous single-point pressure and velocity measurements, at times augmented by the geometry of the large epicardial vessels or their 2D projection.

Despite its simplicity, this approach retains its clinical relevance as the measured waveforms can be fitted to estimate the Windkessel parameters (R-C) providing in-

formation about the distal vasculature. Moreover, when applied to healthy and diseased vessels, deviation in the estimated distal parameters can complement the information available in the clinical setting. Furthermore, a template distal time-varying pressure can be fitted to the measured data, providing an estimate of the left ventricular pressure which is highly desirable but usually inaccessible in the clinical diagnosis.

In an illustrative simulation below, the patient-specific geometry and the inlet and outlet area of the left anterior descending artery (LAD) were extracted from CT data and meshed using spectral elements of 5<sup>th</sup> order [87]. The LAD was assumed to taper linearly. The pressure and velocity waveforms were simultaneously measured using a dual pressure and Doppler sensor (Combowire, Volcano Corp). The PWS of 23 m/s was estimated using the sum-of-squares method (3.51) and  $\beta$  was adjusted such that the PWS is constant throughout the whole vessel (implying constant distensibility [83]). The inlet boundary condition was prescribed to be the pressure measured in the proximal part of the LAD. The values of the distal boundary condition parameters  $R_t = R_1 + R_2 = 4.5 \cdot 10^9 \text{ Pa} \cdot \text{s/m}^3$  and  $C = 0.625 \cdot 10^{-12} \text{ m}^3/\text{Pa}$  are within the physiological range found in literature [57, 83]. The scaled left ventricular pressure and the outlet boundary condition parameters were adjusted to obtain physiological flow. The model was run for several cardiac cycles until periodic flow was achieved.

Physiological coronary pressure and velocity profiles were obtained (shown in Fig. 3.6). Major features of the velocity waveform such as the early-systolic and late-systolic minima [68] and the sharp diastolic rise were represented in the simulated results. The modelled velocity profile (Fig. 3.6) qualitatively reproduces the measured data (from a different patient) shown in Fig. 3.5, demonstrating the capacity of the framework to capture the main features of wave propagation in a coronary vessel. (Direct comparison between the simulated and the measured velocity waveform in the same patient has not been possible due to the poor quality of the acquired velocity data in this case.)

The spatial variation in the velocity profile between the proximal and distal part of the LAD qualitatively follows the expected changes, as measured in [53]. The main relative variations between the proximal and distal velocities are an increase in the early-systolic negative velocity and a less evident early-systolic peak (at  $t \approx 0.1 \text{ s}$ ) and late-systolic minima (at  $t \approx 0.38 \text{ s}$ ), as described in [53].

In the current simulation setup, the calculated distal velocities are higher than in the patient due to the absence of side branches in the model. There are several practical considerations associated – with the current imaging technology, the clinically observable number and length of side branches are inconsistent across the patients and depends strongly on the image quality. If we were to model every observable side branch it will multiply the number of boundary Windkessel models, preventing a standardised interpretation of these parameters and their comparison across a population. Furthermore, the relative magnitudes of the main waves can be considered to be of greater clinical interest than the absolute values. In light of the inter- and intra-patient variabilities and the effect of autoregulation on basal flow and pres-

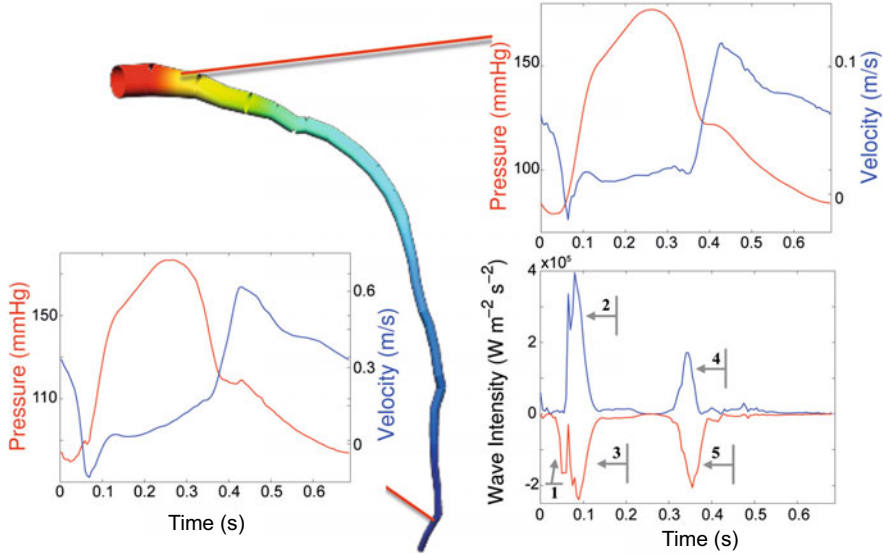


**Fig. 3.6.** The pressure and velocity waveforms in the proximal part of the LAD are visualised along with the coronary WIA profile, where the main waves of the coronary WIA profile [25] are clearly visible. The waves have been numbered following Fig. 3.5. The wave associated to the aortic valve transition is not reproduced, as the valve behaviour at the inlet was not included in the model

sure, the absolute wave intensity magnitude is uninformative unless acquired under several well-defined conditions and compared, thereby limiting its utility.

In conclusion, this model can be used to realistically reproduce the coronary WIA (cWIA), as shown in Fig. 3.6, as well as to investigate the impact that distal parameters ( $R$ ,  $C$  or left ventricular pressure) have on the cWIA outcome. Moreover, by applying this model in an inverse manner, the underlying parameters of the model can be estimated as surrogate measures of distal vascular bed resistance and compliance. However, it is not suitable for investigating the link between each different wave and the mechanisms behind its origin, motivating the modelling approach presented in Sect. 3.4.1.3. Nevertheless, this application of the one-dimensional modelling reaffirms its ability to correctly reproduce wave propagation phenomena, even in the coronary epicardial vessels that are relatively short ( $\approx 10$  cm) with respect to the measured PWS ( $\approx 15\text{--}25$  m/s).

### 3.4.1.3 Wave Intensity and Integrated Cardiac Function

Recent clinical research has shown that a coronary WIA-derived index can predict functional recovery following a myocardial infarction [26], demonstrating the clinical potential of the approach. However, a systematic investigation of the modulating

factors underlying each wave is currently not available. While such a study would be instrumental in advancing our prognostic capabilities through further mechanistic understanding, at present experimental options are limited due to the physiological complexity of the system under study. Detailed biophysical modelling on the other hand offers the possibility to establish quantitative and mechanistic linkages between cardiac function and the observed coronary waves, through parameter sensitivity analyses.

Here we present an integrative framework aimed at enabling an *in silico* WIA. It combines the one-dimensional vascular flow representation with a model of contracting myocardium that incorporates the poromechanical framework outlined in Sect. 3.3.3.2. The coupling between the two systems occurs both distally, at vascular termini distributed throughout the myocardium, and proximally, via the aortic sinus hemodynamics described as part of the reduced-order systemic circulation model. Rather than prescribing measured quantities as boundary conditions, the components of the model interact with one another and drive the evolution of the coronary waves, thus allowing mechanistic investigations of wave generation. The inlet pressure of the coronary system is determined by the aortic sinus pressure in the systemic circulation model, which in turn depends on the outflow from the left ventricle. Mechanical stress generation in the myocardium due to passive filling or the contractile forces contributes to the pore fluid pressure, which in turn feeds back onto the vascular flow. This framework thus allows the coupled wave propagation–perfusion–contraction dynamics to be studied throughout the full heart cycle.

The poroelastic constitutive relation (3.27) was composed of:  $\bar{\Phi}$ , an existing hyperelastic formulation of cardiac tissue [41] supplemented with a linearly viscoelastic term; and  $\hat{\Phi}$ , an adapted coronary pressure-volume relationship characterised from experimental measurements [13]. The compaction barrier potential  $\Theta$  was based on a functional form proposed in [30]. Active tension generation in the myofibres was modelled using a previously proposed relation employed for patient-specific modelling [71], which is a reduced-parameter formulation of [56].

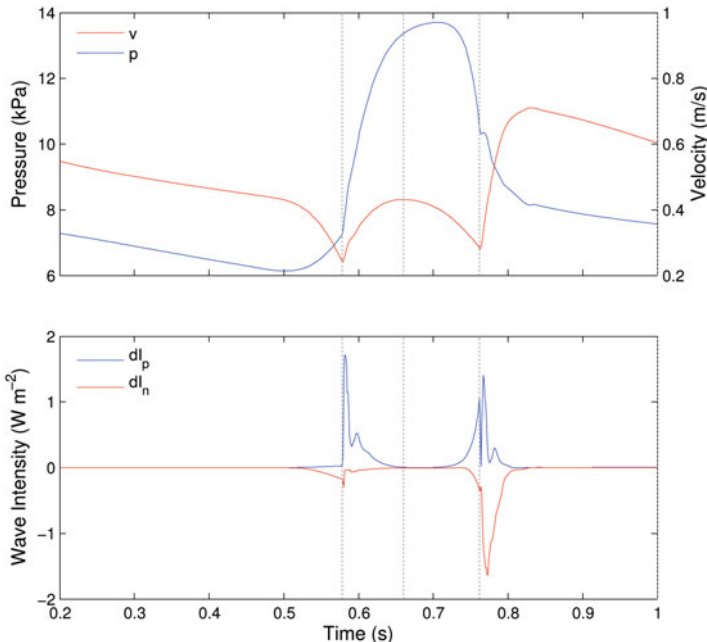
The resulting poroelastic problem was discretised using a Galerkin finite element formulation, with quadratic and linear hexahedral elements for displacement and pressure fields, respectively. The incompressibility constraint (3.15) was addressed via Lagrange multipliers. The 1D vascular flow problem was discretised using a 5th order spectral element basis. Time discretisation was performed using a Crank–Nicolson scheme. The resulting system comprised three sub-problems (poroelasticity (3.16),(3.18) vascular flow (3.1),(3.2) supplemented by the 1D-3D coupling (3.34),(3.35), and systemic windkessel) which were solved via a sequential fixed-point approach, ensuring nonlinear convergence at each time step.

The results are demonstrated on a porcine cardiac geometry obtained via high-resolution cryomicrotome imaging [92], from which the myocardial mesh and a truncated vascular mesh featuring 4000 vessels were obtained. After pre-processing, around 2000 vascular-myocardial coupling interfaces remained, distributed throughout the myocardium. The diameter of the truncated terminal vessels were approxi-

mately  $200\mu m$ . Because the terminal generation of vessels extended to the level of microcirculation in this case, for the current application a single porous compartment was considered adequate. Boundary conditions applied to the myocardium include a viscoelastic support at the base and elastic support over the epicardial surface. The porous medium outflow condition was determined by a distributed resistance reflecting distal vessels. The boundary conditions on the vascular problem was completely defined proximally by the coupling to aortic pressure, and distally by the 1D-3D coupling.

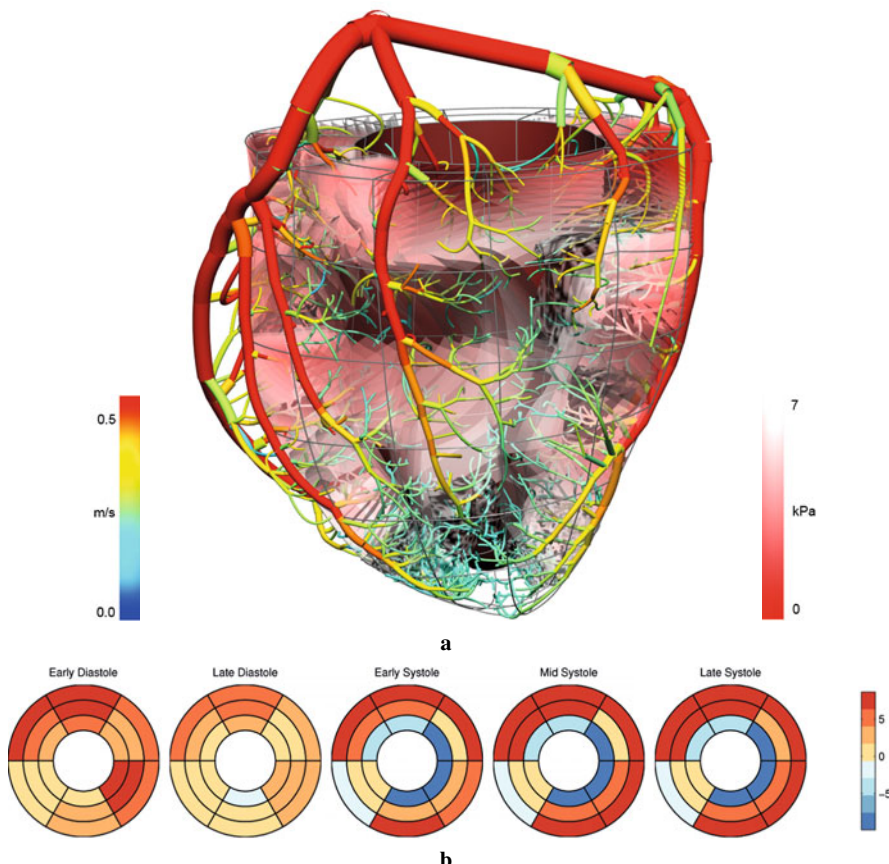
Simulations were performed with CHeart [58], an mpi-based parallel multiphysics solver developed at King's College London. The full set of model parameters and discussions of the results can be found in [59], and expanded descriptions on the employed numerical algorithms in [58].

Figure 3.7 shows an example of the physiological wave intensity profiles reproduced by the model. The dominant forward compression and backward expansion waves are accurately reproduced, as well as the smaller waves which occur during early diastole and late systole. Parameter perturbation analysis revealed key cardiac event-wave associations including a strong dependence of the forward compression wave (2) on the myocyte tension development rate, and the dominant backward expansion wave (5) on QRS duration and vascular resistance. The late forward com-



**Fig. 3.7.** Coronary pressure, velocity and wave intensity profiles from the integrated perfusion model. The results were sampled from a mid-LAD region. Good qualitative reproduction of the major forward and backward waves can be observed. For further discussion, refer to text

pression wave (6) was observed to exhibit sensitivity to the rate at which the aortic valve transitioned between open and closed states. The late backward compression wave (3) is expected to depend strongly on the wave transmission characteristics of the vascular network itself. In the current work, the vascular segments were parameterised based on a simplifying assumption of constant wave speed that is likely to have led to reduced reflections and suppressed backward propagation, that may explain the diminished magnitude of this wave in comparison to experimental findings. Further discussions on the dependence of each wave on the underlying cardiac events are available in [59]. The myocardial perfusion, estimated by the arterial inflow into the porous domain is shown in Fig. 3.8. It can be seen that the model reproduces the layer-dependent perfusion pattern, including systolic subendocardial flow reversal and endo-to-epi redistribution of flow [97].



**Fig. 3.8.** (a) Vascular velocity and tissue pore pressures are shown for a late diastolic phase; (b) Myocardial perfusion throughout the cardiac cycle shows endo-to-epi fluid shift in systole. Perfusion was calculated as the sum of arterial outflow into the segments of the porous domain

In the following section, we present an extension of the current framework to enable a consistent comparison between the perfusion fields calculated by the current approach, with those which are clinically measured using non-invasive imaging.

### **3.4.2 Perfusion Imaging and Modelling**

Perfusion MRI is employed in the assessment of tissue perfusion and provides information about the state of the coronary circulation over various vessel diameter scales. In contrast-enhanced perfusion MRI a bolus of gadolinium-based contrast agent (c.a.) is injected and a fast MRI acquisition is employed in order to obtain image information over every heart beat during the first pass of c.a. through the myocardium. An MR signal increase caused by the inflow of c.a. into the myocardial tissue is compromised in the region of perfusion defect. This can be qualitatively evaluated directly from the image data as shown in Fig. 3.9. A semiquantitative assessment of the time evolution of MR contrast in Fig. 3.10 demonstrates a delayed signal increase, lower peak signal and upslope in the diseased myocardium.

#### **3.4.2.1 Perfusion MRI Background**

The particular behaviour of perfusion MRI depends on the pharmacokinetics of the c.a., for example extravascular agents diffuse freely through capillary membranes into extracellular space, whereas intravascular contrast agents bind strongly to plasma proteins and remain within the blood. There also exist c.a. that contain both extra-cellular and intravascular components. The c.a. concentration, bolus injection duration, and total quantity of c.a. that is administered will also affect the final perfusion images.

Combining rest and stress perfusion scans allows for a detailed functional evaluation. The high spatio-temporal resolution of perfusion MRI makes it possible to observe a number of typical physiological phenomena in *in vivo* conditions, for instance different perfusion levels in subendocardial and subepicardial zones [39] or

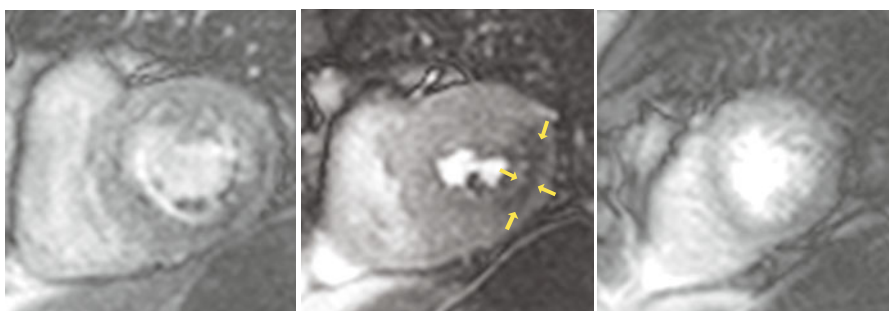


**Fig. 3.9.** Three slices of 2D perfusion MRI (covering base, mid-third and apical part of heart). Note the dark region in the mid-third of the lateral wall of left ventricle corresponding to the perfusion defect (yellow arrows). Courtesy of Prof. Eike Nagel, King's College London

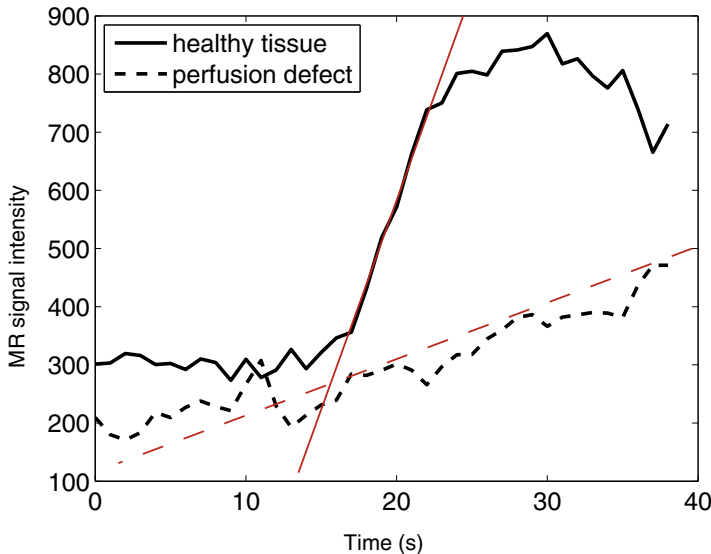


**Fig. 3.10.** Time evolution of MR signal in the middle slice of Fig. 3.9 with regions of interest placed into the healthy LV myocondium and into the perfusion defect. Note the lower peak signal and decreased upslope (dashed red line) in the hypoperfused region

the effect of phasic flow in the coronary circulation during cardiac cycle [81]. This demonstrates the significant potential of MRI in basic research – to better understand cardiac physiology both in healthy and diseased states – and in clinical research – to better stratify patients. Furthermore, the optimal adjustment of the many degrees of freedom in an MRI perfusion exam – some of which have been mentioned above – could ultimately also enhance the diagnostic efficacy of perfusion MRI.

### 3.4.2.2 Contrast Agent Transport Modelling

Although contrast-enhanced perfusion MRI shows great promise, it currently remains a technique which is confined mainly to research environments. The determination of optimal imaging strategies is complicated by the vast array of scanning parameters that can be chosen, the multiple pathologies that the modality can reveal, competing spatial-temporal requirements, and the selection of appropriate contrast agents. In this context computational modelling provides a means to more efficiently assess new imaging protocols and accommodate these disparate requirements.

#### *Mathematical Description*

The suitability of porous media formulations for modelling myocardial perfusion was summarised in Sect. 3.3.3. These justifications remain valid for modelling perfusion imaging. However an additional consideration is that the imaging data against

which the model would be validated is already the result of a volume averaging process as a typical voxel in MR perfusion imaging has dimensions of approximately  $1.2 \times 1.2 \times 10$  mm (Fig. 3.9).

To model the transport of contrast agent through the coronary circulation requires, in the most basic form, two equations, which for the sake of brevity and ease of analysis are presented here in nondimensional form (for full derivation see [20] and earlier works [7] and [88]). The first, an advection-diffusion equation, tracks the transport of c.a. concentration (henceforth denoted  $c$ ) in the fluid phase of the porous medium, which represents the blood (denoted by superscript  $f$ ):

$$\frac{\partial c^f}{\partial t} + \mathbf{u} \cdot \nabla c^f = \frac{1}{Pe} \nabla^2 c^f - Da(1 - \phi^f)(c^f - c^s) + \frac{q}{\phi^f}. \quad (3.53a)$$

Note that  $\mathbf{u}$  is related to the Darcy velocity (Eq. 3.12a) as:  $w/\phi^f$ .

To track the transport of c.a. in the solid phase of the porous medium – representing the extravascular space of the myocardium (superscript  $s$ ) – a diffusion equation is used:

$$\frac{\partial c^s}{\partial t} = \frac{D_r}{Pe} \nabla^2 c^s + Da\phi^f(c^f - c^s). \quad (3.53b)$$

In these equations the concentration  $c$  is defined per phase volume, and therefore the product  $\phi c$  gives the concentration per total volume.  $D^f$  and  $D^s$  are the diffusion coefficients of the contrast agent in the blood and extracellular space, respectively. Finally,  $q$  is a volumetric source term, typically applied at a few nodal points to represent the largest epicardial feeding vessels. In this model a temporal Gaussian inflow pattern is used to approximate the dispersion the bolus undergoes as it travels to and through the large coronary arteries.

These two transport equations are coupled by a reaction term which accounts for the diffusion of contrast agent through the vessel walls and into the extracellular space of the myocardial tissue. This model assumes that the flux through this vessel wall is proportional to the concentration difference that exists across it, which is commonly used in membrane models. The constant of proportionality  $\alpha$  is a phenomenological parameter that encapsulates both the permeability of the vessel wall to a particular contrast agent molecule, and the efficiency of the vascular geometry at allowing mass transfer across its surface and into the tissue.

The four nondimensional parameters are defined as follows.

1. Peclet number ( $Pe$ ) =  $\frac{Ud}{D^f}$ , characterises the relative time scales of advective and diffusive processes in the blood.
2. Damköhler number ( $Da$ ) =  $\frac{\alpha d}{U}$ , characterises the relative rates with which contrast agent passes through the vessel wall and is swept past it by the blood.
3. Diffusivity ratio ( $D_r$ ) =  $\frac{D^s}{D^f}$ , indicates the relative importance of diffusive processes in the intra- and extravascular spaces.
4. Fluid porosity ( $\phi^f$ ), the volume fraction of the porous medium occupied by the blood.

Once the concentration value in each phase has been determined, the total concentration in the bulk volume can be calculated by the following porosity weighted sum of the component concentrations.

$$c^{total} = \phi^f c^f + \phi^s c^s. \quad (3.54a)$$

Denoting the signal response as  $I$ , the observed myocardial signal  $I^{myo}$  is given by:

$$I^{myo} = I(\phi^f, \phi^s, c^f, c^s). \quad (3.55)$$

Data characterising typical nonlinear signal responses  $I(c)$  can be found in [49] and [42]. In the linear regime of  $I$ , before the signal begins to saturate,  $c^{total}$  is proportional to the signal.

In the Darcy flow model zero Neumann conditions are specified on all surfaces of the domain, used for the results in Figs. 3.11 to 3.14. The flow is driven by mass source models of the arteries and distributed sink terms that model the venous circulation [46]. Similarly, zero Neumann boundary conditions are applied in the transport model, with concentration sources specified at the same locations as the fluid mass sources, as used to generate the results in Fig. 3.14. The diffusion equation of the transport model is discretised using the Galerkin finite element method, whilst the advection-diffusion equation uses a Petrov-Galerkin method with streamline up-winding to improve numerical stability of the advection operator. The discrete forms of both equations are assembled into a monolithically-coupled linear system, such that both concentration values are solved simultaneously. The time stepping is performed by a backward-Euler scheme.

### 3.4.2.3 Results

#### Time Series Data

These time series data are taken from an idealised model of perfusion in the capillaries. A rectangular domain – discretised with linear Lagrange, quadrilateral elements – is used to represent the capillary bed, with uniform inflow and outflow boundary conditions in the Darcy model. A point source of concentration is situated near to the inflow and the c.a. swept downstream.

Figures 3.11a–11d show pointwise values of the c.a. concentration (fluid, tissue and total) taken at the centre of the domain, downstream of the point of contrast agent injection, for four values of  $Da$ . All of the figures show the arrival, dispersion and subsequent wash-out of the c.a. bolus. Fig. 3.11a is the concentration signal for a blood-pool (intravascular) c.a., the case  $Da = 0$  and thus all the signal originates in the fluid phase, preserving the Gaussian nature of the input bolus. As  $Da$  is increased to 0.1 in Fig. 3.11b, a small quantity of c.a. now diffuses into the tissue phase, creating a long tail in the total signal as the c.a. slowly diffuses back into the blood to be transported away downstream. At  $Da = 1.0$ , Fig. 3.11d, the storage in the tissue is significant, causing the peak concentration to be roughly halved, but these levels of signal now persist for much longer. Note that because the transport of c.a. through

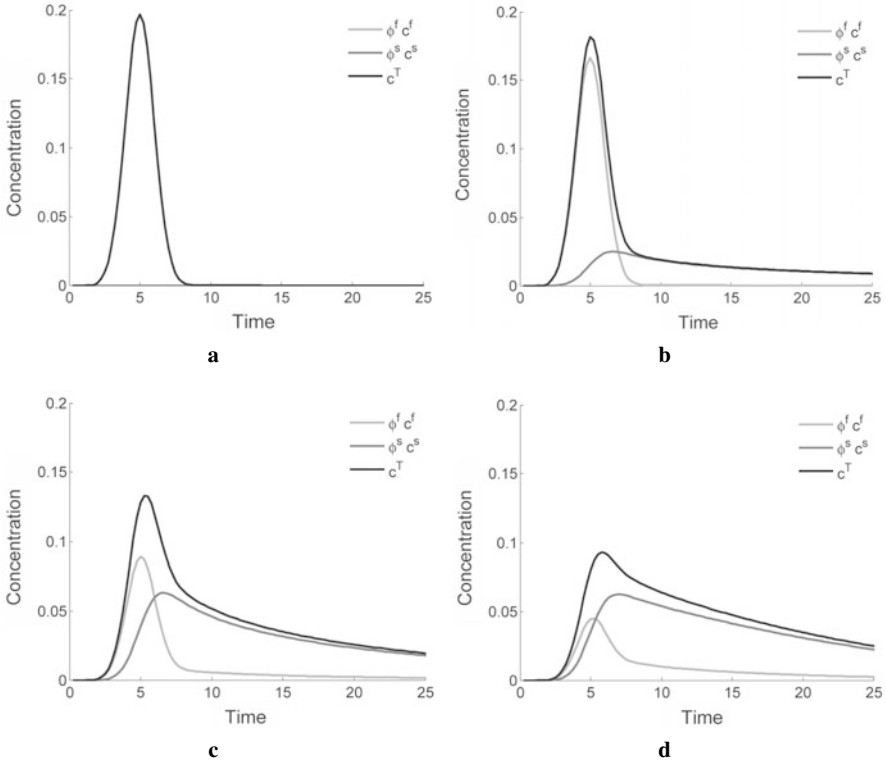


**Fig. 3.11.** Concentration time series data measured downstream from the c.a. injection point, for increasing values of  $Da$ . (a)  $Da = 0$ ; (b)  $Da = 0.1$ ; (c)  $Da = 0.5$ ; (d)  $Da = 1.0$ . Adapted from Cookson et al., 2014 [20]. Reproduced under the Creative Commons License 3.0 (<http://creativecommons.org/licenses/by/3.0/>)

the capillary walls is driven by the concentration difference between fluid and tissue, the c.a. enters the tissue much more quickly than it leaves.

#### Parameter Space Study

A common method for quantitatively estimating perfusion proposed in the clinical literature uses the signal upslope [4] as a key part of the calculation. This upslope is defined as the maximum positive temporal gradient of the time series at a given point (see Fig. 3.10). It is therefore useful to understand the potential variation of this quantity with changing parameter values in the model, and thereby assess the impact on this quantification technique.

Figure 3.12 shows the variation of perfusion signal properties with changing  $Da$  and  $Dr$ . These plots reveal a previously-unknown non-monotonic behaviour in both the peak concentration and upslope with respect to changes in  $Da$ . Parameter estimation suggests that contrast agents currently used for cardiac perfusion imaging lie in

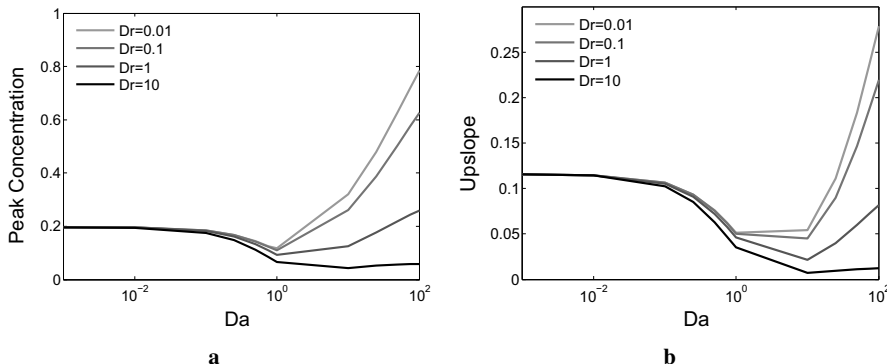


**Fig. 3.12.** Concentration signal properties display non-monotonic behaviour with respect to increases in  $Da$ , which means these properties alone are insufficient for use in parameter estimation. (a) Variation of peak concentration with  $Da$  and  $Dr$ ; (b) Variation of signal upslope with  $Da$  and  $Dr$ . Adapted from Cookson et al., 2014 [20]. Reproduced under the Creative Commons License 3.0 (<http://creativecommons.org/licenses/by/3.0/>)

the range of  $0.25 < Da < 2$ , indicating that this non-monotonic behaviour will be important for interpreting current perfusion images. Furthermore, within this estimated range, the signals are far more sensitive to changes in  $Da$  than they are in  $Dr$ .

Similar trends are observed when varying  $Pe$  and  $Da$ , while keeping the other parameters constant. As in Fig. 3.11, for fixed  $Pe$ , both signal properties display monotonic behaviour, with a minimum point at  $Da \approx 1$ . As  $Pe$  increases, both upslope and peak value increase, which is due to the reduced diffusion of the contrast agent bolus as it travels to the sampling point. Finally, both upslope and peak concentration are largely insensitive to the changes in porosity that might be expected to occur due to regional variation or tissue contraction during the cardiac cycle.

### Simulating Perfusion Images

Figure 3.13 shows the complete modelling framework with respect to its ability to represent a regional perfusion defect in the Darcy flow model, where the regional defect is defined based on the local vascular network in that area. This flow defect is then subsequently observable as an area of very low c.a. concentration in the transport model results. This 3D time-varying dataset can also be presented in the manner observed in clinical perfusion imaging, as in Fig. 3.14. This figure shows a set of three simulated imaging slices, with their locations along the heart long-axis marked. Clearly visible in the upper left portion of the slices is an area of dark blue, signifying low concentration of c.a. and therefore indicating a regional perfusion deficit.

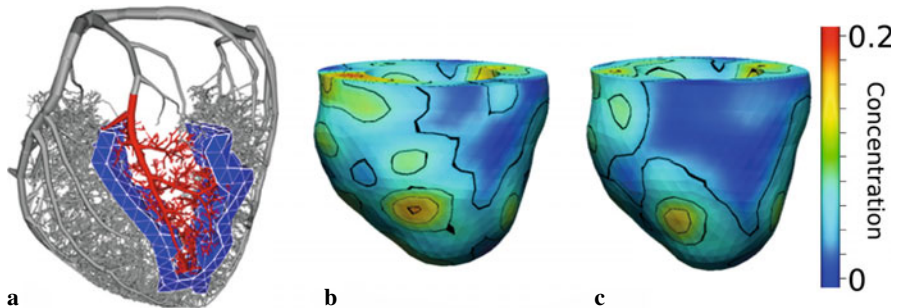


**Fig. 3.13.** (a) The cross-sectional area of the feeding artery of the red subtree was decreased by a factor of 0.7 to model stenosis of a branch of the coronary artery. Total concentration of contrast agent in the tissue 20 seconds after administering a bolus injection for a physiological case is shown in (b) and for the simulated occlusion of a coronary artery branch in (c). Adapted from Nolte et al. (2013) [72]

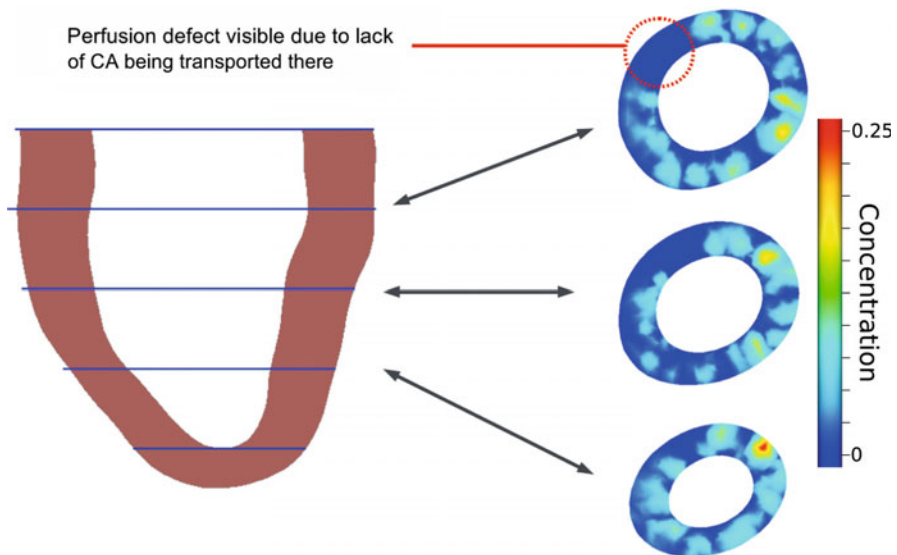


**Fig. 3.14.** A set of simulated perfusion images, taken at the three slice planes used in clinical imaging and using the non-dimensional form of the transport model. A perfusion defect is visible in the upper-left portion of the slices

### 3.5 Conclusions

In this chapter, we have presented a computational modelling framework coupling fluid and structure in order to simulate myocardial perfusion in a physiologically relevant manner. To this end we introduced a model of flow in macroscopic arteries, a multi-compartment Darcy model representing myocardial perfusion over

a range of vessel sizes and a poro-elastic model capturing the flow phenomena in the beating heart. The *in silico* obtained quantities – wave intensity and tissue signal in perfusion MRI, both of which represent the current state-of-the-art in invasive and non-invasive cardiological exams – create a basis for clinical translation of our work.

A key strength of wave intensity analysis in the coronary circulation is its ability to gauge the combined haemodynamic and mechanical function within a specific vascular territory and its associated myocardial region. Under the interventional clinical settings in which an acute coronary event must be managed with speed, WIA offers the potential to simplify the diagnostic procedure and improve its accuracy as recently demonstrated [26]. Despite these promises WIA is rarely, if at all, used in the current clinical landscape, one of the key reasons being that our understanding of the individual waves and their mechanistic origins is incomplete.

To this end we have approached the modelling of WIA via two complementary strategies representing the extremes of the clinical–physiological spectrum. The 1D model of the epicardial flow is oriented towards the real-time clinical usage, due to its reduced complexity, computational time and the amount data required to tune it. It aims to integrate the available *in vivo* patient data (simultaneous measurements of pressure and flow, and optionally the epicardial geometry and left ventricular pressure, if available) against the observed wave intensity characteristics to assess the impact of the disease on the distal and vessel mechanical parameters.

On the other hand, the poroelastic model provides a comprehensive framework with which to investigate the complex interaction between the aortic pressure, wave propagation and the myocardial contraction that underpins the change in the observed wave intensities. This approach facilitates investigations currently inaccessible to experimental means, due to the overwhelming complexity of aquiring such detailed measurements in the beating heart. Together with the 1D model, the combined approaches provide a tool for examination and interpretation of the clinically accessible invasive wave measurements.

In the perfusion MRI simulations we demonstrated the feasibility of coupling the porous medium flow model with advection-reaction-diffusion equations. In terms of validation and translation aspects, this capability to simulate the tracer-kinetic process underlying image formation is crucial to advancing the model into the realm of real-world relevance. The application of this work is primarily aimed at supporting the development of an optimal clinical non-invasive image acquisition protocol. Currently in perfusion MR imaging there are several open questions regarding the 2D vs 3D readout [50], spatio-temporal sampling resolution tradeoffs and the timing of data collection within the cardiac cycle [81]. While such investigations are generally tackled through direct population imaging studies, our integrated modelling framework has the capacity to contribute clarifications to these questions based on fundamental biophysical mechanisms. Further, the framework can be used to perform a parameter space exploration for the optimal design of imaging contrast agents, which is a costly and time-consuming exercise to undertake in the laboratory.

The added value of modelling in clinical practice lies in merging all patient information – beyond the qualitative intuition of the physician – and applying this integrated knowledge in the diagnosis and therapy planning. In this respect the next major challenge remaining in our clinical translation is the characterisation of the patient-specific parameters from clinical data. Of the various inverse estimation techniques available, the variational and sequential data assimilation approaches [16] have received particular recent interest in the cardiac community for image-based tuning of finite element models. To date, estimations of e.g. active [15, 48], passive [108, 109], electrical activation [22], myocardial fiber direction [70], vascular wall stiffness [9, 10] and aortic boundary tissue support parameters [66] have been reported. The application of such techniques to the models outlined in this chapter will reveal distal vascular parameters and porous permeability in a patient-specific manner. In concert with parallel efforts in the image analysis community on perfusion quantification [111] and associated emerging indices such as MRI gradientogram [39], the modelling framework will enable a comprehensive assessment of regional perfusion in ischaemic heart disease.

With an expanded scope for real-world applications, the critical urgency of model validation must be emphasised. Whereas an experimental validation aims to ensure the model accurately reproduces the targeted physical and physiological phenomena, clinical validation is equally important for ensuring that the model will perform robustly on larger patient cohorts in spite of statistical and practical variations. In cardiovascular modelling, although a number of experimental validations have been performed to date [9, 11, 69, 93], clinical validation of models is at present infrequently attempted.

A notable recent exemplar for translation has been achieved through an application of 3D CFD to predict FFR from CT angiography data ( $\text{FFR}_{\text{CT}}$ ), bypassing the need for invasive procedures. This analysis, available as a commercial service, has undergone three prospective multicentre trials to date and has begun to be received by the medical community as a disruptive technology with the potential to transform clinical practice [28]. The outcomes of the most recent trial indicate that  $\text{FFR}_{\text{CT}}$  is capable of providing comparable sensitivity ( $\text{FFR}_{\text{CT}}$  86% vs CTA 94%) and a marked increase in specificity ( $\text{FFR}_{\text{CT}}$  79% vs CTA 34%), as compared to using CTA alone [73].

A key strength of the  $\text{FFR}_{\text{CT}}$  approach therefore derives from its capacity to extrapolate physiological function from purely anatomical information through modelling. But on the other hand, such a task inevitably involves assumptions regarding model parameters, necessitating their estimation from typical group behaviour. Therefore it is likely that the current gap between the diagnostic accuracy of  $\text{FFR}_{\text{CT}}$  and the gold standard invasive FFR is engendered by the intrinsic physiological variability among the individual patients. Particularly with regards to the distal circulation, a recent meta-analysis of published CFVR-FFR measurements showed that on the whole the therapeutic action recommended by these two indices disagree around 40% of the time, reflecting a potentially serious consequence of neglecting the relative contributions of focal, diffuse and microvascular disease in a specific individual [51]. Replacing the generic assumptions on maximal vasodilation of the distal

bed, minimal resistance level and flow distribution parameters with individualised estimations could help to bridge this gap.

At present the experimental validation of our modelling framework is under way, utilising previously established platforms of perfusion phantoms [19] and animal models [84]. Furthermore, recent advances in coronary MR imaging [63] open the future prospect for high-resolution MR-based anatomical characterisation of stenosis geometry that can leverage the perfusion imaging considered in this work. While the clinical utility of the framework remains to be elucidated through future trials, our experience so far has reinforced our belief that a fundamentally interdisciplinary approach is essential in developing new and effective strategies of disease management. A sufficient understanding of the problem through collaboration across multiple disciplines, holds the key to generating a truly revolutionary approach for understanding and treating coronary disease.

**Acknowledgements** The authors acknowledge funding from the Engineering and Physical Sciences Research Council (EP/G0075727/2, EP/J013250/1, EP/H046410/1), the Centre of Excellence in Medical Engineering funded by the Wellcome Trust and EPSRC (WT 088641/Z/09/Z) and British Heart Foundation Centre of Research Excellence hosted at King's College London (BHF RE/08/003). This research was supported by the National Institute for Health Research (NIHR) Biomedical Research Centre at Guy's and St Thomas' NHS Foundation Trust and King's College London. The views expressed are those of the author(s) and not necessarily those of the NHS, the NIHR or the Department of Health.

## References

1. Aguado-Sierra, J., Parker, K., Davies, J., Francis, D., Hughes, A., Mayer, J.: Arterial pulse wave velocity in coronary arteries. EMBS Annual International Conference, pp. 867–870 (2006)
2. Ambrosi, D., Quarteroni, A., Rozza, G.: Modeling of Physiological Flows, Springer, Milan (2012)
3. Anrep, G.V., Saalfeld, E.V.: The effect of the cardiac contraction upon the coronary flow. *J. Physiol.* **79**(3), 31–331 (1933)
4. Aquaro, G.D., Todiere, G., Di Bella, G., Guiducci, L., Pingitore, A., Lionetti, V.: A fast and effective method of quantifying myocardial perfusion by magnetic resonance imaging. *Int. J. Cardiovasc. Imaging.* **29**(6), 1313–1324 (2013)
5. Barnard, A., Hunt, W., Timlake, W., Varley, E.: A theory of fluid flow in compliant tubes. *Biophysical Journal* **6**(6) (1966)
6. J. Bear. Dynamics of Fluids in Porous Media. Number 2. Courier Dover Publications, (Aug. 1972)
7. Beaudoin, A., Dreuzy, J.-R., Erhel, J.: An efficient parallel particle tracker for advection-diffusion simulations in heterogeneous porous media, in: Kermarrec, A.-M., Boug  , L., Priol, T. (eds.): Euro-Par 2007 Parallel Processing, Lecture Notes in Computer Science 4641, pp. 717–726, Springer, Berlin Heidelberg (2007)
8. Beller, G.A., Zaret, B.L.: Contributions of nuclear cardiology to diagnosis and prognosis of patients with coronary artery disease, *Circulation* **101**, 1465–1478 (2000)

9. Bertoglio, C., Barber, D., Gaddum, N., Valverde, I., Rutten, M., Beerbaum, P., Moireau, P., Hose, R., Gerbeau, J.-F.: Identification of artery wall stiffness: in vitro validation and in vivo results of a data assimilation procedure applied to a 3D fluid-structure interaction model. *J. Biomech.* **47**(5), 1027–1034 (2014)
10. Bertoglio, C., Moireau, P., Gerbeau, J.-F.: Sequential parameter estimation in fluid-structure problems. Application to hemodynamics. *Int. J. Num. Meth. Biomed. Eng.* **28**, 434–455 (2012)
11. Bessems, D., Giannopapa, C.G., Rutten, M.C.M., van de Vosse, F.N.: Experimental validation of a time-domain-based wave propagation model of blood flow in viscoelastic vessels. *J. Biomech.* **41**(2), 284–291 (2008)
12. Bishop, A.H., Samady, H.: Fractional flow reserve: Critical review of an important physiologic adjunct to angiography, *American Heart Journal* **147**(5), 792–802 (2004)
13. Bruinsma, P., Arts, T., Dankelman, J., Spaan, J.: Model of the coronary circulation based on pressure dependence of coronary resistance and compliance. *Basic Research in Cardiology* **83**(5), 510–524 (1988)
14. Caruel, M., Chabiniok, R., Moireau, P., Lecarpentier, Y., Chapelle, D.: Dimensional reductions of a cardiac model for effective validation and calibration, *Biomechanics and Modeling in Mechanobiology* (2013), in press
15. Chabiniok, R., Moireau, P., Lesault, P.-F., Rahmouni, A., Deux, J.-F., Chapelle, D.: Estimation of tissue contractility from cardiac cine-MRI using a biomechanical heart model, *Biomechanics and modeling in mechanobiology* **11**(5), 609–30 (2012)
16. Chapelle, D., Fragu, M., Mallet, V., Moireau, P.: Fundamental principles of data assimilation underlying the Verdandi library: applications to biophysical model personalization within euHeart, *Medical & Biological Engineering & Computing* (2013)
17. Chapelle, D., Gerbeau, J.-F., Sainte-Marie, J., Vignon-Clementel, I.: A poroelastic model valid in large strains with applications to perfusion in cardiac modeling, *Computational Mechanics* **46**(1), 91–101 (2010)
18. Chilian, W.M., Layne, S.M., Klausner, E.C., Eastham, C.L., Marcus, M.L.: Redistribution of coronary microvascular resistance produced by dipyridamole. *American Journal of Physiology – Heart and Circulatory Physiology* **256**, H383–H390 (1989)
19. Chiribiri, A., Schuster, A., Ishida, M., Hautvast, G., Zarinabad, N., Morton, G., Otton, J., Plein, S., Breeuwer, M., Batchelor, P., Schaeffter, T., Nagel, E.: Perfusion phantom: An efficient and reproducible method to simulate myocardial first-pass perfusion measurements with cardiovascular magnetic resonance, *Magnetic Resonance in Medicine* **69**(3), 698–707 (2013)
20. Cookson, A.N., Lee, J., Michler, C., Chabiniok, R., Hyde, E., Nordsletten, D., Smith, N.P.: A spatially-distributed computational model to quantify behaviour of contrast agents in MR perfusion imaging. *Medical Image Analysis*, (in review) (2013)
21. Cookson, A.N., Lee, J., Michler, C., Chabiniok, R., Hyde, E.R., Nordsletten, D.A., Sinclair, M., Siebes, M., Smith, N.P.: A novel porous mechanical framework for modelling the interaction between coronary perfusion and myocardial mechanics, *J. Biomech.* **45**(5), 850–855 (2012)
22. Corrado, C., Gerbeau, J., Moireau, P.: Identification of weakly coupled multiphysics problems. Application to the inverse problem of electrocardiology, *J. Computational Physics* (in review) (2014)
23. Coussy, O.: Mechanics of porous continua. Wiley (1995)
24. Coussy, O.: Poromechanics. Wiley (2004)

25. Davies, J.E., Whinnett, Z.I., Francis, D.P., Manisty, C.H., Aguado-Sierra, J., Willson, K., Foale, R., Malik, I.S., Hughes, A.D., Parker, K.H., Mayet, J.: Evidence of a dominant backward-propagating "suction" wave responsible for diastolic coronary filling in humans, attenuated in left ventricular hypertrophy, *Circulation*, **113**(14), 1768–78 (2006)
26. De Silva, K., Foster, P., Guilcher, A., Bandara, A., Jogiya, R., Lockie, T., Chowiencyzk, P., Nagel, E., Marber, M., Redwood, S., Plein, S., Perera, D.: Coronary Wave Energy: A Novel Predictor of Functional Recovery After Myocardial Infarction, *Circulation. Cardiovascular interventions* (March 2013)
27. Dormieux, L., Kondo, D., Ulm, F.-J.: *Microporomechanics*, Wiley (2004)
28. Escaned, J.: Imaging: Can FFRCT replace old indices of coronary stenosis severity? *Nature Reviews Cardiology* (2014)
29. Factor, S.M., Okun, E.M., Minase, T., Kirk, E.S.: The microcirculation of the human heart: end-capillary loops with discrete perfusion fields, *Circulation*, **66**(6), 1241–1248 (1982)
30. Federico, S., Grillo, A.: Elasticity and permeability of porous fibre-reinforced materials under large deformations, *Mechanics of Materials* **44**, 58–71 (2012)
31. Fischer, J.J., Samady, H., McPherson, J.A., Sarembock, I.J., Powers, E.R., Gimple, L.W., Ragosta, M.: Comparison between visual assessment and quantitative angiography versus fractional flow reserve for native coronary narrowings of moderate severity, *The American Journal of Cardiology* **90**, 210–215 (2002)
32. Fiss, D.M.: Normal coronary anatomy and anatomic variations, *Supplement to Applied Radiology*, pp. 14–26 (2007)
33. Formaggia, L., Lamponi, D., Quarteroni, A.: One-dimensional models for blood flow in arteries, *Journal of Engineering Mathematics* (2002)
34. Formaggia, L., Nobile, F., Quarteroni, A., Veneziani, A.: Multiscale modelling of the circulatory system: a preliminary analysis, *Computing and visualization in science* **2**(2–3), 75–83 (1999)
35. Formaggia, L., Quarteroni, A., Veneziani, A.: *Cardiovascular Mathematics: Modeling and simulation of the circulatory system*, Springer, Milan (2009)
36. Fulton, W.F.M.: Arterial anastomoses in the coronary circulation. i. anatomical features in normal and diseased hearts demonstrated by stereoarteriography, *Scottish Med. J.* **8**, 420–434 (1963)
37. Gould, K.L., Kirkeeide, R.L., Buchi, M.: Coronary flow reserve as a physiologic measure of stenosis severity, *JACC* **15**(2), 459–474 (1990)
38. Gregg, D.E., Green, H.D.: Registration and interpretation of normal phasic inflow into the left coronary artery by an improved differential manometric method, *Am. J. Physiol.* **130**, 114–125 (1940)
39. Hautvast, G.L.T.F., Chiribiri, A., Lockie, T., Breeuwer, M., Nagel, E., Plein, S.: Quantitative analysis of transmural gradients in myocardial perfusion magnetic resonance images. *Magnetic Resonance in Medicine* **66**, 1477–1487 (2011)
40. Helfant, R.H., Vokonas, P.S., Gorlin, R.: Functional importance of the human coronary collateral circulation, *New England Journal of Medicine* **284**(23), 1277–1281 (1971)
41. Holzapfel, G.A., Ogden, R.W.: Constitutive modelling of passive myocardium: a structurally based framework for material characterization, *Philosophical transactions. Series A, Mathematical, physical, and engineering sciences* **367**(1902), 3445–75 (2009)
42. Hsu, L.-Y., Kellman, P., Arai, A.E.: Nonlinear myocardial signal intensity correction improves quantification of contrast-enhanced first-pass MR perfusion in humans, *J. Magn. Reson. Imaging* **27**(4), 793–801 (2008)

43. Hughes, T.J., Lubliner, J.: On the one-dimensional theory of blood flow in the larger vessels (1973)
44. Huyghe, J.M., Arts, T., van Campen, D.H., Reneman, R.S.: Porous medium finite element model of the beating left ventricle, *American Journal of Physiology-Heart and Circulatory Physiology* **262**(4), H1256–H1267 (1992)
45. Huyghe, J.M., Van Campen, D.H.: Finite deformation theory of hierarchically arranged porous solids. I: Balance of mass and momentum, *International J. Engineering Science* **33**(13), 1861–1871 (1995)
46. Hyde, E.R., Cookson, A.N., Lee, J., Michler, C., Goyal, A., Sochi, T., Chabiniok, R., Sinclair, M., Nordsletten, D.A., Spaan, J., van den Wijngaard, J.P.H.M., Siebes, M., Smith, N.P.: Multi-Scale Parameterisation of a Myocardial Perfusion Model Using Whole-Organ Arterial Networks, *Annals of biomedical engineering* (Dec. 2013)
47. Hyde, E.R., Michler, C., Lee, J., Cookson, A.N., Chabiniok, R., Nordsletten, D.A., Smith, N.P.: Parameterisation of multi-scale continuum perfusion models from discrete vascular networks, *Med. Biol. Eng. Comput.* **51**(5), 557–570 (2013)
48. Imperiale, A., Chabiniok, R., Moireau, P., Chapelle, D.: Constitutive Parameter Estimation Using Tagged-MRI Data. In D.N. Metaxas and L. Axel, editors, *FIMH'11 – Sixth International Conference on Functional Imaging and Modeling of the Heart*, vol. 6666, pp. 409–417, Springer, New York (2011)
49. Ishida, M., Sakuma, H., Murashima, S., Nishida, J., Senga, M., Kobayasi, S., Takeda, K., Kato, N.: Absolute blood contrast concentration and blood signal saturation on myocardial perfusion MRI: Estimation from CT data, *J. Magnetic Resonance Imaging* **29**(1), 205–210 (2009)
50. Jogiya, R., Kozerke, S., Morton, G., De Silva, K., Redwood, S., Perera, D., Nagel, E., Plein, S.: Validation of dynamic 3-dimensional whole heart magnetic resonance myocardial perfusion imaging against fractional flow reserve for the detection of significant coronary artery disease, *JACC* **60**(5), 756–765 (2012)
51. Johnson, N.P., Kirkeeide, R.L., Gould, K.L.: Is discordance of coronary flow reserve and fractional flow reserve due to methodology or clinically relevant coronary pathophysiology? *JACC Cardiovasc Imaging* **5**(2), 193–202 (2012)
52. Judd, R.M., Levy, B.I.: Effects of barium-induced cardiac contraction on large- and small-vessel intramyocardial blood volume, *Circulation Research* **56**(3), 293–309 (1985)
53. Kajiyama, F., Tomonaga, G., Tsujioka, K., Ogasawara, Y., Nishihara, H.: Evaluation of local blood flow velocity in proximal and distal coronary arteries by laser Doppler method, *Journal of biomechanical engineering* **107**, 10–15 (1985)
54. Kassab, G.S.: Scaling laws of vascular trees: of form and function, *Am J Physiol.*, (2006) 290:H894–903
55. Kassab, G.S., Rider, C.A., Tang, N.J., Fung, Y.: Morphometry of pig coronary arterial trees. *Am. J. Physiol.* **265**, 350–365 (1993)
56. Kerckhoffs, R., Bovendeerd, P., Prinzen, F., Smits, K., Arts, T.: Intra-and interventricular asynchrony of electromechanics in the ventricularly paced heart, *J. Engineering Mathematics* **47**(3–4), 201–216 (2003)
57. Kim, H.J., Vignon-Clementel, I.E., Coogan, J.S., Figueroa, C.A., Jansen, K.E., Taylor, C.A.: Patient-specific modeling of blood flow and pressure in human coronary arteries, *Annals of Biomedical Engineering* **38**(10), 3195–209 (2010)
58. Lee, J., Cookson, A., Roy, I., Kerfoot, E., Asner, L., Vigueras, G., Sochi, T.: C. Michler, N. Smith, and D. Nordsletten. Cheart: A multi-physics parallel computing engine, in prep.

59. Lee, J., Nordsletten, D., Cookson, A., Rivolo, S., Smith, N.: In silico coronary wave intensity analysis: cardiac function to wave generating mechanisms, *J. Physiology*, in review
60. Lee, J., Smith, N.: Development and application of a one-dimensional blood flow model for microvascular networks. *Proceedings of the Institution of Mechanical Engineers, Part H, J. Engineering in Medicine* **222**, 487–511 (2008)
61. Lee, J., Smith, N.P.: The Multi-Scale Modelling of Coronary Blood Flow, *Annals of biomedical engineering* (May 2012)
62. Zamir, H.C.M.: Branching characteristics of human coronary arteries, *Can. J. Physiol. Pharmacol.* **64**, 661–668 (1986)
63. Makowski, M.R., Henningsson, M., Spuentrup, E., Kim, W.Y., Maintz, D., Manning, W., Botnar, R.: Characterization of coronary atherosclerosis by magnetic resonance imaging, *Circulation* **128**, 1244–1255 (2013)
64. Matthys, K.S., Alastrauey, J., Peiró, J., Khir, A.W., Segers, P., Verdonck, P.R., Parker, K.H., Sherwin, S.J.: Pulse wave propagation in a model human arterial network: assessment of 1-D numerical simulations against in vitro measurements, *J. biomechanics* **40**(15), 3476–86 (2007)
65. Meier, P., Gloekler, S., Zbinden, R., Beckh, S., de Marchi, S.F., Zbinden, S., Wustmann, K., Billinger, M., Vogel, R., Cook, S., Wenaweser, P., Togni, M., Windecker, S., Meier, B., Seiler, C.: Beneficial effect of recruitable collaterals a 10-year follow-up study in patients with stable coronary artery disease undergoing quantitative collateral measurements, *Circulation* **116**(9), 975–983 (2007)
66. Moireau, P., Bertoglio, C., Xiao, N., Figueiroa, C.A., Taylor, C., Chapelle, D., Gerbeau, J.-F.: Sequential identification of boundary support parameters in a fluid-structure vascular model using patient image data, *Biomechanics and Modeling in Mechanobiology* **12**(3), 475–496 (2012)
67. Murray, S.W., Rathore, S., Stables, R.H., Palmer, N.D.: Contemporary coronary imaging from patient to plaque – part 1: IVUS-derived virtual histology, *British J. Cardiology* **17**(3), 129–132 (2010)
68. Mynard, J.P., Nithiarasu, P.: A 1D arterial blood flow model incorporating ventricular pressure, aortic valve and regional coronary flow using the locally conservative Galerkin (LCG) method, *Communications In Numerical Methods In Engineering*, 367–417 (March 2008)
69. Mynard, J.P., Penny, D.J., Smolich, J.J.: Scalability and in-vivo validation of a multi-scale numerical model of the left coronary circulation, *American J. Physiology – Heart and Circulatory Physiology* (2013)
70. Nagler, A., Bertoglio, C., Gee, M., Wall, W.: Personalization of cardiac fiber orientations from image data using the unscented kalman filter. In S. Ourselin, D. Rueckert, and N. Smith, editors, *7th International Conference on Functional Imaging and Modeling of the Heart, FIMH 2013, Lecture Notes in Computer Science* 7945, pp. 132–140. Springer-Verlag, Berlin Heidelberg (2013)
71. Niederer, S.A., Plank, G., Chinchapatnam, P., Ginks, M., Lamata, P., Rhode, K.S., Rinaldi, C.A., Razavi, R., Smith, N.P.: Length-dependent tension in the failing heart and the efficacy of cardiac resynchronization therapy, *Cardiovascular Research* **89**(2), 336–343 (2011)

72. Nolte, F., Hyde, E.R., Rolandi, C., Lee, J., van Horssen, P., Asrress, K., van den Wijngaard, J.P.H.M., Cookson, A.N., van de Hoef, T., Chabiniok, R., Razavi, R., Michler, C., Hautvast, G.L.T.F., Piek, J.J., Breeuwer, M., Siebes, M., Nagel, E., Smith, N.P., Spaan, J.A.E.: Myocardial perfusion distribution and coronary arterial pressure and flow signals: clinical relevance in relation to multiscale modeling, a review, *Med. Biol. Eng. Comput.* **51**(11), 1271–1286 (2013)
73. Nørgaard, B.L., Leipsic, J., Gaur, S., Seneviratne, S., Ko, B.S., Ito, H., Jensen, J.M., Mauri, L., De Bruyne, B., Bezerra, H., et al.: Diagnostic performance of non-invasive fractional flow reserve derived from coronary ct angiography in suspected coronary artery disease: The NXT trial, *J. American College of Cardiology* (2014)
74. Obaid, D.R., Murray, S.W., Palmer, N.D., Rudd, J.H.F.: Contemporary coronary imaging from patient to plaque – part 3: cardiac computed tomography, *British J. Cardiology* **17**(5), 235–239 (2010)
75. Olufsen, M.: Structured tree outflow condition for blood flow in larger systemic arteries, *American J. Physiology – Heart and Circulatory Physiology* (1999)
76. Parker, K.H.: An introduction to wave intensity analysis, *Medical & biological engineering & computing* **47**(2), 175–88 (2009)
77. Pedley, T.J.: *The Fluid Mechanics of Large Blood Vessels* (1980)
78. Pijls, N.H., van Son, J.A., Kirkeeide, R.L., De Bruyne, Gould, K.L.: Experimental basis of determining maximum coronary, B., myocardial, and collateral blood flow by pressure measurements for assessing functional stenosis severity before and after percutaneous transluminal coronary angioplasty, *Circulation* **87**, 1354–1367 (1993)
79. Pindera, M.Z., Ding, H., Athavale, M.M., Chen, Z.: Accuracy of 1D microvascular flow models in the limit of low Reynolds numbers, *Microvascular research* **77**(3), 273–280 (2009)
80. Prinzen Bassingthwaite, J.B.: Blood flow distributions by microsphere deposition methods, F.W., *Cardiovascular Research* **45**, 13–21 (2000)
81. Radjenovic, A., Biglands, J.D., Larghat, A., Ridgway, J.P., Ball, S.G., Greenwood, J.P., Jerosch-Herold, M., Plein, S.: Estimates of systolic and diastolic myocardial blood flow by dynamic contrast-enhanced MRI, *Magnetic Resonance in Medicine* **64**, 1696–1703 (2010)
82. Rathore, S., Murray, S., Stables, R., Palmer, N.: From patient to plaque. contemporary coronary imaging, part 2: optical coherence tomography, *British J. Cardiology* **17**(4), 190–193 (2010)
83. Reymond, P., Merenda, F., Perren, F., Rüfenacht, D., Stergiopoulos, N.: Validation of a one-dimensional model of the systemic arterial tree, *American J. Physiology, Heart and circulatory physiology* **297**(1), H208–222 (2009)
84. Schuster, A., Grünwald, I., Chiribiri, A., Southworth, R., Ishida, M., Hay, G., Neumann, N., Morton, Perera, D., G., Schaeffter, T., Nagel, E.: An isolated perfused pig heart model for the development, validation and translation of novel cardiovascular magnetic resonance techniques, *J. Cardiovascular Magnetic Resonance* **12**(53) (2010)
85. Sherwin, S., Formaggia, L., Peiro, J.: Computational modelling of 1D blood flow with variable mechanical properties and its application to the simulation of wave propagation in the human arterial system, *International J. Numerical Methods in Fluids* **43**, 673–700 (2003)
86. Sherwin, S.J., Alastrauey, J., Parker, K.H., Peir, J.: Lumped Parameter Outflow Models for 1-D Blood Flow Simulations: Effect on Pulse Waves and Parameter Estimation, *Communications in Computational Physics* **4**(2), 317–336 (2008)

87. Sherwin, S.J., Franke, V., Peir, J., Parker, K.H.: One-dimensional modelling of a vascular network in space-time variables, *J. Engineering Mathematics* **47**, 217–250 (2003)
88. R. Shipley and S. Chapman. Multiscale modelling of fluid and drug transport in vascular tumours, *Bulletin of Mathematical Biology* **72**(6), 1464–1491 (2010)
89. Smith, N.P., Pullan, A.J., Hunter, P.J.: An Anatomically Based Model of Transient Coronary Blood Flow in the Heart, *SIAM J. Applied Mathematics* **62**(3), 990 (2002)
90. Spaan, J.A.E.: Coronary diastolic pressure-flow relation and zero flow pressure explained on the basis of intramyocardial compliance, *Circulation Research* **56**(3), 293–309 (1985)
91. Spaan, J.A.E., Kolyva, C., van den Wijngaard, J.P.H.M., ter Wee, R., van Horssen, P., Piek, J.J., Siebes, M.: Coronary structure and perfusion in health and disease. *Philosophical transactions, Series A, Mathematical, physical, and engineering sciences* **366**(1878), 3137–53 (2008)
92. Spaan, J.A.E., Siebes, M., Wee, R., Kolyva, C., Vink, H., Fokkema, D.S., Streekstra, G., Vanbavel, E.: Visualisation of intramural coronary vasculature by an imaging cryomicrotome suggests compartmentalisation of myocardial perfusion areas, *Med. Biol. Eng. Comput.* **43**, 43–435 (2005)
93. Steele, B.N., Wan, J., Ku, J.P., Hughes, T.J.R., Taylor, C.A.: In vivo validation of a one-dimensional finite-element method for predicting blood flow in cardiovascular bypass grafts, *IEEE Trans. Biomed. Eng.* **50**(6), 649–656 (2003)
94. Stettler, J., Niederer, P., Anliker, M.: Theoretical analysis of arterial hemodynamics including the influence of bifurcations, *Annals of Biomedical Engineering* **9**(2), 145–164 (1981)
95. Taylor, C.A., Steinman, D.A.: Image-based modeling of blood flow and vessel wall dynamics: applications, methods and future directions, *Annals of Biomedical Engineering* **38**(3), 1188–1203 (2010)
96. Topol, J.E., Nissen, S.E.: Our preoccupation with coronary luminology, *Circulation* **92**, 2333–2342 (1995)
97. Toyota, E., Ogasawara, Y., Hiramatsu, O., Tachibana, H., Kajiya, F., Yamamori, S., Chilian, W.M.: Dynamics of flow velocities in endocardial and epicardial coronary arterioles, *American Journal of Physiology-Heart and Circulatory Physiology* **57**(4), H1598 (2005)
98. Traupe, T., Gloekler, S., de Marchi, S.F., Werner, G.S., Seiler, C.: Assessment of the human coronary collateral circulation, *Circulation* **122**(12), 1210–1220 (2010)
99. van de Vosse, F.N., Stergiopoulos, N.: Pulse Wave Propagation in the Arterial Tree, *Annual Review of Fluid Mechanics* **43**(1), 467–499 (2011)
100. van den Wijngaard, J.P.H.M., van Horssen, P., ter Wee, R., Coronel, R., de Bakker, J.M., de Jonge, N., Siebes, M., Spaan, J.A.E.: Organization and collateralization of a subendocardial plexus in end-stage human heart failure, *American J. Physiology – Heart and circulatory physiology* **298**(1), H158–62 (2010)
101. Vankan, W., Huyghe, J., Janssen, J.: Poroelasticity of saturated solids with an application to blood perfusion, *Int. J. Eng. Sci.* **34**(9), 1019–1031 (1996)
102. Vankan, W.J., Huyghe, J.M., Janssen, J.D., Huson, A., Schreiner, W.: Finite element blood flow through biological tissue, *Int. J. Engng. Sci.* **35**(4), 375–385 (1997)
103. Vignon, I., Taylor, C.: Outflow boundary conditions for one-dimensional finite element modeling of blood flow and pressure waves in arteries, *Wave Motion* **39**(4), 361–374 (2004)

104. Werner, G.S., Ferrari, M., Heinke, S., Kuethe, F., Surber, R., Richartz, B.M., Figulla, H.R.: Angiographic assessment of collateral connections in comparison with invasively determined collateral function in chronic coronary occlusions, *Circulation* **107**(15), 1972–1977 (2003)
105. Westerhof, N., Boer, C., Lamberts, R., Sipkema, P.: Cross-talk between cardiac muscle and coronary vasculature, *Physiol. Rev.* **86**, 1263–1308 (2006)
106. Westerhof, N., Lankhaar, J.-W., Westerhof, B.: The arterial windkessel, *Medical & Biological Engineering & Computing* **47**(2), 131–141 (2009)
107. Willemet, M., Lacroix, V., Marchandise, E.: Inlet boundary conditions for blood flow simulations in truncated arterial networks, *J. Biomechanics* **44**(5), 897–903 (2011)
108. Xi, J., Lamata, P., Lee, J., Moireau, P., Chapelle, D., Smith, N.: Myocardial transversely isotropic material parameter estimation from in-silico measurements based on reduced-order unscented Kalman filter, *J. mechanical behavior of biomedical materials* **4**(7), 1090–1102 (2011)
109. Xi, J., Lamata, P., Shi, W., Niederer, S., Land, S., Rueckert, D., Duckett, S.G., Shetty, A.K., Rinaldi, C.A., Razavi, R., Smith, N.: An Automatic Data Assimilation Framework for Patient-Specific Myocardial Mechanical Parameter Estimation, in: Metaxas, D.N., Axel, L. (eds.), *FIMH'11 – Sixth International Conference on Functional Imaging and Modeling of the Heart*, vol. 6666, pp. 392–400, Springer, New York (2011)
110. Zamir, M.: Cost analysis of arterial branching in the cardiovascular systems of man and animals, *J. Theor. Biol.* **120**, 111–23 (1986)
111. Zarinabad, N., Chiribiri, A., Breeuwer, M.: Myocardial blood flow quantification from MRI – an image analysis perspective, *Current Cardiovascular Imaging Reports* **7**(1), 1–9 (2014)

---

# Using Image-based CFD to Investigate the Intracardiac Turbulence

Christophe Chnafa, Simon Mendez, Ramiro Moreno and Franck Nicoud

**Abstract** A numerical framework designed to compute the blood flow in patient-specific human hearts is presented. The geometry of the heart cavities and associated wall motion are extracted from 4D medical images while the valves of the heart are accounted for thanks to low order geometrical models. The resulting blood flow equations are solved using a fourth-order low-dissipative finite-volume scheme and a mixed Arbitrary Lagrangian-Eulerian / Immersed Boundary framework. On top of retrieving the main fluid flow phenomena commonly observed in the left heart, the methodology allows studying the heart flow dynamics, including the turbulence characteristics and cycle-to-cycle variations.

## 4.1 Introduction

Heart pathologies are closely related to intracardiac hemodynamics. Recent technological innovations in imaging techniques have provided valuable opportunities for direct non-invasive *in vivo* assessment of hemodynamics. Blood flow velocities can be measured *in vivo* using phase-contrast magnetic resonance imaging (PC-MRI) or by echocardiography techniques.

PC-MRI studies have contributed to the understanding of the main hemodynamic features [10, 18, 25]. Although very comprehensive, the PC-MRI velocity mapping

---

C. Chnafa (✉) · S. Mendez

I3M UMR 5149, University Montpellier II, France

e-mail: christophe.chnafa@univ-montp2.fr; simon.mendez@univ-montp2.fr

R. Moreno

Radiology Department, CHU of Rangueil, France

e-mail: moreno.r@chu-toulouse.fr

F. Nicoud

I3M, UMR 5149, University Montpellier II, France

e-mail: franck.nicoud@univ-montp2.fr

is not real-time. Hence, beat-to-beat variations in the flow cannot be recorded (the k-space is filled over many cardiac cycles). Moreover, PC-MRI suffers from a relatively low spatio-temporal resolution, precluding the observation of small scales and fast time-varying flow features [15].

Echocardiography techniques [11, 19], with higher spatio-temporal resolution make an alternative to PC-MRI. However, they only give access to velocity components directed towards or away from the ultrasonic beam, while one would want to measure the full 3D flow vectors. Nevertheless, investigations have been conducted on normal and abnormal hearts and interesting potential indicators of cardiac health hemodynamics arose [4, 13, 16].

With the development of these cardiac imaging techniques, patient-specific geometries have been progressively used in computational fluid dynamics (CFD) [5, 21, 28, 30, 42, 44]. Realistic heart wall movements on the basis of cine MRI or Computed Tomography (CT) scan data can be used: heart movement is prescribed from the patient-specific medical images, which can be acquired using standard clinical imaging procedures, instead of being computed. This strategy allows computation of the patient-specific hemodynamics and provides detailed insights into the cardiac flow field, providing potentially valuable clinical information. If the feasibility of this kind of approach has been shown, the results usually suffer from limited spatial resolution, partial geometry (only the left ventricle (LV) is considered in most cases) or numerical limitations (dissipative schemes). Besides, except in a few experimental works [7, 41], cycle-to-cycle variations in the heart flow is an issue that is rarely dealt with.

In the present work, an image-based CFD method developed to compute flows in aortas [29] is extended to compute intracardiac flows. Medical images are used to generate a moving patient-specific domain, in which the blood flow equations are solved. Heart geometry movements are generated from a 4D sequence (MRI or CT scan images) treated by an appropriate image registration algorithm [35]. A specific attention is paid to the generation of a high-quality mesh which deforms consistently with the heart motion. This allows solving the flow equations with an essentially non-dissipative scheme compatible with the description of unsteady turbulent flows by Large Eddy Simulation. In order to demonstrate the ability of the method to compute heart flows, application to a complete human left heart described by ECG-gated 3D CT scan images is presented. The resulting flow is described, emphasizing the flow characteristics usually reported in the literature. Characteristics of the cycle-to-cycle variations are also reported.

The numerical method is detailed in Sect. 4.2. The characteristics of the applied case is presented in Sect. 4.3 and the flow field obtained is described in Sect. 4.4. Concluding remarks are given in Sect. 4.5.

## 4.2 Methodology

The present computational method approaches couples an Arbitrary-Lagrangian Eulerian framework with an immersed boundary method in order to represent the blood flow within the moving endocardium while accounting for the heart valves motion. This section describes the flow solver and the treatment of the medical images needed to perform the computations.

### 4.2.1 Fluid Problem

Blood is an incompressible, non-Newtonian fluid [9]. However, in large vessels, non-Newtonian effects are usually neglected in numerical simulations [30, 46] and constant kinematic viscosity  $\nu$  is assumed in this paper. Note however that the present numerical method could be applied to non-Newtonian fluids.

The flow is thus governed by the incompressible Navier-Stokes equations (NSE), over a moving domain  $\Omega_f(t) \subset \mathbf{R}^3$  of boundary  $\partial\Omega_f(t)$ . The Arbitrary Lagrangian Eulerian (ALE) framework [8] is used in order to account for the computational domain deformation over time. Introducing the pointwise computational domain velocity  $\mathbf{u}_g$ , the NSE read:

$$\left. \begin{aligned} \frac{d\mathbf{u}}{dt} + ((\mathbf{u} - \mathbf{u}_g) \cdot \nabla) \mathbf{u} &= -\frac{1}{\rho} \nabla p + \nu \nabla^2 \mathbf{u} + \mathbf{f} \\ \nabla \cdot \mathbf{u} &= 0, \end{aligned} \right\} \quad \text{on } \Omega_f(t) \quad (4.1)$$

where  $\mathbf{u}$  is the fluid velocity,  $p$  is the pressure,  $\rho$  the density and  $\mathbf{f}$  a force per mass unit. Note that the time derivative denotes an ALE time derivative [8]. At the boundary of the computational domain, no-slip conditions are applied on walls ( $\mathbf{u} = \mathbf{u}_g$ ) and Dirichlet conditions are applied over the inlet boundaries.

These equations are implemented in the flow solver YALES2BIO ([www.math.univ-montp2.fr/~yales2bio](http://www.math.univ-montp2.fr/~yales2bio)) [27], developed from the massively parallel finite-volume flow solver YALES2 [34]. At each time step, the grid velocity  $\mathbf{u}_g$  at each node of the computational domain is calculated (see next section). A projection method is used to solve the NSE: the momentum equation is first advanced using the fourth-order Runge-Kutta time-advancement scheme. Fluxes are discretized with a 4th-order central scheme. Any forcing term coming from immersed boundaries is accounted for in this prediction step. At the end of the prediction step, the grid reaches the final position of the time step. Hence, the projection step to calculate pressure is performed over a fixed grid. A Deflated Preconditioned Conjugate Gradient algorithm is used to solve the Poisson equation [24] involved in the projection step. Note that due to the transitional nature of the flow, Reynolds Averaged Navier-Stokes (RANS) approaches for modelling turbulence (e.g.  $k-\varepsilon$ ,  $k-\omega$  models, etc) are not appropriate since they rely on the assumption that turbulence is fully developed and ergodic. Even if adaptations have been proposed in order to handle transition, they essentially require the user to prescribe the transition location in advance. Instead, in the present study, the Large Eddy Simulation approach is followed, taking advantage

of the low-dissipative scheme of integration used in YALES2BIO. In this view, only the smallest scales are modelled (scales smaller than the mesh size) while the evolution of the large scales is computed by solving a filtered version of NSE [33, 39, 43]. In the latter, a subgrid-scale model must be used in order to account for the effect of the unresolved scales on the dynamics of the resolved ones. This is usually done by an eddy-viscosity-based model [45]. In the present study, where the flow is strongly confined and piloted by the wall motions, an advanced subgrid scale model able to represent the proper turbulence damping near solid walls was used [36] as well as a well established formulation based on the dynamic procedure of Germano [12].

## 4.2.2 Computational Domain

### 4.2.2.1 Extraction of the Heart Deformation

Determining the movement of the computational domain, where the NSE are solved is all but an easy task. One solution is to compute the deformations of the boundary thanks to a full electrical-fluid-structure interaction solver. Unfortunately, there are many uncertainties regarding the constitutive laws (both mechanical and electrical) of the heart muscle as well as the external constraints the heart is submitted to. Moreover, accurate heart models are still under development today [47] as well as robust numerical method to solve them. A way of bypassing this issue is to extract the computational heart grid from 4D (3D + time) patient medical images. The following question must then be addressed: given several 3D images of a heart taken at different times in the heart cycle, how to extract the heart deformations from these images and how to deform a patient-specific grid accordingly? The first part of the question is actually a classical “image registration” problem.

Nowadays, there is a growing interest in the development of cardiac image registration methods [23]. Given two cardiac images, a *template* and a *reference* one, a transformation is determined to map the *template* image to the *reference* image. The deformation field can notably provide clinical information on the myocardial contractile function. Here, the same process is used to compute the heart deformations, but instead of focusing on functional data of the heart muscle, the computed deformation is used to extract patient-specific boundary conditions for the blood flow computation.

Among many registration algorithms [22, 31], voxel similarity measure techniques were preferred. This class of method operates directly on the image grey values, providing a flexible algorithm suitable for the complex heart movements.

In the present case,  $N$  3D images  $I_i$  of a patient heart are taken at different times  $t_i$ ,  $0 \leq t_0, t_1, \dots, t_{N-1} < T$  during the heart cycle of period  $T$ . One of the  $N$  images is selected as a *template* image. Note that this choice is somewhat arbitrary and that, without loss of generality, one can always tune the time origin so that the *template* corresponds to the  $I_0$  image at time  $t_0$ . From this image,  $N - 1$  transformations  $\psi_i$  are computed such that the transformed *template* image becomes similar to images  $I_i$  ( $i$  between 1 and  $N - 1$ ) successively considered as the *reference* image: transformation

$\psi_i$  is searched so that  $I_0(\psi_i(\mathbf{x})) = I_i(\mathbf{x})$  for each voxel. Here,  $I_i(\mathbf{x})$  stands for the voxel grey-level value at position  $\mathbf{x}$  in the  $i$ -th 3D discrete image.

Each  $\psi_i$  is calculated by minimizing the distance between  $I_0(\psi_i(\mathbf{x}))$  and  $I_i(\mathbf{x})$ , an appropriate distance measure being based on the so-called sum of squared differences. The transformation  $\psi_i$  is computed through an optimisation problem reading: given two images  $I_0$  and  $I_i$ , find a mapping  $\psi_i$  such that the squared intensity differences between  $I_0(\psi_i(\mathbf{x}))$  and  $I_i(\mathbf{x})$  is minimized for each voxel. The number of parameters describing the transformation is too high so that the solution  $\psi_i$  of this problem is not unique. Additional constraints are needed to compute the mapping  $\psi_i$ .

In the present work, a constraint on  $\psi_i$  is applied thanks to prior knowledge of the deformation sought [2]. The idea is to penalize unlikely deformations by imposing the heart deformations to be smooth. Bayesian statistics are used to obtain an *a posteriori* computation of the deformation field. The prior deformation probability is incorporated through the Bayes' theorem:  $p(\mathbf{Y}|\mathbf{I}) \propto p(\mathbf{I}|\mathbf{Y})p(\mathbf{Y})$ , where  $p(\mathbf{I}|\mathbf{Y})$  is the likelihood of observing the images data  $\mathbf{I}$  (*template*  $I_0$  and *reference*  $I_i$  images) given the deformation parameters  $\mathbf{Y}$ .  $p(\mathbf{Y})$  is the prior knowledge of the deformation translated in the *a priori* probability of seeing the parameters  $\mathbf{Y}$  and  $p(\mathbf{Y}|\mathbf{I})$  is the *a posteriori* probability of getting  $\mathbf{Y}$  knowing the two images data  $\mathbf{I}$ . Using this Bayesian framework, the goal is to maximise the probability  $p(\mathbf{Y}|\mathbf{I})$ . Knowing that a probability is related to its Gibbs form by  $p(\mathbf{Y}) \propto e^{-H(\mathbf{Y})}$ , the problem can be seen as a minimisation of the Gibbs potential:

$$H(\mathbf{Y}|\mathbf{I}) = H(\mathbf{I}|\mathbf{Y}) + H(\mathbf{Y}) + c, \quad (4.2)$$

where  $c$  is a constant. The likelihood potential  $H(\mathbf{I}|\mathbf{Y})$  of observing the images data given the deformation parameters  $\mathbf{Y}$  is directly linked to the squared intensity difference between  $I_0(\psi_i(\mathbf{x}))$  and  $I_i(\mathbf{x})$  for each voxel:

$$H(\mathbf{I}|\mathbf{Y}) = \frac{1}{2} \int_{\Omega} (I_0(\psi_i(\mathbf{x})) - I_i(\mathbf{x}))^2 d\Omega, \quad (4.3)$$

where the integral is taken over the image volume  $\Omega$ .

The second term  $H(\mathbf{Y})$  in the right hand side of Eq. (4.2) is the wanted constraint, applied thanks to prior knowledge. The prior deformation knowledge put in this potential is expressed as a geometrical constraint on the mapping through the two studied images. A suitable prior probability is linked to the deformation of each voxel of the *template* image and to the reverse deformation [1]. This potential acting as a regularization term allows a penalization based on the Jacobian of the local deformations  $J$ . A detailed description of this term can be found in [1].

This regularization term is weighted by a parameter  $\lambda$  linked to the belief in the amount of deformation of the heart. A high value of the  $\lambda$  parameter results in a high penalty on the voxels deformation, hence only small and smooth deformations are allowed. Given the high deformation of the left heart, high  $\lambda$  values result in partial deformation and a high residual squared difference between the *template* image and the *reference* one. In the case of small values of  $\lambda$ , a lower residual squared difference will be reached, but the resulting deformation can be non physical due to

excessive warping. Actually, the variability of heart movements is highly different from one region to the other. The aorta needs high values of  $\lambda$ , whereas small values are needed for the atrium or the ventricle.

One method of increasing the likelihood of achieving a good solution without introducing a spatial variability on  $\lambda$  (and consequently avoiding more operator-dependant work as well) is to apply successive filters to the images using a Gaussian smoothing convolution kernel  $\mathcal{G}^\sigma$  of width  $\sigma$ . High-frequency information of the image is removed thanks to this filter then gradually re-introduced as the kernel width  $\sigma$  becomes smaller and smaller. This iterative process is defined as the *outer* iterations: for each kernel width, distance between the images are minimized. This "coarse-to-fine" strategy has the effect of making the registration algorithm estimate the most global deformations during the first *outer* iteration, leaving out fine-scale structures. The optimum transformation for this kernel width is used to initialize the computation of the next optimum computation, which deals with finer details. This method increases the likelihood of finding the globally optimal match while avoiding the classical problem of the intensity-based method: their susceptibility to poor starting estimates.

As the regularization term, the intensity difference (first term  $H(\mathbf{I}|\mathbf{Y})$  in the right hand side of the Eq. (4.2)) is weighted. The weight for the  $j$ -th *inner* iteration is defined as the inverse of the residual sum of the squared differences computed at the previous *inner* iteration of a given *outer* iteration of the algorithm and is denoted by  $\frac{1}{d^{j-1}}$ . Because  $d$  has a high value for the first iterations, more weight is given to the regularization term, in order to get smooth deformations. As the algorithm gets close to the final solution,  $d$  theoretically tends to zero, giving less weight to the priors and letting the algorithm computing more detailed deformations.

Finally, the sought transformation  $\psi_i^{j,k}$  at the *inner* iteration  $j$  and the *outer* iteration  $k$  minimizes the function  $f^{j,k}$  defined as:

$$f_1^{j,k}(\psi_i^{j,k}) = \frac{1}{2d^{j-1}} \int_{\Omega} ([\mathcal{G}^{\sigma^k} * I_0](\psi_i^{j,k}(\mathbf{x})) - [\mathcal{G}^{\sigma^k} * I_i](\mathbf{x}))^2 d\Omega, \quad (4.4)$$

$$f_2^{j,k}(\psi_i^{j,k}) = g(J(\psi_i^{j,k})), \quad (4.5)$$

$$f^{j,k}(\psi_i^{j,k}) = f_1^{j,k}(\psi_i^{j,k}) + \lambda f_2^{j,k}(\psi_i^{j,k}), \quad (4.6)$$

where the function  $g$  is computed from the Jacobian singular values and determinant [2]. Finally the  $N - 1$  deformations are computed through this iterative optimisation process. This approach was successfully applied before to large vessels as the aorta cross [29].

#### 4.2.2.2 Patient-specific Computational Grid and Application of the Patient-specific Deformation

Once the  $N - 1$  mappings  $\psi_i$  are computed, a patient-specific computational grid must be extracted from the *template* image and warped thanks to the computed deformations. The *template* image corresponding to volumetric data  $I_0$  is imported into

an image processing software (ScanIP; Simpleware Ltd., Exeter, UK). Before segmentation, the image  $I_0$  is prepared: the region of interest is isolated and the image is smoothed to erase noise inherent to the medical images protocols. The segmentation itself is done by a classical thresholding method [38]. A suitable image intensity range which encompasses the voxel intensities of the region occupied by blood in the heart is selected. The quality of the segmentation relies on the operator's skills and knowledge of the human heart morphology and the quality of the chosen medical image. Image resolution plays a role in the potential domain simplification at this step. Trabeculae, left atrial appendage or papillary muscles can either be kept or neglected depending on the image quality and spatial resolution available. The 3D geometric reconstruction covers all the space occupied by blood in the left heart cavities. The surface of the geometric reconstruction of the heart is triangulated.

Once a *template* 3D patient-specific surface mesh is created, a procedure to deform this surface model thanks to the images must be provided. For each couple of images  $(I_0, I_i)$  a suitable spatial transformation  $\psi_i$  was found thanks to the method described in the previous section. These deformations  $\psi_i$  are 3D deformation fields. Trilinear interpolation from these deformation fields to the *template* surface mesh is done. Thus, a set of  $N - 1$  successive surface meshes matching the physiological cardiac images at different times  $t_i$  is produced as schematized in Fig. 4.1.

Position and velocity of all surface points are needed at any discrete time of the simulation, not only at the times  $t_0, t_1, \dots, t_{N-1}$ . Since all the generated surface meshes share the same topology (number and connection between nodes, number of cells), interpolation is used to compute the position of each node and the velocity by taking the time derivative of this quantity. As geometry variations are periodic, a trigonometric interpolation is used. The surface position and velocities read:

$$\left. \begin{aligned} \mathbf{x}_s(t) &= \sum_{i=0}^m [a_i \cos(2i\pi \frac{t}{T}) + b_i \sin(2i\pi \frac{t}{T})], \\ \mathbf{u}_s(t) &= \frac{2i\pi}{T} \sum_{i=1}^m [-a_i \sin(2i\pi \frac{t}{T}) + b_i \cos(2i\pi \frac{t}{T})], \end{aligned} \right\} \quad \text{on } \partial\Omega_f(t) \quad (4.7)$$

where  $T$  is the heart cycle period,  $m$  the number of Fourier modes ( $m = \frac{N-1}{2}$  or  $\frac{N}{2}$  depending on the parity of  $N$ ) and  $a_i, b_i$  the Fourier coefficients. Surface velocity  $\mathbf{u}_s$  needed at the computation domain boundary  $\partial\Omega_f(t)$  is hence not computed as a FSI problem, but entirely extracted from the medical images. In the present study, it is used to handle the cardiac chambers and their connected vessels.

The *template* surface is imported in a commercial mesher (Gambit, ANSYS) to generate a *template* unstructured tetrahedral mesh. The computed boundary Fourier coefficients of Eq. (4.7) are interpolated in this *template* numerical domain. The computational mesh boundary now follows the shape of the patient endocardium and is updated in every step of the simulation. Motion of all internal points in the computational mesh is based on the prescribed boundary motion. At each iteration, nodal velocity  $\mathbf{u}_g$  is calculated through the computation of a Laplace equation [26] using the prescribed boundary motion as boundary condition for this problem.

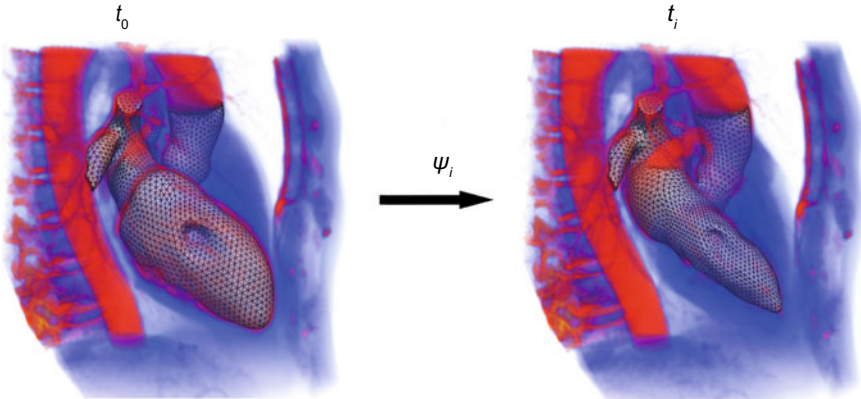


**Fig. 4.1.** Mesh deformation procedure applied to a left human heart. The *template* mesh segmented from the image at time  $t_0$  is deformed thanks to  $\psi_i$  to obtain the mesh at time  $t_i$ . This procedure is done for each image in the cardiac cycle in order to obtain the corresponding meshes

The grid quality is monitored during the simulations. When the boundary displacement becomes too large compared to the local cell sizes, the cell quality can be highly deteriorated. This can lead to convergence problems or negative cell volumes. In this case, the numerical domain is re-meshed, Fourier coefficients are interpolated on this new discretized surface domain, as is the fluid solution at the new internal nodes.

#### 4.2.3 Valves

Given their spatio-temporal resolution, MRI and CT scans fail to provide the necessary information to characterize precisely the movements of the aortic (AV) and of the mitral (MV) valves. Their geometry and movement have thus to be modelled. Accounting for the moving valves with the ALE method would be extremely complex due to grid quality issues. Here, an immersed boundary technique is used instead. A body force is imposed to drive the flow velocity to zero where the valves are located [3].

The opening and closing valve time is generally small (of the order of 5% of the heart cycle [48]). As a first modelling effort, it has been considered that valves open and close instantaneously, following the evolution of the ventricle volume. Systole lasts as long as the ventricle volume decreases. During systole, the AV is open and the MV closed. Diastole is defined as the heart period during which the ventricle volume increases: then, the AV is closed and the MV open.

Valve reconstruction starts with the definition of the valves annuli. Their geometry is reconstructed by inspecting the medical images. A number of markers are placed manually to define the valve annuli at a given time. The motion of these markers is then obtained thanks to the Fourier coefficient defining the boundary motion (Eq. (4.7)).

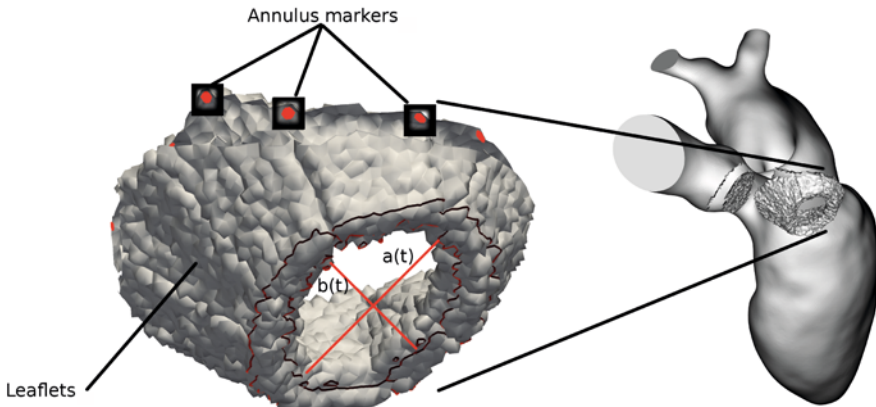


**Fig. 4.2.** *Left plot:* annulus markers and grid cells where a body force is added to model the MV leaflets. Diameters  $a(t)$  and  $b(t)$  of the elliptic opening are indicated. *Right plot:* full MV model included in the numerical domain (the AV is represented as well)

As the focus is on the flow in the atrium and in the ventricle, the aortic valve is modelled very simply. Physiologically, the leaflets of the aortic valve are pushed against the vessel, offering small resistance to the flow. Hence, when the aortic valve is open, no immersed force is applied: aortic valve is only active when closed.

The mitral valve is represented by a more complex model, since its shape is expected to strongly impact the LV haemodynamics. The position of the mitral valve annulus being known over time, the mitral valve opening is defined using an ad hoc model. From visual inspection of the images, parameters as the average leaflets length, the orientation of the valve opening and an ellipse defining the opening area are imposed. Details of the procedure are described in Chnafa et al. [3].

Knowing the MV leaflets position during the heart cycle, their effect on the blood flow is accounted for by using an immersed boundary method (IBM) [32]. For this purpose, the leaflets representations are given a thickness so that a few mesh nodes are located within the valves. Then, the force  $\mathbf{f}$  in the NS Eqs. (4.1) is set to impose the fluid velocity to zero within the leaflets. Figure 4.2 shows an example of the valves models during diastole, when the MV is open.

#### 4.2.4 Inlet Boundary Conditions

Inlet boundary conditions at the pulmonary veins must be provided. Under the present assumptions, either the aortic valve or the mitral valve is closed. Pulmonary veins thus always inject blood in a closed domain. As a consequence, blood being incompressible, the total mass flow rate entering the domain is entirely determined by the mass conservation constraint. With  $Q_{PV}(t)$  denoting the inlet flow rate (sum of the volumetric flow rates at the four pulmonary veins) and  $V_{LA}$ ,  $V_{LV}$  and  $V_{AO}$  denoting

respectively the LA, LV and the aortic root volumes, mass conservation yields:

$$Q_{PV}(t) = \begin{cases} \frac{dV_{LA}}{dt} & \text{during systole} \\ \frac{dV_{LA}}{dt} + \frac{dV_{LV}}{dt} & \text{during diastole.} \end{cases} \quad (4.8)$$

Uniform velocity profile are imposed at each inlet condition. With  $\mathbf{n}_j$  the outward normal vector and  $A_j$  the area of inlet condition  $j$  ( $j=1,\dots,4$ ), the inflow velocity reads:

$$\mathbf{u}_j(t) = - \left( \frac{Q_i(t)}{A_j} \zeta_j \right) \mathbf{n}_j, \quad (4.9)$$

where  $\zeta_j$  determines the distribution of the flow between the four pulmonary veins. In the absence of additional measurement (typically flow rates from PC-MRI), it is fair to assume a uniform distribution between the different pulmonary veins ( $\zeta_j = 0.25$  for all  $j$ ).

## 4.3 Application to a Patient Left Heart: Problem Formulation

### 4.3.1 Heart Model

Using the framework described above, an actual CT exam of a patient treated at the University Hospital of Toulouse Rangueil (France) is used to generate a numerical domain and its deformation. The CT exam consists of  $N = 10$  medical images along the cardiac cycle of period  $T = 1$  s with a spatial resolution  $2 \times 2 \times 2$  mm.

Due to the limited resolution of the images, the intra-cardiac geometry is simplified. As shown in Fig. 4.3, the numerical domain includes the LA, LV, the aortic root and four pulmonary veins. Left atrial appendum and geometrical details as the cordae tendinae or papillary muscles are omitted. The LA has a height of 5.5 cm from the MV to the upper pulmonary root and a maximum diameter of order 4 cm. The LV has a height of 8.8 cm from the MV to the apex (the lowest extremity of the LV in Fig. 4.3) and a maximum diameter of order 5 cm. The four pulmonary veins can be identified at the top of the views shown in Fig. 4.3. Each of the four pulmonary veins directly issues in the LA.

Valves are modeled as explained in Sect. 4.2.3. A close examination of the medical images from the CT scan allowed to set the leaflets length to  $l = 12$  mm for the MV. The open area presented to the blood flow is represented by an ellipse of axis  $a = 15$  mm and  $b = 8$  mm. As a first approximation, this area is supposed constant over the time when the MV is open.

### 4.3.2 Grid Mesh and Simulation Details

A nearly isotropic grid is created from the heart model described in the previous section using the commercial software Ansys Gambit, which was selected for its

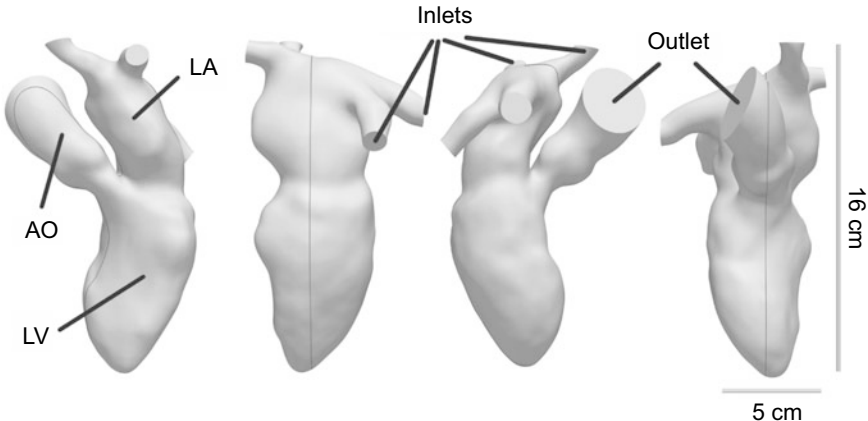


**Fig. 4.3.** Template computational domain extracted from a 3D medical image. The same domain is represented for four different points of view and the left ventricle (LV) and Left atrium (LA) and Aorta (AO) are indicated. Black line passing through the left heart indicates the position of slices used to describe the flow in Sect. 4.4

ability to generate good-quality tetrahedral mesh, appropriate for non-dissipative finite-volume formulations. The spatial resolution is of order 0.8 mm, which yields grids of approximately three-million tetrahedral elements. In this study, in order to maintain the quality of the grid along the cycle, re-meshing (see Sect. 4.2.2.2) was used at each acquisition instants  $t_i$ ,  $i = 1, \dots, N - 1$ .

The simulation time step is fixed by a CFL condition (CFL=0.9) consistent with the explicit time integration used in the CFD solver, which corresponds to a time step of order  $10^{-4}$  s.

Figure 4.4 displays the flow rates at the aortic valve (top plot), mitral valve (middle plot) and the heart inflow (bottom plot) gathering the four PV. Two vertical dotted lines separate the systolic phase and the diastolic one. For this heart, systole lasts  $t/T = 0.36$  (from  $t/T = 0.015$  to  $0.375$ ) and diastole  $t/T = 0.64$ .

The pulmonary flow rate derived from time evolution of the heart cavities is consistent with classical medical data. The aortic valve flow rate behaves as expected: it increases during systole with a maximum flow rate of  $Q_{MV} = 320 \text{ mL.s}^{-1}$ , then decreases until its shutting at  $t/T = 0.375$ . The aortic flow rate stays null during diastole. The mitral flow rate is usually composed by two peaks. The E wave, or rapid filling, and a second one, the A wave corresponding to late diastole. They are separated by a phase with almost no heart motion called diastasis. The flow rate shows only one main peak in the present case: the E wave ( $t/T = 0.51$ ,  $Q_{MV} = 410 \text{ mL.s}^{-1}$ ). The fact that the A wave is weak is symptomatic of pathologies.

The blood properties are:  $\rho = 1040 \text{ kg.m}^{-3}$  and  $\nu = 4 \times 10^{-6} \text{ m}^2\text{s}^{-1}$ . Relevant flow conditions at different locations of the heart are reported in Table 4.1. Inlet Reynolds number for each pulmonary vein varies from 0 to approximately 2000, based on the vein diameter. The Reynolds number at the mitral tips varies from

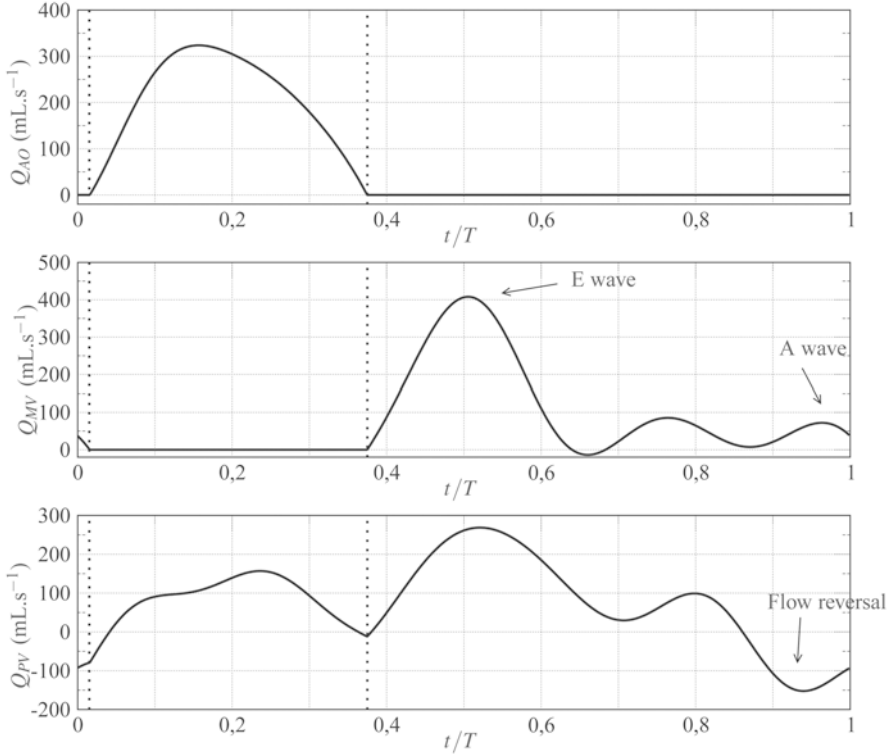


**Fig. 4.4.** Flow rates at the aortic valve (*top plot*), mitral valve (*middle plot*) and the total heart inflow (*bottom plot*) imposed at the pulmonary veins during the heart cycle. Vertical dotted lines mark the limit between the systolic phase ( $t/T$  between 0.015 and 0.375) and the diastolic phase

0 to approximately 5000 (based on the effective mitral mean diameter  $D = 2R_a = 2\sqrt{ab}$ , the area of the open MV, the kinematic viscosity and the maximum flow rate). The maximum transmural velocity  $U_{max}$  falls into the usual measurements (around  $1.0 \text{ m.s}^{-1}$ ) [14]. The Reynolds number of the aortic valve is about 5300. Table 4.1 reports the maximum velocity magnitude and the maximum Reynolds number for different elements of the heart model: pulmonary veins, mitral valve and aortic valve. These ranges of Reynolds numbers and the pulsating nature of the inlet flow clearly indicate that this complex cyclic flow may be transitional if not fully turbulent. This justifies the use of Large-Eddy Simulation (LES) which is more suitable than other simulation approaches for unsteady and/or transitional flows. In order to achieve a quality assessment of the presented simulation, the Pope criterion [40] is used. According to this criterion, a reliable LES should be able to resolve at least 80% of the turbulent kinetic energy. Looking at the phase where the turbulent activity is the highest ( $t/T=0.65$ ), it was found that this criterion is met in 85% of the numerical domain. The last 15% are mainly located in the atrial cavity.

**Table 4.1.** Main flow parameters describing the simulation. The section-averaged maximum velocity is indicated as  $U_{max}$ . Reynolds numbers are based on the diameter  $D$  of the region of interest. The instants when they reach their maximum value  $Re_{max}$  are reported as  $t_m/T$ . For valves,  $A$  is the area of the lumen when open

Element	$U_{max}$	$D = 2\sqrt{\frac{A}{\pi}}$	$Re_{max}$	$t_m/T$
AV	0.96 m.s <sup>-1</sup>	2.20 cm	5300	0.16
MV	1.08 m.s <sup>-1</sup>	1.87 cm	5000	0.52
Pulm. vein	0.79 m.s <sup>-1</sup>	1.00 cm	2000	0.52

## 4.4 Discussion

### 4.4.1 Global Description of the Cardiac Cycle

Fifteen cardiac cycles were simulated and phase-averaged in order to provide a clear view of the flow organization over the cardiac cycle. A detailed flow description can be found in [3]; only the main flow characteristics are recalled here for the sake of completeness. Six salient instants are illustrated in Fig. 4.5: the ventricular mid and end-systole ( $t/T = 0.25–0.35$ ), the beginning, peak and end of the E wave ( $t/T = 0.45–0.55–0.65$ ) and the end of the A wave, just before the beginning of the next ventricular systole ( $t/T = 0.99$ ). The velocity field is scaled by  $u_a = \dot{q}l_s/V_s = 0.1$  ms<sup>-1</sup> where  $\dot{q} = 7.50 \times 10^{-5}$  m<sup>3</sup>s<sup>-1</sup> is the cardiac output,  $V_s = 5.55 \times 10^{-5}$  m<sup>3</sup> is the end systolic volume and  $l_s = 7.40 \times 10^{-2}$  m is the ventricle length at the end of systole. Note that due to the strong velocity variations along the cycle, the vector scale was adapted for each instant.

During systole ( $t/T = 0.25–0.35$ ), the mitral valve is closed (in light gray in Fig. 4.5), preventing backflow towards the atrium, while the aortic valve is open (in dark gray in Fig. 4.5). The decrease of the ventricle volume causes ejection of blood into the aorta. Note that the velocity amplitude is the highest in the ascending aortic root. The computed flow at mid-systole is also highly swirled in the atrium, as reported *in vivo* [18, 25]. This movement is hardly discernible in Fig. 4.5, because the vortical movement is mainly perpendicular to the cutting plane [3]. Two recirculation zones are however visible in Fig. 4.5 (top center): just under the MV and within the aorta, just above the AV, in agreement with [17]. At the end of the ventricle contraction, the aortic valve closes and the mitral valve opens: ventricle filling starts. At  $t/T=0.375$  (not shown), the ventricle diastole starts: the LV volume increases and blood passes from the LA to the LV, forming a strong jet through the MV. The shear layer between the jet generated during the E wave and the surrounding quiescent fluid rolls-up and shapes the jet head as a vortex ring [20]. The E wave vortex ring signature and its evolution are visible in Fig. 4.5 ( $t/T = 0.45–0.55$ ) which illustrates a mechanism already reported by several authors [6]. The vortex ring does not remain symmetric, as the lateral wall prevents its full development. A large recirculating cell is clearly visible in the LV at  $t/T = 0.65$  (Fig. 4.5, bot-

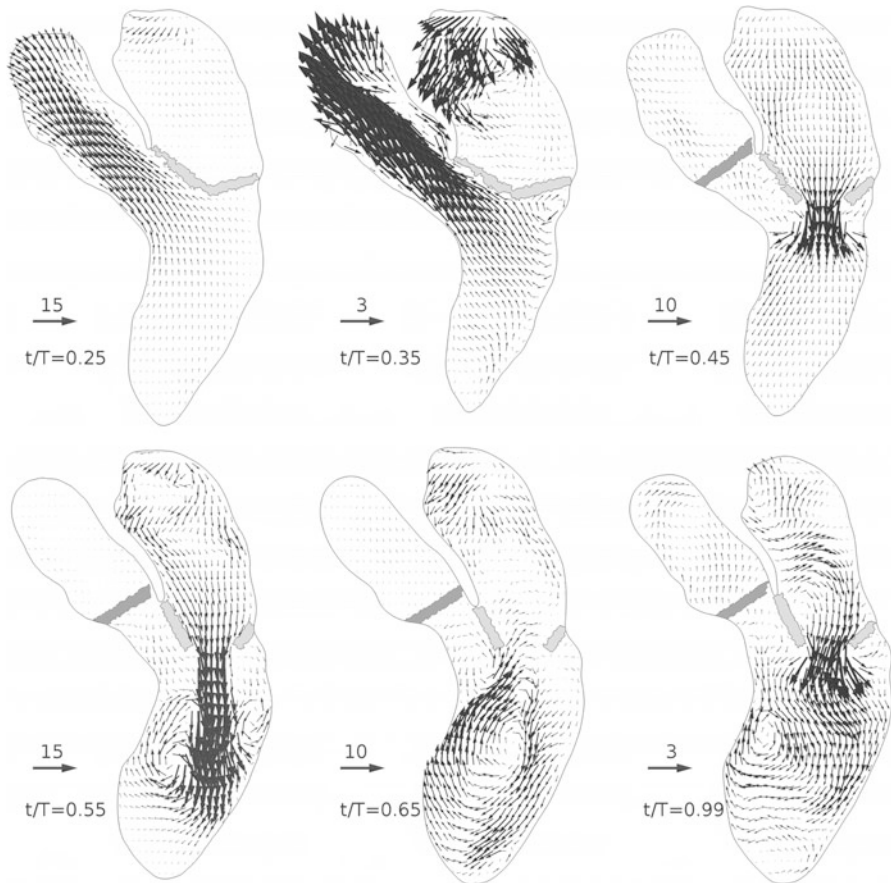


**Fig. 4.5.** Phase-averaged velocity field over a cutting-plane through the left heart. Velocity vector scale is not constant though the heart cycle and is indicated for each plot. Mitral valve is depicted in light grey the aortic one in dark grey

tom center), as often described in the literature [16, 21, 25]. It is characteristic of the flow in the ventricle after the E wave. Two less intense blood recirculation zones can be detected: one at the apex, which is visible during the whole diastole and an intermittent one between the aortic valve and one of the MV leaflet. These blood recirculations are also described *in silico* [5, 30, 44]. Between the E wave and the A wave, the recirculating cell core in the LV moves from the ventricle center to the septum wall. During the A wave occurring at  $t/T=0.99$  (Fig. 4.5, bottom right), the blood flux passing through the MV strengthens the recirculating cell in the LV, as classically reported [37]. Atrial contraction expels blood from the LA, both through the MV, as seen in the lower half part of the LA and through the pulmonary veins, as shown by the upward velocity vectors visible in the upper half part of the LA.

#### 4.4.2 Cycle-to-cycle Variations

The studied flow configuration is a breeding ground for weak turbulence. The transitional nature of this cyclic flow due to the highly complex evolving geometry and the unsteady inflows results in cycle-to-cycle variations. As an illustration, Fig. 4.6 shows the time evolution of the vertical velocity at four different points within the left heart. Velocity signals corresponding to six different heart cycles are superimposed to visualize the cycle-to-cycle variations. Moderate ( $2u_a$ ) to high ( $5u_a$ ) variations are present at all the locations, although not uniformly distributed over the cardiac cycles. The second plot (corresponding to a probe located under the aortic valve) shows the lowest variations: almost no cycle-to-cycle variations are visible during the diastolic phase, which is expected, given the quiescent flow beneath the aortic valve during diastole. Cycle-to-cycle variations decrease during the systolic phase in the LV (see third plot), beginning from variations up to  $4u_a$  to almost null variations. This absence of fluctuations carries on even after the passage of E-wave vortex ring, visible on the signal. Variations are visible from  $t/T = 0.55$  and amplify during the late diastole. A similar behaviour is visible in the lower part of the LV (see fourth plot): during systole, variations decrease, then rise after  $t/T = 0.55$ , reaching an amplitude of order

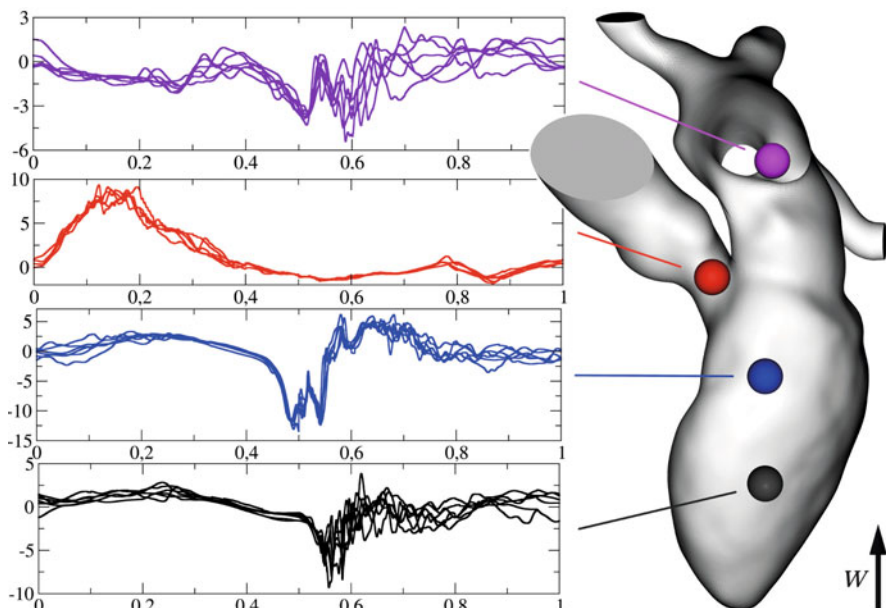


**Fig. 4.6.** Temporal evolutions of the scaled vertical velocity  $w/u_a$  (the  $w$  direction is indicated in the figure and  $u_a = \dot{q}l_s/V_s$ ) at four different points within the left heart. Six cycles are reported to illustrate the cycle-to-cycle variations

$5u_a$ . The largest relative fluctuations are obtained in the left atrium (top plot) with small cycle-to-cycle variations during systole ( $t/T$  between 0.015 and 0.375) but fluctuations as large as  $2u_a$  at  $t/T = 0.35$  and  $5u_a$  at  $t/T = 0.6$ . These variations are related to the interaction between the four inlet flows from the four pulmonary veins.

A more quantitative assessment of the cycle-to-cycle variations is obtained by computing the kinetic energy of the velocity fluctuations. The velocity flow is decomposed in a mean (phase-averaged) velocity field  $\bar{u}$  and a fluctuating part  $u'$ . The turbulent kinetic energy  $k$  and the mean flow kinetic energy  $E_k$  are defined as:

$$k(t) = \frac{1}{2V(t)} \int_{V(t)} (u_{rms}(\mathbf{x}, t)^2 + v_{rms}(\mathbf{x}, t)^2 + w_{rms}(\mathbf{x}, t)^2) dV, \quad (4.10)$$

$$E_k(t) = \frac{1}{2V(t)} \int_{V(t)} (\bar{u}(\mathbf{x}, t)^2 + \bar{v}(\mathbf{x}, t)^2 + \bar{w}(\mathbf{x}, t)^2) dV, \quad (4.11)$$

where  $u_{rms}$ ,  $v_{rms}$  and  $w_{rms}$  are the root-mean-square values of the velocity fluctuations in the three directions. The volume  $V(t)$  is either the volume of the ventricle or the volume of the atrium at time  $t$ .

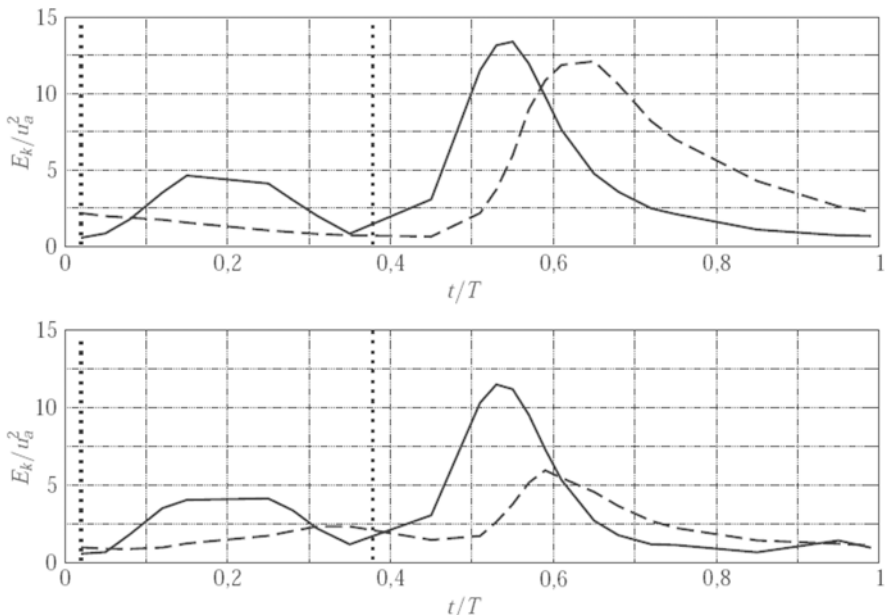


**Fig. 4.7.** Volumetric mean flow kinetic energy  $\bar{E}_k$  (full line) and five times the turbulent kinetic energy  $k$  (dashed line) in the left ventricle (top plot), and in the left atrium (bottom plot). The energies are nondimensionalised by  $u_a^2$ . Vertical dotted lines mark the limit between the systolic phase ( $t/T$  between 0.015 and 0.375) and the diastolic phase

Figure 4.7 shows how these energies evolve over the heart cycle, both in the ventricle (top plot) and the atrium (bottom plot). Note that 5 times  $k$  is plotted, so that the same scale is used to represent both energies. The mean flow kinetic energy evolves similarly in both cavities. During the systolic phase ( $t/T$  between 0.015 and 0.375) it increases and reaches a plateau at  $t/T=0.15$ . After a decrease just before the beginning of diastole, the mean flow kinetic energy increases again and reaches a peak at  $t/T=0.54$ , viz.  $0.04T$  after the peak of the E wave. The maximum value of  $E_k$  corresponds to the presence of high velocities when blood flows from the atrium to the ventricle (see the mitral jet in Fig. 4.5, bottom left). The ventricular turbulent kinetic energy  $k$  remains low during the systolic phase thanks to the stabilizing effect of the flow acceleration, with values of less than 5% of  $E_k$ . It then increases substantially, reflecting the amplification of the disturbance after the jet impingement on the lateral ventricle wall. The turbulent energetic peak is reached  $T/10$  after the peak of mean flow kinetic energy, corresponding to the convection time of the vortex ring and the decelerating phase of the flow. The turbulence intensity  $k/E_k$  in the ventricle is as high as 50% during the  $k$  peak.

The atrial turbulent kinetic energy behaves somewhat differently. First, it increases during the whole systolic phase, because of the interaction/collision of the four inflowing jets issued from the pulmonary veins. A first peak is thus reached near the beginning of the diastolic phase and turbulence intensity is then attenuated during the flow acceleration through the atrium, as expected. The atrial turbulent kinetic energy rises again after  $t/T=0.5$  and reaches its peak before  $t/T = 0.6$  during the flow deceleration. On top of occurring earlier in the heart cycle, this peak is around twice less energetic than the one occurring in the ventricle. Still, it corresponds to a large turbulence intensity of approximatively 20%. As in the ventricle, the turbulent kinetic energy then decreases until the end of the heart cycle.

## 4.5 Conclusions

The approach presented here allows patient-specific blood flow simulations in the heart from a series of gated 3D images. Starting from 4D medical images, the numerical domain is first extracted and the heart wall movements are then calculated thanks to a proper image registration algorithm. In order to demonstrate the ability of the method to reproduce the cardiac flow, a computation of the blood flow in a whole left heart has been conducted. Results consistent with the current knowledge in terms of left heart flow is presented. All presented features have been reported several times in the literature, both in numerical and experimental studies and by medical imaging.

Furthermore, the use of fluid numerical method well adapted to fluctuating turbulent flows enables the observation of cycle-to-cycle variations in the flow field. Such variations are expected in the present flow, due to the high Reynolds numbers encountered and the unsteadiness of the flow incoming from the pulmonary veins. The present results show that in spite of rigorously identical contraction and bound-

ary conditions, fluid inertia makes the flow differ from one cycle to another. More precisely, cycle-to-cycle variations in the left atrium can be observed in its upper part, where the collision of the jets issuing from the pulmonary veins makes the flow particularly chaotic. Spatially averaged kinetic turbulent energy level reaches a turbulent intensity of 20% at its peak then slowly decreases. In the left ventricle, velocity fluctuations are reported mainly during late diastole. Between the impact of the E wave jet on the lateral wall and the end of diastole, the left ventricle displays high levels of cycle-to-cycle fluctuations. Indeed, both the vortex ring impact and the E wave deceleration occur approximately at the same time, and both are features tending to generate turbulence. This translates into turbulent intensity levels as high as 50%. This turbulent activity dissipates little by little, until the flow acceleration at early systole.

The presented method does not include or simplifies some aspects of the physiological heart. Blood is considered as a Newtonian fluid, which is an approximation commonly accepted for the heart flow. A non-Newtonian model could be included in our simulations. The spatio-temporal resolution of medical imaging imposes temporal interpolation and geometrical simplifications of the heart model. Consistently with the poor time resolution of the input medical data, a rough model of the mitral valve was used, which constitutes the main drawback of our method. Valves are instantaneously switch from their closed position to their open position and vice versa. This simple approach is justified by the fact that the opening and closing of the valves last only 5% of the whole cycle. Change of aperture area along time is not considered either. Note however that the model can be refined depending on the available data. Nevertheless, the presented approach allows to retrieve features reported in the literature and, in addition, it can provide detailed information about the complex intermittent flow in the left heart.

**Acknowledgements** The authors thanks Prof. D. Coisne and Dr. S. Nottin for interesting discussions about the presented results and their medical/physiological concordance. Dr. V. Moureau is gratefully acknowledged for giving access to the YALES2 solver.

## References

1. Ashburner, J., Andersson, J.L.R., Friston, K.J.: High-dimensional image registration using symmetric priors, *NeuroImage* **9**(6), 619–628 (1999)
2. Ashburner, J., Neelin, P., Collins, D.L., Evans, A., Friston, K.J.: Incorporating prior knowledge into image registration, *NeuroImage* **6**(4), 344–352 (1997)
3. Chnafa, C., Mendez, S., Nicoud, F.: Image-based large-eddy simulation in a realistic left heart., *Comp. Fluids*, manuscript accepted for publication
4. Cimino, S., Pedrizzetti, G., Tonti, G., Canali, E., Petronilli, V., De Luca, L., Iacoboni, C., Agati, L.: In vivo analysis of intraventricular fluid dynamics in healthy hearts, *Eur. J. Mech. – B/Fluids* **35**, 40–46 (2012)
5. Doenst, T., Spiegel, K., Reik, M., Markl, M., Hennig, J., Nitzsche, S., Beyersdorf, F., Oertel, H.: Fluid-dynamic modeling of the human left ventricle: Methodology and application to surgical ventricular reconstruction, *Ann. Thor. Surg.* **87**, 1187–1195 (2009)

6. Domenichini, F., Pedrizzetti, G., Baccani, B.: Three-dimensional filling flow into a model left ventricle, *J. Fluid Mech.* **539**, 179–198 (2005)
7. Falahatpisheh, A., Kheradvar, A.: High-speed particle image velocimetry to assess cardiac fluid dynamics in vitro: From performance to validation, *Eur. J. Mech. – B/Fluids* **35**, 2–8 (2012)
8. Fernandez, M.A., Formaggia, L., Gerbeau, J.F., Quarteroni, A.: *Cardiovascular Mathematics. Modeling and simulation of the circulatory system, MS&A – Modeling, Simulation and Applications*, vol. 1, chap. 3, The derivation of the equations for fluids and structure, pp. 77–121. Springer, Milan (2009)
9. Fung, Y.C.: *Biomechanics – Circulation*, 2nd edn. Springer-Verlag, New York (1997)
10. Fyrenius, A., Wigstrom, L., Ebbers, T., Karlsson, M., Engvall, J., Bolger, A.: Three dimensional flow in the human left atrium, *Heart* **86**, 448–455 (2001)
11. Garcia, D., del Alamo, J.C., Tanne, D., Yotti, R.L., Cortina, C., Bertrand, E., Antoranz, J.C., Perez-David, E., Rieu, R., Fernandez-Aviles, F., Bermejo, J.: Two-dimensional intraventricular flow mapping by digital processing conventional color-doppler echocardiography images, *IEEE Trans. Med. Imag.* **29**, 1701–1713 (2010)
12. Germano, M., Piomelli, U., Moin, P., Cabot, W.H.: A dynamic subgrid-scale eddy viscosity model, *Phys. Fluids* **3**, 1760–1765 (1991)
13. Gharib, M., Rambod, E., Kheradvar, A., Sahn, D., Dabiri, J.: Optimal vortex formation as an index of cardiac health, *Proc. Natl. Acad. Sci. U.S.A.* **103**, 6305–6308 (2006)
14. Haugen, B.O., Berg, S., Brekke, K.M., Samstad, S.O., Slørdahl, S.A., Skjærpe, T., Torp, H.: Velocity profiles in mitral blood flow based on three-dimensional freehand colour flow imaging acquired at high frame rate, *Eur. J. Echo.* **1**, 252–256 (2000)
15. Hollnagel, D.I., Summers, P.E., Poulikakos, D., Kollias, S.S.: Comparative velocity investigations in cerebral arteries and aneurysms: 3D phase-contrast MR angiography, laser doppler velocimetry and computational fluid dynamics, *NMR in Biomed.* **22**, 795–808 (2009)
16. Hong, G.R., Pedrizzetti, G., Tonti, G., Li, P., Wei, Z., Kim, J., Baweja, A., Liu, S., Chung, N., Houle, H., Narula, J., Vannan, M.: Characterization and quantification of vortex flow in the human left ventricle by contrast echocardiography using vector particle image velocimetry, *J. Am. Coll. Cardiol.* **1**, 705–717 (2008)
17. Kilner, P., Yang, G., Mohiaddin, R., Firmin, D., Longmore, D.: Helical and retrograde secondary flow patterns in the aortic arch studied by three-directional magnetic resonance velocity mapping, *Circulation* **88**, 2235–2247 (1993)
18. Kilner, P., Yang, G.Z., Wilkes, A., Mohiaddin, R.H., Firmin, D.N., Yacoub, M.H.: Asymmetric redirection of flow through the heart, *Nature* **404**, 759–761 (2000)
19. Kim, H., Hertzberg, J., Shandas, R.: Development and validation of echo PIV, *Expe. Fluids* **36**, 455–462 (2004)
20. Le, T.B., Sotiropoulos, F.: On the three-dimensional vortical structure of early diastolic flow in a patient-specific left ventricle. *Eur. J. Mech. – B/Fluids* **35**, 20–24 (2012)
21. Long, Q.: Subject-specific computational simulation of left ventricular flow based on magnetic resonance imaging, *Proceedings of the Institution of Mechanical Engineers, Part H* **222**, 475–485 (2008)
22. Maintz, J.B.A., Viergever, M.A.: A survey of medical image registration, *Medical Image Analysis* **2**(1), 1–36 (1998)
23. Makela, T., Clarysse, P., Sipila, O., Pauna, N., Pham, Q.C., Katila, T., Magnin, I.E.: A review of cardiac image registration methods. *Medical Imaging, IEEE Transactions on* **21**(9), 1011–1021 (2002)

24. Malandin, M., Maheu, N., Moureau, V.: Optimization of the deflated conjugate gradient algorithm for the solving of elliptic equations on massively parallel machines, *J. Comp. Phys.* **238**, 32–47 (2013)
25. Markl, M., Kilner, P., Ebbers, T.: Comprehensive 4D velocity mapping of the heart and great vessels by cardiovascular magnetic resonance, *J. Cardiovasc. Magn. Reson.* **13**, 1–22 (2011)
26. Masud, A., Bhanabhagwanwala, M., Khurram, R.A.: An adaptive mesh rezoning scheme for moving boundary flows and fluid-structure interaction, *Comp. Fluids* **36**(1), 77–91 (2007)
27. Mendez, S., Gibaud, E., Nicoud, E.: An unstructured solver for simulations of deformable particles in flows at arbitrary reynolds numbers, *JCP* **256**, 465–483 (2014)
28. Merrifield, R., Long, Q., Xu, X.Y., Kilner, P.J., Firmin, D.N., Yang, G.Z.: Combined CFD/MRI analysis of left ventricular flow, *Med. Im. and augmented reality* **3150**, 229–236 (2004)
29. Midulla, M., Moreno, R., Baali, A., Chau, M., Negre-Salvayre, A., Nicoud, F., Pruvost, J.P., Haulon, S., Rousseau, H.: Haemodynamic imaging of thoracic stent-grafts by computational fluid dynamics (CFD): presentation of a patient-specific method combining magnetic resonance imaging and numerical simulations, *Eu. Radiol.* **22**, 2094–2102 (2012)
30. Mihalef, V., Ionasec, R.I., Sharma, P., Georgescu, B., Voigt, I., Suehling, M., Comaniciu, D.: Patient-specific modelling of whole heart anatomy, dynamics and haemodynamics from four-dimensional cardiac CT images, *Interface Focus* **1**, 286–296 (2011)
31. Modersitzki, J.: Numerical Methods for Image Registration, Numerical Mathematics and Scientific Computation, Oxford University Press USA (2004)
32. Mohd-Yusof, J.: Combined immersed-boundary/B-spline methods for simulations of flow in complex geometries, *Ann. Research Briefs, Center for Turbulence Research* (1997)
33. Moin, P.: Advances in large eddy simulation methodology for complex flows, *Int. J. Heat Fluid Flow* **23**(5), 710–720 (2002)
34. Moureau, V., Domingo, P., Vervisch, L.: Design of a massively parallel CFD code for complex geometries, *Comptes Rendus Mécanique* **339**, 141–148 (2011). High Performance Computing
35. Nicoud, F., Moreno, R., Tayllamin, B., Chau, M., Rousseau, H.: Computational hemodynamics in moving geometries without solving the fluid-structure interaction problem. In: Conference on Modelling Fluid Flow (2009)
36. Nicoud, F., Toda, H.B., O. Cabrit, S.B., Lee, J.: Using singular values to build a subgrid-scale model for large eddy simulations, *Phys. Fluids* **23**, 085,106 (2011)
37. Pedrizzetti, G., Domenichini, F.: Nature optimizes the swirling flow in the human left ventricle, *Phys. Rev. Lett.* **95**, 108,101 (2005)
38. Pham, D.L., Xu, C., Prince, J.L.: Current methods in medical image segmentation, *Annu. Rev. Biomed. Eng.* **2**, 315–337 (2000)
39. Pope, S.B.: Turbulent flows. Cambridge University Press (2000)
40. Pope, S.B.: Ten questions concerning the large-eddy simulation of turbulent flows, *New J. Phys.* **6**(1), 35 (2004)
41. Querzoli, G., Fortini, S., Cenedese, A.: Effect of the prosthetic mitral valve on vortex dynamics and turbulence of the left ventricular flow, *Phys. Fluids* **22**, 041,901 (2010)

42. Saber, N.R., Wood, N.B., Gosman, A.B., Merrifield, R.D., Yang, G.Z., Charrier, C.L., Gatehouse, P.D., Firmin, D.N.: Progress towards patient-specific computational flow modeling of the left heart via combination of magnetic resonance imaging with computational fluid dynamics, *Ann. Biomed. Eng.* **31**, 42–52 (2003)
43. Sagaut, P.: Large eddy simulation for incompressible flows, vol. 3, Springer, Berlin (2000)
44. Schenkel, T., Malve, M., Reik, M., Markl, M., Jung, B., Oertel, H.: MRI-based CFD analysis of flow in a human left ventricle: Methodology and application to a healthy heart, *Ann. Biomed. Eng.* **37**, 503–515 (2009)
45. Smagorinsky, J.: General circulation experiments with the primitive equations: 1. the basic experiment, *Mon. Weather Rev.* **91**(3), 99–164 (1963)
46. Taylor, C.A., Figueira, C.A.: Patient-specific modeling of cardiovascular mechanics, *Annu. Rev. Biomed. Eng.* **11**, 109–134 (2009)
47. Vadakkumpadan, F., Arevalo, H., Ceritoglu, C., Miller, M., Trayanova, N.: Image-based estimation of ventricular fiber orientations for personalized modeling of cardiac electrophysiology, *IEEE Trans. Med. Imag.* **31**, 1051–1060 (2012)
48. Yoganathan, A.P., He, Z., Casey, J.S.: Fluid mechanics of heart valves, *Annu. Rev. Biomed. Eng.* **6**, 331–362 (2004)

---

# Multiscale Modeling of Sickle Cell Anemia

Huan Lei and George Em Karniadakis

**Abstract** Sickle cell anemia (SCA) is a genetic inherited hematological disorder mainly characterized by three biophysical hallmarks: heterogeneous cell morphology, abnormal rheology and vaso-occlusion crisis. The major challenge for numerical investigation of this disease is to model the dynamic processes over the wide range of length scales incorporated (sickle hemoglobin (HbS) polymerization to vaso-occlusion). In this chapter, we present a multi-scale computational framework of sickle red blood cell (SS-RBC), based on dissipative particle dynamics, to investigate the above three hallmarks. We first predict the heterogeneous SS-RBC morphological transition by coupling a RBC model with a stochastic coarse-grained model representing the intracellular HbS polymerization. We then quantify the abnormal rheology and hemodynamics of SS-RBC suspensions with a multi-scale SS-RBC model accounting for heterogeneous cell rigidity and the previously predicted cell morphologies. Finally, we employ the present model to quantify the mechanism of vaso-occlusion crisis associate with SCA. The heterogeneous cell adhesivity among the different cell groups and their specific contribution to occlusion crisis, as well as the role of inflammation-stimulated leukocyte are discussed.

## 5.1 Introduction

Sickle cell anemia (SCA), the first identified “molecular disease”, is one of the most common genetic inherited hematological disorder, which can cause several types of chronic complications such as vaso-occlusion crisis, splenic sequestration cri-

---

H. Lei  
Pacific Northwest National Laboratory, Richland, WA 99352, USA  
e-mail: huan.lei@pnnl.gov

G.E. Karniadakis (✉)  
Brown University, Providence, RI 02912, USA  
e-mail: George\_Karniadakis@brown.edu

sis, hemolytic crisis, etc. This disease is named by the special “elongated, sickle-shape” cells identified in the blood sample of an American-African patient, as first described by James B. Herrick [51] in 1910. In 1949, Linus Pauling and his colleagues, for the first time, proposed that this disease is attributed to the abnormal hemoglobin molecules within the erythrocyte [85]. Subsequent studies [58] reveal that in the sickle hemoglobin molecule (HbS), the hydrophilic amino acid glutamic acid is substituted by the hydrophobic amino acid valine at the  $\beta$ -6 chain site. In hypoxic conditions, the intracellular HbS solution transitions into a polymerized state, resulting in a series of alterations in the cell membrane functions and blood microcirculation. With regards to pathophysiology, this disease is mainly characterized by three major hallmarks: (i) irregular and heterogeneous cell morphologies, (ii) decrease of cell deformability and abnormal blood rheology, and (iii) vaso-occlusion crisis, which is the major cause of the morbidity and mortality of the SCA patients. Despite modern health care and technology, the life expectancy of an individual with SCA in the US is less than 50 years.

During the past few decades, there have been many successful investigations on different aspects of this disease. At the molecular scale, the HbS polymerization process is well characterized by the double nucleation model [40, 41] and the following experimental studies [2, 13, 14, 18, 42–44, 60, 90, 96, 97]. According to this model, the formation of a HbS polymer domain is triggered by the homogeneous nucleation of the HbS molecules in bulk solution and proceeds with the explosive growth via polymer elongation and heterogeneous nucleation on the pre-existing HbS polymers. These studies successfully revealed the mechanism of the nucleation “delay time” [29, 92] and its high concentration dependence on the intracellular HbS. At the cellular scale, Kaul et al. [65] revealed the heterogeneous cell density groups in suspension of sickle red blood cells (SS-RBCs), as roughly divided into four fractions according to the intracellular mean corpuscular hemoglobin concentration (MCHC). Fraction I (SS1) and II (SS2) with moderate MCHC are mainly composed of reticulocytes and discocytes, respectively, with MCHC similar to healthy cells. On the other hand, fractions III (SS3) and IV (SS4) with high MCHC are mainly composed of rigid discocytes and irreversible sickle cells (ISC). Associated with the heterogeneous cell groups are the heterogeneous cell rigidity [17, 33, 59] and abnormal blood rheology [52, 68, 69, 95]. At the microcirculation scale, recent studies further revealed the *multi-interactional* and *multi-stage* nature of the vaso-occlusion crisis. While early studies postulated that the HbS polymerization resulted in the entrapment of single sickled cell in capillaries, later *in vivo* and *ex vivo* [8, 62–64, 66, 94] studies demonstrate that the vaso-occlusion crisis comprises a complex and multistep process triggered by interaction between multiple SS-RBC density groups, endothelial cells, inflammation activated leukocytes, platelets, etc.

Despite these findings, understanding the mechanism of this disease in an *integrated* way is still an open question [8]. Currently, hydroxyurea (HU) [12, 29, 72, 87] is the only FDA-approved drug used for patients of sickle cell anemia. The major mechanism of this drug is to target the intracellular HbS polymerization process, which is the pre-cursor event of the vaso-occlusion crisis. It can induce the production of the fetal hemoglobin (HbF) and therefore increase the “delay time” of the

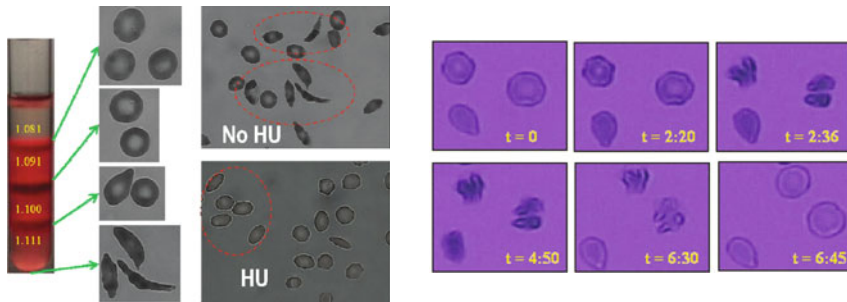


**Fig. 5.1.** *Left:* image of oxygenated SS-RBCs separated by different density; SS-RBCs of different density exhibit heterogeneous cell morphologies; the effect of hydroxyurea (HU) is shown on the densest population (1.11 g/ml), where the red dashed circles represent typical shapes of SS-RBCs under full oxygenated condition. *Right:* shape evolution of SS-RBCs during a deoxygenated-oxygenated cycle. Experimental images courtesy of Dr. E Du and Dr. Ming Dao at MIT, from [1]

cell sickling process. However, clinical studies report that this drug is ineffective for many patients with unclear reason [4]. Moreover, the aforementioned microcirculation studies indicate that the predominant stimuli of the crisis enrolls with heterogeneous cell interactions through multiple steps. Therefore, numerical modeling and quantitative study of this disease by considering cell groups with heterogeneous morphology, rigidity and adhesivity can greatly facilitate our understanding of the specific role and contribution of the individual cell groups in occlusion crisis. Hence computational modeling may provide a new paradigm for investigating therapeutic treatments for this disease by targeting the individual physiological conditions such as endothelium activation and up-regulation, adhesive interaction between endothelium cells and heterogeneous SS-RBC, and secondary entrapment of SS-RBC by the adherent cells.

One of the major challenges for the numerical modeling of SCA is the wide range of the spatial and temporal scales incorporated. While SCA originates from the abnormal HbS molecule on length scale  $O(1)$  Å, the resultant cell sickling process is on length scale of  $O(10)\mu\text{m}$ . Similarly, the adhesive proteins expressed on SS-RBCs interact with endothelial cells in time scale  $O(1)$  ps, in contrast with the vaso-occlusion crisis occurring in time scale of  $O(1)$  s. Several numerical methods and physical models have been developed to investigate SCA in different aspects. In the continuum scale, Berger and King [9, 10] proposed a model to predict the sickle blood velocity in capillary by coupling the oxygen transport to the motion of SS-RBCs; however, this model suffers from the lack of realistic blood rheology. In molecular scale, Lykotrafitis et al. [78] constructed a coarse-grained model for individual HbS fiber and the zipper dynamics, but it cannot be readily extended to cellular level [23, 79] due to the computational cost. Besides these two aforementioned approaches, a number of numerical methods has been developed to model individual *healthy* red blood cells (RBCs) in mesoscopic or semi-continuum scale [26–28, 36, 81, 84, 86], which

can potentially be extended to modeling this hematological disorder by bridging the dynamic processes on the microscopic and macroscopic scales incorporated in SCA. Here, we will focus on the accurate mesoscopic modeling of SS-RBCs. Remarkably, Dong et al. [24] developed a 2D model of sickle cell in capillaries where a SS-RBC is represented as a 2D cylinder with different membrane elasticity and cytosol viscosity. This model does not take into account realistic SS-RBC morphological and biomechanical properties, and therefore it can not quantitatively capture the abnormal rheology of the SS-RBC suspension. Dupin et al. [27] coupled the individual RBC with an Eulerian discretization of fluid domain represented by the Lattice Boltzmann method [91]. Having obtained promising results healthy blood flow, they investigated a collection of SS-RBCs passing through an aperture with diameter less than the size of a single RBC. However, this model does not consider the heterogeneous cell-cell and cell-endothelium interaction discussed above and therefore it is insufficient to quantify the hemodynamics of SS-RBC suspension.

In this chapter, we will present a multi-scale model of SS-RBC to address the three hallmarks of SCA discussed above. This model is based on the multi-scale model of healthy RBC previously developed by Pivkin, Fedosov and Karniadakis et al. [36, 86] and validated in healthy and malaria-infected blood systems [11, 37, 38, 88] using Dissipative Particle Dynamics [30, 45, 54]. The multi-scale nature of the model enables us to directly impose biomechanical properties of the RBC membrane on different length scales. Furthermore, we developed stochastic models to predict the resultant morphology of the intracellular aligned HbS polymer (APH) domains and simulate the adhesive interaction between the SS-RBC and endothelial cells. These models can be used to represent seamlessly the heterogeneous cell-APH, cell-cell and cell-endothelium interactions and hence they can address abnormal SS-RBC morphology, rheology and vaso-occlusion crisis, respectively.

This chapter is organized as follows: in section two we briefly review the DPD simulation method, the multi-scale RBC model, as well as two coarse-grained stochastic models representing the intracellular HbS polymerization and the cell-endothelium adhesive interaction. In section three we investigate the SS-RBC morphologic transition by predicting the resultant heterogeneous SS-RBC morphologies due to the intracellular HbS polymerization and compare the results with experimental measurements. In section four we explore the abnormal rheology of SS-RBC suspensions consisting of heterogeneous cell morphologies and rigidities in shear and tube flows. In section five we probe the mechanism of vaso-occlusion crisis using the multi-scale model of SS-RBC, accounting for diversity in cell morphology and rigidity, interactions between SS-RBC and vascular endothelium as well as SS-RBC and inflammation-activated leukocytes to quantify the specific biophysical characteristics triggering the vaso-occlusion crisis. The main results of this chapter are summarized in section six, adding a brief discussion about possible extension of the present work for studying this hematological disorder.

## 5.2 Models and Simulation Methods

The multi-scale red blood cell (RBC) model is developed within the framework of dissipative particle dynamics (DPD) method. We first briefly review the derivation and formulation of this method. Next we introduce the multi-scale RBC model and the stochastic cell adhesion model. Finally, we present the kinetic model representing the development of intracellular HbS polymer domain.

### 5.2.1 Dissipative Particle Dynamics

Dissipative Particle Dynamics is a Lagrangian based particle method initially proposed by Hoogerbrugge and Koelman [32, 54] to simulate the complex hydrodynamic processes of isothermal fluid systems. This particle-based framework enables us to easily incorporate additional physical features into the systems and extend its application to complex fluid and soft-matter systems. Several studies have shown that the DPD particles can be viewed as coarse-grained (CG) virtual clusters of multiple atomistic particles [31, 53, 71, 74] but at a coarser scale, as sketched in Fig. 5.2. The standard equation of motion is given by

$$\begin{aligned} d\mathbf{r}_i &= \mathbf{v}_i dt \\ d\mathbf{v}_i &= (\mathbf{F}_i^C dt + \mathbf{F}_i^D dt + \mathbf{F}_i^R \sqrt{dt}) / m, \end{aligned} \quad (5.1)$$

where  $\mathbf{r}_i$ ,  $\mathbf{v}_i$ ,  $m$  are the position, velocity, and mass of the particle  $i$ , and  $\mathbf{F}_i^C$ ,  $\mathbf{F}_i^D$ ,  $\mathbf{F}_i^R$  are the total conservative, dissipative and random forces acting on the particle  $i$ , respectively. Under the assumption of pairwise interactions the DPD forces are

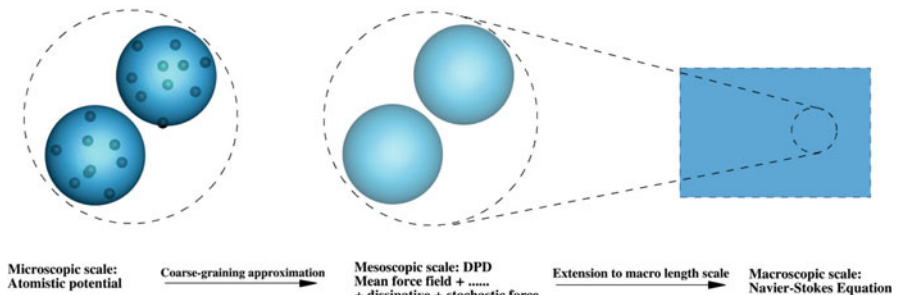


**Fig. 5.2.** Sketch of the length scales for dissipative particle dynamics. Each DPD particle can be viewed as a virtual cluster of multiple atomistic particles. The conservative force field represents the ensemble average of the pairwise approximated atomistic force field. The dissipative and random force terms originate from the eliminated atomistic degrees of freedom in the coarse-graining procedure. In the macroscopic regime, the DPD fluid recovers the continuum fluid governed by the Navier-Stokes equation

given by the sum of the pair interactions with the surrounding particles as follows

$$\mathbf{F}_{ij}^C = \begin{cases} a(1.0 - r_{ij}/r_c)\mathbf{e}_{ij}, & r_{ij} < r_c \\ 0, & r_{ij} > r_c \end{cases} \quad (5.2)$$

$$\begin{aligned} \mathbf{F}_{ij}^D &= -\gamma w^D(r_{ij})(\mathbf{v}_{ij} \cdot \mathbf{e}_{ij})\mathbf{e}_{ij}, \\ \mathbf{F}_{ij}^R &= \sigma w^R(r_{ij})\xi_{ij}\mathbf{e}_{ij}, \end{aligned} \quad (5.3)$$

where  $\mathbf{r}_{ij} = \mathbf{r}_i - \mathbf{r}_j$ ,  $r_{ij} = |\mathbf{r}_{ij}|$ ,  $\mathbf{e}_{ij} = \mathbf{r}_{ij}/r_{ij}$ , and  $\mathbf{v}_{ij} = \mathbf{v}_i - \mathbf{v}_j$ .  $r_c$  is the cut-off radius beyond which all interactions vanish. The coefficients  $a$ ,  $\gamma$  and  $\sigma$  represent the strength of the conservative, dissipative and random force, respectively. The last two coefficients are coupled with the temperature of the system by the fluctuation-dissipation theorem [32] as  $\sigma^2 = 2\gamma k_B T$ . Here,  $\xi_{ij}$  are independent identically distributed (i.i.d.) Gaussian random variables with zero mean and unit variance. The weight functions  $w^D(r)$  and  $w^R(r)$  are defined by

$$\begin{aligned} w^D(r_{ij}) &= [w^R(r_{ij})]^2, \\ w^R(r_{ij}) &= \begin{cases} (1 - r_{ij}/r_c)^k, & r_{ij} < r_c \\ 0, & r_{ij} > r_c \end{cases} \end{aligned} \quad (5.4)$$

where  $k$  is a parameter that determines the extent of dissipative and random force envelopes. The above stochastic equation can be integrated using the velocity-Verlet algorithms [46].

### 5.2.2 Blood Cell Models

#### 5.2.2.1 Red Blood Cell

A healthy red blood cell maintains a biconcave shape in equilibrium state. In the present model, we constructed the RBC membrane as a two-dimensional triangulated surface as described in [35] with  $N_v$  vertices. Each vertex is represented by a DPD particle. The vertices are connected by  $N_s$  visco-elastic bonds to impose proper membrane mechanics [23, 36, 86]. The free energy of each cell is defined by

$$V_{\text{rbc}} = V_s + V_b + V_a + V_v, \quad (5.5)$$

where  $V_s$ ,  $V_b$ ,  $V_a$ ,  $V_v$  represent the in-plane visco-elastic bond interaction, cell membrane bending rigidity, cell area and volume constraint, respectively. In the present work,  $V_s$  is represented as the summation of an attractive wormlike chain potential and a repulsive potential

$$V_s = \sum_{j \in 1 \dots N_s} \left[ \frac{k_B T l_m (3x_j^2 - 2x_j^3)}{4p(1-x_j)} + \frac{k_p}{(n-1)l_j^{n-1}} \right], \quad (5.6)$$

where  $l_j$  is the length of the spring  $j$ ,  $l_m$  is the maximum spring extension,  $x_j = l_j/l_m$ ,  $\rho$  is the persistence length,  $k_B T$  is the energy unit,  $k_p$  is the spring constant, and  $n = 2$  is the adopted power index.

The membrane viscosity is represented by imposing a viscous force on each bond interaction. Following the general framework of the fluid particle model [31], we can define the dissipative force  $\mathbf{F}_{ij}^D$  and random force  $\mathbf{F}_{ij}^R$  given by

$$\mathbf{F}_{ij}^D = -\gamma^T \mathbf{v}_{ij} - \gamma^C (\mathbf{v}_{ij} \cdot \mathbf{e}_{ij}) \mathbf{e}_{ij}, \quad (5.7)$$

$$\mathbf{F}_{ij}^R dt = \sqrt{2k_B T} \left( \sqrt{2\gamma^T d\bar{\mathbf{W}}_{ij}^S} + \sqrt{3\gamma^C - \gamma^T} \frac{\text{tr}[d\mathbf{W}_{ij}]}{3} \mathbf{1} \right) \cdot \mathbf{e}_{ij}, \quad (5.8)$$

where  $\mathbf{v}_{ij}$  is the relative velocity between the two vertices  $i$  and  $j$ ,  $\gamma^T$  and  $\gamma^C$  are dissipative parameters,  $\text{tr}[d\mathbf{W}_{ij}]$  is the trace of a random matrix of independent Wiener increments  $d\mathbf{W}_{ij} = \sqrt{dt} \xi_{ij}$ , where  $\xi_{ij} \sim \mathcal{N}(0, 1)$  is identical independent Gaussian random variable.  $d\bar{\mathbf{W}}_{ij}^S = d\mathbf{W}_{ij}^S - \text{tr}[d\mathbf{W}_{ij}^S] \mathbf{1}/3$  is the traceless symmetric part.

The equilibrium length of individual bond and the visco-elastic properties of the cell membrane can be determined by performing a linear analysis, as proposed in [22] for a regular hexagonal network; the derived shear modulus of the membrane  $\mu_0$  is given by

$$\mu_0 = \frac{\sqrt{3}k_B T}{4pl_m x_0} \left( \frac{x_0}{2(1-x_0)^3} - \frac{1}{4(1-x_0)^2} + \frac{1}{4} \right) + \frac{\sqrt{3}k_p(n+1)}{4l_0^{n+1}}, \quad (5.9)$$

where  $l_0$  is the equilibrium spring length and  $x_0 = l_0/l_m$ . The membrane shear viscosity is given by  $\eta_m = \sqrt{3}\gamma^T + \gamma^C/4$ .

$V_b$  represents the bending energy of the cell membrane. The bending resistance of the RBC membrane is modeled by

$$V_b = \sum_{j \in 1 \dots N_s} k_b [1 - \cos(\theta_j - \theta_0)], \quad (5.10)$$

where  $\theta_j$  is the instantaneous angle between two adjacent triangles having the common edge  $j$ ,  $\theta_0$  is the spontaneous angle, and  $k_b$  is the bending constant. Using the Helfrich model [50], the model bending coefficient  $k_b$  can be related to the macroscopic bending rigidity  $k_c$  as

$$k_b = 2k_c/\sqrt{3} \quad (5.11)$$

by approximating the *local* two adjacent triangle surface as spherical membrane.

$V_a$  and  $V_v$  represent the area and volume constraints to mimic the incompressibility of the lipid bilayer and the intracellular cytosol. The corresponding energy is defined by

$$V_{a+v} = \sum_{j \in 1 \dots N_t} \frac{k_d(A_j - A_0)^2}{2A_0} + \frac{k_a(A - A_0^{tot})^2}{2A_0^{tot}} + \frac{k_v(V - V_0^{tot})^2}{2V_0^{tot}}, \quad (5.12)$$

where  $N_t$  is the number of triangles in the membrane network,  $A_0$  is the triangle area, and  $k_d$ ,  $k_a$  and  $k_v$  are the local area, global area and volume constraint coefficients, respectively. The terms  $A$  and  $V$  are the total RBC area and volume, while  $A_0^{tot}$  and  $V_0^{tot}$  are the specified total area and volume, respectively. The corresponding area-compression  $K$  and Young's modulus  $Y$  are given by

$$K = 2\mu_0 + k_a + k_d, \quad Y = \frac{4K\mu_0}{K + \mu_0}. \quad (5.13)$$

For healthy red blood cell, we set the shear modulus  $\mu_0 = 6.8\mu N/m$  and bending rigidity  $k_{c0} = 2.4 \times 10^{-19}J$ , similar to experimental measurements [57, 83, 93]. The 2D cell membrane viscosity is set to be  $\eta_{mb} = 5.4R_0\eta_0$  by setting  $\gamma^T = 2.97R_0\eta_0$ ,  $\gamma^C = 0.99R_0\eta_0$ , where  $R_0 = 3.3\mu m$  is the mean RBC radius [84] defined by  $\sqrt{S/4\pi}$  ( $S$  is the surface area of a RBC). We refer to [36] for a detailed discussion on scaling from DPD units to physical units.

### 5.2.2.2 Leukocyte

Leukocyte is modeled as a triangulated spherical shape with radius of  $5\mu m$ , where the individual cell free energy is determined by  $V_{wbc}$  similar to Eq. (5.5). According to experimental measurements, a leukocyte exhibits larger cell rigidity than a healthy RBC; we set the Young's modulus to  $0.6 \times 10^{-3}N/m$  [20, 61] and bending rigidity to  $3 \times 10^{-18}J$  [99].

Under inflammation activated state, the experimental study by Turhan *et al.* [94] in transgenic-knockout mice shows that the inflammation stimulated (by cytokine TNF- $\alpha$ ) adherent leukocytes interact with SS-RBCs in later stages. In the present work, we adopt the Morse potential to represent the adhesive interaction between the SS-RBCs and the leukocytes

$$U_M(r) = D_e \left[ e^{2\beta(r_0-r)} - 2e^{\beta(r_0-r)} \right], \quad (5.14)$$

where  $r$  is the distance between cell-membrane vertices of RBCs and leukocytes,  $\beta$  determines interaction range, and  $r_0$  and  $D_e$  are the zero-force distance and well-depth of  $U_M(r)$ , respectively.

### 5.2.2.3 Cell-endothelium interaction

SS-RBC membrane expresses multiple types of abnormal protein epitopes due to the membrane injury by the intracellular HbS polymerization. Therefore, SS-RBCs exhibit adhesive interaction with endothelium cells through multiple pathways, e.g., adhesive interaction between the receptor VLA-4 expressed on the cell membrane and the ligand VCAM-1 expressed on the endothelium. Moreover, other adhesive receptors such as CD36 on SS-RBC membrane can interact with endothelial ligands such as  $\alpha_v\beta_3$  through the extracellular matrix proteins such as TSP. Similarly, leukocytes may interact with vascular endothelium through multiple pathways. A thorough review of the adhesive interaction mediated by the multiple proteins ex-

pressed on the cell membrane and their responses on the different inflammation level are discussed in [48].

Due to the physiological complexity and multi-function characteristics of the adhesive interaction, an explicit modeling of the individual receptor/ligand interactions is out of the scope of the current work. Moreover, the temporal scale of the protein molecular interaction is  $O(1)$  ps; therefore, a complete modeling the dynamic interaction is beyond the computational capacity on the time scale of the present work. Instead, the adhesive proteins are represented as the effective receptor particles expressed on the cell membrane and the effective ligand particles on the vascular endothelium, respectively. We employ a stochastic model [37, 47, 70] to represent the transient bond formation and dissociation. The adhesive interaction is modeled by the transient bond formation and dissociation between the receptor and ligand particles in a stochastic way. Specifically, we assume that the cell vertices can interact with the endothelial ligands within interaction distance  $d_{on}$ . For each time step  $\Delta t$ , transient bonds can be formed between the cell vertices and the endothelial ligands with probability  $P_{on} = 1 - e^{-k_{on}\Delta t}$ , while the existing bonds can be ruptured with probability  $P_{off} = 1 - e^{-k_{off}\Delta t}$ , where  $k_{on}, k_{off}$  are the reaction rates defined by

$$\begin{aligned} k_{on} &= k_{on}^0 \exp\left(-\frac{\sigma_{on}(l - l_0)^2}{2k_B T}\right), \\ k_{off} &= k_{off}^0 \exp\left(\frac{\sigma_{off}(l - l_0)^2}{2k_B T}\right), \end{aligned} \quad (5.15)$$

where  $\sigma_{on}$  and  $\sigma_{off}$  are the effective formation/rupture strengths. For existing bonds, the force between the receptors and ligands is defined by  $F(l) = 2k_s(l - l_0)$ , where  $k_s$  is the spring constant and  $l_0$  is the equilibrium length.

### 5.2.3 Intracellular Aligned HbS Polymer

In hypoxic conditions, a post-homogeneous HbS nucleus develops into polymer state and further form into bundles of sickle hemoglobin fibers. A single HbS fiber is composed of seven double strands in the style of a twisted rope with diameter of about  $d_0 = 21$  nm; fully representing the detailed structure of a single sickle hemoglobin fiber is too expensive in the scale of a single RBC ( $\sim 10\mu\text{m}$ ). On the other hand, experimental studies [16, 19] show that the morphology of SS-RBC is mainly determined by the intracellular *aligned* HbS polymer domain (AHP), e.g., see Fig. 5.3. To investigate the morphological transition of SS-RBC, we develop a CG model to represent a *bundle* of  $N_f$  sickle hemoglobin fibers where the detailed structure of a single fiber is omitted. Each bundle is represented by single DPD particles connected by visco-elastic bond interactions defined by Eqs. (5.6)–(5.8), yielding the Young's modulus  $Y \approx 0.1$  GPa.

The bending rigidity of the aligned hemoglobin polymer bundle is modeled by

$$V_{angle} = k_a(\theta - \theta_0)^2, \quad (5.16)$$

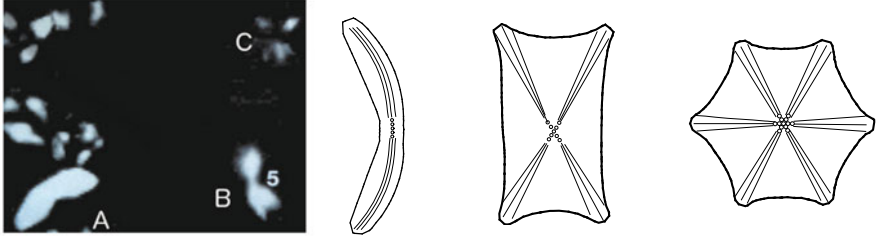


**Fig. 5.3.** *Left:* image of the intracellular aligned hemoglobin polymer (APH) domain. Label A denotes the APH domain within a classic, sickled shape cell. Label B denotes the center constrained APH domain observed in cell with holly leaf shape. Label C denotes the spherulite APH domain. *Right:* Sketches of typical cell shapes for deoxygenated SS-RBCs observed in experiments [19]. The three sketches represent the “sickle”, “holly leaf” and “granular” shapes of SS-RBCs. The various cell morphologies are mainly determined by the specific intracellular AHP configurations, represented by the solid lines. The dots represent the post homogeneous nucleus. Reproduced with permission from [19, 75]

where  $\theta_0$  is the spontaneous angle representing the deflection of the aligned hemoglobin polymer.  $k_a$  is the bending coefficient, determined by the bending modulus  $\kappa = N_f^2 \kappa_0$ , where  $\kappa_0 = 1.0 \times 10^{-24} \text{Nm}^2$  [98] is bending modulus of single HbS fiber. Finally, the aligned hemoglobin polymer model includes an in-plane dihedral potential to represent the fixed growth direction in global scale; the corresponding potential is given by

$$V_{\text{dihedral}} = k_d [1 + \cos(\phi_{ijkl})], \quad (5.17)$$

where  $i, j, k$  and  $l$  are four adjacent DPD particles on the modeled aligned hemoglobin polymer,  $\phi_{ijkl}$  is the instantaneous angle between the triangle  $\Delta_{ijk}$  and  $\Delta_{ikj}$ , and  $k_d$  is the constraint coefficient such that the growing fiber is in the same plane.

The growth rate of the sickle hemoglobin polymer was measured by Aprelev [2] as a function of monomer activity in bulk solution, given by

$$J = k_+ \gamma c - k_-, \quad (5.18)$$

where  $\gamma$  is the activity coefficient, and  $c$  is the monomer concentration determined by intracellular mean corpuscular hemoglobin concentration (MCHC).  $k_+$  and  $k_-$  are the monomer addition and subtraction rates.

The development of the AHP domain is modeled in a coarse-grained manner, where each single DPD particle is added to the end of the sickle hemoglobin polymer, forming elastic bonds with its adjacent particles with equilibrium length  $l_0 = 0.15 \mu\text{m}$ , as shown in Fig. 5.4. Since the CG polymer represents an aligned hemoglobin polymer bundle composed of  $N_f$  HbS fibers. The unit increase length per bundle  $\delta$  scales as

$$\delta = \delta_0 / N_f, \quad (5.19)$$

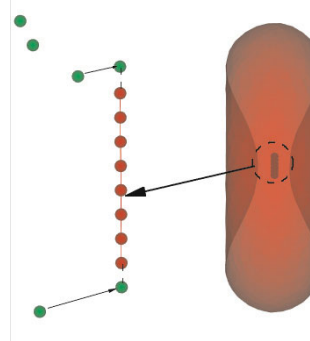


**Fig. 5.4.** Sketch of the coarse-grained model for the AHP domain development: free HbS monomers (green color), represented by the DPD particles, can potentially join with the pre-existed polymers (red color) with probability defined by Eq. (5.22). A linear polymer configuration is adopted in the current case to represent the specific growth direction. Multiple polymers are adopted to represent the AHP domains with finite angle width, see the holly leaf and granular shapes in Fig. 5.5. From [75]

where  $\delta_0 \approx 0.45$  nm is the unit increase length per single fiber. To this end, we choose  $N_f = 100$ , and the polymerization rate  $k_p$  and depolymerization rate  $k_{dp}$  scale as

$$k_p = \frac{N_f k_+ \gamma c \delta}{l_0}; \quad k_{dp} = \frac{N_f k_- \delta}{l_0}. \quad (5.20)$$

Numerical values of  $k_p$  and  $k_{dp}$  for different monomer concentration are presented and discussed in Sect. 5.3.1.

When the HbS polymers approach the cell membrane, the development of the AHP domain is modeled by adding single beads to the end of the polymer as “Brownian Ratchets” with the growth rate  $k_t$  given by

$$k_t = k_p e^{-(\mathbf{f}_s \cdot \hat{\mathbf{e}})\delta/k_B T} - k_{dp}, \quad (5.21)$$

where  $\mathbf{f}_s$  is the instantaneous stall force exerted on the end of the polymer bead, and  $\hat{\mathbf{e}}$  is the polymer growth direction. For each time step  $\Delta t$ , a single DPD particle is added to the polymer end with probability

$$P_t = 1 - e^{-k_t \Delta t}. \quad (5.22)$$

### 5.3 Heterogeneous SS-RBC Morphologies

SS-RBCs can undergo a transition into heterogeneous cell morphologies (sickle, holly leaf, granular, etc.) in hypoxic conditions. Kaul et al. [65] investigated the de-oxygenated SS-RBC morphology using the intracellular MCHC values. While the cell groups with moderate MCHC ( $< 35$  g/dL) exhibit apparent cell deformation

in deoxygenated conditions, most of the cells with high MCHC exhibit granular or near biconcave shapes. Experimental visualization of individual SS-RBCs using optical birefringence [16] and differential polarization microscopy [19] revealed that the wide variety of SS-RBC morphologies is closely related to the intracellular aligned hemoglobin polymer (AHP) configuration. Although AHP occupies only about 5% of the total sickle hemoglobin polymer [82], the SS-RBC morphology is mainly determined by the total number of the AHP domains and the configuration of each domain [16, 19] developed under various MCHC and deoxygenation rate conditions.

In this section, we employ the coarse-grained stochastic model for the growth of intracellular AHP domain presented in Sect. 5.2.3, calibrated with experimental measured bio-mechanical properties (Young's modulus, bending rigidity) and coupled with the multi-scale RBC model presented in Sect. 5.2.2.1, to systematically investigate the SS-RBC morphological transition process. In particular, we examine if the various cell morphologies and degrees of membrane distortion can be obtained from the present kinetic model without introducing any further *ad hoc* assumptions. Finally, we quantify the cell shapes using structural factors and compare the simulation results with medical image results.

### 5.3.1 Morphological Transition

SS-RBCs undergo various membrane distortions due to the variable stress exerted from the growing HbS polymer. The final cell shape is mainly determined by two factors: (i) the intracellular aligned hemoglobin polymer domain configuration. (ii) the effective sickle hemoglobin polymer growth rate  $k_t$ . Double nucleation theory [40, 41] indicates that the formation of a HbS polymer domain is initialized by the homogeneous nucleation of the HbS molecules and proceeds with explosive growth via polymer elongation and heterogeneous nucleation. The structure of the AHP domain is mainly controlled by the heterogeneous nucleation and the fiber growth rates [13, 44, 89], which is highly concentration dependent [16, 60]. With high MCHC values, a post-nucleation aggregate of twofold symmetry tends to develop into spherulitic domain through the fast growth of heterogeneously nucleated fibers and further deflection from the parent fibers. In contrast, for lower MCHC value, the angular widening of the polymer domain, originated from the fiber branching, is largely suppressed due to smaller heterogeneous nucleation rate as observed in both experiments [13] and numerical simulations [25]. Therefore, we relate the various AHP configurations to the MCHC values by constructing different types of post-homogeneous nucleuses, from which the angular width of polymer domain with various MCHC values observed in experiment can be obtained. We emphasize that the Hbs polymer configuration as an input rather than the natural consequence of the simulation output. Here we only model the aligned hemoglobin polymer domain (AHP) instead of the full polymer domain. Starting with a post-nucleus, the detail configuration development is omitted in the present work. Instead, we are particularly interested in the SS-RBC morphological transition process during the intracellular AHP development.

**Table 5.1.** Simulation parameters for each type of SS-RBC. The symbol “S”, “H” and “G” represents the sickle, holly leaf and granular shape of the SS-RBC.  $\mu$  and  $\mu_0$  represent the shear modulus of the deoxygenated SS-RBC and healthy RBC respectively;  $\theta_0$  and  $w$  represent the spontaneous deflection angle and the angular width of the aligned hemoglobin polymer domains, respectively

	MCHC	$\mu$	$\theta_0$	$w$
S	32 g/dL	$[20\mu_0, 80\mu_0]$	$[178.5^\circ, 179^\circ]$	$0^\circ$
H	34 g/dL	$[30\mu_0, 120\mu_0]$	$180^\circ$	$[45^\circ, 60^\circ]$
G	38 g/dL	$[40\mu_0, 2000\mu_0]$	$180^\circ$	$180^\circ$

The effective growth rate  $k_t$ , in contrast, depends not only on the MCHC values but also on the effective cell rigidities. While the HbS polymer growth rate in bulk  $J$  is directly related to HbS concentration by Eq. (5.18), the intracellular effective growth rate  $k_t$  also depends on the stall force  $\mathbf{f}_s$  exerted on the polymer ends by Eq. (5.21) and therefore depends on the cell rigidity. As the growing fibers approach and distort the cell membrane,  $k_t$  decreases due to the increasing stall force. The development of the aligned hemoglobin polymer domain is terminated automatically as the effective growth rate  $k_t$  approaches 0, defining the final cell morphological states without any further *ad hoc* parameters. To explore the dual effects of HbS polymer configuration and effective growth rate  $k_t$  on the morphological transition of SS-RBCs, we simulate the development of the AHP domain with various angular width values  $w$  and cell membrane shear modulus according to the experimental measurements [59]. Values of simulation parameters are summarized in Table 5.1.

First, we consider SS-RBCs with low MCHC value as 32 g/dL, corresponding to a bulk growth rate  $1.2 \times 10^4$  molecules s $^{-1}$ . Heterogeneous nucleation and branching is largely suppressed, yielding the largest portion of AHP domain, as noted in [19] and shown in Fig. 5.3. Therefore, we set the angular width  $w$  to 0. The HbS polymer domain develops along a specific direction with certain deflection due to heterogeneous growth process. To incorporate this effect, we set the spontaneous angle  $\theta_0 = 179^\circ$ . Figure 5.5 shows successive snapshots of the cell morphology at different stages of the aligned hemoglobin polymer development. Starting from the post-homogeneous nucleation, the aligned hemoglobin polymer domain develops towards the cell membrane. As the sickle hemoglobin polymer approaches the membrane, two spicules appear on the cell membrane near the interaction points. Moreover, as the length of the aligned hemoglobin polymer domain continuously increases and exceeds the size of the original cell, the cell membrane undergoes subsequent distortion. Accordingly, the elongated cell membrane follows the spontaneous curvature of the aligned hemoglobin polymer domain, resulting in the classical “sickle” shape of SS-RBC as widely observed under slow deoxygenation.

Next, we consider the SS-RBC morphological transition with medium MCHC value as 34 g/dL, with the bulk growth rate  $1.97 \times 10^4$  molecules/s. The AHP domain has finite angular width represented by the angle between the two main polymer

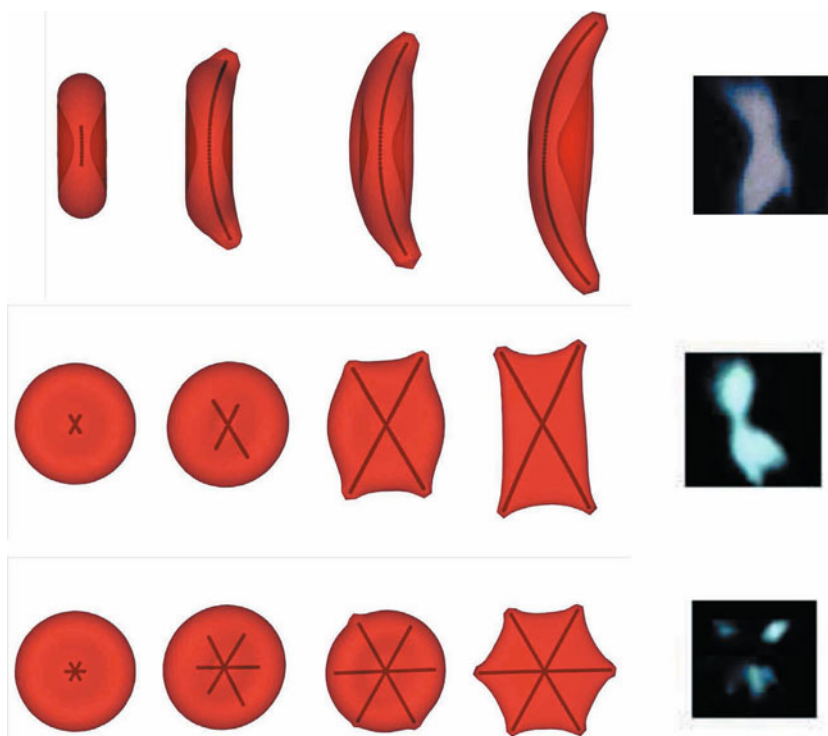


**Fig. 5.5.** Successive snapshots of the sickle cell with growing AHP domain, resulting in the classical “sickle” (upper), holly leaf (middle) and granular (lower) shape. The image on the right hand of each line represents the typical AHP domain in SS-RBCs with various cell morphologies adopted from [19]. Reproduced with permission from [19, 75]

branches, varying from  $45^\circ$  to  $60^\circ$ . Free sickle hemoglobin monomers can join the AHP domain at each of the four polymer ends. This configuration corresponds to another type of widely observed AHP domain named “central-constriction” according to [19]. The polymer domain resembles a dumbbell shape; a limited amount of aligned hemoglobin polymer is observed *near the center* of the nucleation while a large amount of aligned hemoglobin polymer is found in the outer regions. Successive snapshots of a SS-RBC with this type of AHP domain are shown in Fig. 5.5. The growing HbS fibers expand the cell along the growth direction and result in multiple spicules on the cell membrane. The final cell morphology resembles the “holly leaf” shape as widely observed in the SS-RBC with low/medium MCHC values [56, 65, 69].

Finally, we consider SS-RBC morphological transitions with high MCHC value 38 g/dL and the bulk growth rate  $5.3 \times 10^4$  molecules/s, corresponding to the spherulite configuration observed in HbS solution [13], individual cells [19], and numerical simulation [25]. With high MCHC value, the heterogeneous nucleation rate is large; the polymer domain can transform into spherulite configuration and

subsequently develop a radial symmetry, yielding in the smallest AHP density near the spherulite center as reported in experiments [19] and shown in Fig. 5.5. As the isotropic distribution of sickle hemoglobin polymer branches, free HbS monomers are added to the AHP domain with full angular symmetry, resulting in multiple spicules appearing on the cell membrane. However, different from the “sickle” and “holly leaf” cells, this type of SS-RBC does not bear further distortion. This is mainly due to two reasons: (i) the depletion of the free sickle hemoglobin monomers due to the high heterogeneous nucleation and growth rate. The polymer domain may run out of free sickle hemoglobin monomer as the domain develops towards the cell membrane; (ii) the larger cell rigidity with high MCHC values, resulting in much larger stall force on the growing polymer ends. The final cell morphology resembles the near-biconcave shape with multiple spicules on the cell surface, which corresponds to the granular shape of deoxygenated SS-RBC widely observed in the cells of high mean corpuscular hemoglobin concentration value or with fast deoxygenation procedure.

### 5.3.2 Morphology Quantification by 2D/3D Structural Factors

To further quantify the various cell morphologies obtained in the previous section, we introduce both 3D and 2D structural factors to characterize the individual SS-RBC membrane distortion. The 3D structural factors can be identified by the eigenvalue analysis of the gyration tensor defined by

$$G_{mn} = \frac{1}{N_v} \sum_i (r_m^i - r_m^C)(r_n^i - r_n^C), \quad (5.23)$$

where  $r^i$  is the coordinate of RBC vertex  $i$ ,  $r^C$  is the center-of-mass coordinate, and  $m, n$  represent the  $x$ ,  $y$ , or  $z$  direction.  $\lambda_1, \lambda_2$  and  $\lambda_3$  represent the three eigenvalues obtained from the gyration tensor, where  $\lambda_1 < \lambda_2 < \lambda_3$ . The *asphericity* shape factor (ASF) and the elliptical shape factor (ESF) are defined by

$$\begin{aligned} \text{ASF} &= ((\lambda_1 - \lambda_2)^2 + (\lambda_2 - \lambda_3)^2 + (\lambda_3 - \lambda_1)^2)/2R_g^4, \\ \text{ESF} &= \lambda_3/\lambda_2, \end{aligned} \quad (5.24)$$

where  $R_g$  is the radius of gyration defined by  $R_g^2 = \lambda_1 + \lambda_2 + \lambda_3$ . ASF measures the deviation of the RBC from a perfect sphere shape while ESF measures the degree of distortion on the plane perpendicular to the eigenvector of  $\lambda_1$ .

To systematically quantify the heterogeneous SS-RBC morphologies induced by the various AHP domain configuration and intracellular HbS growth rate  $k_t$ , we evaluate the structural shape factors for each type of SS-RBC within the physiological region of the cell shear modulus listed in Table 5.1. As shown in Fig. 5.6, the granular cells show similar characteristics with a healthy cell for both ASF and ESF. On the contrary, the elongated cells exhibit the largest deviation from the perfect biconcave shape. Compared with the elongated cells, the sickle cells exhibit smaller ASF due to the curvature membrane surface while the holly leaf cells exhibit smaller ESF due to the larger angular width of the AHP domain.

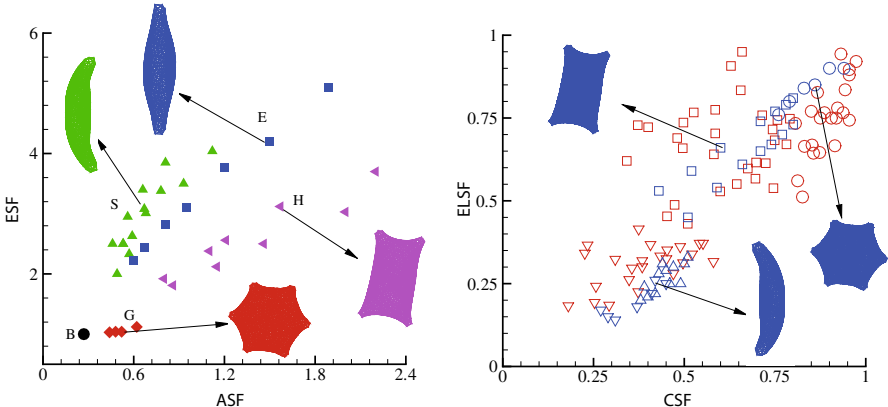


**Fig. 5.6.** *Left:* ASF and ESF for the various cell morphologies obtained. The label “B”, “G”, “S” and “H” represent the biconcave, granular, sickle, holly leaf shape, respectively. “E” represents an elongated cell shape similar to the sickle shape, where  $\theta_0$  is set to be  $180^\circ$ . The snapshots show the typical cell shapes for each type of SS-RBC morphology obtained in the present study. *Right:* 2D Circular (CSF) and 2D elliptical shape factors (ELSF) for different cell morphologies obtained from both medical image processes (red) and present simulations (blue). The circle and square symbols represent the shape factors of the granular and holly leaf SS-RBC. The red inverted triangle symbols represent both the “sickle” and the “elongated” SS-RBC obtained from experiment as they are unclassified in the experiment. The blue inverted triangle symbols represent the simulated “elongated” cells while the blue triangle symbols represent the simulated “sickle” cells. From [75]

Similar to the 3D structural shape factors, 2D morphological analysis has also been conducted using the medical images of different sickle cells, where the circular shape factor (CSF) and 2D elliptical shape factors (ELSF) are adopted to quantify the various SS-RBC morphologies [3,56]. Accordingly, we analyze the 2D structural properties of the SS-RBC with CSF and ELSF defined by

$$\text{CSF} = 4\pi \text{area}/(\text{perimeter})^2$$

$$\text{ELSF} = D_b/D_a, \quad (5.25)$$

where *area* and *perimeter* are the in-plane area and perimeter of the 2D projection of individual cells.  $D_a$  and  $D_b$  are the long and short diameters, respectively. CSF and ELSF characterize the deviation of a curve from the circular shape. These two factors are unit for a perfect circle and close to zero for a “line” shape. Similarly, the structural factors are analyzed for each type of the SS-RBC with shear modulus values shown in Table 5.1. Figure 5.6 plots both CSF and ELSF for the various cell membranes obtained from the above simulations, compared with the experimental results from medical image of SS-RBC in [56]. SS-RBCs are classified into the “sickle”, “holly leaf” and “granular” types according to the cell morphologies under deoxygenated states [56].

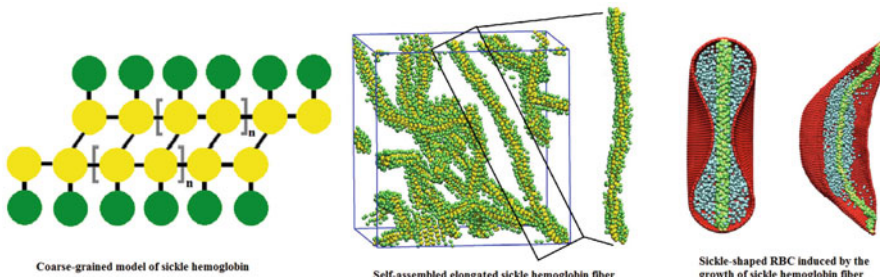


**Fig. 5.7.** Simulating HbS polymerization: *Left*: a schematic of a coarse-grained model of HbS adopted from [80]. One hemoglobin molecule consists of two hydrophilic particles (*green color*) and two hydrophobic particles (*yellow color*). *Middle*: self-assembled elongated step-like fibers. *Right*: Shape deformation of RBC induced by the growth of HbS fibers. From [80]

While the structural factors of SS-RBCs obtained from the simulation fall within the region of the experimental observations, the simulation results do not cover the entire range of experimental results. The difference is probably due to our limited knowledge of the physiological conditions for the SS-RBCs in the experiment as well as the over-simplification of the AHP model adopted in the present studies, where bundles of aligned sickle hemoglobin polymers are modeled on the length scale of  $O(1) \mu\text{m}$ . Modeling the HbS polymerization on sub-micrometer scale may reveal further insight of the SS-RBC sickling process. Some preliminary studies on this direction have been conducted in [80] and presented in Fig. 5.7. Moreover, several other physical conditions omitted in the present model, such as the heterogeneous HbS growth rate, depletion of free HbS monomer and multiple intracellular AHP domain, may also contribute to the heterogeneous distributions of cell morphologies.

Nevertheless, by using only the experimentally measured bulk HbS growth rate, we can successfully predict the major types of the SS-RBC morphologies observed in experiments. These heterogeneous cell morphologies, in turn, result in abnormal rheology of SS-RBC suspensions, as discussed in next section.

## 5.4 Abnormal Rheology of SS-RBC Suspensions

SS-RBC suspensions exhibit abnormal rheology and hemodynamics [65, 68, 69, 95] due to the heterogeneous cell morphology and elevated cell rigidity [34, 59]. In this section, we constructed a multi-scale model of SS-RBC with various cell morphologies resembling to the shapes predicted in the previous section and observed in experiments [65, 69]. Then we employ the constructed SS-RBC model to investigate the abnormal rheology of SS-RBC suspension under constant shear flow. We compute the shear viscosity and compare the simulation results with experimental measurements for heterogeneous cell rigidities and shapes. Next, we investigate the hemodynamics of the SS-RBC suspension by quantifying the elevated flow rate of

SS-RBC suspension in tube flow with a discussion on possible mechanisms for the heterogeneous hemodynamic properties.

### 5.4.1 Multi-scale Model of SS-RBC

As shown in previous section, SS-RBCs exhibit distorted shapes due to the interaction between intracellular HbS polymer and the cell membrane. In this section, we focus on the rheology of a collection of multiple SS-RBC suspension and therefore neglect the modeling of individual HbS polymer. Instead, we directly consider the surface tension applied on the cell membrane exerted by the growing HbS fibers, similar to the systems discussed in previous section and [21]. Fig. 5.8 shows the triangulated mesh of a healthy RBC with biconcave shape. The letters “A”, “B”, “C” and “D” represent four anchor points where the intracellular growing fibers can potentially approach the cell membrane. Surface tension exerted on the cell membrane further depends on the configuration of the HbS polymer domain. Similar to the previous section, for SS-RBCs with low MCHC, the intracellular HbS polymer tend to develop small angular width due to the limited heterogeneous nucleation and branching rates, resulting to the classical sickle shape. Accordingly, the stretching force is applied only on points “A” and “C” to represent the specific direction of the polymer growth. In contrast, for SS-RBCs with high MCHC, the intracellular HbS polymers tend to form spherulitic configurations due to the explosive growth via the high heterogeneous nucleation rate on the pre-existed HbS polymers, resulting in the granular shape. The growing HbS fibers may approach the cell membrane from multiple directions. Therefore, the stretching force is applied on all the four anchor points for this case. Values of simulation parameters are summarized in Table 5.2. Here we note that the stretching force adopted here is about 10 times smaller than

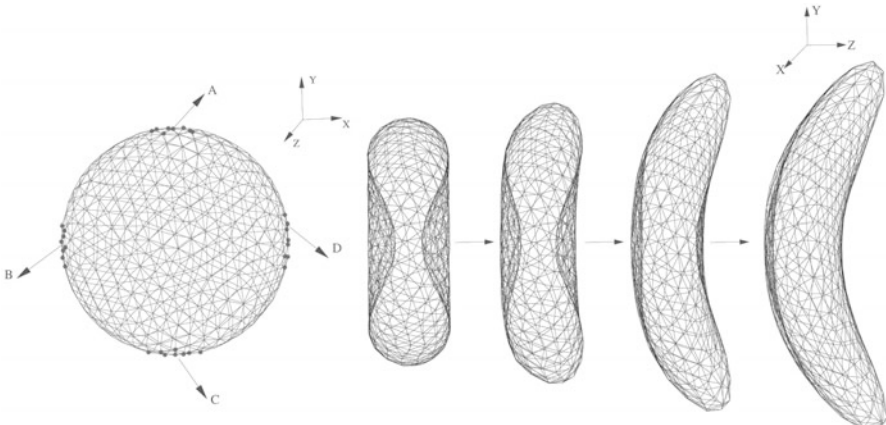


**Fig. 5.8.** *Left:* triangulated mesh of the RBC membrane. The label “A”, “B”, “C” and “D” represents the four anchor points where the stretching force is applied. *Right:* Successive snapshots of a RBC during the morphological transition to the “sickle” shape. From [77]

**Table 5.2.** Stretching force (pN) applied on the anchor points for each type of the cell morphology along x, y and z direction. “A”, “B”, “C”, “D” represents the anchor points sketched in Fig. 5.8

	A	B	C	D
S	(0, 55, 54)	(0, 0, 0)	(0, -55, 54)	(0, 0, 0)
G	(0, 23, 31)	(-23, 0, 31)	(0 - 23, 31)	(23, 0, 31)
E	(0, 55, 11)	(0, 0, 0)	(0, -55, -11)	(0, 0, 0)

the stall force of HbS fiber growth presented in Sect. 5.3. However, this is because we start the cell stretching procedure with a **healthy** RBC, where the cell rigidity is much smaller than the cell rigidity of SS-RBC we adopted in Sect. 5.3. Instead, if we start the cell stretching procedure by assuming the cell rigidity is similar to the value of SS-RBC, the stretching force is about 500 pN, similar to the stall force predicted by the lower scale model.

The successive snapshots in Fig. 5.8 show the shape transition of a SS-RBC from the biconcave to the classical sickle shape. Similarly, the granular shape is constructed by applying the stretching force on all of the four anchor points. Similar to Sect. 5.3.2, we quantify the distortion of SS-RBC membrane with the 3D *asphericity* shape factor (ASF) and the *elliptical* shape factor (ESF) defined in Eq. (5.24), as shown in Fig. 5.9.

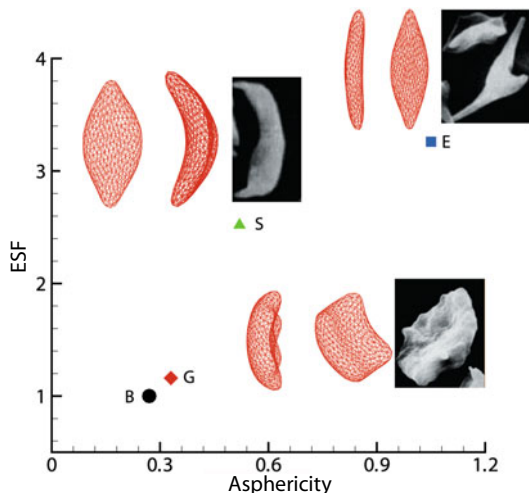


**Fig. 5.9.** Asphericity and elliptical shape factors for the different shapes of the sickle cells. The label “G”, “S” and “E” represents the granular, sickle and elongated shape of the sickle cells respectively, and the inset sketches represent their morphologic projections on the x-z and x-y planes; the inset images represent the experimental observations on different morphologic states of deoxygenated SS-RBC by scanning electron microscopy, reproduced from [69]. The label “B” corresponds to the original biconcave shape, whose morphological projection is shown in Fig. 5.8. Reproduced with permission from [69, 77]

### 5.4.2 Shear Viscosity of SS-RBC Suspensions

With the SS-RBC model constructed above, we investigate the abnormal rheology of SS-RBC suspension in shear flow. We first consider the shear flow system with hematocrit Hct = 45% following the experiment of [95]. The viscosity of the solvent is chosen to be  $\eta_0 = 1.2 \text{ cp}$ . The specific morphological characteristics of the SS-RBCs were not specified in the experiment. However, we note that the reported MCHC value of the sickle cell is relatively high ( $37.7 \text{ g/dL}$ ). Periodic Lees-Edwards boundary conditions are imposed on the fluid system where different shear rates can be obtained. The simulation domain has the size of  $40 \times 38 \times 28$  in DPD units, with 182 cells placed in the system. Therefore, the *granular* shape is adopted for the present simulation. A short range repulsive force is imposed for volume exclusion between the cells. Fig. 5.10 shows the viscosity computed for both healthy and diseased blood under different shear rates. For both types of blood, good agreement with the experimental results is obtained. It is well-known that healthy blood behaves as non-Newtonian fluid with shear-dependent viscosity [39]. Under high shear rate, blood cells undergo large deformation with fluid properties pronounced; in contrast, blood cells behave as solid-like, less deformed under low shear rate conditions, resulting in relatively higher viscosity. Therefore, the viscosity of healthy blood increases as the shear rate decreases, as shown in Fig. 5.10. On the other hand, the deoxygenated SS-RBC suspension shows elevated viscosity values, which are nearly independent of the shear rate. This result is mainly due to the largely elevated cell rigidity; the deoxygenated SS-RBC cannot be deformed under the high shear rate employed in the experiment [95]. Therefore, SS-RBCs exhibit “solid” behavior throughout the entire shear rate regime, leading to this transition from non-Newtonian to Newtonian flow.

Moreover, we examine the effect of the cell morphology on the rheology of SS-RBC suspension under shear flow. A similar experimental study has been conducted by Kaul et al., where the shear viscosity of SS-RBC suspensions subjected to both fast and gradual deoxygenation procedures [69] was measured. Two distinct stages were observed for SS-RBC suspensions subjected to the fast deoxygenation. The shear viscosity of the SS-RBC suspensions exhibits fast elevation within the first 7 mins of deoxygenation accompanied with the cell morphology transition to granular shape. However, the shear viscosity gradually decreased during increased deoxygenation, accompanied with a large portion of cells transitioned into extremely elongated shape with the intracellular HbS fibers aligned in one direction. In contrast, SS-RBC suspensions subjected to gradual deoxygenation procedure showed monotonic elevation of shear viscosity and the formation of the sickle shape of blood cells over a period of 30 mins until the full deoxygenated state was achieved. Following this experimental study, we computed the shear viscosity of SS-RBC suspensions with the three distinct types of sickle cell reported in the experiment (Hct = 40%). Figure 5.11 shows the shear viscosity values under shear rate from  $25$  to  $75 \text{ s}^{-1}$  with similar cell rigidity applied to all the three types. Similar to Fig. 5.10, the SS-RBC suspensions show shear-independent Newtonian behavior. Moreover, shear viscosity further depends on individual cell shapes, with the value 13.8, 13.1

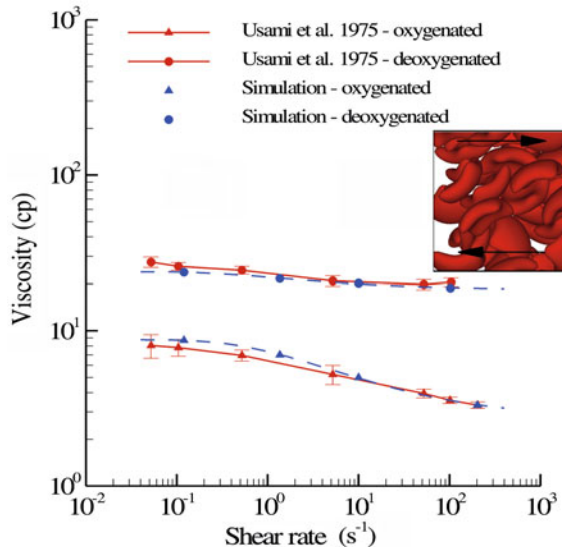


**Fig. 5.10.** Shear viscosity of the healthy blood and SS-RBC suspensions with Hct = 45%. The dash lines represent the fitted curve to the simulation result by  $\eta = be^{-a/\gamma^{0.5}} + c$ , where  $\gamma$  is the shear rate.  $a$ ,  $b$  and  $c$  equal to  $1.43 s^{-1/2}$ ,  $-6.04 \text{ cp}$ ,  $8.78 \text{ cp}$  for healthy blood and  $1.08 s^{-1/2}$ ,  $-5.5 \text{ cp}$ ,  $23.9 \text{ cp}$  for deoxygenated SS-RBC suspension. The inset plot shows a snapshot of the “granular” SS-RBCs in shear flow. From [77]

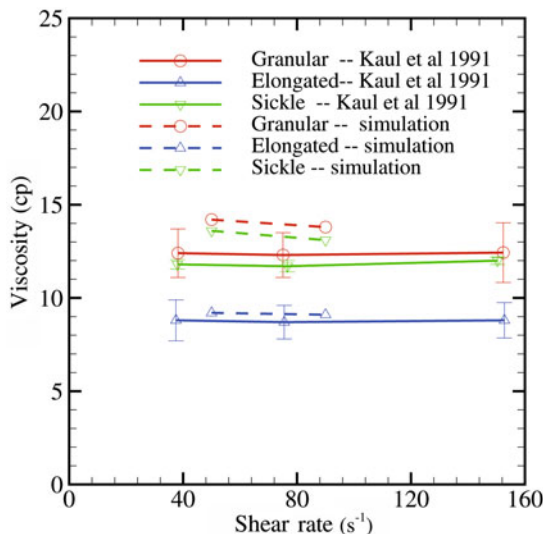


**Fig. 5.11.** Shear viscosity of the sickle blood flow with different cell morphologies reported in [69], Hct = 40%. From [77]

and 9.6 cp for the granular, sickle and elongated shape, respectively. The simulation results are consistent with the experimentally observed progressive decrease of the viscosity during the increased deoxygenation, since a large portion of granular cell transforms into the elongated shape during the procedure. This result reveals the heterogeneous “effective volume” among the different types of SS-RBC under the shear flow system [69]. Given the same Hct, heterogeneous cell morphologies may further affect the momentum transport between the cells, resulting in different shear viscosity values.

### 5.4.3 SS-RBC Suspension in Tube Flow

The hemodynamics of SS-RBC suspensions was studied in an isolated vasculature in [65] with different cell groups. While the oxygenated SS-RBC suspensions exhibit hemodynamics similar to healthy blood flow, the deoxygenated SS-RBC suspensions show heterogeneous hemodynamics among the different cell groups. Similar to the experimental study [65], we simulate SS-RBC suspensions in a tube flow system with  $Hct = 30\%$ . We set the diameter of the tube to  $9.0\mu m$  as in capillary flow, since the detailed size and topology information of the microvasculature for the experiment is unknown. In this sense, we do not expect the apparent viscosity obtained from the simulation to match exactly with the experiment results. Instead, we focus on the effect of different SS-RBCs groups on the flow resistance in the microcirculation.

Deoxygenated blood flow is modeled as a suspension of SS-RBCs with sickle and granular shapes, where the same cell rigidity is applied to both cell groups. The viscosity of the cytosol is set to  $4\eta_0$  and  $50\eta_0$  for the healthy and deoxygenated blood flow, where  $\eta_0 = 1.2$  cp is the viscosity of the blood plasma. The increase of the flow resistance for the sickle and granular shapes under different oxygen tensions is shown in Fig. 5.12a. While SS-RBC suspension of both cell groups show further increased flow resistance at deoxygenated state, the granular type of blood flow shows a more pronounced elevation compared with the sickle shape. This result is also consistent with the experimental study of SS-RBCs transiting in a micro-fluidic channel conducted by E. Du and M. Dao [1]. Figure 5.12b shows the transit velocities of individual SS-RBCs with different cell morphologies (discocyte, oval, sickle) through a periodic array of obstacles ( $4\mu m$  between the two obstacles). The cell group of the “sickle” shape exhibits the largest cell velocity.

One possible explanation for the above result, as proposed by the Kaul et al., is the different orientational distribution of SS-RBCs in the capillary: a cell of sickle shape tends to flow along the axis of the tube as also observed by La Celle et al. in experimental studies in [73]. This is consistent with the inset snapshots of the sickle and granular cells in Fig. 5.12a. To quantify this phenomenon, we computed the *cell orientation angle distribution* for different cell groups in the tube flow, as shown in Fig. 5.13. The cell orientation is defined by the angle  $\theta$  between the flow direction and the eigenvector of the gyration tensor  $V_1$  defined by Eq. (5.23). Compared with the granular cell, the orientation angle of the sickle cell shows a wider distribution for larger value, indicating that the sickle shape SS-RBCs are more likely to ori-

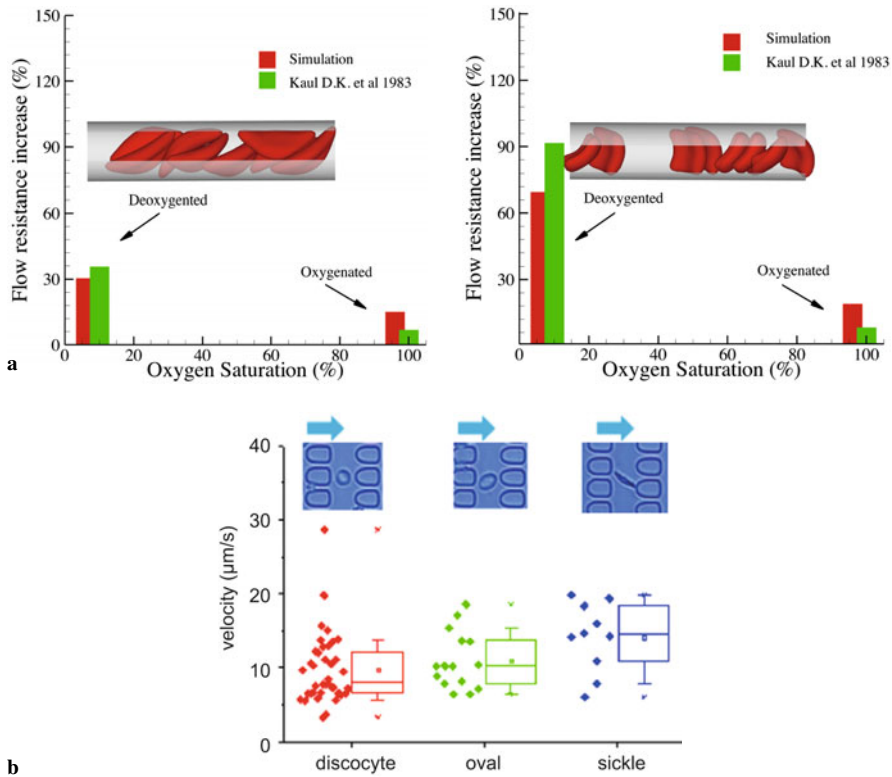


**Fig. 5.12.** (a) Increase of the flow resistance induced by the sickle blood flow for both granular and sickle shapes. The inset plot shows a snapshot of the sickle cells in the tube flow; (b) Experimental study on SS-RBC cell transition velocity for different cell morphologies through a periodic array of obstacles in microchannel, courtesy of Dr. E Du and Dr. Ming Dao at MIT. From [1, 77]

ent along the flow direction. Moreover, we note that this morphology of the sickle SS-RBC in the present study resembles to the irreversible sickle cell (ISC) generated during multiple deoxygenation-reoxygenation cycles, with its rheological properties as consistently noted by Kaul in [65] “[...] deoxygenated ISC once in the capillary microcirculation of mice orient themselves along the vessel axis, posing no significant problem to the capillary flow [...]” Therefore, this configuration results in a lower flow resistance compared with the granular cells.

Finally, we note that the simulation of SS-RBC suspension in tube flow does not induce blood occlusion in the present study. We performed several sets of simulations with different combinations of cell rigidities and cytosol viscosity; however, no full occlusion was observed in any of these simulations. Moreover, the sickle shape SS-RBC, the widely believed pre-cursor of the vaso-occlusion crisis, actually may result in lower flow resistance than other cell groups. We note that this is mainly due

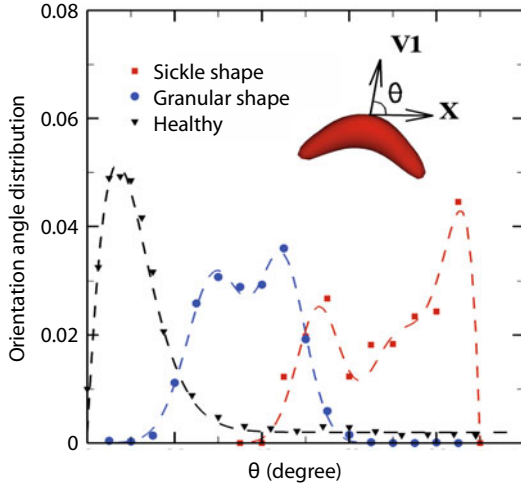


**Fig. 5.13.** Cell orientation angle distribution  $f(\theta)$  for healthy, sickle and granular cells in pipe flow. The cell orientation is defined by the angle  $\theta$  between the flow direction ( $x$ ) and the eigenvector  $V1$  of the gyration tensor, as shown in the inset plot. From [77]

to the omission of the cell-endothelium adhesive interaction in the present study; we address this issue in the next section.

## 5.5 Vaso-occlusion crisis

Vaso-occlusion crisis is the key hallmark out of the three biophysical characteristics related to SCA. While early studies suggested that this crisis is triggered by the blockage of single sickle/elongated SS-RBC in capillaries, later studies [8, 62–64] have shown that vaso-occlusion mainly occurs in post-capillaries (the microvasculatures following the capillaries). Moreover, some studies demonstrated that there exists no direct correlation between the percentage of the dense SS-RBCs and the disease severity [5], which is consistent with our numerical simulation of the hemodynamic of SS-RBC suspensions in capillaries presented in Sect. 5.4.3. On the other hand, Hebbel *et al.* [49] and Hoover *et al.* [55] find that there exists abnormal adhesive interaction between the SS-RBCs and cultivated endothelial cells. Recent studies further revealed that vaso-occlusion is a complex process triggered by the interactions between multiple cell groups [6, 15, 94], including SS-RBCs of heterogeneous density groups, vascular endothelial cells, and inflammation-activated leukocytes, with each group contributing differently to the vaso-occlusion crisis.

In this section, we employ the multi-scale model of SS-RBC to investigate the biophysical characteristics of the vaso-occlusion in SCA. We quantify the specific physiological conditions triggering the occlusion crisis and therefore identify the specific contribution of individual cell groups within the occlusion process. First,

we investigate the adhesive dynamics of different SS-RBC groups under shear flow. Next, we quantify the heterogeneous cell adhesive properties in static condition and examine the results using free energy analysis. Finally, we study the hemodynamics of SS-RBC suspensions in post-capillaries as well as in venular flows, where inflammation-activated leukocytes play an important role.

### 5.5.1 Adhesive Dynamics under Shear Flow

*In vitro* studies [7] by Barabino *et al.* show that SS-RBCs exhibit heterogeneous cell adhesivity among different density groups. The light density group shows the largest adhesion while the densest irreversible sickle cells (ISCs) shows the least adhesion. *Ex vivo* studies by Kaul *et al.* [62] further examined the alteration of SS-RBC adhesivity after a dehydration/rehydration treatment on individual cell groups and found that the cell adhesivity of the deformable SS2 and the dense SS4 cells can be reversed after controlled treatment. They suspected that different cell groups have similar “adhesion potential”, while the heterogeneous cell adhesivity is mainly attributed to the different cell morphological and bio-mechanical properties among the multiple cell density group. Accordingly, we investigate this hypothesis by simulating the adhesive dynamic of SS-RBCs with different cell rigidity and morphologies.

As shown in Fig. 5.14, we consider three different SS-RBCs under shear flow. Cell I represents a SS2 deformable discocyte. The cell rigidity is similar to the healthy RBC and we set the shear modulus  $\mu_0 = 6.8\mu N/m$  and bending rigidity  $k_{c0} = 2.4 \times 10^{-19}J$ , i.e., similar to healthy cell rigidity [57, 83, 93]. Cell III represents an ISC generated through the deoxygenation-reoxygenation process; we set the shear modulus  $\mu = 10\mu_0$  following [17, 59]. Modification to cell bending rigidity in the deoxygenation-reoxygenation process is unknown; here we set  $k_c = 10k_{c0}$  and also conduct sensitivity studies. Cell II represents a rigid discocyte [33] with medium MCHC value; we set  $\mu = 3\mu_0$  and  $k_c = 3k_{c0}$  for the comparative study.

Following [62], we assume that the three cells have similar “adhesive potential,” and set identical adhesive parameters. With the same shear rate  $\dot{\gamma} = 192s^{-1}$ , the three cells exhibit substantially different adhesive dynamics as shown in Fig. 5.14a. Cell I exhibits firm adhesion to the lower plate with contact area around  $40.5\mu m^2$ . Cell II, however, shows weaker adhesivity than Cell I. Although it also exhibits transient adhesion to the lower plate initially, it undergoes a periodic flip movement along the flow direction and eventually detaches from the plate after two to three flips, as characterized by the peak values of the instantaneous cell velocity at 0.30, 0.53 and 0.72s. Accordingly, the contact area achieves minimum values at those times. Different from cells I and II, cell III does not show any adhesion to the plate; instead, it directly detaches from the lower plate and moves freely without adhesive bonds established thereafter. Given the same “adhesive potential”, the present results validate the hypothesis that heterogeneous cell adhesive dynamics is mainly due to the different cell rigidities and peculiar cell morphologies. To further investigate this effect, we use free energy analysis to quantify the cell adhesion in static condition.

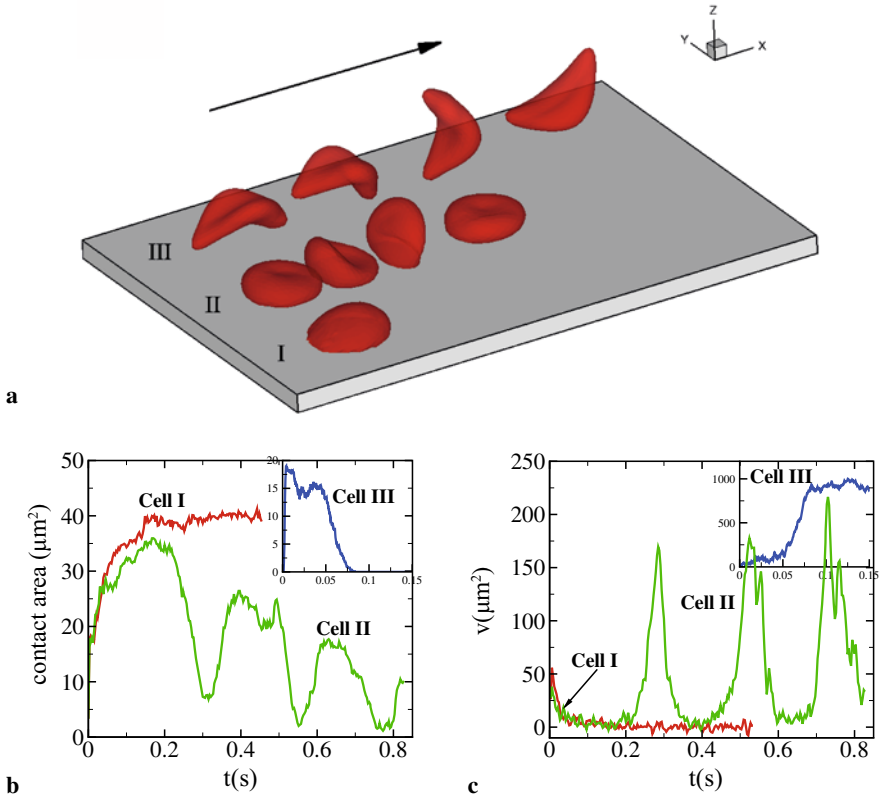


**Fig. 5.14.** Sickle cells in shear flow: (a) Successive snapshots of SS-RBCs in shear flow. The labels I, II and III correspond to a deformable SS2 cell, rigid SS3 cell and ISC, respectively. The arrow indicates the flow direction; (b–c) Instantaneous contact area and velocity for SS-RBC in shear flow conditions. From [76]

### 5.5.2 Static Condition and Free Energy Analysis

Similar to the previous section, cells I, II, and III are initially placed at a distance of  $0.12\mu\text{m}$  from a plane coated with ligand particles, where same adhesive parameters are adopted. We compute the instantaneous contact area for each cell until steady state is reached, as shown in Fig. 5.15a. While the contact area for all of the cells increases sharply to  $10\mu\text{m}^2$  within the initial stage, the contact area between the plate and cell I and II further increases to  $30\mu\text{m}^2$  and  $21\mu\text{m}^2$  at the later stage. This inverse relationship is consistent with the different cell adhesive dynamics in shear flow system, and it can be understood by the free energy analysis during the adhesion process. If we define the cell and the ligand particles as a single system, the change of total free energy  $\Delta E$  during the process can be written as

$$\Delta E = \Delta E_{deform} - \Delta E_{adhesion}, \quad (5.26)$$

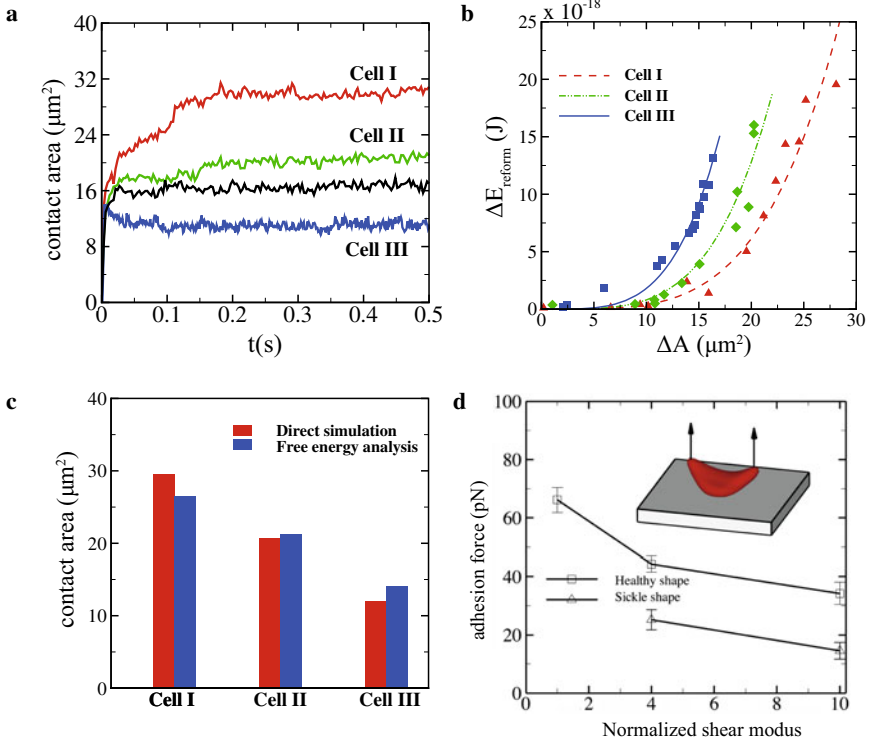


**Fig. 5.15.** Adhesion in static conditions: (a) Instantaneous contact area between the SS-RBC and the plate coated with adhesive ligands. The black curve represents the contact area of a discocyte with cell rigidity similar to the ISC (cell III); (b) Increase of the cell free energy as a function of the contact area; (c) Cell contact area  $\Delta A$  computed from direct simulation and free energy analysis by Eq. (5.27); (d) Adhesive force between the cell and the plate as a function of the membrane rigidities for cell morphologies. The error bar represents the adhesive force computed from four independent simulations. The inset plot shows a sketch of the simulation set up, where a uniform lift force is applied on the upper part of an ISC. From [76]

where  $\Delta E_{\text{deform}}$  represents the increase of the cell free energy due to the deviation of cell shape from the equilibrium state.  $\Delta E_{\text{adhesion}}$  represents the absolute value of the energy decrease due to the adhesive bond formation between the cell and the ligand particles. The final state is determined by the balance between the two free energy terms. A deformable SS2 cell is prone to form larger contact area than the rigid cell; it can be understood as follows. For SS2 cell with smaller cell rigidity, the energy barrier induced by the cell deformation is relatively small, and free energy decrease induced by cell adhesion plays a dominant role, resulting in further cell deformation and larger cell contact area. In contrast, the rigid SS4 cell exhibits “solid” like properties with a larger energy barrier for cell deformation. The adhesive interaction between the cell and plate is more like the attraction between two solid objects where

the cell deformation plays a less important role. After the initial incubation stage, the adhesive interaction driven by the bond formation cannot overcome the free energy increase induced by the cell deformation, and therefore it prohibits further increase of the contact area.

Figure 5.15b shows the  $\Delta E_{deform}$  as a function of the contact area  $\Delta A$  for the three cells induced by different adhesive affinities. The numerical results are fitted by  $\alpha \Delta A^4$ , where  $\alpha$  depends on the cell rigidity of individual cells. The adhesion free energy  $\Delta E_{adhesion}$  can be approximated by  $\beta \Delta A$ , where  $\beta$  is the energy coefficient determined by the adhesive affinity. In the present work, the adhesive interaction is modeled by the adhesive bond interaction between ligands coated on the substrate and the receptors on the cell membrane. While each receptor on cell membrane can form multiple adhesive bonds with ligands, each ligand can only form one adhesive bond with the receptor. Therefore,  $\beta$  can be approximated by  $k_s l_s^2 n_{ligand}$ , where  $k_s$  is the adhesive spring bond constant,  $l_s$  is the cut-off length of the adhesive bond interaction, and  $n_{ligand}$  is number density of the ligands on the substrate. The equilibrium state is determined as the state with minimum free energy term, e.g.

$$\Delta A = \left( \frac{\beta}{4\alpha} \right)^{1/3}. \quad (5.27)$$

According to Fig. 5.15b,  $\alpha$  is about  $3.8 \times 10^{25}$ ,  $8.0 \times 10^{25}$  and  $1.8 \times 10^{26} J/m^8$  for cell I, II and III. This yields the contact area  $A = A_0 + \Delta A$  approximately 26.5, 21.3 and  $14.0 \mu m^2$  for cell I, II and III, where  $A_0$  is the initial contact area without any adhesion, which is  $3.5 \mu m^2$  for cell I and II, and  $0.6 \mu m^2$  for cell III. This result agrees well with the direct simulation results of  $29.5$ ,  $20.7 \mu m^2$  and  $12.0 \mu m^2$ , as shown in Fig. 5.15c. Compared with the shear flow system, the contact area of cell I computed in static condition is smaller. This discrepancy is mainly due to the increased cell deformation induced by the hydrodynamic interaction under shear flow condition. The extended cell membrane facilitates the bond formation and result in larger contact area. For cell III, we note that the contact area is smaller than the value for a discocyte with similar cell rigidity. This result indicates that the peculiar cell morphology may further affect the cell adhesivity.

To quantify the effects discussed above, we directly compute the adhesive force between the plate and SS-RBCs with different cell rigidities and morphologies. The adhesive force is determined as the lift force that detach the cell from the plate in quasi-static process, as shown in Fig. 5.15(d). Similar to the contact area, the adhesive force also exhibits an inverse relationship with the cell rigidity. Moreover, compared with the discocyte, the ISC exhibits smaller adhesive force given the similar cell rigidity, indicating less adhesivity induced by its peculiar cell morphology.

### 5.5.3 SS-RBC Suspensions in Post-capillaries and Venules

We model blood circulation of SS-RBC suspensions in post-capillaries as in a tube with diameter  $D = 10 \mu m$  and hematocrit Hct = 30% similar to [62, 64]. As shown in Fig. 5.16, small green particles represent the adhesive ligands which can interact

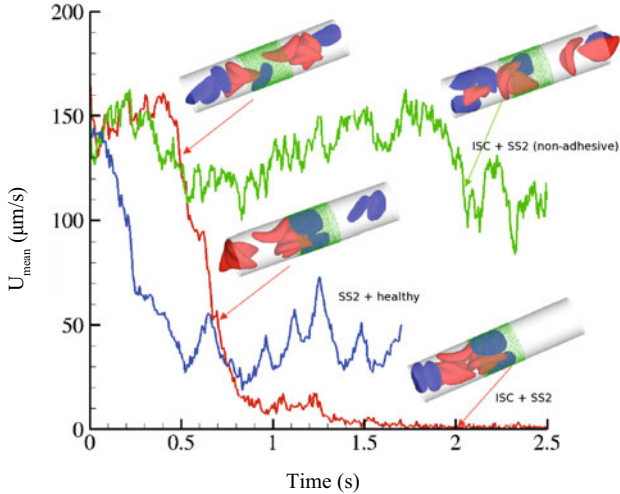


**Fig. 5.16.** Vaso-occlusion in post-capillaries: instantaneous mean velocity of blood flow in a cylindrical tube of  $D = 10\mu\text{m}$  infused with different SS-RBC suspensions. The red curve represents the resultant velocity infused with SS2 and ISC cell groups. The inset plots represent the instantaneous snapshots where SS2 cells adhere to vessel wall, consequently trapping the ISCs and resulting in cell blockage. The green curve represents the blood velocity infused with SS2 and ISC cell groups, where adhesive interaction is only applied to the ISC group. The time axis is scaled by 0.5 for better visualization. The inset plot represents a snapshot where transient adhesion is established between ISC and the tube wall. Steady flow is recovered as the cell detaches from the tube wall. The blue curve represents the instantaneous velocity of blood flow infused with SS2 and healthy cell groups. Blood flow exhibits a slow down but not a full occlusion. From [76]

with the SS-RBCs. To quantify the distinct role of different cell groups, we infuse suspensions of different cell groups into the tube by applying a pressure gradient  $\Delta P/\Delta x = 8.7 \times 10^4 \text{ Pa/m}$ .

First, we consider suspensions composed of SS2 cells (labeled by blue) and ISC cells (labeled by red) with ratio 1 : 1. We prepare the steady flow by turning off the adhesive interaction. The mean flow velocity at the initial stage is round  $150\mu\text{m/s}$ . Starting from the steady state ( $t = 0$ ), we turn on the adhesive interaction between the SS-RBCs and the ligand particles and compute the instantaneous flow velocity across the tube, as represented by the red curve in Fig. 5.16. Blood flow maintains steady state until one of the SS2 cells adheres to the vessel wall, triggering a sharp decrease of blood flow around  $t = 0.5\text{s}$ . As a positive feedback, the decreased blood flow induces more SS2 cells adherent to the vessel wall, leading to a further decrease of flow rate at  $t = 0.63\text{s}$  and  $t = 0.7\text{s}$ . Moreover, these adherent cells decrease the effective vessel lumen near the adherent region resulting in a secondary trapping of the ISC groups. The final occlusion state is reached around  $t \approx 2\text{s}$  with cell patterns similar to the experimental observations [62, 64]. This result demonstrates that under

physiological conditions similar to microcirculation in post-capillaries, the *interplay* of deformable SS2 cells and ISCs can potentially trigger full blood occlusion. Although the same adhesive parameters are applied to the two cell groups, no adherent ISC is observed in the present simulations. Several independent sets of simulation were conducted with different initial conditions and similar patterns of full occlusion were observed.

To identify the unique contribution of the deformable SS2 cell group, we performed a similar simulation for suspension consisting of ISC and healthy RBCs. Starting from the steady flow at  $t = 0$ , we compute the instantaneous velocity of the blood suspension for 6 s, as represented by the green line in Fig. 5.16. Blood flow shows decreased velocity due to the ISC-ligand interaction, where transient adhesive bonds can be formed. However, blood occlusion is not observed in this simulation since blood flow can recover the initial flow rate when the adherent ISCs detach from the tube wall, as consistently observed in *ex vivo* studies [62], where the ISCs, when infused alone, did not result in microvascular blockage. This result reveals the specific contribution of the SS2 cell group in the vaso-occlusion crisis and is consistent with clinical investigation results [5].

In contrast, the ISC cell group, contributes differently to the occlusion crisis. We investigate its unique contribution by simulating the blood suspension mixed with the deformable SS2 and healthy cells. Starting from the steady flow at  $t = 0$ , we compute the instantaneous velocity of the blood flow, as represented by the blue line in Fig. 5.16. Although blood flow slows down due to the cell adhesion at  $t = 0.25s$  and  $t = 0.48s$ , full occlusion is not observed in the present simulation. In particular, we find that healthy RBCs can squeeze through the sieve-like region formed by adherent SS2 cells due to its high deformability. The present result, in turn, identifies the specific contribution of the ISC group in the vaso-occlusion crisis. Although the ISC group may not participate in the cell adhesive interaction with the vascular wall, it serves as the particular cell group trapped by adherent cells in the post-capillaries.

Sensitivity studies have been conducted with different tube diameters and hematocrit values. Simulation results show that for microcirculation of SS-RBC suspensions, blood occlusion mainly occurs in post-capillaries with diameter smaller than  $13.4\mu m$ . However, recent studies [67] have shown that SCA is often accompanied with an inflammatory endothelial phenotype with elevated leukocyte recruitment in blood circulation, where the inflammation-stimulated leukocytes may further interact with SS-RBC, leading to blood occlusion in venular flow [94]. We explore this process by employing the multi-scale model of SS-RBC and the leukocyte model presented in Sect. 5.2.2.2. First, we simulate the SS-RBC suspension with a leukocyte in a tube with diameter  $D = 13.4\mu m$  and Hct = 30%. Starting from the initial condition ( $t = 0s$ ), the leukocyte migrates toward to the tube wall with firm adhesion established at  $t \approx 0.47s$ . The blood velocity drops from  $150\mu m/s$  to  $45\mu m/s$  during this stage. The adherent leukocyte further interacts and traps the SS-RBCs, resulting in full occlusion at  $t \approx 2.4s$ . For venular flow with larger diameter, multiple leukocytes recruitment may occur in the inflammation regions. Following [94], we simulate a SS-RBC suspension with three leukocytes in a tube with diameter  $D = 20.4\mu m$  and Hct = 13.4%. Starting with the steady flow free of cell adhesion ( $t$

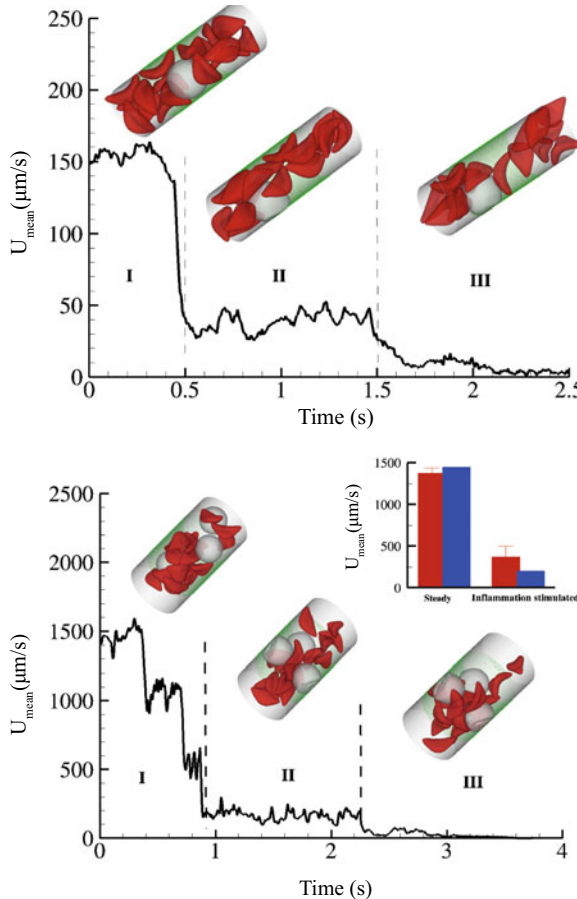


**Fig. 5.17.** Effect of leukocytes: instantaneous mean velocity of the blood flow in a tube of  $D = 13.4\mu m$   $Hct = 30\%$ , 1 leukocyte (a) and  $D = 20.4\mu m$ ,  $Hct = 13\%$ , 3 leukocytes (b). The inset snapshots represent blood cells in free motion, leukocyte adhesion and blood occlusion states. For  $D = 20.4\mu m$ , the inset plot represents the blood flow velocity of the present study (blue) and the experimental results (red) [94], where measurements are taken on 23–41 venules with average diameter  $20.9 \pm 1.3$  and  $24.9 \pm 1.8\mu m$  before and after inflammation-stimulation. From [76]

= 0s), the following blood flow can be roughly divided into three stages. In stage I, instantaneous blood velocity drop to  $160\mu m/s$  due to the leukocyte recruitment at  $t = 0.40, 0.71, 0.88$ s. In stage II, blood flow undergoes further slow down due to the moderate SS-RBC - leukocyte interaction. Stage III represents the late stage of the inflammation response, where the SS-RBC - leukocyte interaction is further intensified, resulting multiple SS-RBC trapped on the leukocytes and the full occlusion at  $t \approx 3.2$ s.

## 5.6 Conclusions

In this chapter, we presented a comprehensive computational framework based on the dissipative particle dynamics (DPD) method to investigate the three key hallmarks (heterogeneous morphology, rheology and vaso-occlusion) of the hematological disorder SCA. The multi-scale nature of the present mesoscopic model enabled us to address the different dynamic processes over a wide range of length and time scales involved in this disease. We modeled the SS-RBC morphological transition by constructing a coarse-grained stochastic model to represent the development of the intracellular aligned sickle hemoglobin polymer domain. By using only the experimentally measured bulk growth rate of the sickle hemoglobin polymer as the input, the model successfully predicted the typical sickle cell morphologies without introducing further *ad hoc* assumptions. The inferred cell morphologies enabled us to further explore the rheology of heterogeneous SS-RBCs suspensions with accurate prediction of the shear viscosity for different cell rigidity and morphologies. In particular, our simulations of the hemodynamics of SS-RBC suspensions suggested that the sickle/elongated SS-RBC suspension, once in microcirculation, does not induce vaso-occlusion by itself. Moreover, the flow resistance induced by this cell group could be even lower than other cell groups. This result, although counter-intuitive, is consistent with recent experimental studies on vaso-occlusion crisis.

We explored the vaso-occlusion crisis by further introducing the adhesive cell-endothelium and RBC-leukocyte interactions. We quantified the particular physiological conditions triggering the vaso-occlusion crisis and further identify the specific role of individual cell groups during the occlusion procedure. The specific cell pattern (ISCs trapped by adherent SS2 cells) widely observed in occlusion region is successfully predicted by the present study. Sensitivity studies on tube diameter and hematocrit values validated the prevalence of blood occlusion in post-capillaries with diameter smaller than  $12\text{--}14 \mu\text{m}$ , as consistently reported in experimental studies. Also, we investigated the effect of the adherent leukocyte under inflammation, which may further trap the sickle cells and result in blood occlusion in venular flow. These results reveal the *multi-stage* and *multi-interactional* nature of vaso-occlusion crisis. While the present medical treatment by hydroxyurea can effectively prolong the “delay time” of cell sickling procedure, targeting other processes such as the vessel endothelium activation and cell-endothelium adhesion may provide alternative paths to the treatment of this disease. This would require further experimental and numerical investigations.

For future work, the present computational framework can be further extended to investigate the following important questions related to SCA: (I) Quantify the hemodynamic properties of SS-RBC suspensions with patient-specific single-cell density (MCHC) distribution. This study can reveal the microcirculation and vaso-occlusion characteristics for patient-specific condition with particular cell morphologies, rigidity and adhesivity. (II) Couple the present model with the oxygen transport equation. We note that the blood occlusion is a dynamic process where the local oxygen saturation may further affect the individual SS-RBC properties. This study may help to quantify the *in vivo* sickle blood circulation with instantaneous

oxygen-controlled SS-RBCs groups. (III) Simulate diffusion of chemicals (e.g., hydroxyurea, decitabine, erythropoietin) to quantify the therapeutic effects of drug treatments on the microcirculation of the sickle blood flow. These numerical studies, combined with microfluidic experiments (e.g., cell transport in microchannels resembling blood vessel and networks, etc.) can be used to evaluate and quantify related therapeutic treatment and clinical outcomes. (IV) Model blood circulation by considering the endothelium surface roughness and the venular tortuosity. In *in vivo* conditions, these effects may further slow down the blood flow velocity and increase the probability of cell-endothelium and cell-cell interactions, resulting an elevated chance of blood occlusion crisis. Therefore, we expect that for *in vivo* system, vaso-occlusion may occur in micro-vasculatures with diameters even larger than the value predicted in the present work. These effect are worth further investigation.

**Acknowledgements** This work is supported by the National Institutes of Health (NIH) Grant U01HL114476 and the new DOE Collaboratory on Mathematics for Mesoscopic Modeling of Materials (CM4). Simulations are carried out at the Argonne Leadership Computing Facility (ALCF) through the Innovative and Novel Computational Impact on Theory and Experiment (INCITE) program at Argonne National Laboratory (ANL). We knowledge Dr. E Du and Dr. Ming Dao for helpful discussion and providing the experimental results.

## References

1. Unpublished data from Ming Dao and Sarah E Du at MIT (private communication)
2. Aprelev, A., Liu, Z., Ferrone, F.A.: The growth of sickle hemoglobin polymers. *Biophysical Journal* **101**, 885–891 (2011)
3. Asakura, T., Mattiello, J.A., Obata, K., Asakura, K., Reilly, M.P., Tomassini, N., Schwartz, E., Ohene-Frempong, K.: Partially oxygenated sickle cells: Sickled-shaped red cells found in circulating blood of patients with sickle cell disease. *Proceedings of the National Academy of Sciences* **91**, 12,589–12,593 (1994)
4. Ataga, K.I., Reid, M., Ballas, S.K., Yasin, Z., Bigelow, C., James, L.S., Smith, W.R., Galacteros, F., Kutlar, A., Hull, J.H., Stocker, J.W., for the ICA-17043-10 Study Investigators: Improvements in haemolysis and indicators of erythrocyte survival do not correlate with acute vaso-occlusive crises in patients with sickle cell disease: a phase III randomized, placebo-controlled, double-blind study of the gardos channel blocker senicapoc (ica-17043). *British Journal of Haematology* **153**(1), 92–104 (2011)
5. Ballas, S.K., Larner, J., Smith, E.D., Surrey, S., Schwartz, E., Rappaport, E.F.: Rheologic predictors of the severity of the painful sickle cell crisis. *Blood* **72**, 1216–1223 (1988)
6. Ballas, S.K., Mohandas, N.: Sickle red cell microrheology and sickle blood rheology. *Microcirculation* **11**, 209–225 (2004)
7. Barabino, G.A., McIntire, L.V., Eskin, S.G., Sears, D.A., Udden, M.: Endothelial cell interactions with sickle cells, sickle cell, sickle trait, mechanically injured, and normal erythrocytes under controlled flow. *Blood* **70**, 152–157 (1987)
8. Barabino, G.A., Platt, M.O., Kaul, D.K.: Sickle cell biomechanics. *Annu. Rev. Biomed. Eng.* **12**, 345–367 (2010)
9. Berger, S.A., King, W.S.: Flow of sickle-cell blood in the capillaries. *Biophysical Journal* **29**(1), 119–148 (1980)

10. Berger, S.A., King, W.S.: Diffusion and convection in the capillaries in sickle-cell disease. *Blood Cells* **8**(1), 153–161 (1982)
11. Bow, H., Pivkin, I.V., Diez-Silva, M., Goldfless, S.J., Dao, M., Niles, J.C., Suresh, S., Han, J.: A microfabricated deformability-based flow cytometer with application to malaria. *Lab on a Chip* **11**, 1065–1073 (2011)
12. Bridges, K., Barabino, G., Brugnara, C., Cho, M., Christoph, G., Dover, G., Ewenstein, B., Golan, D., Guttmann, C., Hofrichter, J., Mulkern, R., Zhang, B., Eaton, W.: A multiparameter analysis of sickle erythrocytes in patients undergoing hydroxyurea therapy. *Blood* **88**, 4701–4710 (1996)
13. Briehl, R.W.: Nucleation, fiber growth and melting and domain formation and structure in sickle cell hemoglobin gels. *Journal of Molecular Biology* **245**, 710–723 (1995)
14. Cao, Z., Ferrone, F.: Homogeneous nucleation in sickle hemoglobin: stochastic measurements with a parallel method. *Biophys. J.* **72**, 343–352 (1997)
15. Chiang, E.Y., Frenette, P.S.: Sickle cell vaso-occlusion. *Hematology/Oncology Clinics of North America* **19**, 771–784 (2005)
16. Christoph, G.W., Hofrichter, J., Eaton, W.A.: Understanding the shape of sickled red cells. *Biophysical Journal* **88**(2), 1371–1376 (2005)
17. Clark, M.R., Mohandas, N., Shohet, S.B.: Deformability of oxygenated irreversibly sickled cells. *Journal of Clinical Investigation* **65**, 189–196 (1980)
18. Coletta, M., Hofrichter, J., Ferrone, F.A., Eaton, W.A.: Kinetics of sickle haemoglobin polymerization in single red cells. *Nature* **300**, 194–197 (1982)
19. Corbett, J.D., Mickols, W.E., Maestre, M.F.: Effect of hemoglobin concentration on nucleation and polymer formation in sickled red blood cells. *J. Biol. Chem.* **270**, 2708–2715 (1995)
20. Damiano, E.R., Westheider, J., Tozeren, A., Ley, K.: Variation in the velocity, deformation, and adhesion energy density of leukocytes rolling within venules. *Circulation Research* **79**, 1122–1130 (1996)
21. Daniels, D.R., Marenduzzo, D., Turner, M.S.: Stall, spiculate, or run away: The fate of fibers growing towards fluctuating membranes. *Phys. Rev. Lett.* **97**, 098,101 (2006)
22. Dao, M., Li, J., Suresh, S.: Molecularly based analysis of deformation of spectrin network and human erythrocyte. *Materials Science and Engineering C* **26**, 1232–1244 (2006)
23. Discher, D.E., Boal, D.H., Boey, S.K.: Simulations of the erythrocyte cytoskeleton at large deformation. II. Micropipette aspiration. *Biophysical Journal* **75**(3), 1584–1597 (1998)
24. Dong, C., Chardwick, R.S., Schechter, A.N.: Influence of sickle hemoglobin polymerization and membrane properties on deformability of sickle erythrocytes in the microcirculation. *Biophysical Journal* **63**, 774–783 (1992)
25. Dou, Q., Ferrone, F.A.: Simulated formation of polymer domains in sickle hemoglobin. *Biophysical Journal* **65**, 2068–2077 (1993)
26. Dupin, M.M., Halliday, I., Care, C.M., Alboul, L., Munn, L.L.: Modeling the flow of dense suspensions of deformable particles in three dimensions. *Physical Review E* **75**(6), 066,707 (2007)
27. Dupin, M.M., Halliday, I., Care, C.M., Munn, L.L.: Lattice boltzmann modelling of blood cell dynamics. *International Journal of Computational Fluid Dynamics* **22**(7), 481–492 (2008)
28. Dzwinel, W., Boryczko, K., Yuen, D.A.: A discrete-particle model of blood dynamics in capillary vessels. *Journal of Colloid and Interface Science* **258**(1), 163–173 (2003)
29. Eaton, W.A., Hofrichter, J.: The biophysics of sickle cell hydroxyurea therapy. *Science* **268**, 1142–1143 (1995)

30. Espanol, P.: Dissipative particle dynamics for a harmonic chain: A first-principles derivation. *Phys. Rev. E* **53**(2), 1572–1578 (1996)
31. Espanol, P.: Fluid particle model. *Physical Review E* **57**(3), 2930–2948 (1998)
32. Espanol, P., Warren, P.: Statistical mechanics of dissipative particle dynamics. *Euro-physics Letters* **30**(4), 191–196 (1995)
33. Evans, E., Mohandas, N.: Membrane-associated sickle hemoglobin: a major determinant of sickle erythrocyte rigidity. *Blood* **70**, 1443–1449 (1987)
34. Evans, E., Mohandas, N., Leung, A.: Static and dynamic rigidities of normal and sickle erythrocytes. major influence of cell hemoglobin concentration. *The Journal of Clinical Investigation* **73**, 477–488 (1984)
35. Evans, E.A., Skalak, R.: Mechanics and thermodynamics of biomembranes. CRC Press, Inc., Boca Raton, Florida (1980)
36. Fedosov, D.A., Caswell, B., Karniadakis, G.E.: A multiscale red blood cell model with accurate mechanics, rheology, and dynamics. *Biophysical Journal* **98**(10), 2215–2225 (2010)
37. Fedosov, D.A., Caswell, B., Karniadakis, G.E.: Wall shear stress-based model for adhesive dynamics of red blood cells in malaria. *Biophysical Journal* **100**(9), 2084–2093 (2011)
38. Fedosov, D.A., Caswell, B., Suresh, S., Karniadakis, G.E.: Quantifying the biophysical characteristics of plasmodium-falciparum-parasitized red blood cells in microcirculation. *Proceedings of the National Academy of Sciences* **108**, 35–39 (2010)
39. Fedosov, D.A., Pan, W., Caswell, B., Gompper, G., Karniadakis, G.E.: Predicting human blood viscosity in silico. *Proceedings of the National Academy of Sciences* **108**(29), 11,772–11,777 (2011)
40. Ferrone, F.A., Hofrichter, J., Eaton, W.A.: Kinetics of sickle hemoglobin polymerization: I. studies using temperature-jump and laser photolysis techniques. *Journal of Molecular Biology* **183**(4), 591 – 610 (1985)
41. Ferrone, F.A., Hofrichter, J., Eaton, W.A.: Kinetics of sickle hemoglobin polymerization : II. a double nucleation mechanism. *Journal of Molecular Biology* **183**(4), 611–631 (1985)
42. Galkin, O., Chen, K., Nagel, R., Hirsch, R., Vekilov, P.: Liquid-liquid separation in solutions of normal and sickle cell hemoglobin. *Proc. Natl. Acad. Sci. USA* **99**, 8479–8483 (2002)
43. Galkin, O., Pan, W., Filobelo, L., Hirsch, R., Nagel, R., Vekilov, P.: Two-step mechanism of homogeneous nucleation of sickle cell hemoglobin polymers. *Biophys. J.* **93**, 902–913 (2007)
44. Galkin, O., Vekilov, P.G.: Mechanisms of homogeneous nucleation of polymers of sickle cell anemia hemoglobin in deoxy state. *Journal of Molecular Biology* **336**, 43–59 (2004)
45. Groot, R.D., Warren, P.B.: Dissipative particle dynamics: Bridging the gap between atomistic and mesoscopic simulation. *J. Chem. Phys.* **107**(11), 4423–4435 (1997)
46. Groot, R.D., Warren, P.B.: Dissipative particle dynamics: Bridging the gap between atomistic and mesoscopic simulation. *Journal of Chemical Physics* **107**(11), 4423–4435 (1997)
47. Hammer, D.A., Apte, S.M.: Simulation of cell rolling and adhesion on surfaces in shear flow: general results and analysis of selectin-mediated neutrophil adhesion. *Biophys. J.* **63**, 35–57 (1992)
48. Hebbel, R.P.: Adhesion of sickle red cells to endothelium: Myths and future directions. *Transfusion Clinique et Biologique* **15**, 14–18 (2008)

49. Hebbel, R.P., Yamada, O., Moldow, C.F., Jacob, H.S., White, J.G., Eaton, J.W.: Abnormal adherence of sickle erythrocytes to cultured vascular endothelium: possible mechanism for microvascular occlusion in sickle cell disease. *Journal of Clinical Investigation* **65**, 154–160 (1980)
50. Helfrich, W.: Elastic properties of lipid bilayers: theory and possible experiments. *Z. Naturforschung C* **28**, 693–703 (1973)
51. Herrick, J.B.: Peculiar elongated sickle-shaped red blood corpuscles in a case of severe anemia. *Arch. Intern. Med.* **6**, 517–521 (1910)
52. Higgins, J.M., Eddington, D.T., Bhatia, S.N., Mahadevan, L.: Sickle cell vasoocclusion and rescue in a microfluidic device. *Proceedings of the National Academy of Sciences* **104**(51), 20,496–20,500 (2007)
53. Hijon, C., Espanol, P., Vanden-Eijnden, E., Delgado-Buscalioni, R.: Mori-Zwanzig formalism as a practical computational tool. *Faraday Discuss.* **144**, 301–322 (2010)
54. Hoogerbrugge, P.J., Koelman, J.M.V.A.: Simulating microscopic hydrodynamic phenomena with dissipative particle dynamics. *Europhysics Letters* **19**(3), 155–160 (1992)
55. Hoover, R., Rubin, R., Wise, G., Warren, R.: Adhesion of normal and sickle erythrocytes to endothelial monolayer cultures. *Blood* **54**, 872–876 (1979)
56. Horiuchi, K., Ohata, J., Hirano, Y., Asakura, T.: Morphologic studies of sickle erythrocytes by image analysis. *J. Lab. Clin. Med.* **115**, 613 (1990)
57. Hupert, C., Baumann, M.: Local membrane curvature affects spontaneous membrane fluctuation characteristics. *Molecular membrane Biology* **20**, 155–162 (2003)
58. Ingram, V.M.: Abnormal human haemoglobins. I. the comparison of normal human and sickle-cell haemoglobins by fingerprinting. *Biochim. Biophys. Acta* **28**, 539–545 (1958)
59. Itoh, T., Chien, S., Usami, S.: Effects of hemoglobin concentration on deformability of individual sickle cells after deoxygenation. *Blood* **85**, 2245–2253 (1995)
60. Ivanova, M., Jasuja, R., Kwong, S., Briehl, R.W., Ferrone, F.A.: Nonideality and the nucleation of sickle hemoglobin. *Biophysical Journal* **79**, 1016–1022 (2000)
61. Jadhav, S., Eggleton, C.D., Konstantopoulos, K.: A 3-D computational model predicts that cell deformation affects selectin-mediated leukocyte rolling. *Biophysical Journal* **88**, 96–104 (2005)
62. Kaul, D.K., Chen, D., Zhan, J.: Adhesion of sickle cells to vascular endothelium is critically dependent on changes in density and shape of the cells. *Blood* **83**, 3006–3017 (1994)
63. Kaul, D.K., Fabry, M.E.: In vivo studies of sickle red blood cells. *Microcirculation* **11**, 153–165 (2004)
64. Kaul, D.K., Fabry, M.E., Nagel, R.L.: Microvascular sites and characteristics of sickle cell adhesion to vascular endothelium in shear flow conditions: Pathophysiological implications. *Proceedings of the National Academy of Sciences* **86**, 3356–3360 (1989)
65. Kaul, D.K., Fabry, M.E., Windisch, P., Baez, S., Nagel, R.L.: Erythrocytes in sickle-cell-anemia are heterogeneous in their rheological and hemodynamic characteristics. *Journal of Clinical Investigation* **72**(1), 22–31 (1983)
66. Kaul, D.K., Finnegan, E., Barabino, G.A.: Sickle red cell-endothelium interactions. *Microcirculation* **16**, 97–111 (2009)
67. Kaul, D.K., Hebbel, R.P.: Hypoxia/reoxygenation causes inflammatory response in transgenic sickle mice but not in normal mice. *Journal of Clinical Investigation* **106**, 411–420 (2000)
68. Kaul, D.K., Liu, X.: Rate of deoxygenation modulates rheologic behavior of sickle red blood cells at a given mean corpuscular hemoglobin concentration. *Clinical Hemorheology and Microcirculation* **21**, 125–135 (1999)

69. Kaul, D.K., Xue, H.: Rate of deoxygenation and rheologic behavior of blood in sickle cell anemia. *Blood* **77**, 1353–1361 (1991)
70. King, M.R., Hammer, D.A.: Multiparticle adhesive dynamics: Hydrodynamic recruitment of rolling leukocytes. *Proceedings of the National Academy of Sciences* **98**(26), 14,919–14,924 (2001)
71. Kinjo, T., Hyodo, S.A.: Equation of motion for coarse-grained simulation based on microscopic description. *Phys. Rev. E* **75**(5), 051,109 (2007)
72. Koren, A., Segal-Kupershmit, D., Zalman, L., Levin, C., Abu Hana, M., Palmor, H., Luder, A., Attias, D.: Effect of hydroxyurea in sickle cell anemia: a clinical trial in children and teenagers with severe sickle cell anemia and sickle cell beta-thalassemia. *Pediatr. Hematol. Oncol.* **16**, 221–232 (1999)
73. LaCelle, P.L.: Oxygen delivery to muscle cells during capillary vascular occlusion by sickle erythrocytes. *Blood Cells* **3**, 263–272 (1977)
74. Lei, H., Caswell, B., Karniadakis, G.E.: Direct construction of mesoscopic models from microscopic simulations. *Phys. Rev. E* **81**, 026,704 (2010)
75. Lei, H., Karniadakis, G.E.: Predicting the morphology of sickle red blood cells using coarse-grained models of intracellular aligned hemoglobin polymers. *Soft Matter* **8**, 4507–4516 (2012)
76. Lei, H., Karniadakis, G.E.: Probing vasoocclusion phenomena in sickle cell anemia via mesoscopic simulations. *Proceedings of the National Academy of Sciences* **110**(28), 11,326–11,330 (2013)
77. Lei, H., Karniadakis, G.E.: Quantifying the rheological and hemodynamic characteristics of sickle cell anemia. *Biophysical Journal* **102**, 185–194 (2012)
78. Li, H., Lykotrafitis, G.: A coarse-grain molecular dynamics model for sickle hemoglobin fibers. *Journal of Mechanical Behavior of Biomedical Materials* **4**, 162–173 (2011)
79. Li, J., Dao, M., Lim, C., Suresh, S.: Spectrin-level modeling of the cytoskeleton and optical tweezers stretching of the erythrocyte. *Biophys J* **88**, 3707–3719 (2005)
80. Li, X., Caswell, B., Karniadakis, G.E.: Effect of chain chirality on the self-assembly of sickle hemoglobin. *Biophysical Journal* **103**(6), 1130–1140 (2012)
81. McWhirter, J.L., Noguchi, H., Gompper, G.: Flow-induced clustering and alignment of vesicles and red blood cells in microcapillaries. *Proceedings of the National Academy of Sciences USA* **106**(15), 6039–6043 (2009)
82. Mickols, W., Maestre, M.F., Iinoco, I.J., Embury, S.H.: Visualization of oriented hemoglobin s in individual erythrocytes by differential extinction of polarized light. *Proceedings of the National Academy of Sciences* **82**, 6527–6531 (1985)
83. Mills, J.P., Qie, L., Lim, C.T., Dao, M., Suresh, S.: Nonlinear elastic and viscoelastic deformation of the human red blood cell with optical tweezers. *Mech Chem Biosyst* **1**(3), 169–180 (2004)
84. Noguchi, H., Gompper, G.: Shape transitions of fluid vesicles and red blood cells in capillary flows. *Proceedings of the National Academy of Sciences USA* **102**(40), 14,159–14,164 (2005)
85. Pauling, L., Itano, H.A., Singer, S.J., Wells, I.C.: Sickle cell anemia, a molecular disease. *Science* **110**, 543–548 (1949)
86. Pivkin, I.V., Karniadakis, G.E.: Accurate coarse-grained modeling of red blood cells. *Physical Review Letters* **101**(11), 118,105 (2008)
87. Platt, O.S., Orkin, S.H., Dover, G., Beardsley, G.P., Miller, B., Nathan, D.G.: Hydroxyurea enhances fetal hemoglobin production in sickle cell anemia. *J. Clin. Invest.* **74**, 652–656 (1984)

88. Quinn, D.J., Pivkin, I., Yong, S.Y., Chiam, K., Dao, M., Karniadakis, G.E., Suresh, S.: Combined simulation and experimental study of large deformation of red blood cells in microfluidic systems. *Annals of Biomedical Engineering* **39**, 1041–1050 (2011)
89. Samuel, R.E., Salmon, E.D., Briehl, R.W.: Nucleation and growth of fibers and gel formation in sickle cell haemoglobin. *Nature* **345**, 833–835 (1990)
90. Samuel, R.E., Salmon, E.D., Briehl, R.W.: Nucleation and growth of fibres and gel formation in sickle cell haemoglobin. *Nature* **345**, 833–835 (1990)
91. Succi, S.: The Lattice Boltzmann equation for fluid dynamics and beyond. Oxford University Press, Oxford (2001)
92. Sunshine, H.R., Hofrichter, J., Eaton, W.A.: Requirements for therapeutic inhibition of sickle haemoglobin gelation. *Nature* **275**, 238–240 (1978)
93. Suresh, S., Spatz, J., Mills, J.P., Micoulet, A., Dao, M., Lim, C.T., Beil, M., Seufferlein, T.: Connections between single-cell biomechanics and human disease states: gastrointestinal cancer and malaria. *Acta Biomaterialia* **1**, 15–30 (2005)
94. Turhan, A., Weiss, L.A., Mohanda, N., Coller, B.S., Frenette, P.S.: Primary role for adherent leukocytes in sickle cell vascular occlusion: A new paradigm. *Proceedings of the National Academy of Sciences* **99**, 3047–3051 (2002)
95. Usami, S., Chien, S., Scholtz, P.M., Bertles, J.F.: Effects of deoxygenation on blood rheology in sickle cell disease. *Microvascular Research* **9**, 324–334 (1975)
96. Uzunova, V., Pan, W., Galkin, O., Vekilov, P.: Free heme and the polymerization of sickle cell hemoglobin. *Biophys. J.* **99**, 1976–1985 (2010)
97. Vekilov, P., Galkin, O., Pettitt, B., Choudhury, N., Nagel, R.: Determination of the transition-state entropy for aggregation suggests how the growth of sickle cell hemoglobin polymers can be slowed. *J. Mol. Biol.* **377**, 882–888 (2008)
98. Wang, J.G., Turner, M.S., Agarwal, G., Kwong, S., Jeseph, R., Ferrone, F.A., Briehl, R.W.: Micromechanics of isolated sickle cell hemoglobin fibers: bending moduli and persistence lengths. *Journal of Molecular Biology* **315**, 601–612 (2002)
99. Zhelev, D.V., Needham, D., Hochmuth, R.M.: Role of the membrane cortex in neutrophil deformation in small pipets. *Biophysical Journal* **67**, 696–705 (1994)

---

# A Three-dimensional Continuum Model of Active Contraction in Single Cardiomyocytes

Alessio Gizzi, Ricardo Ruiz-Baier, Simone Rossi, Aymen Laadhari,  
Christian Cherubini, and Simonetta Filippi

**Abstract** We investigate the interaction of intracellular calcium spatio-temporal variations with the self-sustained contractions in cardiac myocytes. A 3D continuum mathematical model is presented based on a hyperelastic description of the passive mechanical properties of the cell, combined with an active-strain framework to describe the active shortening of myocytes and its coupling with cytosolic and sarcoplasmic calcium dynamics. Some numerical tests of combined boundary conditions and ionic activations illustrate the ability of our model in reproducing key experimentally established features. Potential applications of the study for predicting pathological subcellular mechanisms affecting e.g. cardiac repolarization are discussed.

## 6.1 Introduction

Single cells respond to several endogenous and exogenous mechanical stimuli such as stress, strain, strain-rate, strain energy, etc. [24], according to their internal structure. Active cardiac cells, the cardiomyocytes, contain myofibrils bundles in which

---

A. Gizzi (✉) · C. Cherubini · S. Filippi

Engineering Faculty, University Campus Bio-Medico of Rome, 00128 Rome, Italy  
e-mail: a.gizzi@unicampus.it; c.cherubini@unicampus.it; s.filippi@unicampus.it

R. Ruiz-Baier

Institut des Sciences de la Terre, FGSE, Université de Lausanne, 1015 Lausanne, Switzerland  
e-mail: ricardo.ruizbaier@unil.ch

S. Rossi

Civil & Environmental Engineering, Mechanical Engineering & Material Science, Duke University, Durham NC, USA  
e-mail: simone.rossi@duke.edu

A. Laadhari

Computer Vision Laboratory, ETH Zentrum, CH – 8092 Zurich, Switzerland  
e-mail: laadhari@vision.ee.ethz.ch

the subcellular contractile units, the sarcomeres, consist of thick and thin interacting myofilaments (myosin and actin proteins, respectively) that generate movement. In the context of muscular tissues, several examples of muscle organizations have been proposed [20, 36, 45] as the product of a full functional adaptation spanning from the sarcomere length up to the muscle bundle [53].

The excitation-contraction mechanism in these media is usually coordinated by an external electrical activation and propagated through specialized networks, the Purkinje fibers, to the whole tissue [29].

At the microscale, calcium ions ( $\text{Ca}^{2+}$ ) flow through the cell membrane from the extracellular matrix and are exchanged between the cytosol and sarcoplasmic reticulum thus regulating the interaction of the myofilaments. This chemical process onsets the shortening of the sarcomeres and drives the excitation-contraction coupling of the whole cardiac cell. The Calcium-Induced Calcium Released (CICR) feedback, in particular, originates in the excited state when the sarcolemma gets depolarized inducing the influx of extracellular calcium into the cardiomyocytes; the increase of intracellular calcium induces more  $\text{Ca}^{2+}$  to be released from the sarcoplasmic reticulum; cytosolic  $\text{Ca}^{2+}$  ions bind to troponin-C and activate the myofilaments. The process ends when the cell gets depolarized thus reducing the level of calcium concentration via both outflow fluxes and calcium sequestration in the sarcoplasmic reticulum. Although the excitation-contraction mechanism and the CICR feedback have major evidences both at the theoretical [56] and experimental [12] levels, the full understanding of the exact interplay between the different processes involved is still lacking. Nonetheless, these subcellular mechanisms play a key role in the overall cardiac function. Their understanding can therefore be of utmost importance and interest for the study of many physiological and pathological conditions [2, 22].

Different systemic effects of cardiac mechano-electric interactions can be explored by studying the elastic properties of isolated cardiac myocytes [21, 26, 37, 53]. Experimental evidences have shown that stress concentrations can often be recorded at locations without visible fibers deformations [10]. Such a phenomenon motivates the hypothesis that stresses are induced by micro-structure remodeling acting on a much smaller scale than the cell one and justifies the choice of a contractility model formulated at the continuum level. This allows to characterize a multiscale process rather than the description of an ensemble of particles by assuming: (i) a sufficient level of calcium concentration without limiting the mechanical activation; (ii) a representative volume element (RVE) inside the cell can be identified; and (iii) a mechanical response can be observed from any direction.

In this contribution we provide a quantitative description of the behavior of a single myocyte by proposing a complete chemo-active-mechanical model for three-dimensional cell geometries under specified experimental conditions and in agreement with the current mechanobiology approach [58]. Ionic kinetics and voltage-dependent equations at the cellular level are carefully considered [46]. Due to the complexity of the problem at hand, we focus our numerical simulations on describing the behavior of the principal calcium concentrations inside the cardiomyocyte and their nonlinear interplay with the mechanical quantities. Specific applications in the cardiovascular context analyzing boundary constraints, e.g. cell-cell and cell-matrix

adhesion, are discussed in terms of a positive feedback loop towards the functional organization and stress level on the cell membrane [21, 37].

The mathematical model here proposed is based on the active-strain approach [39, 51] in which the mechanical activation is formulated as a *virtual* multiplicative decomposition of the deformation gradient into a passive elastic response and an active deformation contribution. The latter is directly coupled to a simplified non-linear model of calcium dynamics [19, 54, 61]; this allows us to consider both the anisotropic passive intracellular organization, i.e. the T-tubule system, and the anisotropic active emerging cellular structures.

The generalized formulation is thermodynamically consistent [17, 50, 55] and allows the characterization of the interactions among ionic quantities, cellular mechanical properties and environmental effects. In particular, it explains the influence of cell shape and boundary conditions on the onset of structural anisotropies and stress concentrations. We address all of these requirements with the aid of finite-element-based simulations characterizing the feasibility and adequateness of employing a macroscopic description of the mechano-chemical behavior of a single cell. Such a modeling strategy, moreover, is well suited to explain the complex relations between microscopic cell dynamics and macroscopic cardiac functions. Three-dimensional simulations in this direction will be discussed. Our model is myocyte bending-contraction dynamics and end terminals deformations.

## 6.2 Continuum Model for Single Cell Biomechanics

Let  $\mathbf{x}$  represent the current position of a material particle of the myocyte  $\Omega_t$ , that occupied the position  $\mathbf{X}$  in the natural stress-free configuration  $\Omega_0 \subset \mathbb{R}^3$  with boundary  $\Gamma_0$ . Motion can be expressed in terms of the displacement vector field  $\mathbf{d} = \mathbf{x} - \mathbf{X}$ , and as usual, we denote by  $\mathbf{F} = \nabla_{\mathbf{X}}\mathbf{x}$ ,  $\mathbf{C} = \mathbf{F}^T\mathbf{F}$  and  $\mathbf{B} = \mathbf{F}\mathbf{F}^T$  the deformation gradient tensor and the right, left Cauchy-Green deformation tensors, respectively, where  $\nabla$  is the gradient with respect to material coordinates.

In a general form, the passive mechanical response of an isolated cell can be described through a hyperelastic, anisotropic constitutive law derived from the one proposed in [23] to model tissue properties, here written for a quasi-incompressible material:

$$\begin{aligned} \mathcal{W}(\mathbf{F}) = & \frac{a}{2b} [\exp(b[\bar{I}_1 - 3]) - 1] + \frac{a_f}{2b_f} [\exp(b_f[\bar{I}_{4,f} - 1]^2) - 1] \\ & + \frac{\kappa}{4} [(J - 1)^2 + (\ln J)^2], \end{aligned} \quad (6.1)$$

where  $a$  is a shear modulus,  $\kappa$  a bulk modulus,  $a_f, b, b_f$  are experimentally fitted in order to recover the strain-stress relationships found in [61] employing a polynomial strain energy function (see Fig. 6.1 and Table 6.1), and  $\bar{I}_1 := J^{-2/3} \text{tr}(\mathbf{C})$ ,  $\bar{I}_{4,f} := J^{-2/3} \mathbf{F} \mathbf{f}_0 \cdot \mathbf{F} \mathbf{f}_0$ , are isotropic and direction-dependent invariants. Here  $\mathbf{f}_0$  is a unitary direction vector in the reference configuration representing the myofibrils alignment.

**Table 6.1.** Parameters for passive mechanical anisotropic response on a single cell

*Transversely isotropic passive response*

$a = 3.2639 \text{ kPa}$	$a_f = 0.1354$	$b = 2.7492 \text{ kPa}$	$b_f = 5.4536$	$\kappa = 350 \text{ kPa}$
--------------------------	----------------	--------------------------	----------------	----------------------------

The governing equations of motion are set in the reference configuration and are endowed with Robin boundary conditions:

$$\begin{aligned} \rho \partial_{tt} \mathbf{d} - \nabla \cdot \mathbf{P} &= \rho \mathbf{b} \quad \text{in } \Omega_0 \times (0, T), \\ \mathbf{P} \mathbf{v} + \alpha_R \mathbf{d} &= \mathbf{d}_0 \quad \text{on } \Gamma_0 \times (0, T), \end{aligned} \quad (6.2)$$

where  $\mathbf{b}$  is a body force per unit mass,  $\mathbf{v}$  is the unit normal vector to the cell on  $\Gamma_0$ ,  $\mathbf{d}_0$  is a prescribed boundary load,  $\alpha_R$  is a Robin coefficient,  $\rho$  is the referential mass density, and the (first Piola-Kirchhoff) stress tensor associated to (6.1) is specified as

$$\begin{aligned} \mathbf{P} &= a \exp(b[I_1 - 3]) J^{-2/3} \left( \mathbf{F} - \frac{I_1}{3} \mathbf{F}^{-T} \right) \\ &\quad + 2a_f(I_{4,f} - 1) \exp(b_f[I_{4,f} - 1]^2) J^{-2/3} \left( \mathbf{F} \mathbf{f}_0 \otimes \mathbf{f}_0 - \frac{I_1}{3} \mathbf{F}^{-T} \right) \\ &\quad + \frac{\kappa}{2} (J^2 - J + \ln J) \mathbf{F}^{-T}. \end{aligned}$$

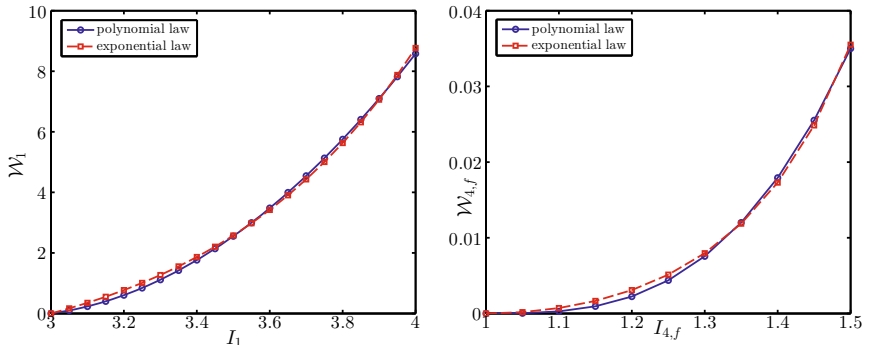


**Fig. 6.1.** Fitting of the transversely isotropic strain energy (6.1) with respect to the polynomial energy function proposed in [61]. Here  $\mathcal{W}_1 = \frac{a}{2b} [\exp(b[I_1 - 3]) - 1]$  and  $\mathcal{W}_{4,f} = \frac{a_f}{2b_f} [\exp(b_f[I_{4,f} - 1]^2) - 1]$ . The obtained parameters are displayed in Table 6.1

### 6.3 Intracellular Ionic Dynamics

This section briefly introduces the model equations of the phenomenological cardiac action potential propagation [6] and of the CICR calcium dynamics [19] for deformable anisotropic media.

#### 6.3.1 Minimal Model

The four-variable minimal phenomenological model for cardiac action potential propagation [5] allows us to quantify the key parameters necessary to correctly reproduce the experimental restitution properties (see also [15]) within minimal levels of computational requirements. Other effects can be recovered with significantly more complex ionic models [14]. Using the monodomain description for cardiac electrophysiology, the model equations are given by:

$$\begin{aligned} C_m \chi_m \partial_t u &= \nabla \cdot (\mathbf{D} \nabla u) - \chi_m (J_{fi} + J_{so} + J_{si}) && \text{in } \Omega_0 \times (0, T), \\ \partial_t v &= [1 - H(u - \theta_v)] v_\infty - v / \tau_v^- - H(u - \theta_v) v / \tau_v^+ && \text{in } \Omega_0 \times (0, T), \\ \partial_t w &= [1 - H(u - \theta_w)] (w_\infty - w) / \tau_w^- - H(u - \theta_w) w / \tau_w^+ && \text{in } \Omega_0 \times (0, T), \\ \partial_t s &= (1 + \tanh[k_s(u - u_s)]) / 2\tau_s - s / \tau_s && \text{in } \Omega_0 \times (0, T), \\ (\mathbf{D} \nabla u) \cdot \mathbf{v} &= 0 && \text{on } \Gamma_0 \times (0, T), \end{aligned} \quad (6.3)$$

where  $C_m$  is the specific membrane capacitance per unit area,  $\chi_m$  is the surface-to-volume ratio of the cell, and  $\mathbf{D} = \mathbf{F}^{-1} \text{diag}(D_f, D_s, D_n) \mathbf{F}^{-T}$  is a tensor of tissue conductivities  $D_f, D_s, D_n$ . The ionic density currents are defined as

$$\begin{aligned} J_{fi} &= -H(u - \theta_v)(u - \theta_v)(u_u - u) \frac{v}{\tau_{fi}}, \\ J_{so} &= [1 - H(u - \theta_w)] \frac{u - u_o}{\tau_o} + \frac{H(u - \theta_w)}{\tau_{so}}, \quad J_{si} = -H(u - \theta_w) \frac{ws}{\tau_{si}}, \end{aligned}$$

and refer to a fast inward,  $J_{fi}$ , a slow outward,  $J_{so}$ , and a slow inward,  $J_{si}$ , flux, respectively. Other than fixed time constants, the model is equipped by the following voltage-dependent time constants

$$\begin{aligned} \tau_v^-(u) &= [1 - H(u - \theta_v^-)] \tau_{v1}^- + H(u - \theta_v^-) \tau_{v2}^-, \\ \tau_w^-(u) &= \tau_{w1}^- + (\tau_{w2}^- - \tau_{w1}^-) \{ \tanh(k_w^- [u - u_w^-]) + 1 \} / 2, \\ \tau_{so}(u) &= \tau_{so1} + (\tau_{so2} - \tau_{so1}) \{ \tanh[k_{so}(u - u_{so})] + 1 \} / 2, \\ \tau_s(u) &= [1 - H(u - \theta_w)] \tau_{s1} + H(u - \theta_w) \tau_{s2}, \\ \tau_o(u) &= [1 - H(u - \theta_o)] \tau_{o1} + H(u - \theta_o) \tau_{o2}. \end{aligned}$$

Here  $H(\cdot)$  is the Heaviside step function;  $u$  is the dimensionless membrane potential rescaled to physical dimensions by using the map  $V_m = (85.7u - 84) mV$ ;  $v, w$  and  $s$

**Table 6.2.** Parameters for ionic activity according to the minimal and Goldbeter models (units are given in  $ms$ ,  $cm$ ,  $mV$ ,  $mS$ ,  $\mu F$ ,  $g$ ,  $k\Omega^{-1}cm^{-1}$ )

---

*Minimal model*

---

$u_o = 0$ ,  $u_u = 1.55$ ,  $\theta_v = 0.3$ ,  $\theta_w = 0.13$ ,  $\theta_v^- = 0.006$ ,  $\theta_o = 0.006$ ,  
 $\tau_v^+ = 1.4506$ ,  $\tau_v^- = 20$ ,  $\tau_{v2}^- = 1150$ ,  $\tau_{w1}^- = 120$ ,  $\tau_{w2}^- = 300$ ,  $\tau_{w1}^+ = 120$ ,  $\tau_{w2}^+ = 140$ ,  
 $k_w^- = 65$ ,  $u_w^- = 0.03$ ,  $k_w^+ = 5.7$ ,  $u_w^+ = 0.15$ ,  $\tau_{fi} = 0.11$ ,  $\tau_{o1} = 400$ ,  $\tau_{o2} = 6$ ,  
 $\tau_{so1} = 30.0181$ ,  $\tau_{so2} = 0.9957$ ,  $k_{so} = 2.0458$ ,  $u_{so} = 0.65$ ,  $\tau_{s1} = 2.7342$ ,  $\tau_{s2} = 16$ ,  
 $k_s = 2.0994$ ,  $u_s = 0.9087$ ,  $\tau_{si} = 1.8875$ ,  $\tau_{w\infty} = 0.07$ ,  $w_\infty^* = 0.94$ ,  
 $D_f = 1.33417721$ ,  $D_s = 0.17606$ ,  $D_n = 0.17606$ ,  $C_m = 1$ ,  $\chi_m = 1400$

---

*Goldbeter model*

---

$\alpha = 0.01$ ,  $a = 0.496$ ,  $v_1 = 1.58$ ,  $v_2 = 16$ ,  $v_3 = 91$ ,  $v_4 = 2$ ,  $v_5 = 1$ ,  
 $k_2 = 4$ ,  $k_3 = 0.7481$ ,  $D_f = 60$ ,  $D_s = 30$ ,  $D_n = 30$

---

are the three local gating variables, and the asymptotic values are given by

$$v_\infty = \begin{cases} 1, & u < \theta_v^- \\ 0, & u \geq \theta_v^- \end{cases}, \quad w_\infty = [1 - H(u - \theta_o)] \left( 1 - \frac{u}{\tau_{w\infty}} \right) + H(u - \theta_o) w_\infty^*.$$

Model parameters are reported in Table 6.2.

### 6.3.2 Goldbeter Model

In experiments on skinned isolated ventricular myocytes, or when the sarcolemma is hyper-permeable to calcium [3, 13], spontaneous contractile waves have been observed. These waves are related to slow calcium propagation ( $\sim 100 \mu m/s$ ) driven by the spontaneous release of calcium from the sarcoplasmic reticulum [60]. While these waves are not physiological (they do not develop during physiological pacing [6]), their occurrence during normal stimulation can be regarded as pathological and may give rise to arrhythmic scenarios [62]. The study of intracellular calcium wave propagation requires a model tuned to recover slow diffusion of  $[Ca^{2+}]$ , coupled to CICR, from channels sensitive to ryanodine release in the sarcoplasmic reticulum [57]. Here we focus on the following system of partial differential equations governing simplified CICR dynamics [19]:

$$\begin{aligned} \partial_t w_c &= \nabla \cdot (\mathbf{D} \nabla w_c) + K(w_c, w_s) && \text{in } \Omega_0 \times (0, T), \\ \partial_t w_s &= L(w_c, w_s) && \text{in } \Omega_0 \times (0, T), \\ (\mathbf{D} \nabla w_c) \cdot v &= 0 && \text{on } \Gamma_0 \times (0, T), \end{aligned} \tag{6.4}$$

where  $w_c$  and  $w_s$  represent the concentrations of cytosolic and sarcoplasmic calcium, respectively. Only two calcium species are considered under the assumption that the level of  $IP_3$  (responsible for the increase in the intracellular calcium concentration) remains constant during external stimulation. Anisotropy of the cell is accounted by

the form of the diffusion tensor  $\mathbf{D} = J\mathbf{F}^{-1} \text{diag}(D_f, D_s, D_n)\mathbf{F}^{-T}$ , where  $D_f, D_s, D_n$  are diffusivities of cytosolic calcium in three orthogonal directions, and the reaction terms are

$$K(w_c, w_s) = v_1 - \frac{v_2 w_c^2}{k_2 + w_c^2} + \frac{v_3 w_c^4 w_s^2}{(k_3 + w_s^2)(k_4 + w_c^4)} - v_4 w_c,$$

$$L(w_c, w_s) = \frac{v_2 w_c^2}{k_2 + w_c^2} - \frac{v_3 w_c^4 w_s^2}{(k_3 + w_s^2)(k_4 + w_c^4)} - v_5 w_s,$$

with  $v_1$  representing an inflow flux plus intracellular calcium pulses originated from the asynchrony of calcium pools receptors,  $v_2$  and  $v_3$  accounting for low and high levels of free cytosolic calcium flux pumped from the sarcoplasmic reticulum, and  $v_4$  modeling an efflux of calcium out of the cell following a chemical exchange process (see also e.g. [61]). Model parameters are displayed in Table 6.2.

## 6.4 A Mathematical Model for Mechanical Activation

Our description follows the active strain approach [8, 38, 50], where the deformation gradient is split into a passive and an active component,  $\mathbf{F} = \mathbf{F}_P \mathbf{F}_A$ , implying that a passive (say, purely elastic) intermediate configuration exists between the reference and the deformed one (see Fig. 6.2). Such a multiplicative decomposition of the deformation gradient is typical in many constitutive theories in finite kinematics (see e.g. [32, 42–44, 63]), and it has been shown to yield computational efficiency in numerical applications.

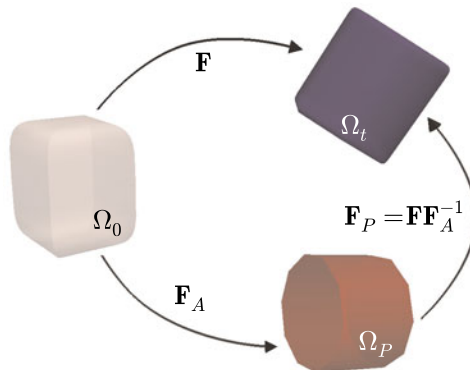


**Fig. 6.2.** Schematic representation of the active strain framework leading to the decomposition of the deformation gradient into a pure active and an elastic (passive) factor. Here  $\Omega_0, \Omega_P, \Omega_t$  represent a body in its reference, incompatible intermediate, and deformed configuration, respectively

The tensor  $\mathbf{F}_A$  represents the intermediate motion and describes the active deformations of the cell. It can be written in the general form

$$\mathbf{F}_A = \mathbf{I} + \gamma_f \mathbf{f}_0 \otimes \mathbf{f}_0 + \gamma_s \mathbf{s}_0 \otimes \mathbf{s}_0 + \gamma_n \mathbf{n}_0 \otimes \mathbf{n}_0,$$

where  $\gamma_f$ ,  $\gamma_s$  and  $\gamma_n$  are smooth scalar functions encoding the active shortening of the cardiomyocytes and their corresponding thickening [25]. If we define  $\mathbf{C}_A = \mathbf{F}_A^T \mathbf{F}_A$ ,  $\mathbf{F}_P = \mathbf{F} \mathbf{F}_A^{-1}$ ,  $\mathbf{C}_P = \mathbf{F}_A^{-T} \mathbf{C} \mathbf{F}_A^{-1}$ ,  $J_A = \det \mathbf{F}_A$ ,  $J_P = \det \mathbf{F}_P$ ,  $J = J_P J_A$ , then the strain energy (6.1) can be rewritten in the intermediate configuration  $\Omega_P$ , now in terms of  $\mathbf{F}_P$  and as a function of the following quantities

$$\begin{aligned} \bar{I}_1^P &:= \bar{I}_1 - \sum_{l \in \{f,s,n\}} \frac{\gamma(\gamma+2)}{(\gamma+1)^2} \mathbf{f}_{l0} \cdot \mathbf{f}_{l0}, \quad \bar{I}_{4,f}^P := (1+\gamma_f)^{-2} \bar{I}_{4,f}, \\ \psi_1^P &:= \frac{a}{2} \exp(b[\bar{I}_1^P - 3]), \quad \psi_{4,f}^P := a_f (\bar{I}_{4,f}^P - 1) \exp(b_f [\bar{I}_{4,f}^P - 1]^2). \end{aligned}$$

Even if the isolated myocyte is not a closed system in equilibrium, energy dissipation, achieved by means of internal state variables, allows us to derive an evolution law for the mechanical activation field  $\gamma_f$ . The multiplicative decomposition of the deformation gradient suggests that the active deformation gradient tensor can be regarded as the internal state variable describing mechanical activation [50]. In practice we consider a free energy  $\psi$  additively decomposed as

$$\psi(\mathbf{F}_E, \mathbf{c}) = \psi(\mathbf{F}, \mathbf{F}_A, \mathbf{c}) = \psi_P(\mathbf{F}) + \psi_A(\mathbf{F}, \mathbf{F}_A) + \psi_C(\mathbf{c}),$$

where  $\mathbf{c}$  is a vector containing all the chemical species involved in the myocyte contraction. We suppose that there exists a microstructural stress  $\mathbf{P}_A$  yielding the microstructural stress power  $\mathbf{P}_A : \dot{\mathbf{F}}_A$ . The active stress  $\mathbf{P}_A$  is a function of subcellular chemical quantities encoded in the vector  $\mathbf{c}$ . By means of the generalized dissipation inequality, using the Coleman-Noll procedure we obtain

$$\left( \mathbf{P} - \frac{\partial \psi_P}{\partial \mathbf{F}} - \frac{\partial \psi_A}{\partial \mathbf{F}} \right) : \dot{\mathbf{F}} + \left( \mathbf{P}_A - \frac{\partial \psi_A}{\partial \mathbf{F}_A} \right) : \dot{\mathbf{F}}_A - \frac{\partial \psi_C}{\partial \mathbf{c}} \dot{\mathbf{c}} \geq 0.$$

The quantity  $\frac{\partial \psi_A}{\partial \mathbf{F}_A}$  represents the configurational forces associated with  $\mathbf{F}_A$ . This relation holds in particular for

$$\begin{aligned} \mathbf{P} &= \frac{\partial \psi_P}{\partial \mathbf{F}} + \frac{\partial \psi_A}{\partial \mathbf{F}}, \\ \mu_A \dot{\mathbf{F}}_A &= \mathbf{P}_A(\mathbf{c}) - \frac{\partial \psi_A}{\partial \mathbf{F}_A}, \\ 0 &\leq \frac{\partial \psi_C}{\partial \mathbf{c}} \cdot \dot{\mathbf{c}}. \end{aligned}$$

We consider an orthotropic stress tensor incorporating an active contribution

$$\mathbf{P} = 2\psi_1^P J^{-2/3} \left[ (1 + \gamma_f)^2 \mathbf{F} - g(\gamma_f) \mathbf{F} \mathbf{f}_0 \otimes \mathbf{f}_0 - \frac{I_1^P}{3} \mathbf{F}^{-T} \right] - \frac{\kappa}{2} (J^2 - J + \ln J) \mathbf{F}^{-T} \\ + 2\psi_{4,f}^P \left[ \frac{1}{(1 + \gamma_f)^2} \mathbf{F} \mathbf{f}_0 \otimes \mathbf{f}_0 - \frac{I_{4,f}^P}{3} \mathbf{F}^{-T} \right], \quad (6.5)$$

where  $g(\gamma_f) = \gamma_f + \gamma_f \frac{\gamma_f+2}{(1+\gamma_f)^2}$ . We consider the activation dynamics to be given as in [51] by the relation

$$\partial_t \gamma_f = \beta^{-1} (P_A - [2(1 + \gamma_f) I_1 + g'(\gamma_f) I_{4,f}] \psi_1^P - \frac{2}{(1 + \gamma_f)^3} I_{4,f} \psi_{4,f}^P) \quad \text{in } \Omega_0 \times (0, T), \quad (6.6)$$

where  $P_A$  is fitted from data and  $\beta$  is a function of calcium concentration, provided by either  $s$  from the minimal model, or  $w_c$  from the Goldbeter model. For more details we refer to [50, 51].

The final set of equations describing the mechano-chemical coupling in a single cell are given by the nonlinear elasticity problem (6.2) with  $\rho = 0$  and  $\mathbf{P}$  as in (6.5), the activation dynamics (6.6), and the ionic activity governed by either (6.3) or (6.4).

## 6.5 Discretization and Numerical Examples

The spatial segregation of cell-matrix and cell-cell adhesions to individual myocyte borders has important effects for the electromechanical coupling within the tissue as well as for the onset of electrical arrhythmias [33]. Such adhesions consist of localized boundary conditions anchoring cells and tissues to the extracellular matrix. From the biomechanical point of view, moreover, these specialized boundaries are mechanosensitive and can act as tunable constraints locally modifying the stress concentration according to the cell function or modulating tissue organization as well. Recently, cell membrane boundary condition effects on cardiomyopathies have been experimentally characterized by increased fibrosis and tissue stiffening [1, 18] via a fine characterization of the interaction between cells and stiff substrates. These complex feedbacks and focal adhesions, moreover, play an important role in the organization of cytoskeletal scaffolds, stabilizing the mechanical response of the myocyte, their structure and function as well as their resulting contractile response [9, 21, 37].

In the following sections we present numerical examples in this direction by comparing different boundary conditions and activation processes on a realistic three-dimensional myocyte geometry. Domain segmentation, mesh generation and FEM implementation are described.

### 6.5.1 Geometry Segmentation and Mesh Generation

A three-dimensional computational domain was obtained with image segmentation tools applied to a canine cardiomyocyte [4] (employing a Zeiss LSM-510 META

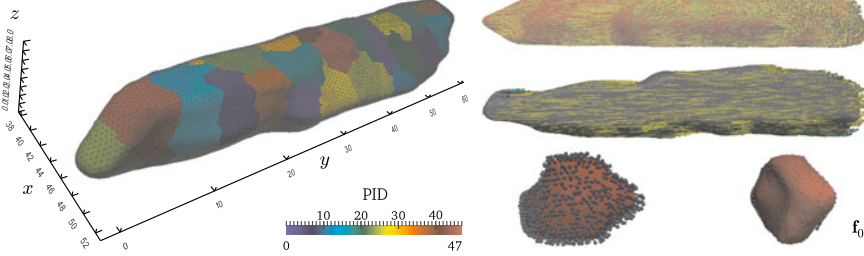


**Fig. 6.3.** Cell geometry, subdomain partitions and tetrahedral mesh (*left*), and lateral, aerial, back and front views of the constructed fibers field (*right*). In the text we mention “left” and “right” ends of the cell referring to the endpoints at  $y = -1.7\mu\text{m}$  and  $y = 61.2\mu\text{m}$ , respectively

confocal microscope). The starting images were in a stress-free/strain-free configuration and the cell has approximate dimensions of  $15.3\mu\text{m} \times 62.9\mu\text{m} \times 8\mu\text{m}$ . An in-house code based on MATLAB and COMSOL Multiphysics interface was used to discretize the surface geometry into an initial triangular mesh that merged the set of confocal cell image slices. Such initial surface mesh exhibits several irregularities (e.g. holes, boundary edges, flipped triangles and poor quality edges) which, in particular, violate the correct cell shape. These issues were solved using Meshlab ([meshlab.sourceforge.net](http://meshlab.sourceforge.net)): we removed self intersecting faces and non-manifold faces, and we applied several local smoothing and remeshing steps in order to obtain a well-resolved boundary. Additional mesh optimization (faces regularity and so on) along with volumetric mesh generation was performed in Gmsh [16]. The final mesh consists of 77031 tetrahedral elements and 18191 vertices (see Fig. 6.3, left).

A preferred direction field for the mechanical activation within the myocyte (here denoted with  $f_0$ ) basically corresponds to the sarcomeres orientation (see e.g. [61]). We generated such a direction field using a general rule-based method detailed in [50] for fibers and sheets directions in ventricular tissue. The algorithm uses a Laplace-Dirichlet approach. Once boundaries patches on the “top” and “bottom” of the cell are defined, we solve a diffusion problem imposing homogeneous Dirichlet conditions on these boundaries. The resulting preferred direction of anisotropy is oriented according to the direction of diffusion gradient (see Fig. 6.3, right).

### 6.5.2 Finite Element Approximation

The equations of nonlinear elasticity and the reaction-diffusion systems for ionic activity and mechanical activation are discretized in space by  $\mathbb{P}_2$  and  $\mathbb{P}_1$ , respectively. The solution of the coupling employs a modular approach, which allows us in particular to use different time steps for the elasticity and reaction-diffusion solvers. All other nonlinearities are treated with a nonlinear Richardson method and the time discretization of the coupled problem is as follows. An operator-splitting scheme is employed for the solution of the electrophysiology (or alternatively calcium) equa-

tions. The diffusion part is discretized in time using the implicit Euler method and the system of equations is solved using the conjugate gradient method with an algebraic multigrid preconditioner using 4 levels computed by smoothed aggregation, where the pre- and post-smoother at each level is two sweeps of Gauss-Seidel iteration, and at the coarse level we take two sweeps of the conjugate gradient method. Further details can be found in [50].

Code implementation has been carried out in the framework of the open source finite element library LifeV ([www.lifev.org](http://www.lifev.org)). All simulations were performed on four cluster nodes with two Sandy Bridge processors (8 core, 2.2 GHz CPU) each, representing a total of 64 CPUs using Infiniband QDR 2:1 connectivity ([hpc.epfl.ch/clusters/bellatrix](http://hpc.epfl.ch/clusters/bellatrix)).

### 6.5.3 Example 1: Single Cell Electromechanics

Under physiological conditions a single myocyte is excited almost instantaneously. In fact, considering a conduction velocity of about 70 cm/s for the electrical signal, a cell with an approximate length of 100  $\mu\text{m}$  is fully electrically activated in about 0.1 ms. In this way the subcellular contraction mechanism is initiated almost simultaneously in all regions of the cell. These circumstances allow us to test the proposed activation model on simplified yet significant cases. The monodomain equation describes the transmembrane potential and therefore cannot be applied in the whole cell. On the other hand, by the considerations above, there is no need to consider electrical propagation. By solving the ionic model alone, we can extend the calcium-like variable  $s$  in the whole intracellular space allowing the triggering of the mechanical activation model and cellular contraction. In Fig. 6.4 (left) we recall the evolution of the minimal model and the calcium-like variables. The gating variable  $s$  is used in the activation model in place of intracellular calcium concentration, not available in the minimal model. The computed evolution of the active strain is also shown in

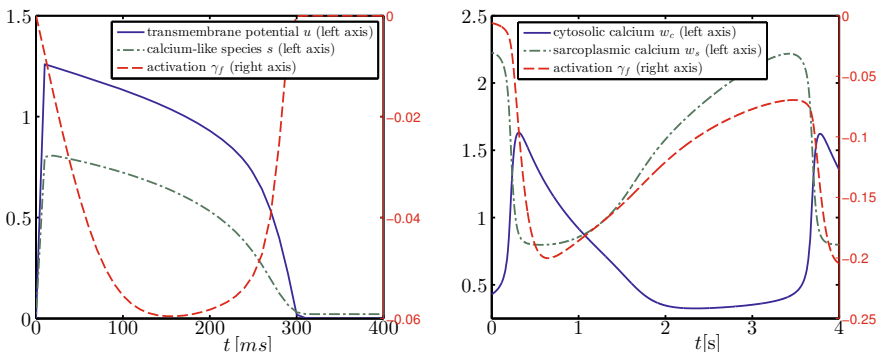


**Fig. 6.4.** Examples 1 and 2: Dynamics of voltage, calcium concentration, and activation measured on a single point near the cell center, through time for the minimal and Goldbeter models (left and right panels, respectively)

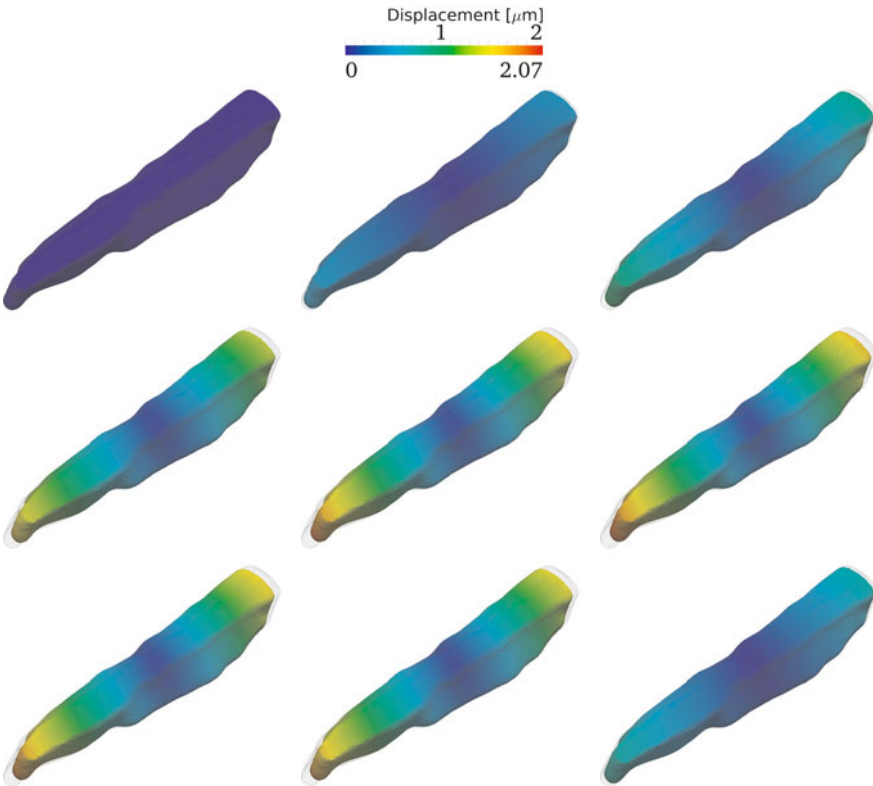


**Fig. 6.5.** Example 1: Displacement field and deformed domain for times  $t = 0, 20, 40, 80, 120, 180, 220, 240, 280$  ms

Fig. 6.4 (left). Given the specific kinetics of species  $s$ , more prolonged with respect to intracellular calcium concentration, the active strain  $\gamma_f$  is able to represent cellular contraction.

Since pure stress-free boundary conditions do not eliminate possible rigid motion, we set Robin boundary conditions as in (6.2), with  $\mathbf{d}_0 = \mathbf{0}$  and  $\alpha_R = 50\text{Pa/m}$  on the left and right ends of the cell, and we put  $\alpha_R = 10\text{Pa/m}$  elsewhere in  $\Gamma_0$ . In this way the cell shortens symmetrically by about 6% of its resting length as shown in Fig. 6.5, in accordance with other cellular models [48, 64].

#### 6.5.4 Example 2: Intracellular Calcium Transients

We now turn to the simulation of slow calcium waves inside the cell. Self-sustained mechano-chemical interactions are initiated by a single cytosolic calcium spark near the nucleus of the cell (as in e.g. [26, 61]). The kinetics of a single point near the cell center are plotted in Fig. 6.4 (right). We test Robin and Dirichlet boundary con-

ditions simulating adhesion regions, or alternatively the contact with surrounding myocytes. In Figs. 6.6 and 6.7 we observe the propagation of  $w_c$  towards the extremities of the cell comparing the two sets of boundary conditions: the displacements are constrained to Robin data on the whole boundary (Fig. 6.7) and fixed to zero the left end of the cell and stress-free elsewhere (Fig. 6.6). As predicted in our previous 2D tests (see [51]) we here observe cell bending in the first case, whereas for spring

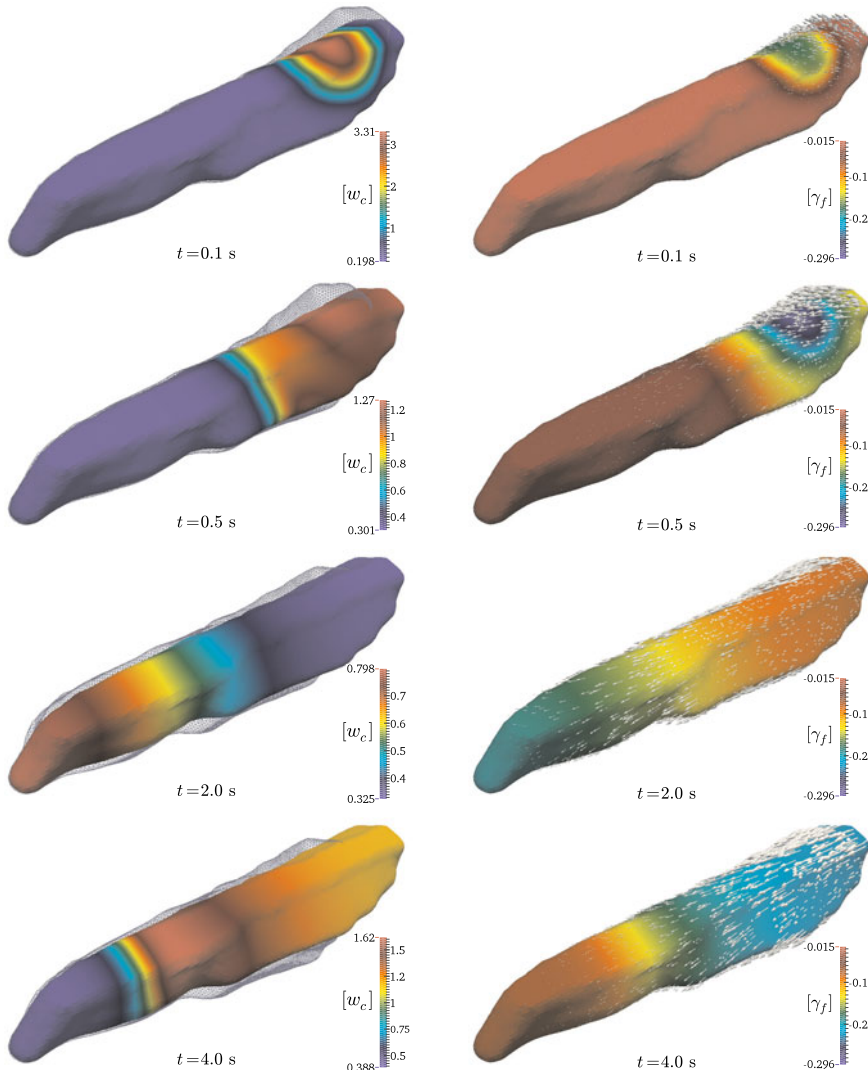


**Fig. 6.6.** Example 2: Snapshots of the propagation of cytosolic calcium and deformed domain (left panels) and activation function  $\gamma_f$  with displacement vectors (right panels) for times  $t = 0.1, 0.5, 2.0, 4.0$  s (from top to bottom) when the cell is fixed on the left end

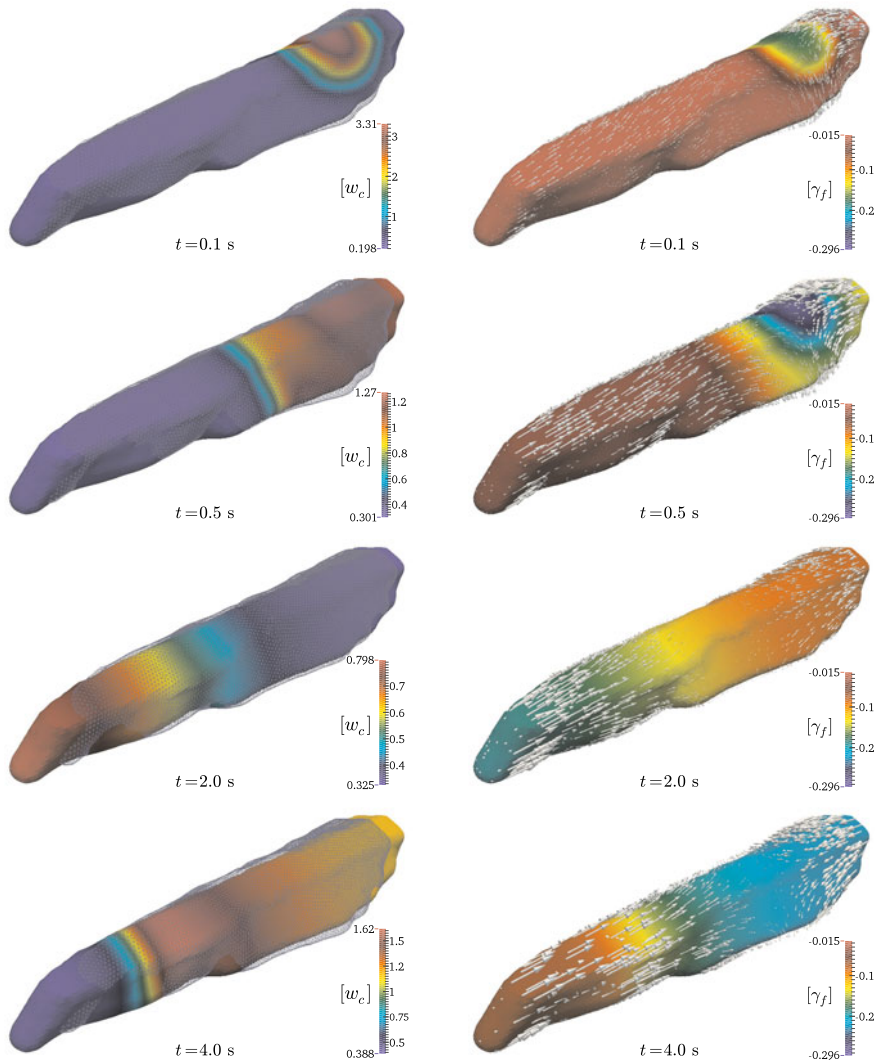


**Fig. 6.7.** Example 2: Snapshots of the propagation of cytosolic calcium and deformed domain (left panels) and activation function  $\gamma_f$  with displacement vectors (right panels) for times  $t = 0.1, 0.5, 2.0, 4.0$  s (from top to bottom) for pure Robin boundary data

boundary data the contraction patterns are symmetric with respect to the cell center. Movement with respect to the principal direction  $\mathbf{f}_0$  and bending are expected in realistic scenarios [9]. Finally we compare our cases with the study reported in [28] in terms of contractility patterns of the cell ends (see also [31]). Our results (for pure Robin boundary data) show a reasonable qualitative agreement, considering that the cell shapes do not coincide (see Fig. 6.8).

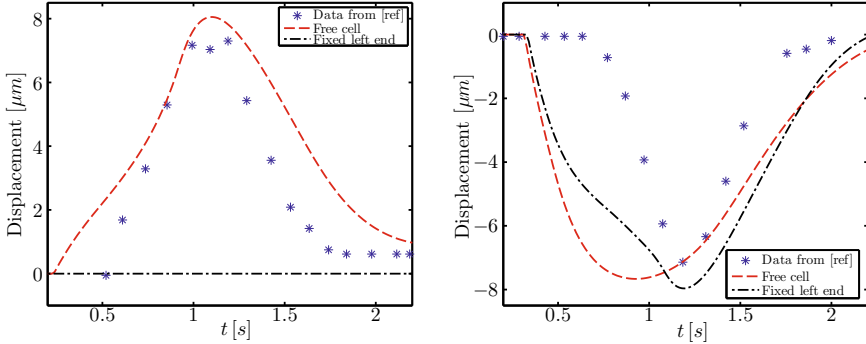


**Fig. 6.8.** Example 2: Cell contraction dynamics measured by displacements on the left and right ends of the myocyte (*left and right panels*, respectively) and comparison with respect to experimental observations from [28]

## 6.6 Discussion

The mathematical model formulation of the mechano-chemical coupling in single cardiomyocytes based on an active strain approach [51] has been analyzed and extended to realistic three-dimensional geometries. The proposed activation mechanism is consistent with a thermodynamic framework [55] entailing a nonlinear coupling among calcium dynamics and local stretches. The continuum approach adopted is on the line of recent bio-chemo-mechanical models of single cells [10, 11, 49] here formulated in terms of active-strain hyperelasticity. The model is capable to reproduce the propagation of calcium waves and the corresponding spontaneous contraction interacting within the cell [59], as well as the bending behavior, peculiar features of a three-dimensional structure. A finite element method is used to discretize the model equations; a set of numerical experiments comparing two- and three-dimensional reconstructed cardiomyocyte geometries give evidence of the main features of the model and its ability in predicting calcium propagation patterns and contractility in good agreement with experimental observations. Different boundary conditions have been analyzed reproducing physiological constraints thus analyzing the resulting stress patterns.

Limitations to the present study deal in particular with the correct treatment of boundary conditions in order to obtain physiological displacements of the cell. For the chemo-mechanic approach here discussed, numerical simulations show that Robin boundary conditions are better suited to reproduce the experimental observations even though a finer tuning of the Robin coefficients would be necessary. In this perspective an effective alternative would consider a level-set approach [31], in which an Eulerian description of the fluid-structure interaction problem considers the extracellular fluid interacting with the elastic cell via a *fictitious* interface. A careful representation of the internal cell anisotropy is equally fundamental due to the highly nonlinear coupling involved in the problem. In particular, intracellular micro-

structures, i.e. intercalated discs, should be taken into account for a more accurate geometric model. However, the lack of specific mechanical properties knowledge requires the usage of simplified cellular models. Therefore, the mathematical problem here addressed represents a good compromise in terms of continuum mechanics theory.

More realistic boundary conditions should be introduced also in terms of ionic exchanges other than calcium, i.e. Na and K [46]. The specific role of gap junctions and stretch-activated channel [52], discarded in the present study, can be addressed extending the numerical simulations to patch of cardiac tissue in a full multiscale approach characterized by a complete electromechanical coupling [66]. In this perspective, a more accurate modeling of the complex intracellular and extracellular calcium dynamics itself (Sodium-Calcium Exchanger and the NCX-NKA system [48]) would be considered for the analysis of rate-dependent effects, i.e. the positive force-frequency staircase effects [26, 35].

Extending the present formulation upon the discussed limitations would give insights and simulation-based predictions both for physiological [41] and pathological conditions [65] (failing myocardium conditions). We foresee the application of our model in describing the intra- and inter-cellular organization and remodeling of the myocyte structures during contraction [30] and the description of the diastolic calcium homeostasis as well [35]. Besides, our modeling approach can be extended to nonlocal constitutive laws mimicking micro-structure cellular adaptation to the external substrate [40]. It is tunable for cell biomechanics measurements tools and could be used as a framework to design and interpret novel experimental settings. We finally stress that the present model could be adopted as a building block in view of a multiscale cardiac model integrating cell, tissue and organ levels. Particular interest for the role of mechano-electric feedback in vulnerability to electric shocks [34] and in tissue pinning phenomena associated with arrhythmias [7, 47] is implied.

**Acknowledgements** We acknowledge the financial support by the European Research Council through the Advanced Grant *Mathcard, Mathematical Modelling and Simulation of the Cardiovascular System*, Project 227058, the International Center for Relativistic Astrophysics Network (ICRANet) and the Young Researcher Grant of the Italian Gruppo Nazionale per la Fisica Matematica (GNFM, INdAM).

## References

- Berry, M.F., Engler, A.J., Woo, Y.J., Pirolli, T.J., Bish, L.T., Jayasankar, V., Morine, K.J., Gardner, T.J., Discher, D.E., Sweeney, H.L.: Mesenchymal stem cell injection after myocardial infarction improves myocardial compliance. *Am. J. Physio. Heart. Circ. Physiol.* **290**, H2196–2203 (2006)
- Bers, D.M.: Cardiac excitation–contraction coupling. *Nature* **415**, 198–205 (2002)
- Bloom, S.: Spontaneous rhythmic contraction of separated heart muscle cells. *Science* **167**(3926), 1727–1729 (1970)
- Cherry, E.M., Fenton, F.H.: Visualization of spiral and scroll waves in simulated and experimental cardiac tissue. *New J. Phys.* **10**, 125016 (2008)

5. Bueno-Orovio, A., Cherry, E.M., Fenton, F.H.: Minimal model for human ventricular action potentials in tissue. *J. Theor. Biol.* **253**, 544–560 (2008)
6. Capogrossi, M.C., Suarez-Isla, B.A., Lakatta, E.G.: The interaction of electrically stimulated twitches and spontaneous contractile waves in single cardiac myocytes. *J. Gen. Physiol.*, **88**, 615–633 (1986)
7. Cherubini, C., Filippi, S., Gizzi, A.: Electroelastic unpinning of rotating vortices in biological excitable media. *Phys. Rev. E*, **85**, 031915 (2012)
8. Cherubini, C., Filippi, S., Nardinocchi, P., Teresi, L.: An electromechanical model of cardiac tissue: Constitutive issues and electrophysiological effects. *Prog. Biophys. Mol. Biol.*, **97**, 562–573 (2008)
9. Delbridge, L.M.D., Roos, K.P.: Optical methods to evaluate the contractile function of unloaded isolated cardiac myocytes. *J. Molec. Cell Cardiol.*, **29**, 11–25 (1997)
10. Deshpande, V.S., McMeeking, R.M., Evans, A.G.: A bio-chemo-mechanical model for cell contractility, *PNAS*, **103**, 14015–14020 (2006)
11. Deshpande, V.S., Mrksich, M., McMeeking, R.M., Evans, A.G.: A bio-mechanical model for coupling cell contractility with focal adhesion formation, *J. Mech. Phys. Sol.*, **56**, 1484–1510 (2008)
12. Fabiato, A.: Appraisal of the physiological relevance of two hypothesis for the mechanism of calcium release from the mammalian cardiac sarcoplasmic reticulum: calcium-induced release versus charge-coupled release, *Mol. Cell. Biochem.*, **89**, 135–140 (1989).
13. Fabiato, A., Fabiato, F.: Contractions induced by a calcium-triggered release of calcium from the sarcoplasmic reticulum of single skinned cardiac cells. *J. Physiol.* **249**(3), 469–495 (1975)
14. Fenton, F.H., Cherry, E.M.: Models of cardiac cells, *Scholarpedia* **3**, 1868 (2008)
15. Fenton, F.H., Gizzi, A., Cherubini, C., Pomella, N., Filippi, S.: Role of temperature on nonlinear cardiac dynamics, *Phys. Rev. E Stat. Nonlin. Soft. Matter. Phys.*, **87**, 042709 (2013)
16. Geuzaine, C., Remacle, J.F.: Gmsh: a three-dimensional finite element mesh generator with built-in pre- and post-processing facilities. *Int. J. Numer. Meth. Engrg.*, **79**, 1309–1331 (2009)
17. Gizzi, A., Cherubini, C., Filippi, S., Pandolfi, A.: Theoretical and Numerical Modeling of Nonlinear Electromechanics with applications to Biological Active Media, *Commun. Comput. Phys.* **17**(1), 93–126 (2015)
18. Göktepe, S., Abilez, O.J., Kuhl, E.: A generic approach towards finite growth with examples of athletes heart, cardiac dilation, and cardiac wall thickening. *J. Mech. Phys. Sol.*, **58**, 1661–1680 (2010)
19. Goldbeter, A., Dupont, G., Berridge, M.J.: Minimal model for signal-induced  $\text{Ca}^{2+}$  oscillations and for their frequency encoding through protein phosphorylation. *Proc. Natl. Acad. Sci. USA*, **87**, 1461–1465 (1990)
20. Goldmann, W.H. Mechanotransduction in cells. *Cell. Biol.* **36**, 567–70 (2012)
21. Grosberg, A., Kuo, P.L., Guo, C.L., Geisse, N.A., Bray, M.A., Adams, W.J., Sheehy, S.P., Parker, K.K.: Self-organization of muscle cell structure and function. *PLoS Comp. Biol.*, **7**, e1001088 (2011)
22. Hatano, A., Okada, J., Washio, T., Hisada, T., Sugiura, S.: A three-dimensional simulation model of cardiomyocyte integrating excitation-contraction coupling and metabolism. *Biophys. J.*, **101**, 2601–2610 (2011)
23. Holzapfel, G.A., Ogden, R.W.: Constitutive modelling of passive myocardium: a structurally based framework for material characterization. *Phil. Trans. R. Soc. Lond. A*, **367**, 3445–3475 (2009)

24. Humphrey, J.D.: Stress, strain, and mechanotransduction in cells. *J. Biomech. Eng.* **123**, 638–641 (2001)
25. Iribe, G., Helmes, M., Kohl, P.: Force-length relations in isolated intact cardiomyocytes subjected to dynamic changes in mechanical load. *Am. J. Physiol. Heart Circ. Physiol.*, **292**, H1487–H1497 (2007)
26. Iribe, G., Ward, C.W., Camelliti, P., Bollensdorff, C., Mason, F., Burton, R.A.B., Garny, A., Morphew, M., Hoenger, A., Lederer, W.J., Kohl, P.: Axial stretch of rat single ventricular cardiomyocytes causes an acute and transient increase in  $\text{Ca}^{2+}$  spark rate. *Circ. Res.*, **104**, 787–795 (2009)
27. Iyer, V., Mazhari, R., Winslow, R.L.: A computational model of the human left ventricular epicardial myocyte. *Biophys. J.*, **87**, 1507–1525 (2004)
28. Kamgoué, A., Ohayon, J., Usson, Y., Riou, L., Tracqui, P.: Quantification of cardiomyocyte contraction based on image correlation analysis. *Cytometry Part A* **75**, 298–308 (2009)
29. Keener, J., Sneyd, J.: Mathematical physiology, Springer-Verlag, New York (1998)
30. Kockskämper, J., von Lewinski, D., Khafaga, M., Elgner, A., Grimm, M., Eschenhagen, T., Gottlieb, P.A., Sachs, F., Pieske, B.: The slow force response to stretch in atrial and ventricular myocardium from human heart: functional relevance and subcellular mechanisms. *Prog. Biophys. Mol. Biol.*, **97**, 250–267 (2008)
31. Laadhari, A., Ruiz-Baier, R., Quarteroni, A.: Fully Eulerian finite element approximation of a fluid-structure interaction problem in cardiac cells. *Int. J. Numer. Meth. Engrg.*, **96**, 712–738 (2013)
32. Lubarda, V.A.: Constitutive theories based on the multiplicative decomposition of deformation gradient: Thermoelasticity, elastoplasticity, and biomechanics. *Appl. Mech. Rev.*, **57**, 95–108 (2004)
33. Li, J., Patel, V.V., Radice, G.L.: Dysregulation of cell adhesion proteins and cardiac arrhythmogenesis, *Clin. Med. Res.*, **4**, 42–52 (2006)
34. Li, W., Gurev, V., McCulloch, A.D., Trayanova, N.A.: The role of mechanolectric feedback in vulnerability to electric shock, *Prog. Biophys. Mol. Biol.*, **97**, 461–478 (2008)
35. Louch, W.E., Stokke, M.K., Sjaastad, I., Christensen, G., Sejersted, O.M.: No rest for the weary: diastolic calcium homeostasis in the normal and failing myocardium, *Physiology*, **27**, 308–323 (2008)
36. Marshall, K.L., Lumpkin, E.A.: The molecular basis of mechanosensory transduction. *Adv. Exp. Med. Biol.*, **739**, 142–55 (2012)
37. McCain, M.L., Lee, H.L., Aratyn-Schaus, Y., Kléber, A.G., Parker, K.K.: Cooperative coupling of cell-matrix and cell-cell adhesions in cardiac muscle. *PNAS*, **109**, 9881–9886 (2012)
38. Nardinocchi, P., Teresi, L.: Electromechanical modeling of anisotropic cardiac tissues. *Math. Mech. Solids*, **18**, 576–591 (2013)
39. Nobile, F., Quarteroni, A., Ruiz-Baier, R.: An active strain electromechanical model for cardiac tissue. *Int. J. Numer. Meth. Biomed. Engrg.*, **28**, 52–71 (2012)
40. Novak, I.L., Slepchenko, B.M., Mogilner, A., Loew, L.M.: Cooperativity between cell contractility and adhesion. *Phys. Rev. Lett.*, **93**, 268109 (2004)
41. Nishimura, S., Seo, K., Nagasaki, M., Hosoya, Y., Yamashita, H., Fujita, H., Nagai, R., Sugiura, S.: Responses of single-ventricular myocytes to dynamic axial stretching. *Prog. Biophys. Mol. Biol.*, **97**, 282–297 (2008)
42. Ortiz, M., Stainier, L.: The variational formulation of viscoplastic constitutive updates. *Comp. Meth. Appl. Mech. Eng.*, **171**, 419–444 (1999)

43. Ortiz, M., Pandolfi, A.: A variational Cam-clay theory of plasticity. *Comp. Meth. Appl. Mech. Eng.*, **193**, 2645–2666 (2004).
44. Pandolfi, A., Conti, S., Ortiz, M.: A recursive-faulting model of distributed damage in confined brittle materials. *J. Mech. Phys. Sol.*, **54**, 1972–2003 (2006)
45. Parker, K.K., Tan, J., Chen, C.S., Tung, L.: Myofibrillar architecture in engineered cardiac myocytes. *Circ. Res.*, **103**, 340–342 (2008)
46. Pullan, A.J., Buist, M.L., Cheng, L.K.: *Mathematically Modeling the Electrical Activity of the Heart: From Cell to Body Surface and Back*, World Scientific, Singapore (2005)
47. Pumir, A., Sinha, S., Sridhar, S., Argentina, M., Horning, M., Filippi, S., Cherubini, C., Luther, S., Krinsky, V.: Wave-train-induced termination of weakly anchored vortices in excitable media. *Phys. Rev. E*, **82**, 010901(R) (2010)
48. Rice, J.J., Wang, F., Bers, D.M., de Tombe, P.P. Approximate model of cooperative activation and crossbridge cycling in cardiac muscle using ordinary differential equations. *Biophys. J.*, **95**, 2368–2390 (2008)
49. Ronan, W., Deshpande, V.S., McMeeking, R.M., McGarry, J.P.: Numerical investigation of the active role of the actin cytoskeleton in the compression resistance of cells. *J. Mech. Behav. Biomed. Mat.*, **14**, 143–157 (2012)
50. Rossi, S., Lassila, T., Ruiz-Baier, R., Sequeira, A., Quarteroni, A.: Thermodynamically consistent orthotropic activation model capturing ventricular systolic wall thickening in cardiac electromechanics. *Eur. J. Mech. A/Solids* **48**, 129–142 (2014)
51. Ruiz-Baier, R., Gizzi, A., Rossi, S., Cherubini, C., Laadhari, A., Filippi, S., Quarteroni, A.: Mathematical modelling of active contraction in isolated cardiomyocytes, *Math. Med. Biol.* **31**, 259–283 (2014)
52. Seol, C.A., Kim, W.T., Ha, J.M., Choe, H., Jang, Y.J., Youm, J.B., Earm, Y.E., Leem, C.H.: Stretch-activated currents in cardiomyocytes isolated from rabbit pulmonary veins. *Prog. Biophys. Mol. Biol.*, **97**, 217–231 (2008)
53. Sheehy, S.P., Grosberg, A., Parker, K.K.: The contribution of cellular mechanotransduction to cardiomyocyte form and function. *Biomech. Model. Mechanobiol.* **11**, 1227–1239 (2012)
54. Sneyd, J., Ed.: *Tutorials in Mathematical Biosciences II: Mathematical Modeling of Calcium Dynamics and Signal Transduction*, Springer, ISBN 978-3-540-25439-3 (2005)
55. Stålhärd, J., Klarbring, A., Holzapfel, G.A.: A mechanochemical 3D continuum model for smooth muscle contraction under finite strains. *J. Theoret. Biol.*, **268**, 120–130 (2011).
56. Stern, M.D.: Theory of excitation-contraction coupling in cardiac muscle. *Biophys. J.*, **63**, 497–517 (1992)
57. Subramanian, S., Viatchenko-Karpinski, S., Lukyanenko, V., Györk, S., Wiesner, T.F. Underlying mechanisms of symmetric calcium wave propagation in rat ventricular myocytes. *Biophys. J.*, **80**, 1–11 (2001)
58. Taber, L.A.: Biomechanics of cardiovascular development. *Annu. Rev. Biomed. Eng.*, **3**, 1–25 (2001)
59. Takamatsu, T., Wier, W.G.: Calcium waves in mammalian heart: quantification of origin, magnitude, waveform and velocity. *Fed. Am. Soc. Exp. Biol.*, **4**, 1519–1525 (1990)
60. Ter Keurs, H.E.D.J., Boyden, P.A.: Calcium and arrhythmogenesis. *Physiol. Rev.* **87**(2), 457–506 (2007)
61. Tracqui, P., Ohayon, J.: An integrated formulation of anisotropic force-calcium relations driving spatio-temporal contractions of cardiac myocytes. *Phil. Trans. Royal Soc. London A*, **367**, 4887–4905 (2009)

62. Tveito, A., Lines, G.T., Edwards, A.G., Maleckar, M.M., Michailova, A., Hake, J., McCulloch, A.D.: Slow Calcium-Depolarization-Calcium waves may initiate fast local depolarization waves in ventricular tissue. *Prog. Biophys. Molec. Biol.*, **110**, 295–304 (2012)
63. Vogel, F., Bustamante, R., Steinmann, P.: On some mixed variational principles in electro-elastostatics. *Int. J. Nonlin. Mech.*, **47**, 341–354 (2012)
64. Washio, T., Okada, J., Sugiura, S., Hisada, T.: Approximation for cooperative interactions of a spatially-detailed cardiac sarcomere model. *Cell. Mol. Bioeng.*, **5**, 113–126 (2012)
65. Ward, M.L., Williams, I.A., Chu, Y., Cooper, P.J., Ju, Y.K., Allen, D.G.: Stretch-activated channels in the heart: contributions to length-dependence and to cardiomyopathy. *Prog. Biophys. Mol. Biol.*, **97**, 232–249 (2008)
66. Zhang, Y., Sekar, R.B., McCulloch, A.D., Tung, L.: Cell cultures as models of cardiac mechanoelectric feedback. *Prog. Biophys. Mol. Biol.*, **97**, 367–382 (2008)

---

# On the Assumption of Laminar Flow in Physiological Flows: Cerebral Aneurysms as an Illustrative Example

Øyvind Evju and Kent-Andre Mardal

**Abstract** In physiological fluid flows, except for in the heart and the aorta, the Reynolds numbers are moderate (below 1000). This is far below the typical point of transition in pipe flow, which occurs around Reynolds number 2300. Because of this, laminar flow is commonly assumed in the modelling of these flows, resulting in computational methods tailored for this flow regime.

This chapter presents a critical review of this assumption, and both clinical and numerical evidence of transitional physiological flows are presented. The pulsatility and complex geometries in physiological flow are highlighted as the main reasons for a lower transition point in physiological flows.

Furthermore, we discuss the threshold of transition in a particular case of an aneurysm with respect to resolution, Reynolds number and non-Newtonian viscosity modelling.

## 7.1 Introduction

Most fluid flows in our human body, except for the blood flow in heart and aorta, are believed to be laminar in healthy individuals. A good reason for this, from an evolutionary point of view, is that turbulence introduces extra friction and hence transport is more efficient in the laminar regime than in the turbulent regime. It has also been shown that laminar flow ensures a healthy mechanotransduction<sup>1</sup> in the vessel walls. On the other hand, various pathologies, like for example atheroscle-

---

Ø. Evju  
Simula Research Laboratory, P.O. Box 134, 1325 Lysaker, Norway  
e-mail: oyvinev@simula.no

K.-A. Mardal (✉)  
Simula Research Laboratory, P.O. Box 134, 1325 Lysaker, Norway and  
Department of Informatics, University of Oslo, P.O. Box 1080 Blindern 0316 Oslo, Norway  
e-mail: kent-and@simula.no

<sup>1</sup> Mechanotransduction refers to the process where cells convert mechanical stimuli to chemical activity and is vital in the remodelling that occur in vessels.

rosis and aneurysms, involve anatomies causing disturbed flow and possibly even turbulent flow. The disturbances trigger a downward spiral where the disturbed flow leads to an unhealthy mechanotransduction causing remodelling of the vasculature which again worsen the flow disturbances. Recent research has therefore challenged the assumption of laminar flow in such pathologies and put the focus on the possible role of transitional or turbulent flow in these pathologies.

Transition to turbulence in steady pipe flow occurs at Reynolds number ( $Re$ ) around 2300, while fully developed turbulence is obtained around 4000. The Reynolds number in large arteries and also elsewhere in our body is usually far below 2300 and laminar flow is therefore usually assumed. However, both the pulsatile nature of the flow and deviations from straight pipe geometry might introduce transition to turbulence at lower Reynolds numbers, as we will demonstrate in this chapter.

While the laminar regime and in many applications the fully developed turbulent regime are reasonably well understood from both a modelling and numerical point of view, the transitional regime with occasional turbulence poses additional challenges. Modelling is difficult in particular, because it is challenging to precisely predict the onset of the turbulent spots. Instead of modelling the turbulence, one might increase the resolution in space and time and resolve all scales of the turbulent flow numerically, a technique called direct numerical simulation (DNS). This approach is feasible only for flows with moderate Reynolds numbers because resolving the small structures (Kolmogorov microscales) induces computational costs scaling as  $Re^3$ . In addition to the high resolution requirement, it is necessary to employ schemes that introduce as little dissipation as possible. It may also be necessary to carefully construct the boundary conditions such that these allow for or induce small perturbations or unstable modes that may grow into turbulence. In numerical simulations that do not sufficiently address these requirements, transition is often not seen even though physical experiments reveal them under similar flow conditions.

This chapter is devoted to a critical review on the assumption of laminar flow in physiological flow applications and we will use blood flow in cerebral aneurysms as an illustrating example. We will discuss the consequences of this assumption, which lowers the requirement on the resolution and validates the use of stabilization techniques and time discretizations with dissipation. We will also review clinical and biomechanical findings suggesting that transitional flow is common or at least not unusual in many pathologies. Finally, we discuss cerebral aneurysms in depth and show that for some aneurysms transition may occur already for Reynolds number as low as 300.

## 7.2 On the Definition of Turbulence

Defining and identifying transitional or turbulent flow in a pulsatile and complex 3D geometry is a challenging task. For completeness we include a formal definition of turbulence:

*Turbulent flow is an irregular condition of flow in which the various quantities show a random variation with time and space coordinates, so that statistically distinct average values can be discerned.*

The above definition was provided in [18] and later Bradshaw adds an important observation; namely that *turbulence has a wide range of scales*. See for example [46] for discussions concerning this definition. Following this definition we consider random fluctuations on a wide range of scales as the defining characteristics of turbulence. Laminar flow on the other hand is characterized as smooth and deterministic.

Between the regimes of laminar and fully developed turbulent flows there is a regime with complex flow such as occasional turbulence or spots of turbulence that is often called the transitional regime. According to White [45, p. 344] most analyses are devoted to either the fully developed turbulent regime or the laminar regime and engineers are advised to avoid the transitional regime. While engineers may choose to avoid this regime, several diseased states may lead to transitional flow and the unpredictability of transition may even be a factor that worsen the condition, as will be discussed in the following.

The distinction between laminar, transitional and turbulent flow dates back to 1883 when Osbourne Reynolds observed that the flow condition was governed by the ratio of inertial forces to viscous forces (the Reynolds number) in stationary pipe flow. In his famous experiments Reynolds showed that transition to turbulence in stationary pipe flow occurs at  $Re=2300$  and fully developed turbulence is achieved at  $Re=4000$ . Subsequent experiments have shown that turbulence might be suppressed until  $Re=40\,000$  given sufficiently smooth pipe, inflow and outflow. On the other hand, the lower limit seems to be about 2000 [31].

Transitional or turbulent flow causes extra friction. For example, in stationary pipe flow the pressure drop needed to drive the flow under laminar conditions scales as  $V$ , where  $V$  is the mean flow, while in transitional or turbulent flow the pressure drop scales as  $\approx V^{1.75}$ . This was observed by Hagen in 1839. In pipe flow the transition point is clearly defined as the pressure drop increases from  $V$  and  $V^{1.75}$  and it occurs around around Reynolds number 2100. The sharpness of the transition point suggests that the pressure drop might give insight into the precise transition point and we will therefore also discuss pressure drops in the following.

Pulsatility may both increase and decrease the threshold for transition. In particular, flow deceleration typically promote transition, while acceleration delay transition. Concerning flow in straight pipes, it was demonstrated in [40] that transition to turbulence is highly dependent on the Womersley number. Of particular importance for physiological flow is the fact that the transitional regime occur early for Womersley numbers between 2–5, numbers that are physiologically reasonable. Alternative definitions of the Reynolds number that put the focus on the pulsatility was proposed in this publication.

Probably even more important than the pulsatility is the geometry. For instance, in Couette flow or flow around cylinders, transition occurs at  $Re=500$  and  $Re=300$ , respectively. For this reason a wide range of other Reynolds numbers has also been

proposed in the literature, see [31] for an overview, but it remains difficult to employ these numbers as guidelines for when transition occurs in the complex vasculature of the body. Still, many works consider the Reynolds number as an important guideline for whether the flow is laminar or not and justify their laminar assumption by a Reynolds number calculation.

### 7.3 Clinical Observations

Clinically, turbulent blood flow has been observed *in vivo* associated with the heart valves, the ascending aorta, and in arteriovenous grafts. Audible sounds (20-20 000 Hz) caused by the high frequency pressure fluctuation of turbulence are for some conditions symptoms of severely disturbed flow. For instance heart murmurs are associated with turbulence generated by malfunctioning mitral valves or a stenosed aorta. Arteriovenous grafts sometimes produce audible thrills at frequencies 100-200 Hz caused by vein wall vibration.

Turbulence or transition have received less attention in other pathologies like atherosclerosis and aneurysms, but there are still significant evidence in the clinical literature suggesting that it is common or at least not unusual. For example, severe stenosis in the carotid artery can result in transition to turbulent flow, which may produce an audible sound (bruit) that physicians can detect. Another manifestation of turbulence is pulsatile tinnitus, or tinnitus that is synchronous with a person's heartbeat, which are audible sounds that is transmitted to the inner ear [15]. This condition is likely caused by the abnormal blood flow associated with conditions such as arteriovenous malformations, stenosed carotid arteries, cerebral aneurysms etc. The topic of pulsatile tinnitus in association with cerebral aneurysms dates back to 1936 where Bergstrand et.al. [6] demonstrated pulsatile tinnitus in 4 of 22 cases of intra cranial aneurysms. While their relative high fraction of pulsatile tinnitus per aneurysms have been challenged in, e.g. Beadles [5], several resent studies report that pulsatile tinnitus is indeed present and caused by aneurysms [3, 35]. Pulsatile tinnitus, both subjective (as experienced by the patients) and objective (detected by the clinician), does however require that the sounds generated by the turbulent or transitional flow are transmitted either to the patients inner ear or through the skull for detection. To improve the sound detection procedure, Ferguson employed a phonocatheter on the exposed aneurysm during craniotomy and found that 10 out of 17 aneurysms had bruits of sounds with predominate frequencies in the range of 270 to 660 Hz [10]. This suggests that a significant fraction of aneurysms may have transitional blood flow.

Clinicians have performed various glass model studies to consider the issue of turbulence in blood flow. Already in 1958, Stehbens [36] investigated the transition threshold in idealized bifurcations and S-shaped arteries modelling the carotid siphon. The critical Reynolds numbers in the bifurcation and the S-shaped geometry were 600 and 900, respectively. In all cases he used stationary inflow conditions. Later, in 1972, Roach et.al. [29] considered bifurcations and bifurcations with

aneurysms at the apex using glass models and found that turbulence was present in bifurcations (depending on the angle of the bifurcation) at  $Re=1200$  under steady conditions and around 800 under pulsatile condition. In aneurysms transition occurred already at Reynolds numbers between 400 and 500, with only a slight difference between stationary and pulsatile flow.

## 7.4 Mechanotransduction and the Remodelling of the Vasculature

The vasculature is an active system that adapt to facilitate a healthy blood flow. In particular, it seems that the arterial system adapt vessel radius to a flow that on average has a uniform wall shear stress (WSS) of around 5 Pa [13]. This finding is called the uniform WSS hypothesis and has been found to apply to most parts of the cardiovascular systems. Furthermore, bifurcations in most part of the vasculature have angles and radii that satisfy an optimum principle known as Murray's law. This law states that the energy requirements for metabolism and transport are minimized in blood flow. Murray used this optimum principle to derive a relationship between angles and radii in bifurcations and this relationship has been validated in various parts of the cardiovascular in e.g. rats, dogs and humans [32, 48]. This law suggest that the cardiovascular system is tuned to be cost efficient. However, a notable exception from this law is the bifurcations associated with the circle of Willis, where cerebral aneurysms form [1, 20]. Hence, large parts of the vasculature appear to be constructed for an energy efficient transport of blood throughout the body. Moreover, the vasculature plays an active role and remodel itself to optimize the flow and maintain a uniform WSS. An example of this process can be found in [19, 26]. Here, the authors surgically closed both of the carotid arteries in a rabbit. The consequence was an increased flow of about 400% in the basilar artery. Over the course of a week, the artery grew radially until a baseline WSS was again obtained and the artery remained rather unchanged in the following weeks. Complex geometries like many bifurcations lead to deviations from the principle of uniform WSS and are particularly prone to e.g. atherosclerosis [23] and aneurysms [1]. These complex geometry also often cause early transition.

Research on the mechanotransduction, the process where living cells turn mechanical stimuli to chemical signals, have firmly established that endothelial cells (EC), the cells that surface the innermost layer of the blood vessels, play an active role in the remodelling of blood vessels. Experiments have shown that EC respond to flow, and in particular that undisturbed flow leads to healthy remodelling, while disturbed or oscillating flow fail to do so [4, 7]. Turbulent shear stress also substantially increases the endothelial cell turnover when compared to laminar flow with similar shear [8].

It is however an open question at what time scales the mechanotransduction occur. The biomechanical signalling of EC involves reaction-diffusion process that are slow (tens of seconds) compared to the high-frequency fluctuations in blood flow.

However, recent research suggest that the mechanical signaling can be transmitted more rapidly (within 100 ms) through the cytoskeletal filaments within the EC layer and allow for rapid transmission over longer distances. Furthermore, there is evidence that also the medial and adventitial layers are responsive to this mechanical signalling [4]. It is, however, not known precisely how the various vessel layers remodel themselves and to what extent there are individual variations in the mechanotransduction and remodelling.

Finally, turbulent blood flow introduce clot formation. In fact, in [37] they generated turbulent flow in canine models and it was found that the weight of the thrombosis was proportional to the Reynolds number and turbulence intensity.

## 7.5 Modelling of Blood Flow

Blood is a suspension of blood cells, platelets and plasma and does therefore not necessarily display a Newtonian rheology. A wide range of different models have been proposed and analysed, see e.g. [30]. For blood flow in larger arteries and aneurysms, Newtonian models typically capture the main flow quite accurately, for example maximal WSS, average WSS and area of low WSS correlate strongly ( $>0.95$ ) between Newtonian and commonly used non-Newtonian models [9], but may overestimate WSS in areas of low shear [47].

In large arteries there is also a pulsatile response in the vessel to the blood flow, and this fluid-structure interaction has been the subject of many recent publications [27, 28]. The pressure propagation throughout the vasculature can only be described by fluid-structure interaction models, but there is evidence that the main flow in localized regions can often be modelled by assuming rigid vessels. The main reason for this is that for localized vessel segments the whole segment deforms in synchrony [38]. Hence, for modelling of main flow features in large localized arteries it appears that Newtonian modelling with rigid vessels may be adequate under the assumption of laminar flow, bearing in mind the large flow differences caused by the geometrical variations between different patients.

The previously mentioned studies that report turbulence, all consider Newtonian flow within rigid geometries. However, both non-Newtonian viscosity and fluid-structure interaction may both delay or accelerate transition. From an engineering point of view, delay of transition has been a hot topic for over 50 years because of its potential to reduce drag and suppress noise.

Concerning transition and fluid-structure interaction, Kramer [22] demonstrated already in 1960 that compliant coating, based on the dolphin's epidermis, may substantially delay transition. Naturally, this spurred a lot of research activity, which mostly failed to reproduce the drag reduction demonstrated by Kramer. Now, more than 50 years after the initial experiments of Kramer, there is little doubt that compliant coating may delay transition, c.f. e.g., [16]. Reynolds numbers for transition in geometries with compliant coating may exceed corresponding Reynolds numbers for flow within rigid geometries by more than an order of magnitude. However, it is

also clear that delaying transition is delicate and that compliance might even introduce instabilities.

An interesting case here is the audible sounds caused by vein wall vibration in arteriovenous grafts. The vein wall vibration is present *in vivo* and is believed to be caused by high frequency pressure fluctuation in the turbulent blood flow occurring already at Reynolds number as low as 500. However, *in vitro* models and also numerical simulations have failed to demonstrate turbulent flow in models of arteriovenous grafts at such low Reynolds numbers [34]. In fact, the studies suggest that the graft geometry and flow pulsatility are not sufficient to explain the transition at such low Reynolds numbers and it appears that the only likely explanation is either the non-linear viscosity of blood or the compliance of the vessel walls. In particular, the high frequency content of the vortical structures appear to be strongly linked with the natural harmonics of the wall. We also remark that in arteriovenous grafts there is a strong correlation between vein wall vibration and intimal thickening [11], suggesting that the veins are able to sense and react to the turbulence although not in a beneficial manner.

## 7.6 On the Modelling of Transitional Flow

The process of transition is a difficult topic that has been under intensive research since Reynolds and Hagen did their famous experiments. Transition occurs because unstable modes are triggered, starting often as minor perturbations to the flow that grow either in space, time or both. The Navier-Stokes equations are non-linear and non-normal and a consequence is that the standard approach of stability analysis in terms of eigenvalue fail to predict the occurrence of unstable mode leading to transition. For instance, transition in simple flow problems as Couette and Poiseuille can not be explained in terms the linear analysis of eigenvalues [41]. Because the exact mechanism behind transition (or the procedure to calculate the unstable modes) is not known, it is difficult to model transition using for instance Reynolds averaged Navier-Stokes equations for transition even though they often are powerful tools for fully developed turbulence.

For flow problems such as physiological flow applications where the Reynolds number is moderate, it is usually not possible to predict whether transition will occur or not. The only feasible approach seems to be to perform a DNS. This is, however, challenging for at least three reasons: 1) special care needs to be taken to construct discretization schemes to avoid dissipation, 2) the resolution needs to be extremely high compared to corresponding laminar simulations, and 3) boundary conditions needs to be chosen such that instabilities are allowed.

This is in sharp contrast to simulations where laminar flow is assumed and where most simulations, at least for aneurysms studies, employ first order schemes with built-in dissipation that avoid stability issues [44]. Here, the justification for these schemes is that laminar flow is assumed. Moreover, as [44] points out, convergence studies are not always reported or are performed in a poor fashion. It is therefore

difficult to determine whether transition would occur at a higher resolution in these studies. A recent benchmark study [39], where 25 research groups performed CFD analysis in a prescribed geometry of a cerebral aneurysm with a proximal stenosis given boundary conditions, reveals that the flow varied remarkably inside the aneurysms among the results of the different research groups. There was a clear tendency that simulations with research codes on high resolutions demonstrated flow instabilities to a greater extent than low resolution simulations performed with commercial codes.

Concerning the resolution of the discretization, the requirement of a DNS is that the so-called Kolmogorov scales are resolved. Determining the Kolmogorov scale is challenging from a numerical point of view as it needs to be estimated based on the simulation results, and grid independence of local quantities needs to be established. However, as pointed out in [2], performing DNS studies that concern blood flow is particularly challenging as the Kolmogorov length scale may be on the same scale as the red blood cells and thus it is on the scale where the continuum hypothesis breaks down.

Still, several attempts of DNS studies in carotid arteries [24], arteriovenous grafts [25], cerebral aneurysms [42] have been performed, albeit at a much coarser resolution than the estimates provided in [2]. These simulations report cycle-to-cycle variations on a wide range of scales, e.g., temporal fluctuations in the range of 100–1000 Hz. An important observation is that instabilities seems to be caused by geometry rather than the pulsatility and therefore that stationary inflow/outflow conditions can be used to detect possible transition effects and for grid-independence studies, c.f. e.g. [24, 43, 44]. This is because the pulsatility is relatively slow as compared with the velocities in the sense that the number of flow-throughs per cycle is sufficiently high. However, it has been pointed out that transition most often occurs in the deceleration phase [42]. Simulations with constant flow can therefore be assumed to predict a higher critical Reynolds number, than a similar simulation with pulsatile flow.

## 7.7 An Illustrating Example: Transition in a Cerebral Aneurysm

To investigate the threshold to transition, we consider an aneurysms from a canine model [21]. The aneurysm, although artificially produced, is a prototype for human aneurysms created by a technique often used in clinical trials. The aneurysm is shown in Fig. 7.1.

The aneurysm model was meshed with 3,275,000 tetrahedra, with a coarser mesh at the distal parts of the geometry. This corresponds to approximately 25–50 cells across the parent artery diameter and 120–150 cells across the diameter of the aneurysm, with an average edge length of 0.137mm. This is not claimed to be fully converged, as Fig. 7.2 illustrates, but it is in the upper range of resolutions used in CFD studies within the field. However, to capture any high-frequency flow effects, the time step was set to 7.5e–6s, several orders of magnitude below what is typically



**Fig. 7.1.** The canine aneurysm that is used in our computations. The dark slice is used to display the flow field, the red dot denoted by a P shows the point used in our analysis of the turbulent characteristics, and the balls A, B1 and B2 are used to calculate the pressure drop over the aneurysm ( $\Delta p := \bar{p}_A - \frac{\bar{p}_{B1} + \bar{p}_{B2}}{2}$ )

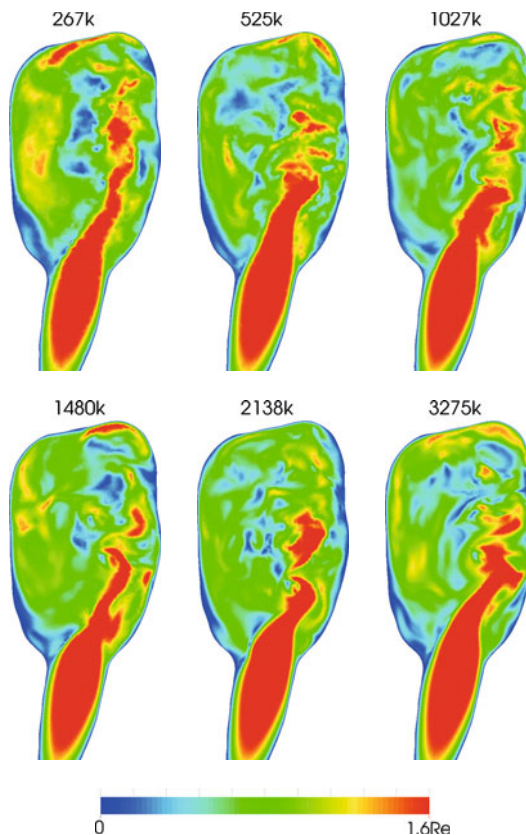


**Fig. 7.2.** The figure shows the velocity magnitude in a slice through the aneurysm at Reynolds numbers 1000 at various resolutions

employed. Blood was modelled with a density of  $1056 \text{ kg/m}^3$  and a Newtonian viscosity of  $3.45 \text{ mPa s}$ .

Dirichlet boundary conditions were set for the velocity, with no-slip conditions at the walls, and paraboloid-shaped inflows and outflows, with the flow rate distributed evenly between the two outflows. For the pressure, natural boundary conditions were used, and the resulting pressure was normalized around zero.

As was demonstrated in [12, 24], the transition to turbulence in larger arteries is predominantly governed by the geometry rather than the relatively slow pulsatility that merely turns the turbulence on and off. That is, given the relatively long cardiac cycle ( $> 10$  flow-throughs in a typical model), it is preferable to consider the question of turbulence under static conditions, which is done in the following. Notice, however, that while the boundary conditions are static, as the Reynolds number increase, the flow inside the aneurysm and surrounding will not be stationary. In fact, as was demonstrated in [43], we might expect high frequency fluctuations ( $> 100 \text{ Hz}$ ) already at Reynolds numbers around 200–300.

The Navier-Stokes equations were solved with a finite element incremental pressure correction scheme, following the idea of [14]. The scheme applies a Crank-Nicolson method for the time stepping and a linear handling of the convection term as introduced by [33], making the tentative velocity step second order in both time and space. This scheme is chosen because it preserves the exact same stability properties as Navier-Stokes and hence does not introduce additional dissipation in the flow. The scheme reads as:

At  $t = t^{n+1} := (n + 1)\Delta t$  with the solution  $(u^k, p^k) := (u(t^k), p(t^k))$  known for  $k = 0, \dots, n$ , kinematic viscosity  $\nu$ , and density  $\rho$ , do

1. Solve a reaction-diffusion-advection equation for a tentative velocity,  $\tilde{u}^{n+1}$ :

$$\frac{1}{\Delta t} (\tilde{u}^{n+1} - u^n) - \nabla \cdot \nu \nabla \tilde{u}^{n+\alpha} + u^* \cdot \nabla \tilde{u}^{n+\alpha} + \nabla p^{n-1} = 0,$$

where

$$\begin{aligned} \tilde{u}^{n+\alpha} &= \alpha \tilde{u}^{n+1} + (1 - \alpha) u^n \quad (\alpha = \frac{1}{2} \text{ for Crank-Nicolson}), \\ u^* &= \frac{3}{2} u^n - \frac{1}{2} u^{n-1}. \end{aligned}$$

2. Solve a Poisson equation for the pressure,  $p^{n+1}$ :

$$\Delta p^{n+1} = \Delta p^n + \frac{\rho}{\Delta t} \nabla \cdot \tilde{u}^{n+1}.$$

3. Update for the correct velocity,  $u^{n+1}$ :

$$u^{n+1} = \tilde{u}^{n+1} - \frac{\Delta t}{\rho} \nabla (p^{n+1} - p^n).$$

4. Increment ( $n \leftarrow n + 1$ ) and repeat.

The scheme was implemented in the open source software package FEniCS<sup>2</sup>, and is available through the open source CFD package *cbc.flow*<sup>3</sup>. Linear elements were used for both velocity and pressure.

We first ran simulations at a coarser time resolution to obtain steady state solutions to be used as initial condition for our main simulations with 0.2 to 6 flow-throughs depending on the Reynolds number. We then disregarded the first 5000 time steps of our main simulations to allow for the finer time scales to reach a quasi-steady state.

To analyse the turbulent characteristics of the flow over time, we analyse the power spectral density (PSD) of the velocity magnitude in a point of the interior of the aneurysm sac, as shown in Fig. 7.1. The PSD for a discrete time-signal is as follows. Let

$$S_{xx}(\omega) = \frac{(\Delta t)^2}{T} \left| \sum_{n=1}^N x_n e^{-i\omega n} \right|^2,$$

where  $\omega$  is the frequency,  $\Delta t$  is the time step,  $T$  is the time interval,  $N$  is the number of samples and  $x_n$  denotes the sample at  $t = n\Delta t$ . Since the velocity magnitude is real-valued, the PSD is symmetric, i.e.  $S_{\|\mathbf{u}\| \|\mathbf{u}\|}(\omega) = S_{\|\mathbf{u}\| \|\mathbf{u}\|}(-\omega)$ . We therefore define  $PSD_{\|\mathbf{u}\|}$  as

$$PSD_{\|\mathbf{u}\|}(\omega) := 2S_{\|\mathbf{u}\| \|\mathbf{u}\|}(\omega), \quad \omega > 0.$$

This is related to the sample variance of  $\|\mathbf{u}\|$  with the relation

$$\sigma^2 = \int_0^\infty PSD_{\|\mathbf{u}\|}(\omega) d\omega.$$

Thus,  $PSD_{\|\mathbf{u}\|}$  can provide information about which frequencies are required to resolve, in our case, the pointwise velocity magnitude. In the following, we report  $\omega_{0.95}$  as the approximate frequency that is required to capture 95% of the variance, that is,

$$\int_0^{\omega_{0.95}} PSD_{\|\mathbf{u}\|}(\omega) d\omega = 0.95\sigma^2.$$

Given our time stepping, we are limited by the Nyquist frequency of  $\frac{1}{2\Delta t} \approx 66667$  Hz. The number of bins in the discrete Fourier transform are given by  $T \frac{1}{\Delta t} = 20000$ , and the bin size is thus 3.33 Hz.

The PSD analysis seen in Fig. 7.3 revealed a significant change in the frequencies of the flow between  $Re=250$  and  $Re=500$ . When  $Re<250$ ,  $\omega_{0.95}$  is less than 60 Hz, but this jumps to 313 Hz at  $Re=500$  and further to 923 Hz and 2046 Hz at  $Re=1000$  and  $Re=2000$ , respectively. To capture any flow effects at these frequencies, the resolution requirements are minimum twice the reported frequency. However, this is no guarantee for the *correct* flow effects at these frequencies. It should also be noted that when considering pulsatile flows, the frequencies present in the flow are likely

<sup>2</sup> <http://fenicsproject.org>

<sup>3</sup> [https://bitbucket.org/simula\\_cbc/cbcflow](https://bitbucket.org/simula_cbc/cbcflow)

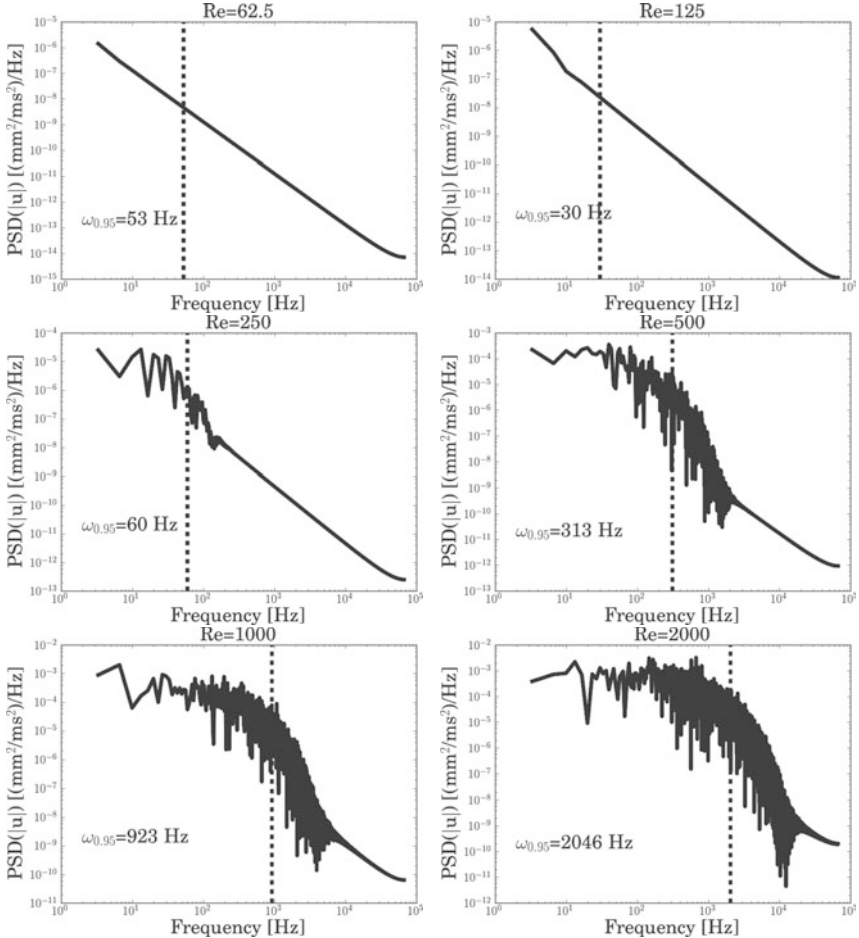


**Fig. 7.3.** The figure shows the power spectrum of a point in the aneurysm at different Reynolds numbers

significantly higher, due to the deceleration phase of the flow at late systole/early diastole.

Considering the slice views in Fig. 7.4, the pattern is clearly seen of the increasing complexity in the flow from  $Re = 250$  and upwards. Worth noting is also the flow field in the parent artery, which appears laminar as expected.

While blood displays non-Newtonian rheology, in many CFD studies the shear rates are assumed adequately high to assume a Newtonian behaviour. While this assumption is often adequate [9], its effect on the transition of flow has not been studied. To address this, we employ a Modified Cross viscosity presented in Fig. 7.5. The model parameters are fitted to viscometer data [30], and the computation was done explicitly. We re-ran simulations at the flow rates corresponding to  $Re=250$  and

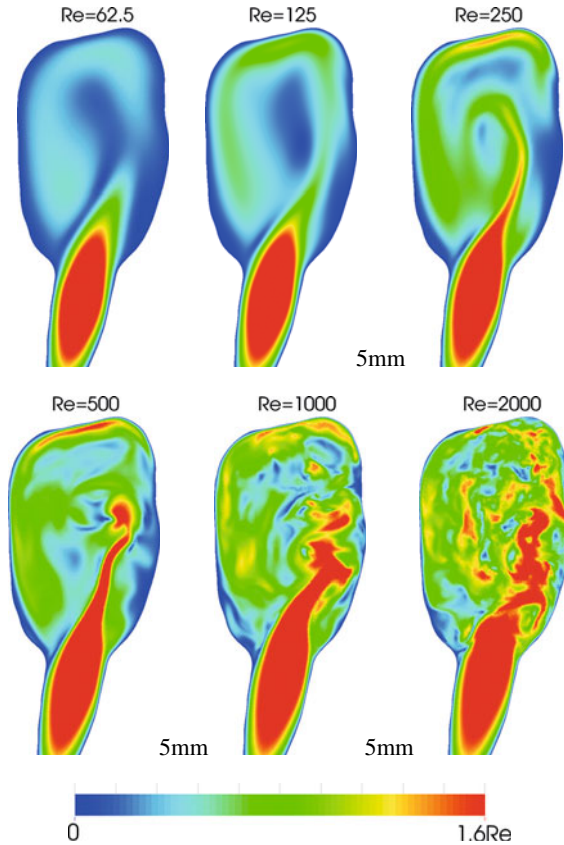


**Fig. 7.4.** The figure shows the velocity magnitude in a slice through the aneurysm at different Reynolds numbers

Re=500 in the Newtonian case. Since the flow rates are equal, but the viscosity is not, the actual Reynolds number is somewhat lower for the non-Newtonian case. The Reynolds number will be similar to the Newtonian case in the parent artery, where the shear rate is high, but will change in the parts of the geometry where the shear rate drops. On average, the Modified Cross model predicted 20% higher viscosity compared to the Newtonian case.

The resulting PSD can be seen in Fig. 7.6, with slice-views of the flow in Fig. 7.7. Keeping in mind the effects on the Reynolds number, it would appear that the non-Newtonian viscosity model delays the transition of the flow significantly.

In pipe flow the transition to turbulence is clearly identified by a marked change in the pressure drop relation to velocity. The pressure drop increases linearly as the velocity (or Reynolds number) increase in laminar flow, but has a sharp point of transition that occur around  $Re=2000$  after which the pressure drop grows like  $\approx V^{1.75}$ , see e.g. Fig. 6.4 in [45]. In Fig. 7.8, we show the pressure drop as a function of the

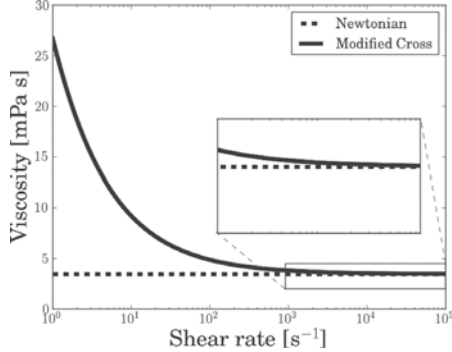


**Fig. 7.5.** The two viscosity models used. The Modified Cross model is given by  $\frac{\mu - \mu_\infty}{\mu_0 - \mu_\infty} = \frac{1}{(1 + (l\dot{\gamma})^m)^a}$  with  $l = 3.736s$ ,  $m = 2.406$ ,  $a = 0.254$ ,  $\mu_0 = 0.056\text{ Pas}$ ,  $\mu_\infty = 0.00345\text{ Pas}$ . Note that the Modified Cross approaches the Newtonian model used as  $\dot{\gamma} \rightarrow \infty$

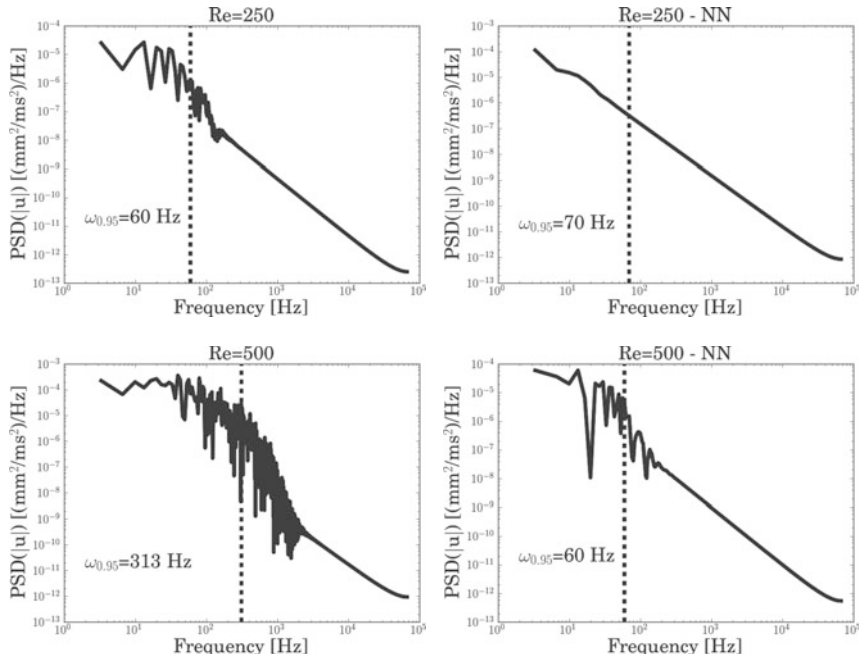


**Fig. 7.6.** The figure shows the  $PSD_{||\mathbf{u}||}$  Reynolds numbers 250 and 500 with a Newtonian and non-Newtonian viscosity model

Reynolds number in the parent vessel. For Reynolds number between 0 and 200, the pressure drop demonstrate a linear dependency to the Reynolds number. However, already at  $Re=200$  deviations start to occur, also with notable variations over time. The transition point is, however, not as easily identified as in stationary pipe flow.

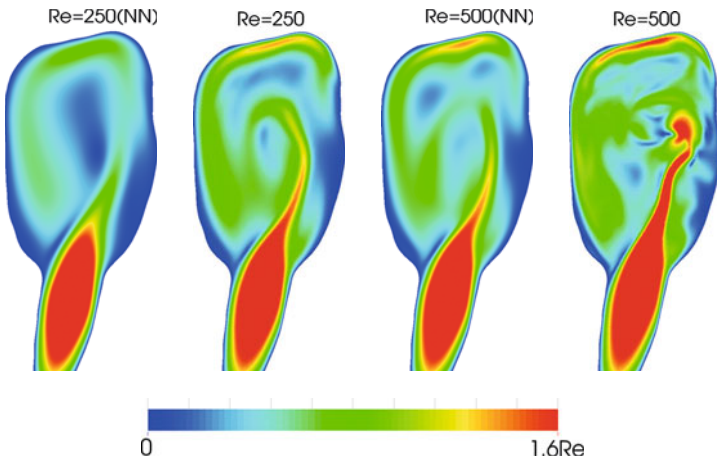


**Fig. 7.7.** The figure shows the velocity magnitude of the flow for simulations with a non-Newtonian viscosity compared to simulations with a Newtonian viscosity

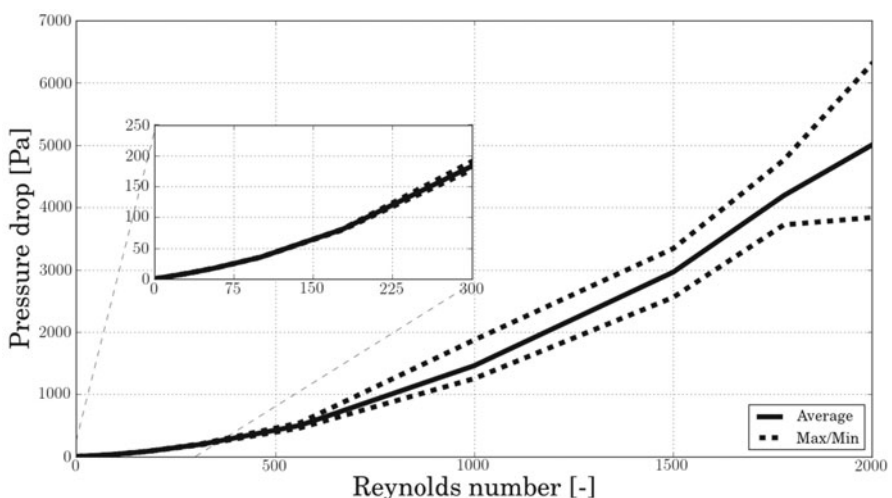


**Fig. 7.8.** The figure shows the pressure drop over the aneurysm as a function of the Reynolds number. Clearly, the pressure drop demonstrate a close to linear relation with respect to the Reynolds number for low numbers, but already at around Reynolds number 200 deviations from the linear relation occur and the pressure drop is no longer static in time

## 7.8 Discussion

This chapter mainly discuss aspects of cerebral aneurysms and aim to illustrate that transition to turbulence might be an important factor for some aneurysms. We modelled a canine aneurysm model, under steady in- and outflow conditions, and transi-

tion occurred already at Reynolds number around 200–500. It remains to be investigated whether transition is important *in vivo* and whether it is linked to rupture.

Aneurysms have strong geometrical variation. A recent publication [43] found transition in 5 of 12 middle cerebral artery aneurysms at comparable Reynolds numbers (also under stationary conditions). Some clinical research have also reported signs of transition. For instance, Ferguson found that 10 out of 17 aneurysms had bruits of sounds with predominate frequencies in the range of 270 to 660 Hz [10] and suggested that the sounds were generated by transitional or turbulent flow inside the aneurysm. Other studies such as [3, 6, 35] suggest that pulsatile tinnitus sometimes is caused by transition to turbulent flow inside aneurysms.

There are many factors that may both promote and delay transition. In addition to the geometry, both flow pulsatility, non-Newtonian rheology, and fluid–structure interaction between blood and vessels may significantly both decrease and increase the threshold for transition. Furthermore, these factors may even promote transition in some aneurysm and delay transition in others. In this paper, we have demonstrated that a non-Newtonian model (Modified Cross) delayed transition in one particular aneurysm. It is not clear whether this applies to other aneurysm or non-Newtonian models.

Many other conditions related to abnormal blood flow, such as stenosed carotid arteries, aortic aneurysms, arteriovenous malformation share the characteristics of Reynolds number significantly less than 2000, but involve flow in highly complex geometry that might significantly reduce the threshold of transition. Furthermore, audible sounds are often indicative of the severity of the conditions. It therefore seems that transitional or turbulent flow may be associated with many cardiovascular conditions and this observation suggest that an increased focus on transition in the computational modelling community might be needed.

The flow of cerebrospinal fluid flow that surrounding the central nervous system is in many respect similar to cardiovascular flow. Rough calculations of the Reynolds number suggest that it is around 200 in healthy flow, but several conditions are associated with hyper-kinetic flow. Clinicians often report turbulence in normal pressure hydrocephalus, a form of dementia. A recent publication [17] shows that the cerebrospinal fluid flow is on the threshold to transition in a patient with the Chiari malformation – a condition where the lower part of the brain is herniated through the skull and obstruct the pulsatile flow between the neck and skull. Hence, transition may also be an issue for conditions associated with abnormal cerebrospinal fluid flow.

Detecting transitional or turbulent flow by performing numerical simulations are challenging because the mechanism behind transition is only partly understood. Delaying or removing transition in numerical simulations are easily done by for example employing stabilizing schemes or using too coarse resolution. However, clinical evidence over a wide range of applications suggest that flow instabilities, transition and turbulence might be important in several conditions. Finally, the fluid–structure interaction between the flow and surrounding tissue and the non-linear viscosity of blood might both stabilize and de-stabilize the flow depending on the circumstances.

Hence, at this point, it seem that there are many open questions and unresolved issues concerning transitional flow in several important diseases.

## 7.9 Conclusions

Some evidence in the clinical literature suggest that conditions such as for example cerebral aneurysms may sometimes cause transition to turbulence. Still, this issue has largely been neglected in the biomechanical modelling and numerical simulations. The current chapter present simulations that demonstrate that transition may occur already at Reynolds number of the order of 300–500 in a typical canine model aneurysm. Aneurysm geometry, flow pulsatility, non-Newtonian rheology, and fluid–structure interaction may both promote and delay transition and it is therefore unclear how important transition is *in vivo*.

## References

1. Alnæs, M.S., Isaksen, J., Mardal, K.A., Romner, B., Morgan, M.K., Ingebrigtsen, T.: Computation of hemodynamics in the circle of willis. *Stroke* **38**(9), 2500–2505 (2007)
2. Antiga, L., Steinman, D.A.: Rethinking turbulence in blood. *Biorheology* **46**(2), 77–81 (2009)
3. Austin, J., Maceri, D.: Anterior communicating artery aneurysm presenting as pulsatile tinnitus. *ORL; Journal for oto-rhino-laryngology and its related specialties* **55**(1), 54–57 (1993)
4. Barakat, A.I.: Blood flow and arterial endothelial dysfunction: Mechanisms and implications. *Comptes Rendus Physique* (2013)
5. Beadles, C.F.: Aneurisms of the larger cerebral arteries. *Brain* **30**(3), 285–336 (1907)
6. Bergstrand, H., Olivecrona, H., Tönnis, W.: Gefässmissbildungen und Gefässgeschwülste des Gehirns. Georg Thieme (1936)
7. Chien, S.: Mechanotransduction and endothelial cell homeostasis: the wisdom of the cell. *American Journal of Physiology-Heart and Circulatory Physiology* **292**(3), H1209–H1224 (2007)
8. Davies, P.F., Remuzzi, A., Gordon, E.J., Dewey, C.F., Gimbrone, M.A.: Turbulent fluid shear stress induces vascular endothelial cell turnover in vitro. *Proceedings of the National Academy of Sciences* **83**(7), 2114–2117 (1986)
9. Evju, Ø., Valen-Sendstad, K., Mardal, K.A.: A study of wall shear stress in 12 aneurysms with respect to different viscosity models and flow conditions. *Journal of biomechanics* **46**(16), 2802–2808 (2013)
10. Ferguson, G.G.: Turbulence in human intracranial saccular aneurysms. *Journal of neurosurgery* **33**(5), 485–497 (1970)
11. Fillinger, M.F., Reinitz, E.R., Schwartz, R.A., Resetarits, D.E., Paskanik, A.M., Bruch, D., Bredenberg, C.E.: Graft geometry and venous intimal-medial hyperplasia in arterio-venous loop grafts. *Journal of Vascular Surgery* **11**(4), 556–566 (1990)
12. Fischer, P.F., Loth, F., Lee, S.E., Lee, S.W., Smith, D.S., Bassiouny, H.S.: Simulation of high-Reynolds number vascular flows. *Computer methods in applied mechanics and engineering* **196**(31), 3049–3060 (2007)

13. Fung, Y.c.: Biomechanics: circulation. Springer, New York (1997)
14. Goda, K.: A multistep technique with implicit difference schemes for calculating two- or three-dimensional cavity flows. *Journal of Computational Physics* **30**(1), 76–95 (1979)
15. Hafeez, F., Levine, R.L., Dulli, D.A.: Pulsatile tinnitus in cerebrovascular arterial diseases. *Journal of Stroke and Cerebrovascular Diseases* **8**(4), 217–223 (1999)
16. Gad-el Hak, M., et al.: Compliant coatings: a decade of progress. *Applied Mechanics Reviews* **49**, S147–S160 (1996)
17. Helgeland, A., Mardal, K.A., Haughton, V., Pettersson Reif, B.A.: Numerical simulations of the pulsating flow of cerebrospinal fluid flow in the cervical spinal canal of a chiari patient. *Journal of Biomechanics* (2014)
18. Hinze, J.: Turbulence. McGraw-Hill Book Company (1959)
19. Hoi, Y., Gao, L., Tremmel, M., Paluch, R.A., Siddiqui, A.H., Meng, H., Mocco, J.: In vivo assessment of rapid cerebrovascular morphological adaptation following acute blood flow increase. *Journal of neurosurgery* **109**(6), 1141 (2008)
20. Ingebrigtsen, T., Morgan, M.K., Faulder, K., Ingebrigtsen, L., Sparr, T., Schirmer, H.: Bifurcation geometry and the presence of cerebral artery aneurysms. *Journal of neurosurgery* **101**(1), 108–113 (2004)
21. Jiang, J., Johnson, K., Valen-Sendstad, K., Mardal, K.A., Wieben, O., Strother, C.: Flow characteristics in a canine aneurysm model: A comparison of 4D accelerated phase-contrast MR measurements and computational fluid dynamics simulations. *Medical Physics* **38**, 6300 (2011)
22. Kramer, M.O.: Boundary layer stabilization by distributed damping. *Journal of the American Society for Naval Engineers* **72**(1), 25–34 (1960)
23. Ku, D.N.: Blood flow in arteries. *Annual Review of Fluid Mechanics* **29**(1), 399–434 (1997)
24. Lee, S.E., Lee, S.W., Fischer, P.F., Bassiouny, H.S., Loth, F.: Direct numerical simulation of transitional flow in a stenosed carotid bifurcation. *Journal of biomechanics* **41**(11), 2551–2561 (2008)
25. Lee, S.W., Fischer, P., Loth, F., Royston, T., Grogan, J., Bassiouny, H.: Flow-induced vein-wall vibration in an arteriovenous graft. *Journal of fluids and structures* **20**(6), 837–852 (2005)
26. Meng, H., Swartz, D.D., Wang, Z., Hoi, Y., Kolega, J., Metaxa, E.M., Szymanski, M.P., Yamamoto, J., Sauvageau, E., Levy, E.I.: A model system for mapping vascular responses to complex hemodynamics at arterial bifurcations *in vivo*. *Neurosurgery* **59**(5), 1094 (2006)
27. Quarteroni, A., Formaggia, L.: Mathematical modelling and numerical simulation of the cardiovascular system. *Handbook of numerical analysis* **12**, 3–127 (2004)
28. Quarteroni, A., Tuveri, M., Veneziani, A.: Computational vascular fluid dynamics: problems, models and methods. *Computing and Visualization in Science* **2**(4), 163–197 (2000)
29. Roach, M.R., Scott, S., Ferguson, G.G.: The hemodynamic importance of the geometry of bifurcations in the circle of willis (glass model studies). *Stroke* **3**(3), 255–267 (1972)
30. Robertson, A.M., Sequeira, A., Owense, R.G.: Rheological models for blood. In: *Cardiovascular mathematics. Modeling and simulation of the circulatory system*, pp. 211–241. Springer-Verlag Italia, Milano (2009)
31. Schlichting, H., Kestin, J.: Boundary-layer theory, vol. 539. McGraw-Hill, New York (1968)
32. Sherman, T.F.: On connecting large vessels to small. The meaning of Murray's law. *The Journal of general physiology* **78**(4), 431–453 (1981)

33. Simo, J., Armero, F.: Unconditional stability and long-term behavior of transient algorithms for the incompressible Navier-Stokes and Euler equations. *Computer Methods in Applied Mechanics and Engineering* **111**(1), 111–154 (1994)
34. Smith, D.S.: Experimental investigation of transition to turbulence in arteriovenous grafts. Ph.D. thesis, University of Illinois at Chicago (2008)
35. Sonmez, G., Basekim, C.C., Ozturk, E., Gungor, A., Kizilkaya, E.: Imaging of pulsatile tinnitus: a review of 74 patients. *Clinical imaging* **31**(2), 102–108 (2007)
36. Stehbens, W.: Turbulence of blood flow. *Experimental Physiology* **44**(1), 110–117 (1959)
37. Stein, P.D., Sabbah, H.N.: Measured turbulence and its effect on thrombus formation. *Circulation Research* **35**(4), 608–614 (1974)
38. Steinman, D.A.: Assumptions in modelling of large artery hemodynamics. In: *Modeling of Physiological Flows*, pp. 1–18, Springer, Milan (2012)
39. Steinman, D.A., Hoi, Y., Fahy, P., Morris, L., Walsh, M., Aristokleous, N., Anayiotis, A.S., Papaharilaou, Y., Arzani, A., Shadden, S., et al.: Variability of CFD solutions for pressure and flow in a giant aneurysm: The SBC2012 CFD challenge. *Journal of biomechanical engineering* **1**, 542 (2013)
40. Stettler, J., Hussain, A.: On transition of the pulsatile pipe flow. *Journal of Fluid Mechanics* **170**(1), 169–197 (1986)
41. Trefethen, L., Trefethen, A., Reddy, S., Driscoll, T., et al.: Hydrodynamic stability without eigenvalues. *Science* **261**(5121), 578–584 (1993)
42. Valen-Sendstad, K., Mardal, K.A., Mortensen, M., Reif, B.A.P., Langtangen, H.P.: Direct numerical simulation of transitional flow in a patient-specific intracranial aneurysm. *Journal of biomechanics* **44**(16), 2826–2832 (2011)
43. Valen-Sendstad, K., Mardal, K.A., Steinman, D.A.: High-resolution cfd detects high-frequency velocity fluctuations in bifurcation, but not sidewall, aneurysms. *Journal of Biomechanics* **46**(2), 402–407 (2013)
44. Valen-Sendstad, K., Steinman, D.: Mind the gap: Impact of computational fluid dynamics solution strategy on prediction of intracranial aneurysm hemodynamics and rupture status indicators. *American Journal of Neuroradiology* (2013). DOI 10.3174/ajnr.A3793
45. White, F.M.: *Fluid mechanics*. WCB/McGraw-Hill, Boston (1999)
46. Wilcox, D.C.: *Turbulence modeling for CFD*, vol. 2. DCW industries La Canada (1998)
47. Xiang, J., Tremmel, M., Kolega, J., Levy, E.I., Natarajan, S.K., Meng, H.: Newtonian viscosity model could overestimate wall shear stress in intracranial aneurysm domes and underestimate rupture risk. *Journal of NeuroInterventional Surgery* **4**(5), 351–357 (2012)
48. Zamir, M.: Nonsymmetrical bifurcations in arterial branching. *The Journal of general physiology* **72**(6), 837–845 (1978)

---

# Effects of Poroelasticity on Fluid-Structure Interaction in Arteries: a Computational Sensitivity Study

Martina Bukac, Ivan Yotov, Rana Zakerzadeh and Paolo Zunino

**Abstract** We model blood flow in arteries as an incompressible Newtonian fluid confined by a poroelastic wall. The blood and the artery are coupled at multiple levels. Fluid forces affect the deformation of the artery. In turn, the mechanical deformation of the wall influences both blood flow and transmural plasma filtration. We analyze these phenomena using a two layer model for the artery, where the inner layers (the endothelium and the intima) behave as a thin membrane modeled as a linearly elastic Koiter shell, while the outer part of the artery (accounting for the media and the adventitia) is described by the Biot model. We assume that the membrane can transduce displacements and stresses to the artery and it is permeable to flow.

We develop a numerical scheme based on the finite element method to approximate this problem. Particular attention must be addressed to the discrete enforcement of the interface conditions. Because of poroelasticity, the interaction of the fluid and the structure at the interface is more complicated than in the case of a standard fluid-structure interaction problem. Among different possible strategies to address this task, we consider the weak enforcement of interface conditions based on Nitsche's type mortaring, which is easily adapted to this particular problem and it guarantees stability.

The ultimate objective of this work is to use the available solver to investigate the effect of poroelastic coupling on the behavior of fluid-stucture interaction for large arteries. In particular, we are interested to qualitatively characterize how the presence of intramural flow coupled to the arterial wall deformation affects the displacement field as well as the propagation of pressure waves.

---

M. Bukac · I. Yotov

Department of Mathematics, University of Pittsburgh, Pittsburgh, PA, USA  
e-mail: bukac@math.pitt.edu; yotov@math.pitt.edu

R. Zakerzadeh · P. Zunino (✉)

Department of Mechanical Engineering and Materials Science, University of Pittsburgh, Pittsburgh, PA, USA  
e-mail: raz25@pitt.edu; paz13@pitt.edu

## 8.1 Introduction

The material properties of arteries have been widely studied [1, 6, 14, 18, 22, 32, 36]. Pseudo-elastic [18, 37], viscoelastic [1, 6, 14] and nonlinear material models represent well known examples. Poroelastic phenomena are interesting in different applications where soft biological tissues are involved. We mention for example cerebrospinal flow [25], which also involves fluid-structure interaction (FSI), the study of hysteresis effects observed in the myocardial tissue [20, 21], as well as the modeling of lungs as a continuum material [31]. Poroelasticity becomes particularly interesting when looking at the coupling of flow with mass transport. This is a significant potential application, since mass transport provides nourishment, removes wastes, affects pathologies and allows to deliver drugs to arteries [29]. Besides biological applications, this model can also be used in numerous other applications: geomechanics, ground-surface water flow, reservoir compaction and surface subsidence, seabed-wave interaction problem, etc.

To our knowledge, only a few of these constitutive models for the arterial wall have been deeply analyzed in the time dependent domain, when coupled with the pulsation induced by heartbeat. The coupling between a fluid and a single layer poroelastic structure has been previously studied in [4, 28, 33, 35]. In particular, the work in [4] is based on the modeling and a numerical solution of the interaction between an incompressible, Newtonian fluid, described using the Navier Stokes equations, and a poroelastic structure modeled as a Biot system. The problem was solved using both a monolithic and a partitioned approach.

With respect to the previous studies, an innovative aspect of the proposed investigation, is to represent the artery as a multilayered structure. While there exist many complex and detailed models for multilayered structures in different applications [7, 15, 23, 34], the dynamic interaction between the fluid and a multilayered structure remains an area of active research. To our knowledge, the only theoretical result was presented in [27], where the authors proved existence of a solution to a fluid-two-layered-structure interaction problem, in which one layer is modeled as a thin (visco)elastic shell and the other layer as a linearly elastic structure.

In this work, we propose a model that captures interaction between a fluid and a multilayered structure, which consists of a thin elastic layer and a thick poroelastic layer. We assume that the thin layer represents a homogenized combination of the endothelium, tunica intima, and internal elastic lamina, while the thick layer represents the tunica media. The thin elastic layer is modeled using the linearly elastic Koiter membrane model, while the poroelastic medium is modeled using the Biot equations. The Biot system consists of an elastic skeleton and connecting pores filled with fluid. We assume that the elastic skeleton is homogeneous and isotropic, while the fluid in the pores is modeled using the Darcy equations. The Biot system is coupled to the fluid and the elastic membrane via the kinematic (no-slip and conservation of mass) and dynamic (conservation of momentum) boundary conditions. More precisely, we assume that the elastic membrane can not store fluid, but allows the flow through it in the normal direction. In the tangential direction, we prescribe the no-slip boundary condition. This assumption is reasonable in blood flow modeling,

since it has been shown in [24] that predominant direction of intimal transport is the radial direction normal to the endothelial surface, for all ranges of relative intimal thickness.

A similar problem setting is addressed in [10], where we propose and thoroughly analyze the approximation properties of an operator splitting method aiming at decoupling the solution of the governing equation at every time step. Here, we consider an alternative strategy to come up with a loosely coupled FSI algorithm. It is based on the weak enforcement of interface conditions by means of Nitsche's type mortaring combined with the introduction of suitable stabilization operators, as originally proposed for a more standard FSI problem in [11].

The objective of this work is to use the latter computational model to investigate the role of poroelastic effects on the characteristic traits of FSI in arteries. In particular, we aim to determine how much intramural plasma filtration and its dynamic coupling with the mechanical stresses within the artery affect arterial wall deformation when pressure waves are propagated along an arterial segment. To this purpose, we perform a sensitivity analysis of the model parameters, centred in the range relevant to cardiovascular applications. More precisely, we use the numerical scheme applied to a classical FSI benchmark problem, to determine how and why FSI simulations based on a poroelastic material differ from the more classical case where a linear elastic constitutive law is adopted. The numerical investigation is also supported by heuristic considerations arising from appropriate manipulations of the Biot model.

## 8.2 Description of the Problem

We are interested in simulating a pressure-driven flow through the deformable channel with a two-way coupling between the fluid, thin elastic interface, and poroelastic structure. Without loss of generality, we restrict the model to a two-dimensional (2D) geometrical model representing a deformable channel. We consider only the upper half of the fluid domain supplemented by a symmetry condition at the axis of symmetry, see Fig. 8.1. We consider the flow of an incompressible, viscous fluid in a two-dimensional channel of reference length  $L$ , and reference width  $2R$ . The channel is bounded by a poroelastic wall, where the lateral boundary of the channel represents a thin elastic interface between the fluid and poroelastic structure. We assume that the volume of the thin elastic interface is negligible. Thus, it acts as a membrane that can not store fluid, but allows the flow through it in the normal direction. We denote the thickness of the membrane by  $r_m$ , and the thickness of poroelastic structure by  $r_p$ . Thus, the reference fluid and structure domains in our problem are given, respectively, by

$$\begin{aligned}\hat{\Omega}^f &:= \{(x, y) \mid 0 < x < L, 0 < y < R\}, \\ \hat{\Omega}^p &:= \{(x, y) \mid 0 < x < L, R < y < R + r_p\},\end{aligned}$$

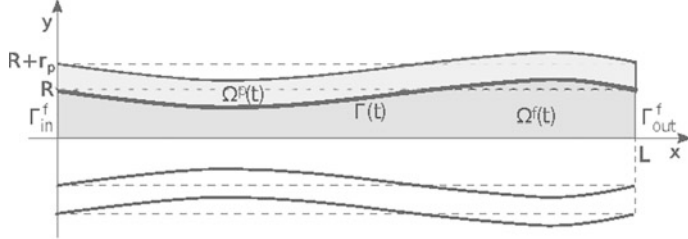


**Fig. 8.1.** Deformed domains  $\Omega^f(t) \cup \Omega^P(t)$

and the reference lateral boundary by  $\hat{\Gamma} = \{(x, R) | 0 < x < L\}$ . The inlet and outlet fluid boundaries are defined, respectively, as  $\Gamma_{in}^f = \{(0, y) | 0 < y < R\}$  and  $\Gamma_{out}^f = \{(L, y) | 0 < y < R\}$ .

We model the flow using the Navier-Stokes equations for a viscous, incompressible, Newtonian fluid:

$$\rho_f \left( \frac{\partial \mathbf{v}}{\partial t} + \mathbf{v} \cdot \nabla \mathbf{v} \right) = \nabla \cdot \boldsymbol{\sigma}_f + \mathbf{g} \quad \text{in } \Omega^f(t) \times (0, T), \quad (8.1)$$

$$\nabla \cdot \mathbf{v} = 0 \quad \text{in } \Omega^f(t) \times (0, T), \quad (8.2)$$

where  $\mathbf{v} = (v_x, v_y)$  is the fluid velocity,  $\boldsymbol{\sigma}_f = -p_f \mathbf{I} + 2\mu_f \mathbf{D}(\mathbf{v})$  is the fluid stress tensor,  $p_f$  is the fluid pressure,  $\rho_f$  is the fluid density,  $\mu_f$  is the fluid viscosity and  $\mathbf{D}(\mathbf{v}) = (\nabla \mathbf{v} + (\nabla \mathbf{v})^\top)/2$  is the rate-of-strain tensor. At the inlet and outlet boundary we prescribe the normal stress:

$$\boldsymbol{\sigma}^f \mathbf{n}_f(0, y, t) = -\delta p_{in}(t) \mathbf{n}_f \quad \text{on } \Gamma_{in}^f \times (0, T), \quad (8.3)$$

$$\boldsymbol{\sigma}^f \mathbf{n}_f(L, y, t) = 0 \quad \text{on } \Gamma_{out}^f \times (0, T), \quad (8.4)$$

where  $\mathbf{n}_f$  is the outward normal unit vector to the fluid boundaries and  $\delta p_{in}(t)$  is the pressure increment with respect to the ambient pressure surrounding the artery. Along the middle line of the channel  $y = 0$  we impose the symmetry conditions:

$$\frac{\partial v_x}{\partial y}(x, 0, t) = 0, \quad v_y(x, 0, t) = 0 \quad \text{on } (0, L) \times (0, T). \quad (8.5)$$

The lateral boundary represents a deformable, thin elastic wall, whose dynamics is modeled by the linearly elastic Koiter membrane model, given in the Lagrangian formulation by:

$$\rho_m r_m \frac{\partial^2 \hat{\eta}_x}{\partial t^2} - C_2 \frac{\partial \hat{\eta}_y}{\partial \hat{x}} - C_1 \frac{\partial^2 \hat{\eta}_x}{\partial \hat{x}^2} = \hat{f}_x \quad \text{on } \hat{\Gamma} \times (0, T), \quad (8.6)$$

$$\rho_m r_m \frac{\partial^2 \hat{\eta}_y}{\partial t^2} + C_0 \hat{\eta}_y + C_2 \frac{\partial \hat{\eta}_x}{\partial \hat{x}} = \hat{f}_y \quad \text{on } \hat{\Gamma} \times (0, T), \quad (8.7)$$

where  $\hat{\eta}(\hat{x}, t) = (\hat{\eta}_x(\hat{x}, t), \hat{\eta}_y(\hat{x}, t))$  denotes the axial and radial displacement,  $\hat{\mathbf{f}} = (\hat{f}_x, \hat{f}_y)$  is a vector of surface density of the force applied to the membrane,  $\rho_m$  de-

notes the membrane density and, given the Lamé coefficients for the membrane coefficients  $\mu_m$  and  $\lambda_m$ , we define,

$$C_0 = \frac{r_m}{R^2} \left( \frac{2\mu_m\lambda_m}{\lambda_m+2\mu_m} + 2\mu_m \right), C_1 = r_m \left( \frac{2\mu_m\lambda_m}{\lambda_m+2\mu_m} + 2\mu_m \right), C_2 = \frac{r_m}{R} \frac{2\mu_m\lambda_m}{\lambda_m+2\mu_m}.$$

The fluid domain is bounded by a deformable porous matrix consisting of a skeleton and connecting pores filled with fluid, whose dynamics is described by the Biot model, which in the Eulerian formulation reads as follows:

$$\rho_p \frac{D^2 \mathbf{U}}{Dt^2} - \nabla \cdot \boldsymbol{\sigma}^p = \mathbf{0} \quad \text{in } \Omega^p(t) \times (0, T), \quad (8.8)$$

$$\kappa^{-1} \mathbf{q} = -\nabla p_p \quad \text{in } \Omega^p(t) \times (0, T), \quad (8.9)$$

$$\frac{D}{Dt}(s_0 p_p + \alpha \nabla \cdot \mathbf{U}) + \nabla \cdot \mathbf{q} = 0 \quad \text{in } \Omega^p(t) \times (0, T), \quad (8.10)$$

where  $\frac{D}{Dt}$  denotes the classical concept of material derivative. The stress tensor of the poroelastic medium is given by  $\boldsymbol{\sigma}^p = \boldsymbol{\sigma}^E - \alpha p_p \mathbf{I}$ , where  $\boldsymbol{\sigma}^E$  denotes the elasticity stress tensor. With the assumption that the displacement  $\mathbf{U} = (U_x, U_y)$  of the skeleton is connected to stress tensor  $\boldsymbol{\sigma}^E$  via the Saint-Venant Kirchhoff elastic model, we have  $\boldsymbol{\sigma}^E(\mathbf{U}) = 2\mu_p \mathbf{D}(\mathbf{U}) + \lambda_p \text{tr}(\mathbf{D}(\mathbf{U})) \mathbf{I}$ , where  $\lambda_p$  and  $\mu_p$  denote the Lamé coefficients for the skeleton, and, with the hypothesis of “small” deformations,  $\mathbf{D}(\mathbf{U}) = (\nabla \mathbf{U} + (\nabla \mathbf{U})^T)/2$ . System (8.8)–(8.10) consists of the momentum equation for the balance of total forces (8.8), Darcy’s law (8.9), and the storage equation (8.10) for the fluid mass conservation in the pores of the matrix, where the flux  $\mathbf{q}$  is the relative velocity of the fluid within the porous structure and  $p_p$  is the fluid pressure. The density of saturated porous medium is denoted by  $\rho_p$ , and the hydraulic conductivity is denoted by  $\kappa$ . To account for anisotropic transport properties,  $\kappa$  is in general a symmetric positive definite tensor. For simplicity of notation, but without loss of generality with respect to the derivation of the numerical scheme, in what follows we consider it as a scalar quantity. The coefficient  $s_0 > 0$  is the storage coefficient, and the Biot-Willis constant  $\alpha$  is the pressure-storage coupling coefficient. We assume that the poroelastic structure is fixed at the inlet and outlet boundaries:

$$\mathbf{U}(0, y, t) = \mathbf{U}(L, y, t) = \mathbf{0} \quad \text{on } [R, R+r_p] \times (0, T), \quad (8.11)$$

that the external structure boundary  $\Gamma_{ext}^p$  is exposed to external ambient pressure

$$\mathbf{n}_p \cdot \boldsymbol{\sigma}^E \mathbf{n}_p = 0 \quad \text{on } \Gamma_{ext}^p \times (0, T), \quad (8.12)$$

where  $\mathbf{n}_p$  is the outward unit normal vector on  $\partial \Omega^p$ , and that the tangential displacement of the exterior boundary is zero:

$$U_x(x, R+r_p, t) = 0 \quad \text{on } \Gamma_{ext}^p \times (0, T). \quad (8.13)$$

On the fluid pressure in the porous medium, we impose following boundary conditions:

$$p_p = 0 \quad \text{on } \Gamma_{ext}^p, \quad \mathbf{q} \cdot \mathbf{n}_p = 0 \quad \text{on } \Gamma_{in}^p \cup \Gamma_{out}^p \times (0, T), \quad (8.14)$$

where  $\Gamma_{in}^p = \{(0, y) | R < y < R + r_p\}$  and  $\Gamma_{out}^p = \{(L, y) | R < y < R + r_p\}$  are inlet and outlet porous medium boundaries, respectively. Initially, the fluid, elastic membrane and the poroelastic structure are assumed to be at rest, with zero displacement from the reference configuration

$$\mathbf{v} = 0, \quad \mathbf{U} = 0, \quad \frac{D\mathbf{U}}{Dt} = 0, \quad \boldsymbol{\eta} = 0, \quad \frac{D\boldsymbol{\eta}}{Dt} = 0, \quad \mathbf{q} = 0. \quad (8.15)$$

To deal with the motion of the fluid domain we adopt the Arbitrary Lagrangian-Eulerian (ALE) approach. We introduce a (arbitrary, invertible, smooth) mapping  $\mathcal{A}_t$ , defined on  $\hat{\Omega}^f$ , which tracks the domain in time:

$$\mathcal{A}_t : \hat{\Omega}^f \rightarrow \Omega^f(t) \subset \mathbb{R}^2, \quad \mathbf{x} = \mathcal{A}_t(\hat{\mathbf{x}}) \in \Omega^f(t), \quad \text{for } \hat{\mathbf{x}} \in \hat{\Omega}^f. \quad (8.16)$$

Since the mapping  $\mathcal{A}_t$  is arbitrary, with the only requirement that it matches the displacement of the structure on  $\Gamma(t)$ , we define  $\mathcal{A}_t$  as

$$\mathcal{A}_t(\hat{\mathbf{x}}) = \hat{\mathbf{x}} + \text{Ext}(\hat{\boldsymbol{\eta}}(\hat{\mathbf{x}}, t)) = \hat{\mathbf{x}} + \text{Ext}(\hat{\mathbf{U}}(\hat{\mathbf{x}}, t)|_{\hat{\Gamma}}), \quad \forall \hat{\mathbf{x}} \in \hat{\Omega}^f. \quad (8.17)$$

In order to prescribe the coupling conditions on the physical fluid-structure interface  $\Gamma(t)$ , denote by  $\boldsymbol{\eta} := \hat{\boldsymbol{\eta}} \circ (\mathcal{A}_t^{-1}|_{\Gamma(t)})$ , the displacement of the membrane in the physical domain. While the lumen and the poroelastic medium contain fluid, we assume that the elastic membrane is not able to store fluid, but allows the flow through it in the normal direction. Denote by  $\mathbf{n}$  the outward normal to the fluid domain and by  $\boldsymbol{\tau}$  the tangential unit vector. Since the thin lamina allows the flow through it, the continuity of normal flux is

$$\mathbf{v} \cdot \mathbf{n} - \frac{D\boldsymbol{\eta}}{Dt} = \mathbf{q} \cdot \mathbf{n} \quad \text{on } \Gamma(t). \quad (8.18)$$

We prescribe no-slip boundary conditions between the fluid in the lumen and the elastic membrane in the tangential direction, and between the elastic membrane and poroelastic medium:

$$\mathbf{v} \cdot \boldsymbol{\tau} = \frac{D\boldsymbol{\eta}}{Dt} \cdot \boldsymbol{\tau}, \quad \boldsymbol{\eta} = \mathbf{U} \quad \text{on } \Gamma(t). \quad (8.19)$$

We notice that this condition prevents filtration in the tangential direction. The balance of normal components of the stress in the fluid phase requires that the following is satisfied

$$\mathbf{n} \cdot \boldsymbol{\sigma}^f \mathbf{n} = -p_p \quad \text{on } \Gamma(t). \quad (8.20)$$

The conservation of momentum implies balance of contact forces, that is:

$$\boldsymbol{\sigma}^f \mathbf{n} - \boldsymbol{\sigma}^p \mathbf{n} + J^{-1} \mathbf{f} = \mathbf{0} \quad \text{on } \Gamma(t), \quad (8.21)$$

where  $\mathbf{f} := \hat{\mathbf{f}} \circ (\mathcal{A}_t^{-1}|_{\Gamma(t)})$ , and  $J$  denotes the Jacobian of the transformation from  $\Gamma(t)$  to  $\hat{\Gamma}$  given by

$$J = \sqrt{\left(1 + \frac{\partial \eta_x}{\partial x}\right)^2 + \left(\frac{\partial \eta_y}{\partial x}\right)^2}. \quad (8.22)$$

### 8.3 A Qualitative Study of the Poroelastic Effects on FSI

From the inspection of Eqs. (8.8), (8.9), (8.10) we observe that  $\alpha$ ,  $\kappa$ ,  $s_0$  are the parameters that characterize the influence of poroelasticity on the mechanical behavior of the artery. The purpose of this section is to qualitatively compare the mechanical properties of the arterial walls when the poroelastic behavior of the arterial wall is enabled or not. To this purpose, we aim to reformulate the Biot model, namely (8.8), (8.9), (8.10) using one single equation. As a result, we will be able to compare this equivalent representation of Biot model with a simple elasticity equation, such as (8.8). Appropriate considerations will then emerge. To manipulate Biot model such that it can be represented into one single expression, we multiply (8.8) by the operator  $s_0 D(\cdot)/Dt$  and we define  $\mathbf{V}$  as the velocity of the arterial wall, namely  $\mathbf{V} := D\mathbf{U}/Dt$ . We obtain,

$$\rho_p s_0 \frac{D^2 \mathbf{V}}{Dt^2} - s_0 \mu_p \nabla \cdot \mathbf{D}(\mathbf{V}) - s_0 \lambda_p \nabla (\nabla \cdot \mathbf{V}) + s_0 \alpha \frac{D \nabla p_p}{Dt} = \mathbf{0}. \quad (8.23)$$

Then, we apply the operator  $\alpha \nabla$  to Eq. (8.10) obtaining,

$$\alpha s_0 \nabla \frac{D p_p}{Dt} + \alpha^2 \nabla (\nabla \cdot \mathbf{V}) + \alpha \nabla (\nabla \cdot \mathbf{q}) = \mathbf{0}. \quad (8.24)$$

Finally, in order to account for (8.9) we observe that

$$\nabla (\nabla \cdot \mathbf{q}) = \Delta \mathbf{q} + \nabla \times \nabla \times \mathbf{q} = \Delta \mathbf{q} \quad (8.25)$$

because  $\nabla \times \nabla \times \mathbf{q} = \mathbf{0}$  since  $\mathbf{q} = -\kappa \nabla p$  and  $\kappa$  is assumed to be a scalar parameter. Replacing (8.25) and (8.24) into (8.23) and dividing by  $s_0$ , we obtain the desired equivalent representation of Biot equation,

$$\rho_p \frac{D^2 \mathbf{V}}{Dt^2} - \mu_p \nabla \cdot \mathbf{D}(\mathbf{V}) - \left( \lambda_p + \frac{\alpha^2}{s_0} \right) \nabla (\nabla \cdot \mathbf{V}) = \frac{\alpha}{s_0} \Delta \mathbf{q} \quad (8.26)$$

which can be compared term by term to the following equivalent expression of the standard elastodynamic equation,

$$\rho_p \frac{D^2 \mathbf{V}}{Dt^2} - \mu \nabla \cdot \mathbf{D}(\mathbf{V}) - \lambda \nabla (\nabla \cdot \mathbf{V}) = \mathbf{0}, \quad (8.27)$$

for a material characterized by the same Lamé parameters as the ones used for the poroelastic model. The comparison of Eqs. (8.26) and (8.27) informs us about the effects of poroelastic effects on the mechanical behavior of the arterial wall. Two major considerations emerge:

(i) Poroelasticity introduces an additional forcing term, that is  $\frac{\alpha}{s_0} \Delta \mathbf{q}$ . Since the reference elastodynamics Eq. (8.27) preserves the energy of the system, it is clear that the additional term breaks this equilibrium. It may either positively or negatively contribute to the energy balance. We also remark that the magnitude of  $\Delta \mathbf{q}$  is proportional to the hydraulic permeability  $\kappa$ , which appears in (8.9). At this stage, it is difficult to determine whether  $\Delta \mathbf{q}$  does add or subtracts energy to the system, because

$\mathbf{q}$  is indeed coupled to the solution of the problem. However, the energy estimate that will be discussed later on for the discrete scheme, clearly puts into evidence that this term dissipates energy, at a rate which is directly proportional to  $\kappa$ .

(ii) Poroelasticity affects the natural Lamé parameters of the material. Denoting with  $\mu^*, \lambda^*$  the new Lamé constants of (8.26) we easily observe that

$$\mu^* = \mu_p, \quad \lambda^* = \left( \lambda_p + \frac{\alpha^2}{s_0} \right). \quad (8.28)$$

In other words, poroelasticity only affects the physical behavior that is governed by the second Lamé constant,  $\lambda$ . Some conclusions are more easily obtained if the result is interpreted using the Young modulus  $E$  and the Poisson ratio  $\nu$ . We remind the classical expressions,

$$E = \mu \frac{3\lambda + 2\mu}{\lambda + \mu}, \quad \nu = \frac{\lambda}{2(\lambda + \mu)},$$

and that the arterial wall is modeled as a quasi-incompressible material, which means that  $\lambda$  is usually large. Accordingly, we conclude that: (a) introducing poroelasticity only slightly affects the stiffness of the material, i.e. the Young modulus remains almost unchanged; (b) the poroelastic effects significantly perturb the original compressibility of the material. Surprisingly, the analysis shows that as long as the parameter  $\alpha^2/s_0$  increases, the equivalent Poisson ratio  $\nu^*$  approaches the ideally incompressible limit 0.5. This behavior can be explained observing that accounting for poroelasticity corresponds to introducing an incompressible liquid into a porous deformable structure. As a result, the original compressibility of the material may naturally decrease.

In the final section of this work, we will support these qualitative conclusions on the basis of numerical simulations, which will be performed using the numerical scheme that is introduced and analyzed below.

The analysis of the Biot-Willis constant  $\alpha$  deserves additional attention. Admissible values of  $\alpha$  span in the interval  $[0, 1]$ . The case  $\alpha = 1$  corresponds to the full poroelastic coupling in the Biot equation. Conversely, for  $\alpha = 0$  the displacement of the structure no longer affects the intramural flow. More precisely, Eq. (8.8) is decoupled from (8.9) and (8.10). It is thus interesting to analyze the asymptotic behavior of the interface conditions for poroelastic FSI coupling approaching the limit  $\alpha = 0$ . From the inspection of Eqs. (8.18)–(8.21), we observe that the system of coupling conditions is almost invariant with respect to  $\alpha$ . The presence of  $\alpha$  is hidden in the definition of  $\boldsymbol{\sigma}^P$ . Anyway, in the limit case  $\alpha = 0$  Eq. (8.21) simply transforms into

$$\boldsymbol{\sigma}^f \mathbf{n} - \boldsymbol{\sigma}^E \mathbf{n} + J^{-1} \mathbf{f} = \mathbf{0} \quad \text{on } \Gamma(t),$$

which represents the equilibrium of mechanical and fluid stresses acting on the membrane. The approach we will adopt to enforce these interface conditions into the numerical scheme is fully robust and stable for the entire admissible range of  $\alpha$ . This property enables us to investigate the role of this parameter by means of numerical simulations.

## 8.4 Finite Element Approximation of the Coupled Problem Using Nitsche's Type Mortaring for the Interface Conditions

For the sake of simplicity, we develop and analyze the numerical scheme under the assumption that domains  $\Omega^f(t)$  and  $\Omega^p(t)$  are fixed, namely

$$\Omega^f(t) = \hat{\Omega}^f, \quad \Omega^p(t) = \hat{\Omega}^p, \quad \forall t \in (0, T).$$

Although simplified, this problem still retains the main difficulties associated with the added-mass effect and with the fluid-porous media coupling. Since now all the variables are defined on the fixed domain, we will drop the hat notation to avoid cumbersome expressions. For the sake of simplicity, we also restrict the analysis to the linear case, namely to the Stokes flow model.

To define the weak form of the problem, introduce the appropriate function spaces:

$$\begin{aligned} \mathbf{V}^f &= \{\boldsymbol{\varphi} \in (H^1(\Omega^f))^2, \quad \boldsymbol{\varphi}_y|_{y=0} = 0\}, \quad Q^f = L^2(\Omega^f), \\ \mathbf{V}^p &= \{\boldsymbol{\varphi} \in (H(\text{div}, \Omega^p))^2, \quad \boldsymbol{\varphi} \cdot \mathbf{n}_p = 0 \text{ on } \Gamma_{in}^p \cup \Gamma_{out}^p\}, \\ Q^p &= \{\psi \in H^1(\Omega^p), \psi|_{\partial\Omega^p \setminus \Gamma} = 0\}. \\ \mathbf{X}^p &= \{\boldsymbol{\varphi} \in (H^1(\Omega^p))^2, \quad \boldsymbol{\varphi} = 0 \text{ on } \Gamma_{in}^p \cup \Gamma_{out}^p, \quad \boldsymbol{\varphi}_x = 0 \text{ on } \Gamma_{ext}^p\}, \end{aligned}$$

and  $\mathbf{X}^m = (H_0^1(\Gamma))^2$ . Finally, we denote with  $\mathbf{W}$  the joint space where the weak solution and test functions are defined. The weak formulation of the coupled Navier-Stokes/Koiter/Biot system reads as follows: given  $t \in (0, T)$  find  $(\mathbf{v}, \boldsymbol{\eta}, \mathbf{q}, \mathbf{U}, p_f, p_p) \in \mathbf{W}^*$  such that for all  $(\boldsymbol{\varphi}^f, \boldsymbol{\zeta}, \mathbf{r}, \boldsymbol{\varphi}^p, \psi^f, \psi^p) \in \mathbf{W}$ :

$$\begin{aligned} &\int_{\Omega^f} \left( \rho_f \frac{\partial \mathbf{v}}{\partial t} \cdot \boldsymbol{\varphi}^f d + 2\mu_f \mathbf{D}(\mathbf{v}) : \mathbf{D}(\boldsymbol{\varphi}^f) d - p_f \nabla \cdot \boldsymbol{\varphi}^f + \psi^f \nabla \cdot \mathbf{v} \right) dx \\ &+ \rho_m r_m \int_{\Gamma} \left( \frac{\partial^2 \hat{\eta}_x}{\partial t^2} \hat{\zeta}_x dx + \frac{\partial^2 \hat{\eta}_y}{\partial t^2} \hat{\zeta}_y \right) ds \\ &+ \int_{\Gamma} \left( C_0 \hat{\eta}_y \hat{\zeta}_y + C_1 \frac{\partial \hat{\eta}_x}{\partial \hat{x}} \frac{\partial \hat{\zeta}_x}{\partial \hat{x}} + C_2 \frac{\partial \hat{\eta}_x}{\partial \hat{x}} \hat{\zeta}_y - C_2 \frac{\partial \hat{\eta}_y}{\partial \hat{x}} \hat{\zeta}_x \right) ds \\ &+ \int_{\Omega^p} \left( \rho_p \frac{\partial^2 \mathbf{U}}{\partial t^2} \boldsymbol{\varphi}^p + \boldsymbol{\sigma}^E : \nabla \boldsymbol{\varphi}^p d - \alpha p_p \nabla \cdot \boldsymbol{\varphi}^p d + \kappa^{-1} \mathbf{q} \cdot \mathbf{r} - p_p \nabla \cdot \mathbf{r} \right. \\ &\quad \left. + s_0 \frac{\partial p_p}{\partial t} \psi^p + \alpha \nabla \cdot \frac{\partial \mathbf{U}}{\partial t} \psi^p + \nabla \cdot \mathbf{q} \psi^p \right) dx \\ &= \int_{\Gamma} \left( \boldsymbol{\sigma}^f \mathbf{n} \cdot \boldsymbol{\varphi}^f - \boldsymbol{\sigma}^p \mathbf{n} \cdot \boldsymbol{\varphi}^p + p_p \mathbf{r} \cdot \mathbf{n} + J^{-1} \mathbf{f} \cdot \boldsymbol{\zeta} \right) ds \\ &+ \int_0^T p_{in}(t) \boldsymbol{\varphi}_x^f |_{x=0} dy. \end{aligned} \tag{8.29}$$

where  $\mathbf{W}^*$  is the space of admissible solutions

$$\begin{aligned}\mathbf{W}^* = \{(\boldsymbol{\varphi}^f, \boldsymbol{\zeta}, \mathbf{r}, \boldsymbol{\varphi}^p) &\in V^f \times V^m \times V^q \times V^p | \\ \boldsymbol{\zeta} \cdot \mathbf{n} &= \boldsymbol{\varphi}^p|_\Gamma \cdot \mathbf{n}, \boldsymbol{\varphi}^f|_\Gamma \cdot \mathbf{n} = \left( \alpha \boldsymbol{\zeta} + \mathbf{r}|_\Gamma \right) \cdot \mathbf{n}, \\ \boldsymbol{\varphi}^f|_\Gamma \cdot \boldsymbol{\tau} &= \boldsymbol{\zeta} \cdot \boldsymbol{\tau}, \boldsymbol{\zeta} \cdot \boldsymbol{\tau} = \boldsymbol{\varphi}^p|_\Gamma \cdot \boldsymbol{\tau}\}.\end{aligned}$$

We denote by  $I_\Gamma$  the interface integral

$$I_\Gamma = \int_\Gamma (\boldsymbol{\sigma}^f \mathbf{n} \cdot \boldsymbol{\varphi}^f - \boldsymbol{\sigma}^p \mathbf{n} \cdot \boldsymbol{\varphi}^p + p_p \mathbf{r} \cdot \mathbf{n} + J^{-1} \mathbf{f} \cdot \boldsymbol{\zeta}) ds.$$

Owing to the interface conditions, we observe that  $I_\Gamma = 0$  if the trial and test functions are selected in  $\mathbf{W}^*$ .

Working in this constrained space, it is straightforward to prove the energy estimate corresponding to Eq. (8.29). The main advantage of this problem formulation is indeed the cancellation of the interface terms, which no longer pose technical difficulties in the analysis. However, Eq. (8.29) is not prone to directly proceed with the numerical discretization based on the finite element method. The main drawback at the discrete level consists in the difficulty to satisfy the constraints on test functions required by  $\mathbf{W}^*$ . As a result, for the discrete enforcement of interface conditions we adopt a different strategy, based on the weak enforcement of such conditions using penalty operators. This approach, usually called Nitsche's method when used to boundary conditions or Nitsche's mortaring when applied on an internal interface, will be applied below to enforce Eqs. (8.18)–(8.21) into (8.29). For an introduction to this technique applied to general boundary and interface conditions we refer to [19], while this method is applied to FSI in [11].

We denote with  $\mathbf{V}_h^f, Q_h^f$  the finite element spaces for the velocity and pressure approximation and with  $\mathbf{V}_h^p, Q_h^p$  the spaces for velocity and pressure approximation in the porous matrix,  $\Omega_p$ . The discrete spaces for the approximation of displacements and velocities of the thick structure and the membrane are denoted with  $\mathbf{X}_h^p, \mathbf{X}_h^m, \dot{\mathbf{X}}_h^p, \dot{\mathbf{X}}_h^m$ . Before addressing the time discretization, we rewrite Eq. (8.8) as a system of first order equations in time. As a result, for the time discretization we adopt the Backward Euler scheme for all the equations. We denote with  $t_n$  the current time step and with  $d_\tau$  the first order discrete time derivative  $d_\tau u^n := \tau^{-1}(u^n - u^{n-1})$ .

According to Eq. (8.29), the bilinear forms for the *structure problem*, namely the problem accounting for the deformation of the porous matrix ( $s, p$ ) and the membrane ( $m$ ) in the arterial wall are:

$$\begin{aligned}a_s(\mathbf{U}_h, \boldsymbol{\varphi}_{p,h}) &:= \int_{\Omega_p} \left( 2\mu_p \mathbf{D}(\mathbf{U}_h) : \mathbf{D}(\boldsymbol{\varphi}_{p,h}) + \lambda_p (\nabla \cdot \mathbf{U}_h)(\nabla \cdot \boldsymbol{\varphi}_{p,h}) \right) dx \\ b_s(p_{p,h}, \boldsymbol{\varphi}_{p,h}) &:= \alpha \int_{\Omega_p} p_{p,h} \nabla \cdot \boldsymbol{\varphi}_{p,h} dx \\ a_m(\boldsymbol{\eta}_h, \boldsymbol{\xi}_h) &:= + \int_\Gamma \left( C_0 \hat{\eta}_y \hat{\xi}_y + C_1 \frac{\partial \hat{\eta}_x}{\partial \hat{x}} \frac{\partial \hat{\xi}_x}{\partial \hat{x}} + C_2 \frac{\partial \hat{\eta}_x}{\partial \hat{x}} \hat{\xi}_y - C_2 \frac{\partial \hat{\eta}_y}{\partial \hat{x}} \hat{\xi}_x \right) ds.\end{aligned}$$

The *fluid-problem*, accounts for the free flow ( $f$ ) and the filtration through the porous matrix ( $p$ ). The corresponding bilinear forms are:

$$\begin{aligned} a_f(\mathbf{v}_h, \boldsymbol{\varphi}_{f,h}; \mathbf{u}_h) &:= 2\mu_f \int_{\Omega_f} \mathbf{D}(\mathbf{v}_h) : \mathbf{D}(\boldsymbol{\varphi}_{f,h}) d\mathbf{x} \\ b_f(p_{f,h}, \boldsymbol{\varphi}_{f,h}) &:= \int_{\Omega_f} p_{f,h} \nabla \cdot \boldsymbol{\varphi}_{f,h} d\mathbf{x} \\ a_p(\mathbf{q}_h, \mathbf{r}_h) &:= \int_{\Omega_p} \kappa^{-1} \mathbf{q}_h \cdot \mathbf{r}_h d\mathbf{x} \\ b_p(p_{p,h}, \mathbf{r}_h) &:= \int_{\Omega_p} p_{p,h} \nabla \cdot \mathbf{r}_h d\mathbf{x} \\ c_p(p_{p,h}, \psi_{p,h}) &:= \int_{\Omega_p} s_0 d_\tau p_{p,h} \psi_{p,h} d\mathbf{x}. \end{aligned}$$

The application of Nitsche's type mortaring to (8.18)–(8.21) allows us to rewrite the interface terms collected in  $I_\Gamma$  as follows,

$$\begin{aligned} -I_\Gamma(\mathbf{v}_h, \mathbf{q}_h, p_{f,h}, p_{p,h}, \mathbf{U}_h, \boldsymbol{\eta}_h; \boldsymbol{\varphi}_{f,h}, \mathbf{r}_h, \psi_{f,h}, \psi_{p,h}, \boldsymbol{\varphi}_{p,h}, \boldsymbol{\xi}_h) &= \\ -\int_\Gamma \mathbf{n} \cdot \boldsymbol{\sigma}_{f,h}(\mathbf{v}_h, p_{f,h}) \mathbf{n} (\boldsymbol{\varphi}_{f,h} - \mathbf{r}_h - \boldsymbol{\xi}_h) \cdot \mathbf{n} \\ -\int_\Gamma \mathbf{t} \cdot \boldsymbol{\sigma}_{f,h}(\mathbf{v}_h, p_{f,h}) \mathbf{n} (\boldsymbol{\varphi}_{f,h} - \boldsymbol{\xi}_h) \cdot \mathbf{t} \\ + \int_\Gamma \gamma_f \mu_f h^{-1} (\mathbf{v}_h - \mathbf{q}_h - d_\tau \boldsymbol{\eta}_h) \cdot \mathbf{n} (\boldsymbol{\varphi}_{f,h} - \mathbf{r}_h - \boldsymbol{\xi}_h) \cdot \mathbf{n} \\ + \int_\Gamma \gamma_f \mu_f h^{-1} (\mathbf{v}_h - d_\tau \boldsymbol{\eta}_h) \cdot \mathbf{t} (\boldsymbol{\varphi}_{f,h} - \boldsymbol{\xi}_h) \cdot \mathbf{t} \\ + \int_\Gamma \gamma_p (\mu_p + \lambda_p/2) h^{-1} (\boldsymbol{\eta}_h - \mathbf{U}_h) \cdot (\boldsymbol{\xi}_h - \boldsymbol{\varphi}_{p,h}) \\ - \int_\Gamma (\boldsymbol{\sigma}_{E,h}(\mathbf{U}_h) \mathbf{n} - \alpha p_{p,h} \mathbf{n}) \cdot (\boldsymbol{\xi}_h - \boldsymbol{\varphi}_{p,h}) \end{aligned}$$

where  $\gamma_f, \gamma_p > 0$  denote penalty parameters that will be suitably chosen. Furthermore, in order to account for the symmetric, incomplete or skew-symmetric variants of Nitsche's type mortaring, we introduce the following additional terms

$$\begin{aligned} -S_\Gamma^\zeta(\mathbf{v}_h, \mathbf{q}_h, p_{f,h}, p_{p,h}, \mathbf{U}_h, \boldsymbol{\eta}_h; \boldsymbol{\varphi}_{f,h}, \mathbf{r}_h, \psi_{f,h}, \psi_{p,h}, \boldsymbol{\varphi}_{p,h}, \boldsymbol{\xi}_h) &= \\ -\int_\Gamma \mathbf{n} \cdot \boldsymbol{\sigma}_{f,h}(\zeta \boldsymbol{\varphi}_{f,h}, -\psi_{f,h}) \mathbf{n} (\mathbf{v}_h - \mathbf{q}_h - d_\tau \boldsymbol{\eta}_h) \cdot \mathbf{n} \\ -\int_\Gamma \mathbf{t} \cdot \boldsymbol{\sigma}_{f,h}(\zeta \boldsymbol{\varphi}_{f,h}, -\psi_{f,h}) \mathbf{n} (\mathbf{v}_h - d_\tau \boldsymbol{\eta}_h) \cdot \mathbf{t} \\ -\int_\Gamma \boldsymbol{\sigma}_{E,h}(\boldsymbol{\varphi}_{p,h}) \mathbf{n} \cdot (\boldsymbol{\eta}_h^{n-1} - \mathbf{U}_h^{n-1}) - \int_\Gamma \alpha \psi_{p,h} (d_\tau \boldsymbol{\eta}_h - d_\tau \mathbf{U}_h) \end{aligned}$$

which anyway do not violate the consistency of the original scheme because they vanish if the kinematic constraints are exactly satisfied. The flag  $\zeta \in \{1, 0, -1\}$  in  $\boldsymbol{\sigma}_{f,h}(\zeta \boldsymbol{\varphi}_{f,h}, -\psi_{f,h})$  determines if we adopt a symmetric, incomplete or skew sym-

metric formulation for the interface terms coupling the fluid and the membrane. A similar technique is not applied to  $\sigma_{E,h}(\varphi_{p,h})$ , because this part of the operator  $S_\Gamma^\zeta$  requires special attention. In particular, the symmetry terms relative to the coupling between the structure and the membrane are evaluated at the previous time step, i.e. we use  $\sigma_{E,h}(\varphi_{p,h})\mathbf{n} \cdot (\boldsymbol{\eta}_h^{n-1} - \mathbf{U}_h^{n-1})$  instead of  $\sigma_{E,h}(\varphi_{p,h})\mathbf{n} \cdot (\boldsymbol{\eta}_h^n - \mathbf{U}_h^n)$ , in order to preserve the energy of the structure. This is shown choosing the test functions  $\varphi_{p,h} = d_\tau \mathbf{U}_h^n$ ,  $\xi_h = d_\tau \boldsymbol{\eta}_h^n$ , summing up with respect to  $n$  and applying discrete time integration by parts as follows,

$$\begin{aligned} -\tau \sum_{n=1}^N \int_\Gamma \sigma_{E,h}(\mathbf{U}_h^n) \mathbf{n} \cdot (d_\tau \boldsymbol{\eta}_h^n - d_\tau \mathbf{U}_h^n) &= \tau \sum_{n=1}^N \int_\Gamma \sigma_{E,h}(d_\tau \mathbf{U}_h^n) \mathbf{n} \cdot (\boldsymbol{\eta}_h^{n-1} - \mathbf{U}_h^{n-1}) \\ &\quad + \int_\Gamma \sigma_{E,h}(\mathbf{U}_h^0) \mathbf{n} \cdot (\boldsymbol{\eta}_h^0 - \mathbf{U}_h^0) - \int_\Gamma \sigma_{E,h}(\mathbf{U}_h^N) \mathbf{n} \cdot (\boldsymbol{\eta}_h^N - \mathbf{U}_h^N). \end{aligned}$$

As a result, the interface terms coupling the membrane with the structure preserve the energy of the elastic structure, because the following identity holds true,

$$\begin{aligned} -\tau \sum_{n=1}^N \left( \int_\Gamma \sigma_{E,h}(\mathbf{U}_h^n) \mathbf{n} \cdot (d_\tau \boldsymbol{\eta}_h^n - d_\tau \mathbf{U}_h^n) + \int_\Gamma \sigma_{E,h}(d_\tau \mathbf{U}_h^n) \mathbf{n} \cdot (\boldsymbol{\eta}_h^{n-1} - \mathbf{U}_h^{n-1}) \right) \\ = \int_\Gamma \sigma_{E,h}(\mathbf{U}_h^0) \mathbf{n} \cdot (\boldsymbol{\eta}_h^0 - \mathbf{U}_h^0) - \int_\Gamma \sigma_{E,h}(\mathbf{U}_h^N) \mathbf{n} \cdot (\boldsymbol{\eta}_h^N - \mathbf{U}_h^N). \end{aligned}$$

Numerical experiments confirm that this adjustment of the Nitsche's type mortaring to the wave equation is essential to ensure the stability of the scheme.

The coupled fluid / solid problem consists to find  $\mathbf{v}_h, p_{f,h}, \mathbf{q}_h, p_{p,h} \in \mathbf{V}_h^f \times Q_h^f \times \mathbf{V}_h^p \times Q_h^p$  and  $\mathbf{U}_h, \boldsymbol{\eta}_h, \dot{\mathbf{U}}_h, \dot{\boldsymbol{\eta}}_h \in \mathbf{X}_h^p \times \mathbf{X}_h^m \times \dot{\mathbf{X}}_h^p \times \dot{\mathbf{X}}_h^m$  such that for any  $\varphi_{f,h}, \psi_{f,h}, \mathbf{r}_h, \psi_{p,h} \in \mathbf{V}_h^f \times Q_h^f \times \mathbf{V}_h^p \times Q_h^p$  and  $\varphi_{p,h}, \xi_h, \dot{\varphi}_{p,h}, \dot{\xi}_h \in \mathbf{X}_h^p \times \mathbf{X}_h^m \times \dot{\mathbf{X}}_h^p \times \dot{\mathbf{X}}_h^m$  we have

$$\begin{aligned} &\rho_p \int_{\Omega_p} d_\tau \dot{\mathbf{U}}_h \cdot \varphi_{p,h} + \rho_p \int_{\Omega_p} (\dot{\mathbf{U}}_h - d_\tau \mathbf{U}_h) \cdot \dot{\varphi}_{p,h} \\ &\quad + \rho_m r_m \int_0^L d_\tau \dot{\boldsymbol{\eta}}_h \cdot \xi_h + \rho_m r_m \int_0^L (\dot{\boldsymbol{\eta}}_h - d_\tau \boldsymbol{\eta}_h) \cdot \dot{\xi}_h \\ &\quad + a_s(\mathbf{U}_h, \varphi_{p,h}) + a_m(\boldsymbol{\eta}_h, \xi_h) - b_s(p_{p,h}, \varphi_{p,h}) + b_s(\psi_{p,h}, d_\tau \mathbf{U}_h) \\ &\quad + \rho_f \int_{\Omega_f} d_\tau \mathbf{v}_h^n \cdot \varphi_{f,h} dx + a_f(\mathbf{v}_h, \varphi_{f,h}; \mathbf{v}_h^{n-1}) - b_f(p_{f,h}, \varphi_{f,h}) + b_f(\psi_{f,h}, \mathbf{v}_h) \\ &\quad + a_p(\mathbf{q}_h, \mathbf{r}_h) - b_p(p_{p,h}, \mathbf{r}_h) + b_p(\psi_{p,h}, \mathbf{q}_h) + c_p(p_{p,h}, \psi_{p,h}) \\ &\quad - (I_\Gamma + S_\Gamma^\zeta)(\mathbf{v}_h, \mathbf{q}_h, p_{f,h}, p_{p,h}, \mathbf{U}_h, \boldsymbol{\eta}_h; \varphi_{f,h}, \mathbf{r}_h, -\psi_{f,h}, -\psi_{p,h}, \varphi_{p,h}, \xi_h) \\ &= - \int_{\Gamma_{in}^f} p_{in}(t) \varphi_{f,h} \cdot \mathbf{n}_f. \end{aligned} \tag{8.30}$$

To address the stability of the scheme, we define the energy of the system as follows:

$$\begin{aligned} \text{(Fluid)} E_{f,h}^n &:= \frac{1}{2} \rho_f \|\mathbf{v}_h^n\|_{L^2(\Omega_f)}^2 \\ \text{(Wall)} E_{p,h}^n &:= \frac{1}{2} \left( \rho_p \|\dot{\mathbf{U}}_h^n\|_{L^2(\Omega_p)}^2 + a_s(\mathbf{U}_h^n, \mathbf{U}_h^n) + s_0 \|p_{p,h}^n\|_{L^2(\Omega_p)}^2 \right) \\ \text{(Membrane)} E_{m,h}^n &:= \frac{1}{2} \left( \rho_m r_m \|\dot{\boldsymbol{\eta}}_h^n\|_{L^2(0,L)}^2 + a_m(\boldsymbol{\eta}_h^n, \boldsymbol{\eta}_h^n) \right). \end{aligned}$$

Following the lines of [9], we derive the following stability result, where  $C_{TI}$ ,  $C_T$ ,  $C_{PF}$ ,  $C_K$  denote the constants related to the standard forms of trace, Poincare-Friedrichs and Korn inequalities [16, 30] that are used in the proof.

**Property 1.** For any  $\widehat{\epsilon}'_f, \check{\epsilon}'_f, \epsilon'_p$  that satisfy

$$0 < \epsilon'_p < C_{TI}^{-1}, \quad \left( 1 - \frac{(\zeta+1)}{2} \widehat{\epsilon}'_f C_{TI} - \frac{\check{\epsilon}'_f}{2} C_T^2 C_{PF} C_K \right) > 0$$

where  $\zeta \in \{-1, 0, 1\}$  provided that  $\gamma_p \geq (\epsilon'_p)^{-1}$  and  $\gamma_f > (\zeta+1)(\widehat{\epsilon}'_f)^{-1}$ , there exist constants  $0 < c, c_p < 1$  and  $C_p, C_f > 1$ , uniformly independent from the mesh characteristic size, such that

$$\begin{aligned} &E_{f,h}^N + c_p E_{p,h}^N + E_{m,h}^N + c \tau \sum_{n=1}^N \left[ 2\mu_f \|\mathbf{D}(\mathbf{v}_h^n)\|_{\Omega_f}^2 + \kappa^{-1} \|\mathbf{q}_h^n\|_{\Omega_p}^2 \right. \\ &\quad + \frac{\tau}{2} \left( \rho_f \|d_\tau \mathbf{v}_h^n\|_{\Omega_f}^2 + 2\mu_p \|d_\tau \mathbf{D}(\mathbf{U}_h^n)\|_{\Omega_p}^2 + C \mu_m r_m \|d_\tau \boldsymbol{\eta}_h^n\|_I^2 + s_0 \|d_\tau p_{p,h}^n\|_{\Omega_p}^2 \right. \\ &\quad \left. + \lambda_p \|d_\tau \nabla \cdot \mathbf{U}_h^n\|_{\Omega_p}^2 + \gamma_p (2\mu_p + \lambda_p) h^{-1} \|d_\tau \boldsymbol{\eta}_h^n - d_\tau \mathbf{U}_h^n\|_I^2 \right) \\ &\quad \left. + \mu_f h^{-1} (\|(\mathbf{v}_h^n - \mathbf{q}_h^n - d_\tau \boldsymbol{\eta}_h^n) \cdot \mathbf{n}\|_I^2 + \|(\mathbf{v}_h^n - d_\tau \boldsymbol{\eta}_h^n) \cdot \mathbf{t}\|_I^2) \right] \\ &\leq E_{f,h}^0 + C_p E_{p,h}^0 + E_{m,h}^0 + C_p (2\mu_p + \lambda_p) h^{-1} \|\boldsymbol{\eta}_h^0 - \mathbf{U}_h^0\|_I^2 + \tau \sum_{n=1}^N \frac{C_f}{\mu_f} \|p_{in}(t^n)\|_{\Gamma_{in}^f}^2. \end{aligned}$$

More precisely, we have

$$\begin{aligned} c_p &< (1 - \epsilon'_p C_{TI}) \\ c &< \min \left\{ \left( 1 - \frac{(\zeta+1)}{2} \widehat{\epsilon}'_f C_{TI} - \frac{\check{\epsilon}'_f}{2} C_T^2 C_{PF} C_K \right), ((\gamma_f - (\zeta+1)(\widehat{\epsilon}'_f)^{-1}) \right\} \\ C_f &> (2\check{\epsilon}'_f)^{-1} \\ C_p &> \max \left\{ (1 + \epsilon'_p C_{TI}), \frac{1}{2} (\gamma_p + (\epsilon'_p)^{-1}) \right\}. \end{aligned}$$

In practice, we will not use the fully coupled scheme to solve the FSI problem. We adopt a partitioned scheme instead, where structure mechanics, the intramural filtration and the blood flow problem are solved separately at each time step. In particular, the following subproblems are solved once at each time step:

1. given  $\mathbf{v}_h^{n-1}, p_{f,h}^{n-1}, \mathbf{q}_h^{n-1}, p_{p,h}^{n-1}$  find  $\mathbf{U}_h, \boldsymbol{\eta}_h, \dot{\mathbf{U}}_h, \dot{\boldsymbol{\eta}}_h$  in  $\Omega_p$  such that

$$\begin{aligned}
& \rho_p \int_{\Omega_p} \left( d_\tau \dot{\mathbf{U}}_h \cdot \boldsymbol{\phi}_{p,h} + (\dot{\mathbf{U}}_h - d_\tau \mathbf{U}_h) \cdot \dot{\boldsymbol{\phi}}_{p,h} \right) \\
& + \rho_m r_m \int_{\Gamma} \left( d_\tau \dot{\boldsymbol{\eta}}_h \cdot \boldsymbol{\xi}_h + (\dot{\boldsymbol{\eta}}_h - d_\tau \boldsymbol{\eta}_h) \cdot \dot{\boldsymbol{\xi}}_h \right) \\
& + a_s(\mathbf{U}_h, \boldsymbol{\phi}_{p,h}) + a_m(\boldsymbol{\eta}_h, \boldsymbol{\xi}_h) + \int_{\Omega_p} \beta \mathbf{U}_h \cdot \boldsymbol{\phi}_{p,h} \\
& + \int_{\Gamma} \boldsymbol{\sigma}_{E,h}(\mathbf{U}_h) \mathbf{n}_p \cdot (\boldsymbol{\xi}_h - \boldsymbol{\phi}_{p,h}) + \int_{\Gamma} \gamma_p (\mu_p + \lambda_p/2) h^{-1} (\boldsymbol{\eta}_h - \mathbf{U}_h) \cdot (\boldsymbol{\xi}_h - \boldsymbol{\phi}_{p,h}) \\
& + \int_{\Gamma} \gamma_f \mu_f h^{-1} d_\tau \boldsymbol{\eta}_h \cdot \mathbf{t}_p \boldsymbol{\xi}_h \cdot \mathbf{t}_p + \int_{\Gamma} \gamma_f \mu_f h^{-1} d_\tau \boldsymbol{\eta}_h \cdot \mathbf{n}_p \boldsymbol{\xi}_h \cdot \mathbf{n}_p \\
& = b_s(p_{p,h}^{n-1}, \boldsymbol{\phi}_{p,h}) + \int_{\Gamma} \alpha p_{p,h}^{n-1} (\boldsymbol{\xi}_h - \boldsymbol{\phi}_{p,h}) \cdot \mathbf{n}_p - \int_{\Gamma} \boldsymbol{\sigma}_{E,h}(\boldsymbol{\phi}_{p,h}) \mathbf{n}_p \cdot (\boldsymbol{\eta}_h^{n-1} - \mathbf{U}_h^{n-1}) \\
& - \int_{\Gamma} \mathbf{n}_p \cdot \boldsymbol{\sigma}_{f,h}^{n-1} \mathbf{n}_p (-\boldsymbol{\xi}_h) \cdot \mathbf{n}_p - \int_{\Gamma} \mathbf{t}_p \cdot \boldsymbol{\sigma}_{f,h}^{n-1} \mathbf{n}_p (-\boldsymbol{\xi}_h) \cdot \mathbf{t}_p \\
& + \int_{\Gamma} \gamma_f \mu_f h^{-1} \mathbf{v}_h^{n-1} \cdot \mathbf{t}_p \boldsymbol{\xi}_h \cdot \mathbf{t}_p + \int_{\Gamma} \gamma_f \mu_f h^{-1} (\mathbf{v}_h^{n-1} - \mathbf{q}_h^{n-1}) \cdot \mathbf{n}_p \boldsymbol{\xi}_h \cdot \mathbf{n}_p;
\end{aligned}$$

2. given  $\mathbf{v}_h^{n-1}, p_{f,h}^{n-1}$  and  $\mathbf{U}_h, \boldsymbol{\eta}_h$ , find  $\mathbf{q}_h, p_{p,h}$  in  $\Omega_p$  such that

$$\begin{aligned}
& a_p(\mathbf{q}_h, \mathbf{r}_h) - b_p(p_{p,h}, \mathbf{r}_h) + b_p(\psi_{p,h}, \mathbf{q}_h) + c_p(p_{p,h}, \psi_{p,h}) \\
& + s_{f,q}(d_\tau \mathbf{q}_h \cdot \mathbf{n}_p, \mathbf{r}_h \cdot \mathbf{n}_p) + \int_{\Gamma} \gamma_f \mu_f h^{-1} \mathbf{q}_h \cdot \mathbf{n}_p \mathbf{r}_h \cdot \mathbf{n}_p \\
& = -b_s(\psi_{p,h}, d_\tau \mathbf{U}_h) - \int_{\Gamma} \alpha \psi_{p,h} (d_\tau \boldsymbol{\eta}_h - d_\tau \mathbf{U}_h) \cdot \mathbf{n}_p \\
& + \int_{\Gamma} \gamma_f \mu_f h^{-1} (\mathbf{v}_h^{n-1} - d_\tau \boldsymbol{\eta}_h^{n-1}) \cdot \mathbf{n}_p \mathbf{r}_h \cdot \mathbf{n}_p + \int_{\Gamma} \mathbf{n}_p \cdot \boldsymbol{\sigma}_{f,h}^{n-1} \mathbf{n}_p \mathbf{r}_h \cdot \mathbf{n}_p;
\end{aligned}$$

3. given  $\mathbf{q}_h, p_{p,h}, \mathbf{U}_h, \boldsymbol{\eta}_h$ , find  $\mathbf{v}_h, p_{f,h}$  in  $\Omega_f$  such that

$$\begin{aligned}
& \rho_f \int_{\Omega_f} d_\tau \mathbf{v}_h \cdot \boldsymbol{\phi}_{f,h} d\mathbf{x} + a_f(\mathbf{v}_h, \boldsymbol{\phi}_{f,h}; \mathbf{v}_h^{n-1}) - b_f(p_{f,h}, \boldsymbol{\phi}_{f,h}) + b_f(\psi_{f,h}, \mathbf{v}_h) \\
& + s_{f,p}(d_\tau p_{f,h}, \psi_{f,h}) + s_{f,v}(d_\tau \mathbf{v}_h \cdot \mathbf{n}_f, \boldsymbol{\phi}_{f,h} \cdot \mathbf{n}_f) \\
& - \int_{\Gamma} \boldsymbol{\sigma}_{f,h}(\zeta \boldsymbol{\phi}_{f,h}, -\psi_{f,h}) \mathbf{n}_f \cdot \mathbf{v}_h + \int_{\Gamma} \gamma_f \mu_f h^{-1} \mathbf{v}_h \cdot \boldsymbol{\phi}_{f,h} \\
& = \int_{\Gamma} \boldsymbol{\sigma}_{f,h}^{n-1} \mathbf{n}_f \cdot \boldsymbol{\phi}_{f,h} - \int_{\Gamma} \mathbf{t}_f \cdot \boldsymbol{\sigma}_{f,h}(\zeta \boldsymbol{\phi}_{f,h}, -\psi_{f,h}) \mathbf{n}_f d_\tau \boldsymbol{\eta}_h \cdot \mathbf{t}_f \\
& - \int_{\Gamma} \mathbf{n}_f \cdot \boldsymbol{\sigma}_{f,h}(\zeta \boldsymbol{\phi}_{f,h}, -\psi_{f,h}) \mathbf{n}_f (\mathbf{q}_h^n + d_\tau \boldsymbol{\eta}_h) \cdot \mathbf{n}_f \\
& + \int_{\Gamma} \gamma_f \mu_f h^{-1} (\mathbf{q}_h + d_\tau \boldsymbol{\eta}_h) \cdot \mathbf{n}_f \boldsymbol{\phi}_{f,h} \cdot \mathbf{n}_f + \int_{\Gamma} \gamma_f \mu_f h^{-1} d_\tau \boldsymbol{\eta}_h \cdot \mathbf{t}_f \boldsymbol{\phi}_{f,h} \cdot \mathbf{t}_f;
\end{aligned}$$

4. (*optional*) When the movement of the fluid domain is taken into account, we calculate the discrete ALE velocity: given  $\dot{\boldsymbol{\eta}}_h^n$  find  $\boldsymbol{w}_h^n$  in  $\Omega_f$  such that

$$\begin{aligned} \int_{\Omega_f} \nabla \boldsymbol{w}_h^n \cdot \nabla \boldsymbol{z}_h - \int_{\partial \Omega_f} ((\nabla \boldsymbol{w}_h^n \boldsymbol{n}_f) \cdot \boldsymbol{z}_h + (\nabla \boldsymbol{z}_h \boldsymbol{n}_f) \cdot \boldsymbol{w}_h^n) + \int_{\partial \Omega_f} \gamma_f h^{-1} \boldsymbol{w}_h^n \cdot \boldsymbol{z}_h \\ = - \int_{\Gamma} (\nabla \boldsymbol{z}_h \boldsymbol{n}_f) \cdot \dot{\boldsymbol{\eta}}_h^n + \int_{\Gamma} \gamma_f h^{-1} \dot{\boldsymbol{\eta}}_h^n \cdot \boldsymbol{z}_h. \end{aligned}$$

Then,  $\boldsymbol{w}_h^n$  is used to move the points of the fluid domain and in particular the nodes of the corresponding mesh  $\boldsymbol{x}^n = \boldsymbol{x}^{n-1} + \tau \boldsymbol{w}_h^n$ .

The stability of the partitioned algorithm is a very delicate question that has been addressed by the authors in [9]. In particular we observe that the stability properties are guaranteed thanks to the introduction of the following stabilization operators. When the blood flow and the structure problems are decoupled, we introduce a stabilization term proposed in [12, 13] and acting on the free fluid pressure,

$$s_{f,p}(d_{\tau} p_{f,h}, \psi_{f,h}) := \gamma'_{stab} \frac{h\tau}{\gamma_f \mu_f} \int_{\Gamma} d_{\tau} p_{f,h} \psi_{f,h}.$$

According to the analysis performed in [9], when the solution of mechanical and flow problems into the Biot equation are solved in two separate steps, the following new stabilization terms are recommended in order to control the increment of  $\boldsymbol{v}_h, \boldsymbol{q}_h$  over two subsequent time steps,

$$\begin{aligned} s_{f,q}(d_{\tau} \boldsymbol{q}_h \cdot \boldsymbol{n}, \boldsymbol{r}_h \cdot \boldsymbol{n}) &= \gamma'_{stab} \gamma_f \mu_f \frac{\tau}{h} \int_{\Gamma} d_{\tau} \boldsymbol{q}_h \cdot \boldsymbol{n} \boldsymbol{r}_h \cdot \boldsymbol{n}, \\ s_{f,v}(d_{\tau} \boldsymbol{v}_h \cdot \boldsymbol{n}, \boldsymbol{\phi}_{f,h} \cdot \boldsymbol{n}) &= \gamma'_{stab} \gamma_f \mu_f \frac{\tau}{h} \int_{\Gamma} d_{\tau} \boldsymbol{v}_h \cdot \boldsymbol{n} \boldsymbol{\phi}_{f,h} \cdot \boldsymbol{n}. \end{aligned}$$

## 8.5 Numerical Results and Discussion

In this section we discuss a collection of numerical experiments aiming at clarifying and supporting the qualitative considerations on the role of poroelasticity on FSI in arteries, addressed in Sect. 8.3. We adopt a classical benchmark problem used for FSI problems [2, 5, 8, 11, 17], which consists in studying the propagation of a single pressure wave whose amplitude is comparable to the pressure difference between systolic and diastolic phases of the heartbeat. In particular, the following time-dependent inflow pressure profile is prescribed,

$$p_{in}(t) = \begin{cases} \frac{p_{max}}{2} (1 - \cos(\frac{2\pi t}{T_{max}})) & \text{if } t \leq T_{max} \\ 0 & \text{if } t > T_{max}, \end{cases} \quad (8.31)$$

where  $p_{max} = 13334 \text{ dyne/cm}^2$  and  $T_{max} = 0.003 \text{ s}$ . At the outflow, we prescribe homogeneous (traction-free) Neumann type boundary conditions. To make this test case represent more closely the behavior of an artery, we also slightly modify the

governing equation for elastic skeleton as follows,

$$\rho_p \frac{D^2 \mathbf{U}}{Dt^2} + \beta \mathbf{U} - \nabla \cdot \boldsymbol{\sigma}^p = 0.$$

The additional term  $\beta \mathbf{U}$  comes from the axially symmetric formulation, accounting for the recoil due to the circumferential strain. Namely, it acts like a spring term, keeping the top and bottom structure displacements connected in 2D, see, e.g., [3, 5, 26]. The reference values of the parameters used in this study fall within the range of physiological values for blood flow and are reported in Table 8.1. The propagation of the pressure wave is analyzed over the time interval  $[0, 0.006]$  s. The final time is selected such that the pressure wave barely reaches the outflow section. In this way, the unphysical reflected waves that may originate at the outflow section when the pressure wave passes through (because of homogeneous Neumann conditions) do not pollute the considered results. All the forthcoming simulations are obtained using Stokes flow model and a fixed mesh algorithm. In order to assess the impact of these simplifications on the conclusions of the work, we have preformed some additional simulations using Navier-Stokes equations, a deformable fluid computational domain and the physiological parameters of Table 8.1. The results, shown in Fig. 8.2, confirm that for the considered test case the deformation of the computational mesh and the inertial effects of the flow do not play a significant role on the calculated blood flow rate and the arterial wall displacement. As a result, we claim that the final conclusions of this study are still valid when Navier-Stokes equations and a deformable fluid mesh are used.

**Table 8.1.** Geometry, fluid and structure parameters

Parameter	Symbol	Units	Reference value
Radius	$R$	(cm)	0.5
Length	$L$	(cm)	6
Membrane thickness	$r_m$	(cm)	0.02
Poroelastic wall thickness	$r_p$	(cm)	0.1
Membrane density	$\rho_m$	(g/cm <sup>3</sup> )	1.1
Poroelastic wall density	$\rho_p$	(g/cm <sup>3</sup> )	1.1
Fluid density	$\rho_f$	(g/cm <sup>3</sup> )	1
Dyn. viscosity	$\mu$	(g/cm s)	0.035
Lamé coeff.	$\mu_m$	(dyne/cm <sup>2</sup> )	$1.07 \times 10^6$
Lamé coeff.	$\lambda_m$	(dyne/cm <sup>2</sup> )	$4.28 \times 10^6$
Lamé coeff.	$\mu_p$	(dyne/cm <sup>2</sup> )	$1.07 \times 10^6$
Lamé coeff.	$\lambda_p$	(dyne/cm <sup>2</sup> )	$4.28 \times 10^6$
Hydraulic conductivity	$\kappa$	(cm <sup>3</sup> s/g)	$5 \times 10^{-9}$
Mass storativity coeff.	$s_0$	(cm <sup>2</sup> /dyne)	$5 \times 10^{-6}$
Biot-Willis constant	$\alpha$		1
Spring coeff.	$\beta$	(dyne/cm <sup>4</sup> )	$5 \times 10^7$

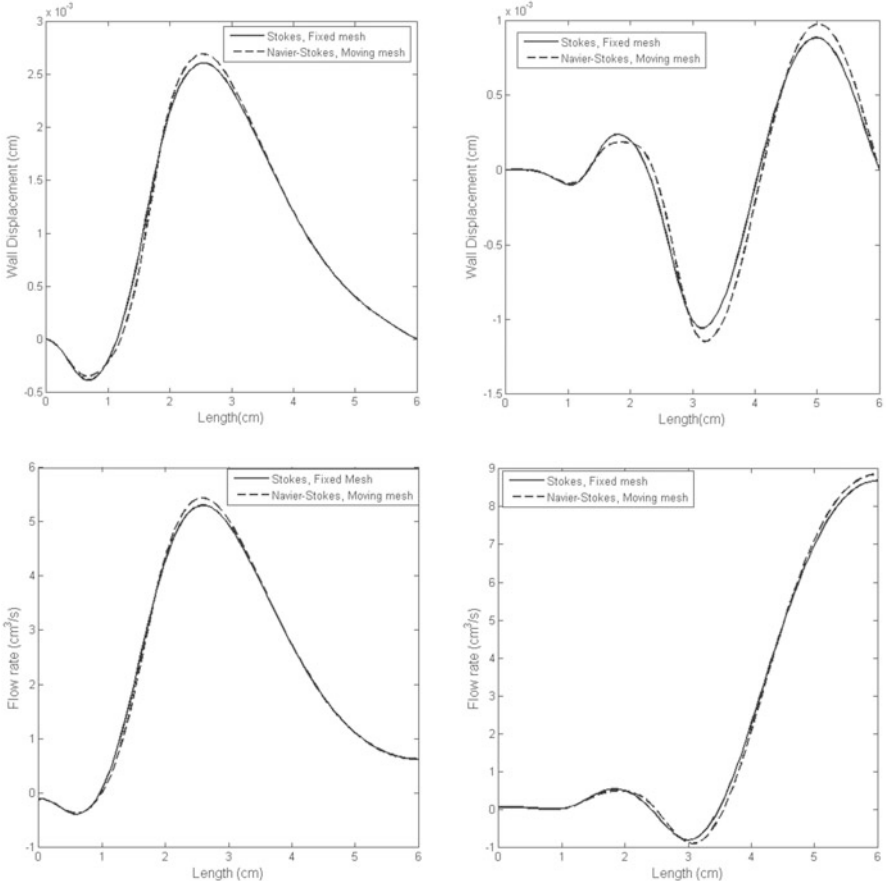


**Fig. 8.2.** A simulation using Stokes flow model and a fixed fluid domain is compared with one obtained by Navier-Stokes equations and a deformable fluid domain. The *top row* shows the displacement of the fluid-wall interface at  $t = 3.5, 5.5$  ms (the snapshot  $t = 1.5$  ms is omitted because we could not observe any significant difference between the two sets of plots). The *bottom row* shows the blood flow rate variation along the longitudinal axis, for the same time snapshots

For the discretization of the blood flow equations we adopt  $\mathbb{P}^2 - \mathbb{P}^1$  approximations for velocity and pressure respectively. This choice ensures *inf-sup* stability of the scheme [16, 30]. For simplicity of implementation, the same type of spaces are used for the intramural filtration and pressure, namely  $\mathbf{q}_h, p_{p,h}$ . To facilitate the exchange of information across the interface and avoid issues with interpolation of finite element functions, we use conforming computational meshes for the discretization of the fluid and solid domains. In addition, we also use  $\mathbb{P}^2$  finite elements for the discretization of the structure and membrane displacement fields. These choices may not be extremely efficient from the computational standpoint, but this aspects

do not represent an issue for the simple 2-dimensional test case that is considered here. We remind that the proposed numerical scheme turns out to be stable provided that several penalty and stabilization parameters are appropriately selected. According to the analysis and the numerical tests discussed in [11] for a similar scheme, we have used the following values:  $\gamma_f = \gamma_p = 2500$ ,  $\gamma_{stab} = 1$ ,  $\gamma'_{stab} = 0$ . Finally, all the simulations discussed below have been performed using an uniform time step  $\tau = 10^{-5}$  seconds.

### 8.5.1 Sensitivity of $\kappa$

We compare the results obtained using three exponentially increasing values of the hydraulic conductivity  $\kappa = 5 \times 10^{-9}, 5 \times 10^{-7}, 5 \times 10^{-5}$ , starting from the reference value of Table 8.1. In Fig. 8.3 (top) we analyze the displacement of the fluid-wall interface  $\Gamma$  at the intermediate time  $t = 3.5\text{ ms}$  when the peak of the pressure wave is located almost at the center of the arterial segment. The results show that the amplitude of the pressure wave inversely depends on the hydraulic conductivity. For the same test cases, we visualize in Fig. 8.3 (bottom) the evolution in time of the total energy of the system, precisely,

$$E_{f,h}^n + E_{p,h}^n + E_{m,h}^n \quad \text{for } n = 1, \dots, N. \quad (8.32)$$

The energy plot nicely illustrates the mechanics of this particular example. The initial increasing trend of the energy is motivated by the incoming pressure wave, which acts as a forcing term pumping energy into the system. Once the wave has completely entered the domain, by the time  $t = 3\text{ ms}$ , in absence of dissipation the energy would reach a constant plateau. The combination of the results shown in Fig. 8.3 clearly suggests that the hydraulic conductivity is responsible for energy dissipation. From the theoretical standpoint, this conclusion is supported by the presence of the term

$$\tau \sum_{n=1}^N \kappa^{-1} \|\mathbf{q}_h^n\|_{\Omega_p}^2 = \tau \sum_{n=1}^N \kappa \|\nabla p_{p,h}^n\|_{\Omega_p}^2$$

on the left-hand side of the discrete energy estimate. In conclusion, the intramural flow activated by the deformations of the wall subtracts mechanical energy from the artery.

### 8.5.2 Sensitivity of $s_0$

We expect that changing  $s_0$  corresponds to modifying the second Lamé parameter characterizing the arterial wall. However, looking at the elasticity Eq. (8.8), it is not straightforward to determine what is the role of  $\lambda$  on the fluid-structure interaction. The numerical simulations based on the proposed FSI scheme turn out to be effective also in this respect. More precisely, we have simplified the discrete scheme (8.30) in order to model the interaction of a viscous fluid with a purely elastic impermeable structure. We notice that the resulting scheme is exactly the one proposed in [11]. Using this tool, we have performed a simple sensitivity study of the parameter  $\lambda$  in

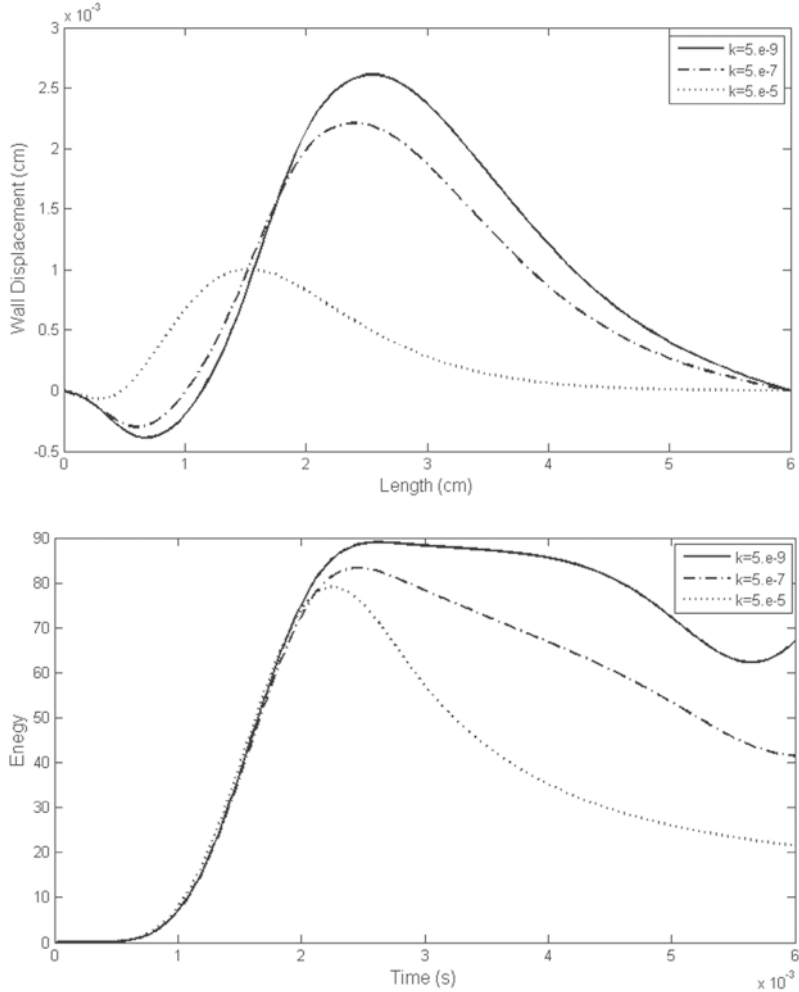


**Fig. 8.3.** Displacement of the fluid-wall interface for  $\kappa = 5 \times 10^{-9}, 5 \times 10^{-7}, 5 \times 10^{-5}$  at  $t = 3.5$  ms (top). Time evolution of the total energy of the system (8.32) for the same values of  $\kappa$  (bottom)

the linear wave Eq. (8.8). The results reported in Fig. 8.4 (top) suggest that decreasing  $\lambda$  slightly slows down the propagation of the pressure waves. Using this result, we can then proceed to test the validity of our hypothesis on the effect of  $s_0$ . To this purpose, we now use the FSI scheme for the poroelastic model where  $\lambda$  is set to the reference value of Table 8.1 but the value of the mass storativity is varied as  $s_0 = 5 \times 10^{-7}, 5 \times 10^{-6}, 10^{-5}$ . The results shown in Fig. 8.4 (bottom) completely agree with the conclusions of Sect. 8.3 and in particular with the formula (8.28). More precisely, increasing  $s_0$  from  $5 \times 10^{-6}$  to  $10^{-5}$  corresponds to decrease  $\lambda^*$ ,

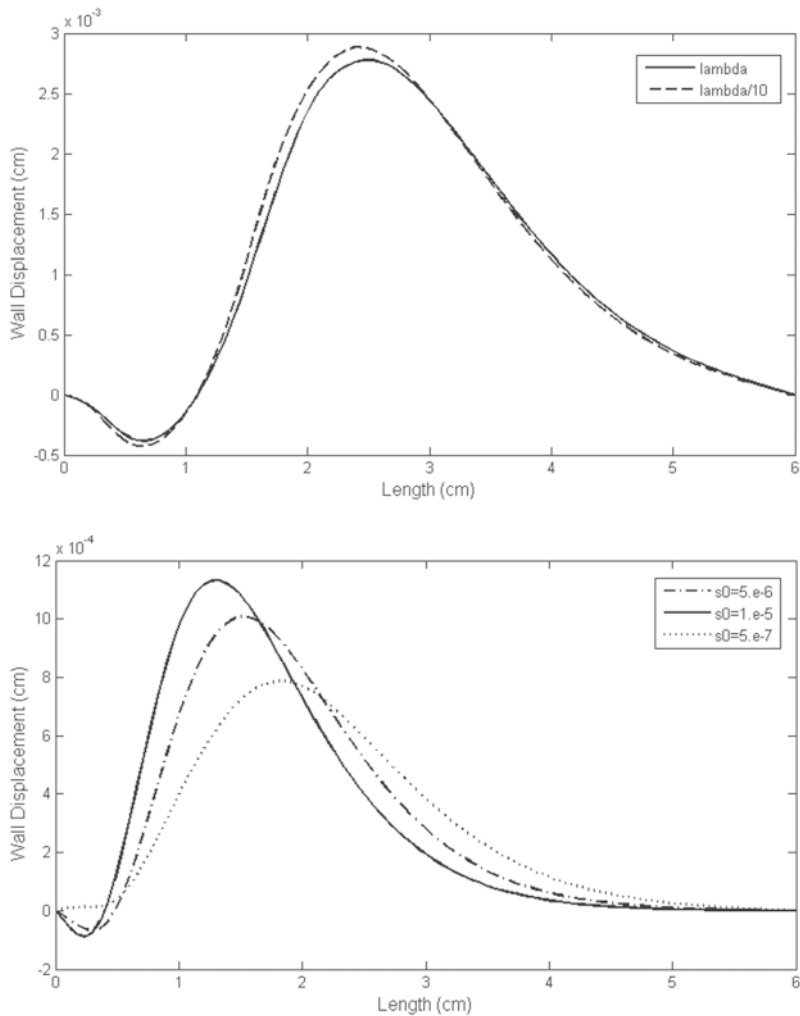


**Fig. 8.4.** Displacement of the fluid-wall interface at  $t = 3.5$  ms for  $\lambda = 4.28 \times 10^6$  and  $\lambda = 4.28 \times 10^5$  using a purely elastic material model (*top*). The same quantity is plotted when using the parameter  $s_0 = 5 \times 10^{-7}, 5 \times 10^{-6}, 10^{-5}$  for a poroelastic material (*bottom*)

which in turn slows down the pressure wave propagation. Conversely, decreasing the mass storativity corresponds to increase the equivalent second Lamé parameter. As a result, the pressure wave speeds up.

### 8.5.3 Sensitivity of $\alpha$

Figure 8.5 shows the sensitivity of the solution with respect to the Biot-Willis constant, when it varies in the range [0, 1]. Surprisingly, the solution is almost insensitive to  $\alpha$ , even in the limit case  $\alpha = 0$  where the displacement and intramural flow in Biot system, Eqs. (8.8) and (8.9), (8.10) respectively, are uncoupled. This observation seems to contradict the previous conclusions. How can the FSI dynamics be

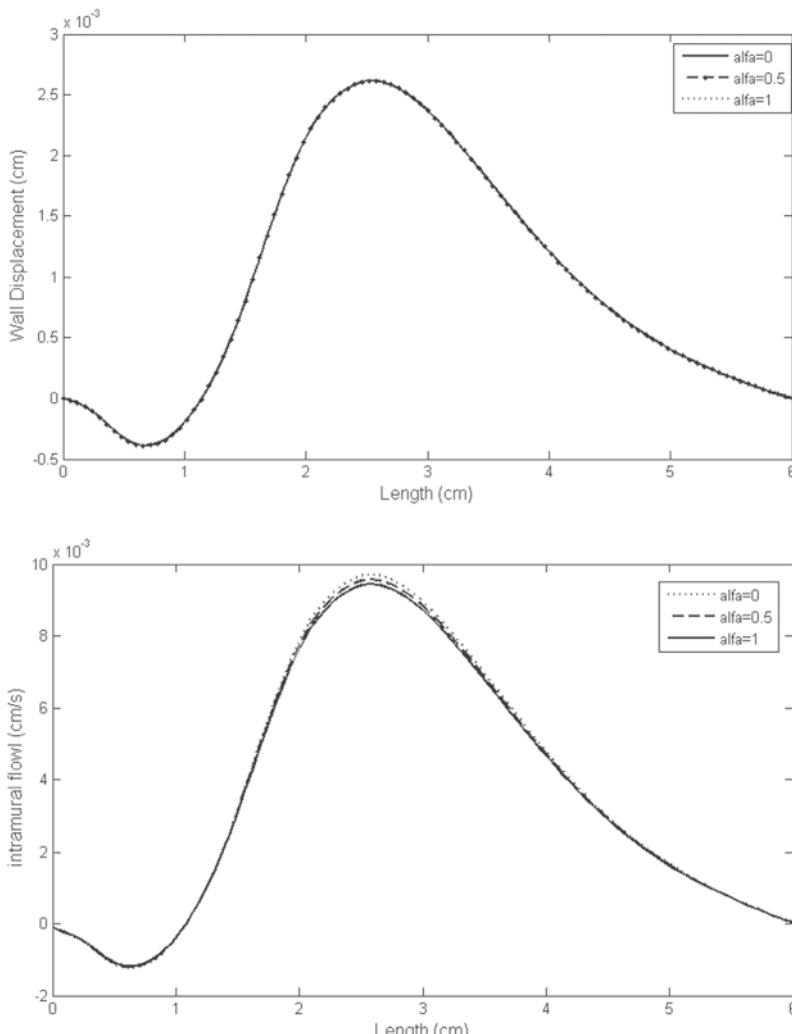


**Fig. 8.5.** Displacement of the fluid-wall interface at  $t = 3.5$  ms for  $\alpha = 1.0, 0.5, 0.0$ . Almost no influence of the parameter  $\alpha$  can be detected (*top*). The normal component of the intramural flow  $\mathbf{q}_h \cdot \mathbf{n}$  is displayed along the length of the arterial segment (*bottom*). Only a modest influence of  $\alpha$  can be detected in the region of maximum flow

affected by  $s_0$  and  $\kappa$  in (8.9), (8.10) and not by the parameter regulating the coupling of these equations with (8.8)? A plausible explanation arises from the analysis of interface conditions, namely (8.18)–(8.21). Indeed, they provide a secondary way of coupling blood flow, intramural filtration and arterial displacement. Then, the results of Fig. 8.5 lead us to conclude that the motion of the artery is barely affected by the poroelastic coupling *per-se*. What mostly affects the differences between the considered model, namely Eqs. (8.8), (8.9), (8.10), and the purely elastic case is the presence of intramural flow in the wall, coupled with the velocity and displacement fields through the kinematic conditions enforced at the fluid-structure interface.

## 8.6 Conclusions

We have investigated the role of poroelasticity on FSI using a computational method that allows us to simulate the propagation of pressure waves and the related arterial wall deformation into a straight arterial segment. Owing to the poroelastic material model, blood flow, intramural plasma filtration and mechanical deformation of the wall are coupled. The solution of the corresponding equations by means of a numerical method may become computationally intensive. We have facilitated this task by developing a loosely coupled algorithm, which allows to independently solve the equations at each time step. This tool enabled us to perform a sensitivity analysis of the effects of poroelasticity on FSI in arteries, guided by the qualitative comparison of the governing equations for a poroelastic material with the ones for pure linear elasticity. The numerical results support and complement the observations arising from the analysis. These results suggest that accounting for the intramural plasma filtration significantly affects the arterial wall displacement as well as the propagation of pressure waves. However, resorting to a poroelastic material model is not essential to capture these effects. A simpler model based on Darcy equations combined with appropriate kinematic conditions may be adequate to capture similar effects.

**Acknowledgements** The author Martina Bukac is partially supported by the NSF grant DMS 1216465 and Paolo Zunino is partially supported by the NSF grant DMS 1311983. Rana Zakerzadeh and Paolo Zunino acknowledge the partial support of the University of Pittsburgh under the Computational Modeling and Simulation program.

## References

1. Armentano, R., Barra, J., Levenson, J., Simon, A., Pichel, R.: Arterial wall mechanics in conscious dogs: assessment of viscous, inertial, and elastic moduli to characterize aortic wall behavior. *Circ. Res.* **76**(3), 468–478 (1995)
2. Badia, S., Nobile, F., Vergara, C.: Fluid-structure partitioned procedures based on Robin transmission conditions. *J. Comput. Phys.* **227**, 7027–7051 (2008)
3. Badia, S., Quaini, A., Quarteroni, A.: Splitting methods based on algebraic factorization for fluid-structure interaction. *SIAM J. Sci. Comput.* **30**(4), 1778–1805 (2008)

4. Badia, S., Quaini, A., Quarteroni, A.: Coupling Biot and Navier–Stokes equations for modelling fluid–poroelastic media interaction. *Journal of Computational Physics* **228**(21), 7986–8014 (2009)
5. Barker, A., Cai, X.: Scalable parallel methods for monolithic coupling in fluid-structure interaction with application to blood flow modeling. *Journal of Computational Physics* **229**(3), 642–659 (2010)
6. Bauer, R., Busse, R., Schabert, A., Summa, Y., Wetterer, E.: Separate determination of the pulsatile elastic and viscous forces developed in the arterial wall *in vivo*. *Pflügers Archiv* **380**(3), 221–226 (1979)
7. Botkin, N., Hoffmann, K.H., Pykhteev, O., Turova, V.: Dispersion relations for acoustic waves in heterogeneous multi-layered structures contacting with fluids. *Journal of the Franklin Institute* **344**(5), 520–534 (2007)
8. Bukač, M., Čanić, S., Glowinski, R., Tambaca, J., Quaini, A.: Fluid-structure interaction in blood flow capturing non-zero longitudinal structure displacement. *Journal of Computational Physics* (2012)
9. Bukac, M., Yotov, I., Zakerzadeh, R., Zunino, P.: Partitioning strategies based on a Nitsche’s coupling approach for interaction of a fluid with a poroelastic material. arXiv preprint arXiv:1403.5707 (2014)
10. Bukac, M., Zunino, P., Yotov, I.: Explicit partitioning strategies for the interaction between a fluid and a multilayered poroelastic structure: an operator-splitting approach. arXiv preprint arXiv:1308.4454 (2013)
11. Burman, E., Fernández, M.A.: Stabilization of explicit coupling in fluid-structure interaction involving fluid incompressibility. *Comput. Methods Appl. Mech. Eng.* **198**, 766–784 (2009)
12. Burman, E., Fernández, M.A.: Stabilization of explicit coupling in fluid-structure interaction involving fluid incompressibility. *Comput. Methods Appl. Mech. Engrg.* **198**(5–8), 766–784 (2009)
13. Burman, E., Fernández, M.: Explicit strategies for incompressible fluid-structure interaction problems: Nitsche type mortaring versus robin–robin coupling. *International Journal for Numerical Methods in Engineering* pp. n/a–n/a (2013). DOI 10.1002/nme.4607
14. Canic, S., Tambaca, J., Guidoboni, G., Mikelić, A., Hartley, C., Rosenstrauch, D.: Modeling viscoelastic behavior of arterial walls and their interaction with pulsatile blood flow. *SIAM Journal on Applied Mathematics* **67**(1), 164–193 (2006)
15. Chung, S., Vafai, K.: Effect of the fluid–structure interactions on low-density lipoprotein transport within a multi-layered arterial wall. *Journal of biomechanics* **45**(2), 371–381 (2012)
16. Ern, A., Guermond, J.L.: Theory and practice of finite elements, *Applied Mathematical Sciences*, vol. 159. Springer-Verlag, New York (2004)
17. Formaggia, L., Gerbeau, J., Nobile, F., Quarteroni, A.: On the coupling of 3D and 1D Navier–Stokes equations for flow problems in compliant vessels. *Comput. Methods Appl. Mech. Eng.* **191**(6–7), 561–582 (2001)
18. Fung, Y.C.: Biomechanics: Its Foundation and Objectives, Y.C.Fung, N.Perrone, M.Anliker (Eds). Prentice-Hall, Englewood Cliff, NJ (1972)
19. Hansbo, P.: Nitsche’s method for interface problems in computational mechanics. *GAMM-Mitt.* **28**(2), 183–206 (2005)

20. Holzapfel, G.A., Ogden, R.W.: Constitutive modelling of passive myocardium: a structurally based framework for material characterization. *Philosophical Transactions of the Royal Society A: Mathematical, Physical and Engineering Sciences* **367**(1902), 3445–3475 (2009)
21. Holzapfel, G.A., Sommer, G., Regitnig, P.: Anisotropic mechanical properties of tissue components in human atherosclerotic plaques. *Transactions of the ASME-K-Journal of Biomechanical Engineering* **126**(5), 657–665 (2004)
22. Humphrey, J.D., et al.: Mechanics of the arterial wall: Review and directions. *Critical reviews in biomedical engineering* **23**(1–2), 1 (1995)
23. Kim, J.M., Chang, S.H., Yun, C.B.: Fluid-structure-soil interaction analysis of cylindrical liquid storage tanks subjected to horizontal earthquake loading. *Structural Engineering and Mechanics* **13**(6), 615–638 (2002)
24. Lee, K., Saidel, G., Penn, M.: Permeability change of arterial endothelium is an age-dependent function of lesion size in apolipoprotein e-null mice. *American Journal of Physiology-Heart and Circulatory Physiology* **295**(6), H2273–H2279 (2008)
25. Lesinigo, M.: Lumped mathematical models for intracranial dynamics. Ph.D. thesis, EPFL, Switzerland (2013)
26. Ma, X., Lee, G., Wu, S.: Numerical simulation for the propagation of nonlinear pulsatile waves in arteries. *Journal of biomechanical engineering* **114**, 490 (1992)
27. Muha, B., Canić, S.: Existence of a weak solution to a fluid-multi-layered-structure interaction problem. Submitted, arXiv:1305.5310 (2013)
28. Murad, M.A., Guerreiro, J.N., Loula, A.F.: Micromechanical computational modeling of secondary consolidation and hereditary creep in soils. *Computer methods in applied mechanics and engineering* **190**(15), 1985–2016 (2001)
29. Prosi, M., Zunino, P., Perktold, K., Quarteroni, A.: Mathematical and numerical models for transfer of low-density lipoproteins through the arterial walls: a new methodology for the model set up with applications to the study of disturbed luminal flow. *Journal of biomechanics* **38**(4), 903–917 (2005)
30. Quarteroni, A., Valli, A.: Numerical approximation of partial differential equations, Springer Series in Computational Mathematics, vol. 23. Springer-Verlag, Berlin (1994)
31. Rausch, S., Martin, C., Bornemann, P., Uhlig, S., Wall, W.: Material model of lung parenchyma based on living precision-cut lung slice testing. *Journal of the Mechanical Behavior of Biomedical Materials* **4**(4), 583–592 (2011)
32. Robertson, A., Hill, M., Li, D.: Structurally motivated damage models for arterial walls. Theory and application. In: *Modeling of Physiological Flows*, pp. 143–185. Springer (2012)
33. Showalter, R.: Poroelastic filtration coupled to Stokes flow. *Lecture Notes in Pure and Applied Mathematics* **242**, 229–241 (2010)
34. Tang, D., Yang, C., Geva, T., Gaudette, G., Del Nido, P.: Multi-physics MRI-based two-layer fluid–structure interaction anisotropic models of human right and left ventricles with different patch materials: Cardiac function assessment and mechanical stress analysis. *Computers & structures* **89**(11), 1059–1068 (2011)
35. Tully, B., Ventikos, Y.: Coupling poroelasticity and CFD for cerebrospinal fluid hydrodynamics. *Biomedical Engineering, IEEE Transactions on* **56**(6), 1644–1651 (2009)
36. Vito, R., Dixon, S.: Blood vessel constitutive models-1995-2002. *Annual review of biomedical engineering* **5**(1), 413–439 (2003)
37. Zhou, J., Fung, Y.: The degree of nonlinearity and anisotropy of blood vessel elasticity. *Proceedings of the National Academy of Sciences* **94**(26), 14,255–14,260 (1997)

---

# Personalized Anatomical Meshing of the Human Body with Applications

**Yuri Vassilevski, Alexander Danilov, Yuri Ivanov, Sergey Simakov and Timur Gamilov**

**Abstract** The frontier research in computational modeling of human physiology and medical applications is tightly connected to computational meshing technique. Meshes of hard and soft tissues, organs and network-like structures such as vessels network, trachea-bronchial tree and similar ones provide the basis for lots of simulations. We present two applications and associated numerical models requiring personalized anatomically correct meshing of the whole human body or its vascular network.

## 9.1 Introduction

The frontier research in computational modeling of human physiology and medical applications is tightly connected to computational meshing technique. Meshes of hard and soft tissues, organs and network-like structures such as vessels network, trachea-bronchial tree and similar ones provide the basis for lots of simulations. They are closely related to a modern virtual physiological human concept [14]. Accuracy of geometric models plays important role in every biomechanical simulation. One of the two anatomical data types is commonly assumed: general data from human

---

Y. Vassilevski (✉) · A. Danilov

Institute of Numerical Mathematics of Russian Academy of Sciences, 119333, Gubkina St. 8, Moscow, Russia, and Moscow Institute of Physics and Technology, 141707, Institutskii Lane 9, Dolgoprudny, Russia

e-mail: yuri.vassilevski@gmail.com; a.a.danilov@gmail.com

Y. Ivanov

Institute of Numerical Mathematics of Russian Academy of Sciences, 119333, Gubkina St. 8, Moscow, Russia

e-mail: yura-vtm@ya.ru

S. Simakov · T. Gamilov

Moscow Institute of Physics and Technology, 141707, Institutskii Lane 9, Dolgoprudny, Russia

e-mail: simakov@crec.mipt.ru; gamilov@crec.mipt.ru

anatomy atlases or individual data of the particular organism. Both data types require technical work on correct volume extraction, meshing, network skeletonisation etc.

In this paper we present two applications and associated numerical models requiring personalized anatomically correct meshing of the whole human body or its subsystems.

The first application, numerical simulation of bioelectrical impedance analysis (BIA) [5–7, 29, 44], requests a 3D meshing technique for hard and soft tissues and organs of the patient. BIA is generally used for body composition and abdominal adiposity assessment in clinical medicine, dietology, and sports medicine [12]. It is also used for body fluids redistribution monitoring under various physiological conditions.

Many factors affect correct BIA. The measured signal highly depends on electrode position, electric frequency, body constitution and shape. Accurate modeling of these processes requires adaptive geometric models either individual or the set of generic models adapted to sex, age, and important morphometry parameters (height, weight, etc). Computational analysis of the measurement schemes is the essential part of accurate data interpretation and optimization of electrode positions. Our approach is based on the direct simulation of electric current propagation through tissues and organs during bioimpedance measurements of a body segment. In this work we suggest a multi-stage algorithm to produce a personalized anatomically correct 3D mesh of the patient body. The first preliminary stage is performed once for all simulations: we use Visible Human Project data [40] as input for generation of a reference segmented model similar to [13]. At the next stages, on the basis of individual imaging data from CT/MRI we design the piecewise affine transformation of the reference body to the patient body, in order to produce its segmented geometric model. Finally, we generate the adapted tetrahedral mesh on the basis of the personalized segmented model.

The second application, network blood flow simulation [1, 10, 18, 19, 24, 30] requires a correct structural scheme (a vascular graph with nodes connected by edges) of the 3D individual vascular network. Given a 3D vascular domain extracted from CT/MRI data, one needs an algorithm producing the vascular graph. Two state-of-the-art software libraries provide tools for such functionality, commercial code Amira® [42] and open source code VMTK [41]. We use VMTK for 3D volume extraction from individual CT/MRI data for the vascular centerlines reconstruction. The vascular graph is produced from the set of centerlines by a new algorithm presented in detail in [26]. As a practical example of the personalized hemodynamic model we present simulations of revascularization procedure for the case of thigh artery stenting caused by atherosclerotic occlusion.

The proposed approach is described below. In Sect. 9.2 we introduce two examples of models which demand personalized anatomical meshing. In Sect. 9.3 we present our approach to anatomical meshing of patient body. In Sect. 9.4 we describe our methodology for automated generation of vascular graphs on the basis of patient CT/MRI data.

## 9.2 Examples of Mathematical Models Requiring Personalized Anatomical Meshing

*Bioelectrical Impedance Analysis (BIA) numerical simulations* require anatomically correct 3D geometrical model of the body including internal structure of organs and tissues with different electrical properties. As stated in [6], the electrical fields generated during bioimpedance measurements are governed by the equation

$$\operatorname{div}(\mathbf{C}\nabla U) = 0 \quad \text{in } \Omega \quad (9.1)$$

with the boundary conditions

$$(\mathbf{J}, \mathbf{n}) = \pm I_0 / S_{\pm} \quad \text{on } \Gamma_{\pm} \quad (9.2)$$

$$(\mathbf{J}, \mathbf{n}) = 0 \quad \text{on } \partial\Omega \setminus \Gamma_{\pm} \quad (9.3)$$

$$U(x_0, y_0, z_0) = 0 \quad (9.4)$$

$$\mathbf{J} = \mathbf{C}\nabla U \quad (9.5)$$

where  $\Omega$  is the computational domain,  $\partial\Omega$  is its boundary,  $\Gamma_{\pm}$  are the electrode contact surfaces,  $\mathbf{n}$  is the external unit normal vector,  $U$  is the complex-valued electric potential,  $\mathbf{C}$  is the complex-valued conductivity tensor,  $\mathbf{J}$  is the current density,  $I_0$  is the electric current,  $S_{\pm}$  are areas of the electrode contacts. Equation (9.1) determines the distribution of electric field in the domain with heterogeneous conductivity  $\mathbf{C}$ . Equation (9.2) sets the constant current density on the electrode contact surfaces. Equation (9.3) defines the no-flow condition on the domain boundary. Uniqueness of the solution is guaranteed by Eq. (9.4), where  $(x_0, y_0, z_0)$  is some point in the domain  $\Omega$ .

Discretization of Eqs. (9.1)–(9.5) is obtained on the basis of the conventional finite element method with the piecewise linear elements on unstructured tetrahedral meshes. We use the open source finite element and meshing library Ani3D [39]. Our approach to personalized tetrahedral meshing is presented in Sect. 9.3. Figure 9.1 represents the simulation results for the conventional four-electrode scheme with a pairs of electrodes placed on right hand and right leg.

*Blood flow in the cardio-vascular network numerical simulations* require anatomically correct vessel graph reconstruction. The governing equations of the hemodynamic model describe viscous incompressible fluid flow through the network of elastic tubes, see [24, 25, 30, 31] and references therein. The flow in every tube is described by mass and momentum balance as

$$\partial S_k / \partial t + \partial(S_k u_k) / \partial x = 0, \quad (9.6)$$

$$\partial u_k / \partial t + \partial(u_k^2 / 2 + p_k / \rho) / \partial x = f_{fr}(S_k, u_k), \quad (9.7)$$

where  $k$  is index of the tube,  $t$  is the time,  $x$  is the distance along the tube,  $\rho$  is the blood density (constant),  $S_k(t, x)$  is the cross-section area,  $u_k(t, x)$  is the linear velocity averaged over the cross-section,  $p_k(S_k)$  is the blood pressure,  $f_{fr}$  is the

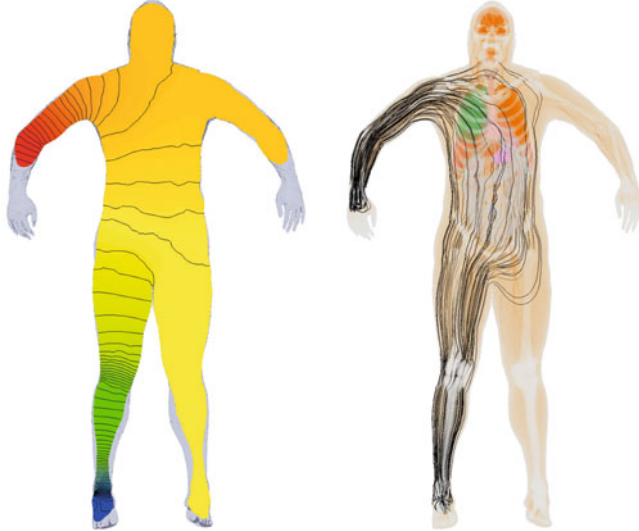


**Fig. 9.1.** Cutplane of the potential field (*left*) and current lines (*right*) for conventional bioimpedance measuring scheme

friction force given by

$$f_{fr}(S_k, u_k) = -\frac{4\pi\mu u_k}{S_k \tilde{S}_k} (\tilde{S}_k + \tilde{S}_k^{-1}), \quad (9.8)$$

where  $\mu$  is the blood viscosity,  $\tilde{S}_k = S_k/S_k^0$  and  $S_k^0$  is the reference unstressed cross-section. At the vessels junctions the Poiseuille's pressure drop and mass conservation conditions are applied

$$p_k(S_k(t, \tilde{x}_k)) - p_{node}^l(t) = \varepsilon_k R_k^l S_k(t, \tilde{x}_k) u_k(t, \tilde{x}_k), k = k_1, k_2, \dots, k_M, \quad (9.9)$$

$$\sum_{k=k_1, k_2, \dots, k_M} \varepsilon_k S_k(t, \tilde{x}_k) u_k(t, \tilde{x}_k) = 0, \quad (9.10)$$

where  $M$  is the number of the connected tubes,  $\{k_1, \dots, k_M\}$  is the range of the indexes of the connected tubes,  $l$  is the node index;  $p_{node}^l(t)$  is the pressure at the  $l$ -th junction point;  $\varepsilon_k = 1$ ,  $\tilde{x}_k = L_k$  for incoming tubes,  $\varepsilon_k = -1$ , and  $\tilde{x}_k = 0$  for outgoing tubes,  $R_k^l$  is the hydraulic resistance. The set (9.9)–(9.10) is closed by finite differences approximation of compatibility conditions along outgoing characteristics [25]. The resulting system is reduced from  $2M + 1$  to  $M$  equations and is solved by Newton method separately for each junction point [24, 30]. Elasticity of the tube wall is described by the transmural pressure to cross-section relationship (wall state equation)

$$p_k(S_k) - p_{*k} = \rho c_k^2 f(S_k), \quad (9.11)$$

where S-like function  $f(S)$  studied in [20] is approximated as

$$f(S_k) = \begin{cases} \exp(\tilde{S}_k - 1) - 1, & \tilde{S}_k > 1, \\ \ln \tilde{S}_k, & \tilde{S}_k \leq 1, \end{cases} \quad (9.12)$$

where  $p_{*k}$  is the pressure in the tissues surrounding the vessel,  $c_k$  is the pulse wave velocity (PWV) in the unstressed vessel characterizing material stiffness [35]. The relationship was verified by fiber-spring model of vessel wall elasticity [32, 33]. Equations (9.9)–(9.10) are discretized by a hybrid explicit scheme corresponding to the most accurate first order monotone scheme and the less oscillating second order scheme [15, 17].

The main geometric data for the model (9.6)–(9.12) is the vessel network in terms of 3D graph with given edge lengths, diameters and nodes positions. Our approach to personalized graph construction and meshing is presented in Sect. 9.4. In the same section we show an example of the personalized hemodynamic simulation of thigh vasculature.

## 9.3 Personalized 3D Meshing of the Human Body

The ideal approach for construction of anatomically correct 3D geometric model is to produce 3D geometry from individual medical images (CT, MRI or other slice-like data). This requires strong involvement of human expertise. Moreover, such data can be unavailable or have low quality due to hardware limitations, human expert qualification, medical restrictions, etc. The other reasonable approach analysed below is to fit a reference anatomically correct model. Such reference model should be based on individual data (*in vivo* [37] or detailed *post mortem* examination [40]), or a conventional database [43]. It should provide correct detailed anatomy without organs intersection and void regions due to errors in processing, segmentation, and 3D volume reconstruction algorithms. This tedious work, of course, requires human expert involvement but once the reference model is approved it could be used in automatic or semi-automatic manner.

### 9.3.1 Segmentation and Meshing of Reference Models

As input for the reference model we have chosen Visible Human Project (VHP) [40] data and applied a semi-automatic algorithm implemented by ITK-SNAP software [38] in order to produce a grid of labeled voxels with resolution  $1 \times 1 \times 1$  mm. A detailed description of this algorithm can be found in [6].

The voxel-based geometric model of the human body is a building block to produce the unstructured tetrahedral mesh. The surface mesh can be generated by marching cubes algorithm for surface reconstruction [36], surface triangulation, smoothing and coarsening [28, 34]. The volume mesh can be generated using 3D Delaunay triangulation [9] or advancing front technique [4, 9]. We applied the Delaunay triangulation algorithm from the CGAL-Mesh library [21]. This algorithm

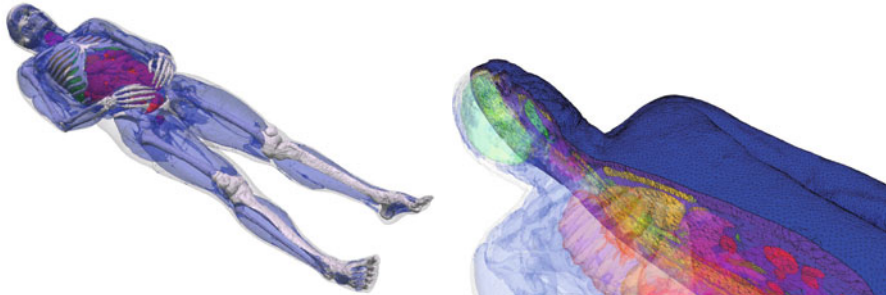


**Fig. 9.2.** Segmented whole body model of the Visible Human Man (*left*) and a part of related generated mesh (*right*)

allows one to use specific mesh size definition for each model material. In order to preserve geometric features of the segmented model while keeping a feasible number of vertices, we assigned smaller mesh size for the blood vessels and larger mesh size for the fat and muscle tissues. The resulted mesh contains 32 materials, 574.128 vertices and 3.300.481 tetrahedra (Fig. 9.2). This mesh retains most anatomical features of the human male body [7]. Similar model have been developed for the whole female body model.

The model was finalized by adding skin layer and multi-layered electrodes to the surface of the mesh. Boundary triangulation was used to create a prismatic mesh on the surface. Then each prism was split into three tetrahedra resulting in a conformal mesh. Mesh cosmetics algorithms from Ani3D library [39] were used to improve mesh quality. This essential step reduces discretization errors and the stiffness of the resulted system of linear equations.

### 9.3.2 Segmentation and Meshing of Patient-specific Models

The segmentation process is a tedious work which requires a lot of processing time. Although existing technologies of semi-automatic segmentation can speed-up the work, creating a new personalized segmented model from scratch is time consuming process. In order to construct a patient-specific segmented model, we propose to fit the anatomically correct reference segmented model by patient anthropometric and CT/MRI data.

The first step is anthropometric scaling. The reference model can be split into several parts and adjusted by the height according to the height of the related parts of the actual patient. In the same way the width is adjusted. This scaling is not sufficient since the patient may have different body constitution: fat/muscle ratio, pathologies, anatomical features, etc.

On the second step we propose a transformation of the segmented reference model using control planes and control points. At first, several control planes are selected and patient CT/MRI image is fitted to the reference model image in these planes.

Model fitting in every plane is based on the piecewise affine mapping defined by the set of control points. The user marks the same set of control points both on the reference image and on the patient image. Then the reference image is mapped to the patient image shifting the control points from original positions to the new ones. The control points may represent anatomical or geometric features of the human body. We assume here that anatomical structure on the segmented images of the reference and patient models is the same. The size and the form of the contours (material boundaries) may be varied using this fitting.

The piecewise affine transformation is constructed on the basis of the Delaunay triangulation for the control points from the patient image. The same triangulation with the identical topology is constructed using the corresponding control points in the reference image. Assuming the latter triangulation is not tangled we can construct the piecewise affine mapping of each triangle from one mesh to the corresponding triangle in the second mesh. An example of the transformed segmented image is presented in Fig. 9.3.

Once the transformations on two parallel control planes are constructed we can define the transformation on any plane between these planes using linear combination of these two transformations.

To make the piecewise affine transformation isomorphic, we assume that both Delaunay meshes are not tangled. If the user specifies the positions of control points in such a way that the Delaunay mesh tangles, we propose to set auxiliary points. These points and the control points are used to construct a more flexible Delaunay mesh. Auxiliary points are placed between user defined control points in order to

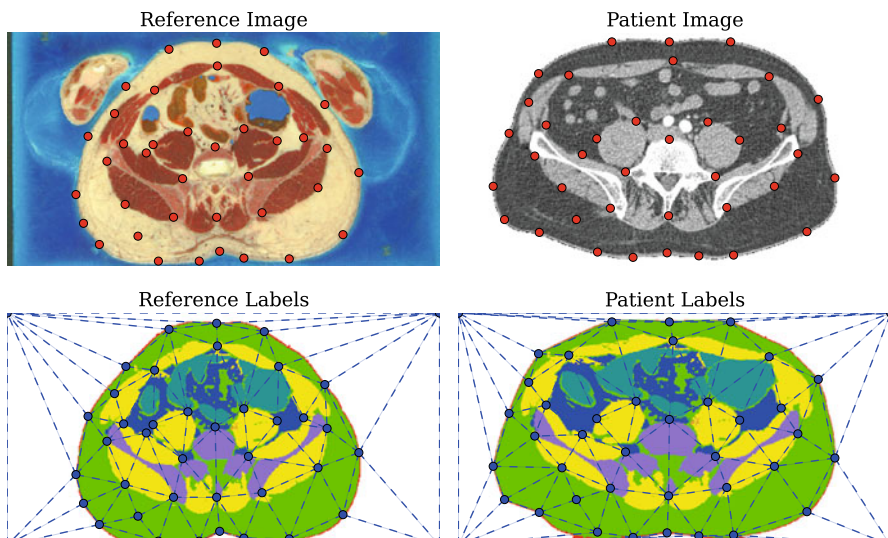


**Fig. 9.3.** Control points mapping. *Left:* the reference segmented image with control points. *Right:* the mapped image with control points

smooth the mesh deformation. The positions of the auxiliary points are determined by the variational mesh modification method. The detailed algorithm for such mesh adaptation is presented in [5]. The number of auxiliary points needed to create a set of two untangled meshes may vary depending on the positions of control points. In practice, if the control points movements are small enough, we do not need any auxiliary points. If the deformation is not very large, the number of auxiliary points is also not too large.

Once the segmented patient-specific model is ready, one can apply already discussed *automated* tetrahedral meshing procedures.

The proposed technique is used to fit reference segmented model for patients with the same anatomical structure. This process relies on some expert-defined control points sets. Once the new automated control point detection algorithm is developed, this mapping technique may be extended automatically. Patients with different anatomical structure, i.e. with some pathologies, should be treated with other reference models.

## 9.4 Personalized Skeletonisation and Meshing of Network Structures

The algorithm of vessel graph reconstruction is divided into the following steps: 3D volume segmentation of vascular structure, meshing and centerlines extraction by VMTK, centerlines merging and graph reconstruction.

We should note that commercial software Amira® provides about the same functionality. It helps to perform semi-automatic blood vessels segmentation as well as to produce skeletonisation based on distance map and thinning methods providing connected set of voxels. After that Euclidean distance to the nearest boundary is calculated at every point to generate centerlines and spatial vascular graph.

In this work we propose a method which uses open source library VMTK. This library can be modified and easily extended with new methods. We use VMTK to produce centerlines of the 3D vascular domain extracted from CT/MRI data and extend it with the new algorithm for graph reconstruction. To perform vascular domain extraction, we filter input data and eliminate bones, void regions and surrounding tissues from the original image by thresholding. The level set method is used for tracking vascular branches and marching cubes method is used to extract the surface. The result of this preprocessing stage based on patient CT data is presented in Fig. 9.4.

The spatial vascular graph of the vascular network is described by a set of vertices  $A_i$  with radius vectors  $\mathbf{a}_i = (x_i, y_i, z_i)$  and a set of edges given in terms of edge endpoints, length of the vessel segment and its averaged radius. This representation can be produced from centerline extraction of the initial 3D vascular domain. Several methods of centerline extraction are compared in [8, 16]. We select the method from VMTK based on Voronoi diagrams [2]. The result of meshing and centerlines computation is presented in Fig. 9.5.

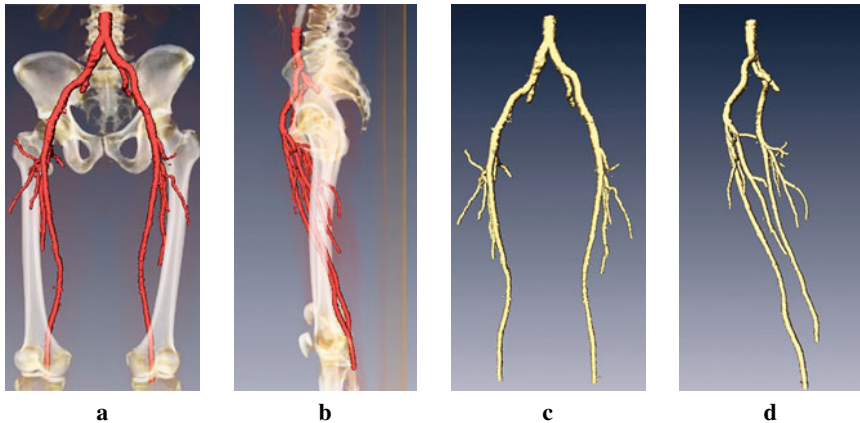


**Fig. 9.4.** 3D segmentation based on CT data: vessels with bones (a,b); vessels (c,d)

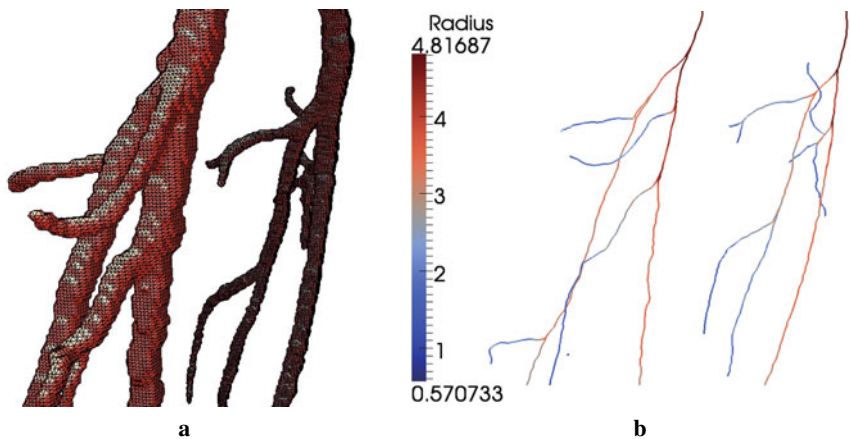


**Fig. 9.5.** 3D vascular domain: polygonal surface mesh (a); computed centerlines (b)

#### 9.4.1 Skeletonisation Algorithm

Every centerline extracted with VMTK goes from every chosen inlet to every outlet. It is described by ordered set of pairs  $(\mathbf{a}_i, r_i)$ , where  $\mathbf{a}_i = (x_i, y_i, z_i)$  is radius vector of the central point in the vessel cross section and  $r_i$  is the mean radius of the vessel at this point. These centerlines are merged by removing coincided parts and segmented with junction points. In Fig. 9.6 we demonstrate the set of centerlines  $[O, P], [O, Q], [O, R], [O, S]$  before splitting and the new segmented set  $[O, P], [O_1, Q], [O_2, R], [O_3, S]$ .

Centerlines intersection is determined by the following condition. Centerline  $C' = \{(\mathbf{a}'_i, r'_i)\}_{i=1}^{n'}$  intersects centerline  $C = \{(\mathbf{a}_i, r_i)\}_{i=1}^n$  if

$$\exists \mathbf{a} \in \{\mathbf{a}'_1, \dots, \mathbf{a}'_{n'}\}, \exists k \in \{1, \dots, n-1\} : |\mathbf{a} - \mathbf{a}^*| \leq r_{k+0.5}(\mathbf{a}^*)$$

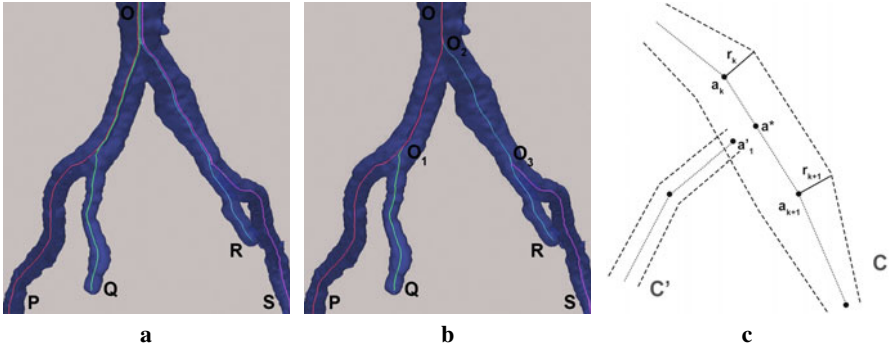


**Fig. 9.6.** Centerlines before (a) and after (b) splitting; intersection of centerlines (c)

where  $\mathbf{a}^*$  is the projection of  $\mathbf{a}$  onto  $[\mathbf{a}_k, \mathbf{a}_{k+1}]$  and  $r_{k+0.5}$  is obtained by the linear interpolation between the radii of two neighbours

$$r_{k+0.5}(\mathbf{a}^*) = \begin{cases} r_k(1 - \lambda_{k+0.5}(\mathbf{a}^*)) + r_{k+1}\lambda_{k+0.5}(\mathbf{a}^*), & \mathbf{a}^* \in [\mathbf{a}_k, \mathbf{a}_{k+1}] \\ 0, & \mathbf{a}^* \notin [\mathbf{a}_k, \mathbf{a}_{k+1}], \end{cases}$$

$$\lambda_{k+0.5}(\mathbf{a}^*) = \frac{|\mathbf{a}^* - \mathbf{a}_k|}{|\mathbf{a}_{k+1} - \mathbf{a}_k|}.$$

We define  $\mathbf{a}^*$  as the branching point (Fig. 9.6c).

The algorithm of skeletonisation is initialized by choosing the root centerline. The other centerlines are checked for the intersection with the root; branching points are determined for every intersection. After that the algorithm recursively proceeds through the centerlines intersecting the root taking them subsequently as new roots. This can produce a graph with loops, but with vertices degree not greater than 3.

In order to avoid generation of branches with extra small length, we define the minimal branch length value  $\Delta \in [2R(x), 4R(x)]$ , where  $R(x)$  is the local vessel radius at centerline point  $x$ . Then we merge points for centerline  $C = \{(\mathbf{a}_i, r_i)\}_{i=1}^n$  as follows.

If

$$\exists \mathbf{a}_i, \dots, \mathbf{a}_{i+k} \in C : \sum_{j=0}^{k-1} |\mathbf{a}_{i+j+1} - \mathbf{a}_{i+j}| < \Delta,$$

and

$$\nexists \mathbf{a}_{i-1}, \mathbf{a}_{i+k+1} : |\mathbf{a}_i - \mathbf{a}_{i-1}| < \Delta, |\mathbf{a}_{i+k+1} - \mathbf{a}_{i+k}| < \Delta,$$

then redefine

$$\mathbf{a}_i = \dots = \mathbf{a}_{i+k} = \sum_{j=0}^k \frac{\mathbf{a}_{i+j}}{k+1}.$$

The process is illustrated in Fig. 9.7 where only one vertex  $P_k$  is added to the set of graph nodes.

The complexity of the skeletonisation algorithm is  $O(M^2N)$  where  $M$  is the number of centerlines,  $N$  is the maximal number of points in the centerlines. The PC run

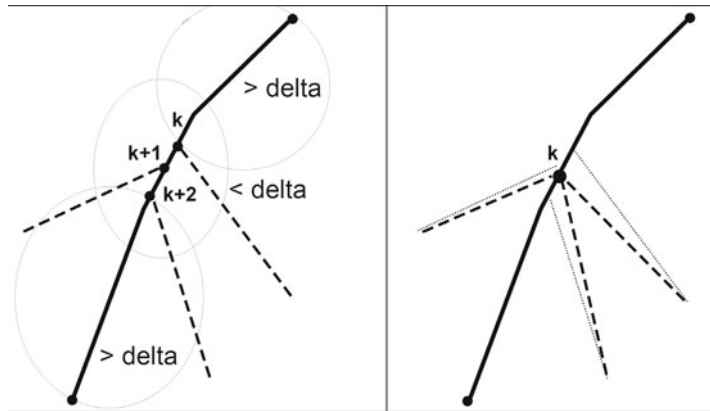


**Fig. 9.7.** Points merge due to the minimal branch length

time for the automated skeletonisation is of order of one minute in case of  $M = 200$  and  $N = 200$ . The meshing procedure for the vascular graph is trivial since the mesh nodes are added uniformly on each graph edge.

The skeletonisation and meshing algorithm was tested on the vessel network given by the vascular 3D geometric model [43]. The resulting core graph for systemic arteries is presented in Fig. 9.8.

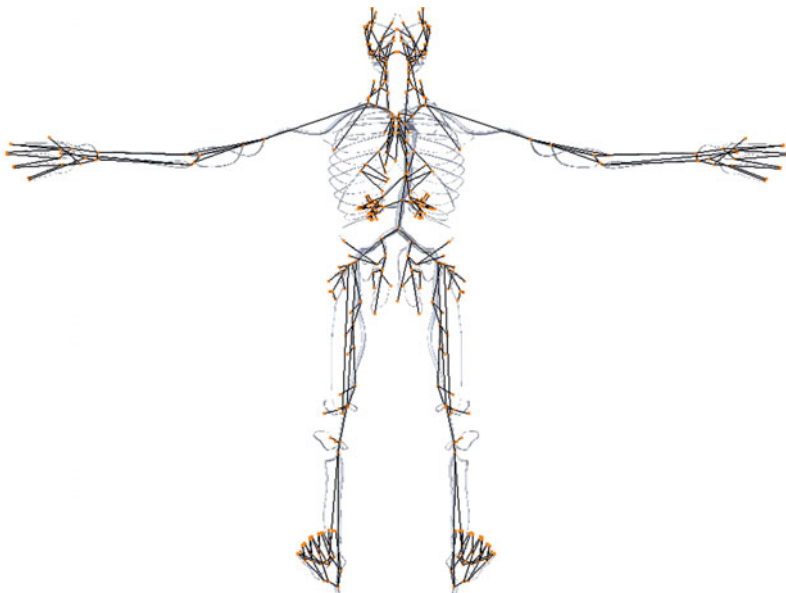


**Fig. 9.8.** The vascular network of arterial part of systemic circulation based on virtual 3D model [43]

### 9.4.2 Application to Occlusion Treatment of the Femoral Artery

We consider the application of the hemodynamic model for thigh vasculature in the case of the occlusion treatment in femoral artery.

Presurgical patient specific CT data were used to produce vascular graph of the thigh arterial vasculature with the method discussed above. The arteries and resulting graph of vessels are presented in Fig. 9.4 and Fig. 9.9, respectively. The geometric parameters of the vascular network are identified by our skeletonisation algorithm and correspond to the patient specific morphology.

In this paper we omit the description of boundary conditions at the network inlet and outlet as well as the description of parameters  $c_k$  in (9.11) and the hydraulic resistances  $R_k^l$  in (9.9). Presurgical values of  $c_k$  and  $R_k^l$  are fitted to match the available presurgical Doppler ultrasound measurements at some points of the vascular network and general values provided by [3, 11, 22, 23]. These issues constitute the body of another paper [26]. Here we present only geometric parameters identified by the skeletonisation algorithm (Table 9.1).

**Table 9.1.** Parameters of the arterial part:  $l_k$  is length of the  $k^{th}$  vessel,  $d_k$  is diameter of the  $k^{th}$  vessel

$k$	1	2	3	4	5*	5**	6	7	8	9	10	11	12	13	14
$l_k$ , cm	4.63	6.51	14.09	1.0	0.79	0.79	4.11	2.08	8.07	38.75	1.67	4.5	8.17	3.55	12.7
$d_k$ , cm	1.25	0.72	0.94	0.93	0.93	0.37	0.45	0.84	0.41	0.61	0.83	0.46	0.63	0.45	0.44

\* denotes vessel without occlusion, \*\* denotes vessel with occlusion

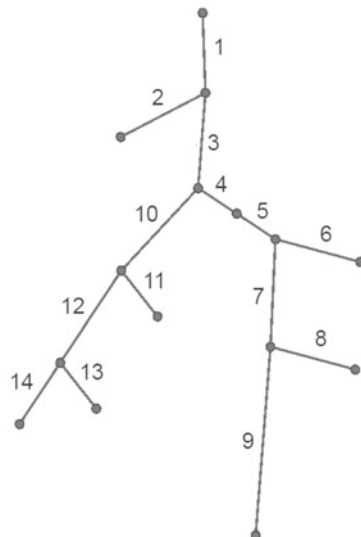


**Fig. 9.9.** Arterial network of the left thigh

The occlusion is modeled as a fragment of femoral artery (vessel 5 in Fig. 9.9). Except for vessel 5 we assume the model parameters  $l_k, d_k, c_k, R_k^l$  remain the same for the postsurgical case since the Reynolds number is not changed significantly in the most vessels in presurgical and postsurgical simulations. During presurgical simulations parameters of vessel 5 are modified as follows. The hydraulic resistance is increased by the factor 3, diameter is decreased by 60% thus providing lumen decrease ( $S_0$  in (9.11)) by 84%. During postsurgical simulations parameters of vessel 5 were set equal to parameters of the normal femoral region 4 (Fig. 9.9).

We applied the personalized hemodynamic model to predict postsurgical blood flow through the left thigh arteries without occlusion. Measured peak velocities were used in this case to check the model output. The column *postsurgical* in Table 9.2 (for details see [26]) shows quite good coincidence between these data sets. The maximum relative error is not greater than 20% that is observed in distal part of superficial femoral artery. The maximal error is attributable to insufficient CT resolution. General anatomy [27] states that one of the deep femoral artery branches has a connection with the popliteal artery which provides an alternate pass in the case of femoral artery occlusion. We failed to observe this connection in patient CT data. Being introduced to the model, the alternate pass would decrease the peak velocity due to occurrence of the collateral flow and thus decrease the error.

**Table 9.2.** Peak blood velocities

<i>Measurement points (see Fig. 9.9)</i>	<i>Peak blood velocity (cm/s)</i>			
	<i>presurgical</i> <i>patient</i>	<i>model</i>	<i>postsurgical</i> <i>patient</i>	<i>model</i>
3 - common femoral art.	148	149	150	155
4 - superficial femoral art. (proximal)	48	54	65	70
12 - deep femoral art.	103	93	69	83
5 - occlusion	above 300	340	–	71
7 - superficial femoral art. (distal)	–	67	98	86
9 - popliteal art.	52	56	72	72

## 9.5 Conclusions

In this work we addressed approaches for personalized anatomical meshing of the patient body or patient vascular network.

For patient-specific body meshing we adopt the four-stage algorithm which relies on the assumption that the patient has the same structural body composition as the reference VHP model, i.e. the same set of tissues and organs. First, we apply the semi-automatic segmentation of the reference VHP images. This is tedious work to be done only once. Second, we perform the anthropometric mapping of the reference model to the patient dimensions. Third, for selected cross section planes we generate the piecewise affine transformation to map the reference segmentation to the patient

segmentation on the basis of user-defined control points on both reference and patient images. The future development of the adaptation technique is expected to utilise either the automatic control points placement, or automatic mapping reconstruction techniques.

For patient-specific vascular network reconstruction we adopt the open source library VMTK to produce vascular centerlines on the basis of CT/MRI data followed by the automated skeletonisation algorithm. The produced vascular graph possesses all necessary geometric data for hemodynamic simulations. We demonstrated applicability of our approach to predictive personalized postsurgical blood flow simulations.

**Acknowledgements** We acknowledge the Moscow Institute of Physics and Technology (State University), The Department of Applied Mathematics, The International Translational Medicine and Biomodeling Research team. This work was partially supported by the RFBR grants 14-01-00779 and 14-01-00830, Russian Federation President Grant for Government Support of Young Russian Scientists MK-3675.2013.1, Federal programs “Research and Development”. The blood flow numerical model and the results of blood flow simulations in Sect. 9.4.2 were supported by Russian Science Foundation grant 14-01-00877. We also appreciate the staff of I.M. Sechenov’s First Moscow State Medical University and personally P. Kopylov for providing the CT data on femoral artery occlusion treatment.

## References

1. Abakumov, N.V., Mukhin, S.I., Favorski, A.P. et al.: Strategy of mathematical cardiovascular system modeling. *Matem. Mod.* **12**, 106–117 (2000)
2. Antiga L.: Patient-specific modeling of geometry and blood-flow in large arteries. PhD thesis. Politecnico di Milano, Milan (2003)
3. Caro, C.G., Pedley, T.J., Schroter, R.C., Seed, W.A.: *The Mechanics of the circulation*, Oxford University Press, Oxford, New York (1978)
4. Danilov, A.A.: Unstructured tetrahedral mesh generation technology. *Comp. Math. and Math. Phys.* **50**, 139–156 (2010)
5. Danilov, A.A., Kramarenko, V.K., Nikolaev, D.V., Yurova, A.S.: Personalized model adaptation for bioimpedance measurements optimization. *Russ. J. Numer. Anal. Math. Modelling* **28**, 459–470 (2013)
6. Danilov, A.A., Nikolaev, D.V., Rudnev, S.G., Salamatova, V.Yu., Vassilevski, Yu.V.: Modelling of bioimpedance measurements: unstructured mesh application to real human anatomy. *Russ. J. Numer. Anal. Math. Modelling* **27**, 431–440 (2012)
7. Danilov, A.A., Salamatova, V.Yu., Vassilevski, Yu.V.: Mesh generation and computational modeling techniques for bioimpedance measurements: an example using the VHP data. *J. Phys.: Conf. Series* (2012) doi: 10.1088/1742-6596/407/1/012004
8. Diedrich, K.T., Roberts, J.A., Schmidt, R.H., Parker, D.L.: Comparing performance of centerline algorithms for quantitative assessment of brain vascular anatomy. *Anat. Rec. (Hoboken)*, **295**, 2179 (2012)
9. Frey, P., George, P.-L.: *Mesh generation: application to finite elements*. Hermes Science, Paris, Oxford (2000)
10. Formaggia, L., Quarteroni, A., Veneziani, A.: *Cardiovascular mathematics: Modeling and simulation of the circulatory system*, DE: Springer, Heidelberg (2009)

11. Ganz, V., Hlavova, A., Fronek, A., Linhart, J., Prerovsky, I.: Measurement of blood flow in the femoral artery in man at rest and during exercise by local thermodilution. *Circulation* **30**, 86–89 (1964)
12. Grimnes, S., Martinsen, O.G.: Bioimpedance and bioelectricity basics. Elsevier, Amsterdam (2008)
13. Höhne, K.H., Pflessner, B., Pommert, A., Riemer, M., Schubert, R., Schiemann, T., Tiede, U., Schumacher, U.: A realistic model of human structure from the Visible Human data. *Meth. Inform. Med.* **40**, 83–89 (2001)
14. Hunter, P., Coveney, P.V., de Bono, B., Diaz, V., Fenner, J., Frangi, A.F., Harris, P., Hose, R., Kohl, P., Lawford, P., McCormack, K., Mendes, M., Omholt, S., Quarteroni, A., Skr, J., Tegner, J., Thomas, S.R., Tollis, Tsamardinos, I., I., HGM van Beek, J., Viceconti, A vision and strategy for the virtual physiological human in 2010 and beyond, M.: Philosophical Transactions of the Royal Society A: Mathematical, Physical and Engineering Sciences **368**, 2595–2614 (2010)
15. Kholodov, Y.A., Kholodov, A.S., Simakov, S.S., et al.: Computational models on graphs for nonlinear hyperbolic and parabolic system of equations. *Proc. III European Conf. Comp. Mech.* 43 (2006)
16. Liu, J., Subramanian, K.: Accurate and robust centerline extraction from tubular structures in medical images. In: Advances in Information and Intelligent Systems, part 2, Vol. 251, Springer Berlin Heidelberg, 139–162 (2009)
17. Magomedov, K., Kholodov, A.: Grid-characteristic numerical methods. Nauka, Moscow (1988) (in Russian)
18. Müller, L.O., Parés, C., Toro, E.F.: Well-balanced high-order numerical schemes for one-dimensional blood flow in vessels with varying mechanical properties. *J. Comp. Phys.* **242** 53–85 (2013)
19. Mynard, J.P., Nithiarasu, P.: A 1D arterial blood flow model incorporating ventricular pressure, aortic valve and regional coronary flow using the locally conservative Galerkin (LCG) method. *Comm. Num. Met. Eng.* **24**, 367–417 (2008)
20. Pedley, T.J., Luo, X.Y.: Modelling Flow and Oscillations in Collapsible Tubes. *Theoret. Comput. Fluid Dynamics* **10**, 277–294 (1998)
21. Rineau, L., Yvinec, M.: A generic software design for Delaunay refinement meshing. *Comp. Geom. Theory Appl.* **38**, 100–110 (2007)
22. Sala, R., Rossel, C., Encinas, P., Lahiguera, P.: Continuum of pulse wave velocity from young elite athletes to uncontrolled older patients with resistant hypertension. *J. Hypertens* **28**, 19.216 (2010)
23. Schmidt, R.F., Thews, G.: Human Physiology, Springer-Verlag, Berlin, Heidelberg (1989)
24. Simakov, S.S., Kholodov, A.S.: Computational study of oxygen concentration in human blood under low frequency disturbances. *Mat. Mod. Comp. Sim.* **1**, 283–295 (2009)
25. Simakov, S.S., Gamilov, T.M., Soe, Y.N.: Computational study of blood flow in lower extremities under intense physical load. *Russ. J. Numer. Anal. Math. Mod.* **28**, 485–504 (2013)
26. Simakov, S., Gamilov, T., Vassilevskii, Yu., Ivanov, Yu., Kopylov, P.: Patient specific haemodynamics modeling after occlusion treatment in leg. *Math. Model. Nat. Phenom.* **9**, 85–97 (2014)
27. Standring, S.: Gray's Anatomy: The Anatomical Basis of Clinical Practice, 40th ed., Elsevier, Churchill-Livingstone (2008)
28. Taubin, G.: A signal processing approach to fair surface design. In: Proc. of the 22nd Annual Conf. on Comp. Graphics and Interactive Techniques, 351–358. ACM, N.Y. (1995)

29. Vassilevski, Y.V., Danilov, A.A., Nikolaev, D.V., Rudnev, S.G., Salamatova, V.Y., Smirnov, A.V.: Finite-element analysis of bioimpedance measurements. *Zh. Vych. Mat. Matem. Fiz.* **52**, 733–745 (2012) (in Russian)
30. Vassilevski, Y.V., Simakov, S.S., Dobroserdova, T.K., Salamatova, V.Yu.: Numerical issues of modelling blood flow in networks of vessels with pathologies. *Russ. J. Numer. Anal. Math. Mod.* **26**, 605–622 (2011)
31. Vassilevski, Y.V., Simakov, S.S., Kapranov, S.A.: A multi-model approach to intra-venous filter optimization. *Int. J. Numer. Meth. Biomed. Eng.* **26**, 915–925 (2010)
32. Vassilevski, Y.V., Simakov, S.S., Salamatova, V.Yu., Ivanov, Yu.A., Dobroserdova, T.K.: Blood flow simulation in atherosclerotic vascular network using fiber-spring representation of diseased wall. *Math. Model. Nat. Phenom.* **6**, 333–349 (2011)
33. Vassilevski, Y.V., Simakov, S.S., Salamatova, V.Yu., Ivanov, Yu.A., Dobroserdova, T.K.: Vessel wall models for simulation of atherosclerotic vascular networks. *Math. Model. Nat. Phenom.* **6**, 82–99 (2011)
34. Vassilevski, Y.V., Vershinin, A.V., Danilov, A.A., Plenkin, A.V.: Tetrahedral Mesh Generation in Domains Defined in CAD Systems. In: *Matrix methods and technology for solving large problems*, pp. 21–32. Inst. Num. Math., Moscow (2005) (in Russian)
35. Wilkinson, I.B., Cockcroft, J.R., Webb, D.J.: Pulse wave analysis and arterial stiffness. *J. Cardiovasc. Pharmacol.* **32** Suppl.3, S33–7 (1998)
36. Wu, Z., Sullivan, J.M.: Multiple material marching cubes algorithm. *Int. J. Numer. Meth. Eng.* **58**, 189–207 (2003)
37. Xiao, N., Humphrey, J.D., Figueroa, C.A.: Multi-scale computational model of three-dimensional hemodynamics within a deformable full-body arterial network. *J. Comp. Phys.* **244**, 22–40 (2013)
38. Yushkevich, P.A., Piven, J., Hazlett, H.C., Smith, R.G., Ho, S., Gee, J.C., Gerig, G.: User-guided 3D active contour segmentation of anatomical structures: significantly improved efficiency and reliability. *Neuroimage* **31**, 1116–1128 (2006)
39. Advanced Numerical Instruments 3D  
<http://sourceforge.net/projects/ani3d>
40. The National Library of Medicine's Visible Human Project, <http://www.nlm.nih.gov/research/visible>
41. <http://www.vmtk.org>
42. <http://www.amira.com>, <http://www.vsg3d.com/amira>
43. Anatomy 3D Models – Plasticboy. <http://www.plasticboy.co.uk>
44. <http://www.inm.ras.ru/research/bioimpedance>

# **MS&A – Modeling, Simulation and Applications**

---

## **Series Editors:**

Alfio Quarteroni  
École Polytechnique Fédérale  
de Lausanne (Switzerland)

Tom Hou  
California Institute of Technology  
Pasadena, CA (USA)

Claude Le Bris  
École des Ponts ParisTech  
Paris (France)

Anthony T. Patera  
Massachusetts Institute of Technology  
Cambridge, MA (USA)

Enrique Zuazua  
Basque Center for Applied  
Mathematics  
Bilbao (Spain)

## **Editor at Springer:**

Francesca Bonadei  
[francesca.bonadei@springer.com](mailto:francesca.bonadei@springer.com)

1. L. Formaggia, A. Quarteroni, A. Veneziani (Eds.)  
Cardiovascular Mathematics  
2009, XIV+522 pp, ISBN 978-88-470-1151-9
2. A. Quarteroni  
Numerical Models for Differential Problems  
2009, XVI+602 pp, ISBN 978-88-470-1070-3
3. M. Emmer, A. Quarteroni (Eds.)  
MATHKNOW  
2009, XII+264 pp, ISBN 978-88-470-1121-2
4. A. Alonso Rodríguez, A. Valli  
Eddy Current Approximation of Maxwell Equations  
2010, XIV+348 pp, ISBN 978-88-470-1934-8
5. D. Ambrosi, A. Quarteroni, G. Rozza (Eds.)  
Modeling of Physiological Flows  
2012, X+414 pp, ISBN 978-88-470-1934-8
6. W. Liu  
Introduction to Modeling Biological Cellular Control Systems  
2012, XII+268 pp, ISBN 978-88-470-2489-2

7. B. Maury  
The Respiratory System in Equations  
2013, XVIII+276 pp, ISBN 978-88-470-5213-0
8. A. Quarteroni  
Numerical Models for Differential Problems, 2nd Edition  
2014, XX+656pp, ISBN 978-88-470-5521-6
9. A. Quarteroni, G. Rozza (Eds.)  
Reduced Order Methods for modeling and computational reduction  
2014, X+332pp, ISBN 978-3-319-02089-1
10. J. Xin, Y. Qi  
Mathematical Modeling and Signal Processing in Speech and Hearing Sciences  
2014, XII+208pp, ISBN 978-3-319-03085-2
11. L. Beirão da Veiga, K. Lipnikov, G. Manzini  
The Mimetic Finite Difference Method for Elliptic Problems  
2014, XVI+392pp, ISBN 978-3-319-02662-6
12. E. Cristiani, B. Piccoli, A. Tosin  
Multiscale Modeling of Pedestrian Dynamics  
2014, XVI+260pp, ISBN 978-3-319-06619-6
13. P. Colli Franzone, L. Franco Pavarino, S. Scacchi  
Mathematical Cardiac Electrophysiology  
2014, XIV+399pp, ISBN 978-3-319-04800-0
14. A. Quarteroni (Ed.)  
Modeling the Heart and the Circulatory System  
2015, XIV+236pp, ISBN 978-3-319-05229-8

For further information, please visit the following link:  
<http://www.springer.com/series/8377>